Max-Planck-Institut
für Meteorologie

MAX-PLANCK-GESELLSCHAFT

Climate and Climate Variability in an Aquaplanet Set-up

Eileen Dahms

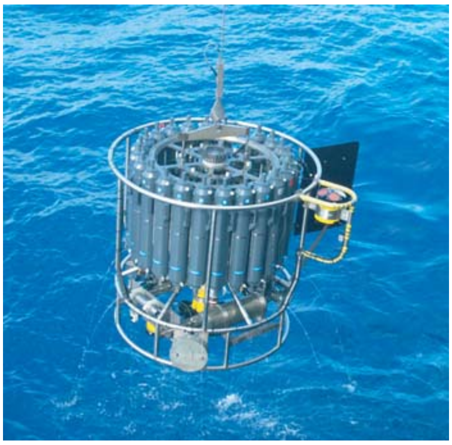

Berichte zur Erdsystemforschung

132
2013

Reports on Earth System Science

Hinweis

Die Berichte zur Erdsystemforschung werden vom Max-Planck-Institut für Meteorologie in Hamburg in unregelmäßiger Abfolge herausgegeben.

Sie enthalten wissenschaftliche und technische Beiträge, inklusive Dissertationen.

Die Beiträge geben nicht notwendigerweise die Auffassung des Instituts wieder.

Die "Berichte zur Erdsystemforschung" führen die vorherigen Reihen "Reports" und "Examensarbeiten" weiter.

Notice

The Reports on Earth System Science are published by the Max Planck Institute for Meteorology in Hamburg. They appear in irregular intervals.

They contain scientific and technical contributions, including Ph. D. theses.

The Reports do not necessarily reflect the opinion of the Institute.

The "Reports on Earth System Science" continue the former "Reports" and "Examensarbeiten" of the Max Planck Institute.

Anschrift / Address

Max-Planck-Institut für Meteorologie
Bundesstrasse 53
20146 Hamburg
Deutschland

Tel.: +49-(0)40-4 11 73-0
Fax: +49-(0)40-4 11 73-298
Web: www.mpimet.mpg.de

Layout:

Bettina Diallo, PR & Grafik

Titelfotos:
vorne:
Christian Klepp - Jochem Marotzke - Christian Klepp
hinten:
Clotilde Dubois - Christian Klepp - Katsumasa Tanaka

Berichte zur Erdsystemforschung 132/2013

Climate and Climate Variability in an Aquaplanet Set-up

Eileen Dahms

aus Henstedt Ulzburg

Hamburg 2013

Reports on Earth System Science 132/2013

ISSN 1614-1199

Eileen Dahms

Meteorologisches Institut der Universität Hamburg
Bundesstrasse 55

Max-Planck-Institut für Meteorologie
Bundesstrasse 53
20146 Hamburg

Als Dissertation angenommen
vom Department Geowissenschaften der Universität Hamburg

auf Grund der Gutachten von
Prof. Dr. Klaus Fraedrich
und
Dr. Frank Lunkeit

Hamburg, den 22. Januar 2013
Prof. Dr. Jürgen Oßenbrügge
Leiter des Departments für Geowissenschaften

ISSN 1614-1199

Climate and Climate Variability in an Aquaplanet Set-up

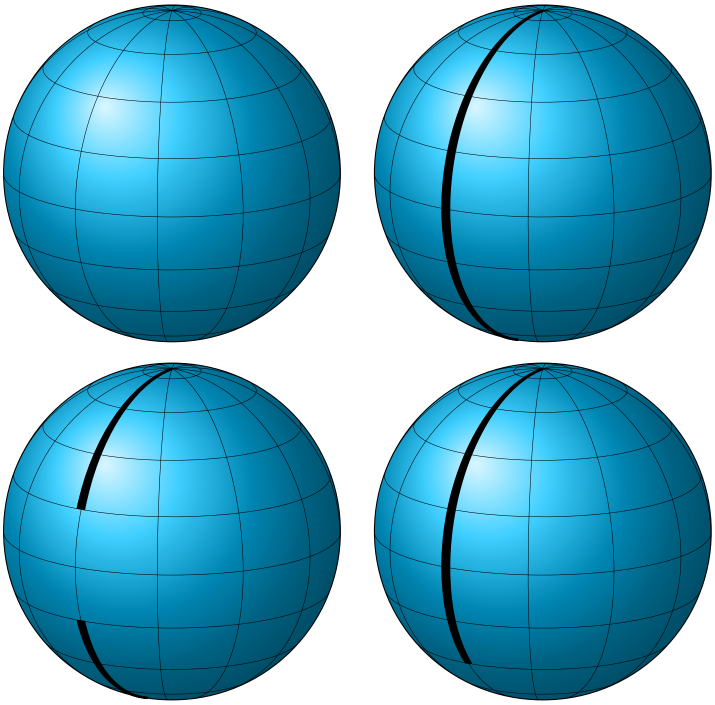

Eileen Dahms

Hamburg 2013

Abstract

There are many fundamental problems in climate research, which have not been solved up to this day. This thesis aims at contributing to a better understanding of the influence of topographic ocean barriers on the circulation regime and the global climate state, of internally generated long-term variability mechanisms, and of processes that may be responsible for past climate changes, in particular for the onset of the Antarctic glaciation. To address these questions, an idealized model of atmosphere and ocean is applied. While complex models, which simulate the climate system as realistically as possible, have many advantages, idealized models are very helpful tools to understand basic physical mechanisms. Aquaplanets are used for studying the climate in its most elemental form by reducing the complex Earth system to its fundamental governing processes.

In the first part of this thesis, different aquaplanet configurations are analyzed, which contain meridional barriers in the ocean. While the pure aquaplanet cannot support geostrophically balanced flow, the insertion of a meridional barrier completely alters the ocean circulation regime. Moreover, the impact of ocean gateways is studied. A passage in the barrier, which is located in the tropics (representing the isthmus of Panama), causes strong equatorial upwelling but also increased poleward ocean heat transport at higher latitudes. An idealized Drake Passage (a passage in the barrier located in the southern ocean) leads to a large cross-equatorial overturning cell in the ocean with increased northward and decreased southward ocean heat transport.

In the second part of the study, long-term variability of the aquaplanet climate is analyzed. The main feature is a very dominant low-frequency oscillation between colder and warmer climate states with a period of approximately 700 years. The warm phases are characterized by ice-free polar waters and a weaker meridional overturning circulation. During cold phases, the poles are completely covered with sea ice and the meridional overturning cells are stronger. The climate state changes throughout atmosphere and ocean, however, surface areas in high latitudes are especially affected due to the changing sea ice cover.

In the third part of this thesis, sensitivity simulations are conducted to test three hypotheses about the onset of the Antarctic glaciation: the opening of the Drake Passage, declining atmospheric CO_2, and changing orbital parameters. The simulations are carried out under idealized conditions to focus on the essentials. When all three forcings are included, temperatures decrease and snow accumulates, creating favorable conditions for glaciation. The relative importance of each forcing is explored. While all mechanisms indeed cool the climate of the southern high latitudes, the contributions from declining CO_2 and from the opening of the Drake Passage are relatively small compared to the impact of changing orbital parameters, which appears to be the main forcing in this set-up.

Zusammenfassung

Es gibt immer noch viele grundlegende Fragen in der Klimawissenschaft, die bis heute nicht beantwortet werden konnten. Diese Dissertation hat zum einen das Ziel, den Einfluss von topographischen Hindernissen im Ozean auf die Zirkulation und auf das globale Klima zu untersuchen. Zum anderen soll sie zu einem besseren Verständnis von intern erzeugter, langfristiger Klimavariabilität und von Prozessen, die für vergangene Klimaveränderungen, insbesondere für die Vereisung der Antarktis, verantwortlich sind, beitragen. Um sich mit diesen Fragen zu befassen, wird ein idealisiertes Modell von Atmosphäre und Ozean verwendet. Während komplexe Modelle das Klimasystem so wirklichkeitsgetreu wie möglich abbilden, sind idealisierte Modelle hilfreiche Instrumente, um einfache Mechanismen zu verstehen. Aquaplaneten, in denen das komplexe Erdsystem auf seine fundamentalen, wichtigsten Prozesse reduziert wird, werden angewandt, um das Klima in seiner elementarsten Form zu untersuchen.

Im ersten Teil dieser Arbeit werden Aquaplaneten analysiert, die um unterschiedliche meridionale Begrenzungen im Ozean erweitert werden. Während der reine Aquaplanet keine geostrophisch ausbalancierte Strömung aufrecht erhalten kann, wird die Ozeanzirkulation durch das Einsetzen einer meridionalen Berandung komplett modifiziert. Darüber hinaus wird der Einfluss von Meeresstraßen untersucht. Wenn die Berandung eine Passage in den Tropen aufweist (die den Isthmus von Panama repräsentiert), hat dies äquatorialen Tiefenwasseraufstieg zur Folge sowie verstärkten polwärtigen ozeanischen Wärmetransport in höheren Breiten. Eine idealisierte Drake Passage (im Südpolarmeer) führt zu einer großen interhemisphärischen Zirkulationszelle im Ozean mit verstärktem nordwärts und abgeschwächtem südwärts gerichteten ozeanischen Wärmetransport.

Im zweiten Teil wird die langfristige Klimavariabilität des Aquaplaneten untersucht. Hauptsächlich ergibt sich eine ausgeprägte, niederfrequente Schwankung zwischen kälteren und wärmeren Klimazuständen mit einer Periode von ca. 700 Jahren. Die warmen Phasen sind durch eisfreie Polarmeere und eine schwächere meridionale Umwälzbewegung gekennzeichnet. In kälteren Phasen sind die Pole mit Eis bedeckt und die Zellen der Umwälzzirkulation sind stärker ausgeprägt. Das Klima ändert sich in Atmosphäre und Ozean, wobei die Meeresoberflächen durch die schwankende Meereisbedeckung besonders stark betroffen sind.

Im dritten Teil der Arbeit werden Sensitivitätsstudien durchgeführt, um drei Hypothesen zu untersuchen, die die Vereisung der Antarktis erklären sollen: die Öffnung der Drake Passage, abnehmendes atmosphärisches CO_2 und sich verändernde Erdbahnparameter. Um sich auf die wesentlichen Mechanismen zu konzentrieren, werden die Simulationen unter idealisierten Bedingungen durchgeführt. Unter Einbezug aller drei Antriebe nehmen die Temperaturen ab und Schnee akkumuliert, was günstige Bedingungen für eine Vereisung schafft. Die relative Bedeutung jedes einzelnen Einflussfaktors wird untersucht. Obwohl alle Mechanismen zu einer Abkühlung des Klimas der südlichen hohen Breiten beitragen, sind die Anteile vom abnehmenden CO_2 und von der Öffnung der Drake Passage relativ klein im Vergleich zur Auswirkung der veränderten Erdbahnparameter, dem wichtigsten Einflussfaktor in dieser Studie.

Contents

1 Introduction

> *"If we knew what it was*
> *we were doing, it would*
> *not be called research,*
> *would it?"*
> — Albert Einstein

In climate science the methods that are available to observe or to model the atmosphere and the ocean improve continuously. Since the introduction of satellite remote sensing into climate research, an entirely new spectrum of possibilities has opened up and many phenomena have been discovered or documented. Hubert *et al.* (1969), for example, were among the first to employ satellite images to prove the existence of double intertropical convergence zones (ITCZs). While satellites have been by far the greatest advancement and remote sensing techniques are constantly refined, new observation technologies are regularly introduced into climate science. Furthermore, over the past decades there has been huge progress in climate modeling and general circulation models (GCMs) have benefited greatly from enhanced computational power. While model formulations and parameterizations are becoming more sophisticated, the increasing computational resources allow a finer resolution, faster (and therefore longer) simulations, and the explicit inclusion of more differentiated processes. Hence, climate simulations increasingly improve.

In spite of the considerable progress already achieved in climate research, fundamental questions about our climate system remain that have not been answered up to this day. Abrupt climate changes are, for example, not well understood. There is ample evidence from paleorecords that the climate system is not only slowly varying but may also undergo sudden shifts from one regime to another (Broecker *et al.*, 1985; Dansgaard *et* *al.*, 1993; Jouzel *et al.*, 1995). However, what sets the time scales of these abrupt climate changes and what causes them, is still under discussion. The role of the ocean, more specifically the thermohaline circulation (THC), has often been studied in this context (e.g. Winton & Sarachik, 1993; Rahmstorf, 1995), but a definite answer has not been given.

A prominent example of past climate changes is the glaciation of Antarctica, for which the main forcing mechanism remains to be determined. The opening of the Drake Passage and the subsequent build-up of the Antarctic Circumpolar Current (ACC) has often been in the center of discussion (e.g. Mikolajewicz & Maier-Reimer, 1993; Toggweiler & Bjornsson, 2000; Sijp & England, 2004; Cristini *et al.*, 2012). If and how the opening of an ocean gateway has influenced the global climate has not been conclusively answered. More generally, the question how topographic constraints on the ocean circulation impact the global climate or have influenced the climate during past eras has not yet been fully answered.

Closely connected to sudden climate changes are multiple steady states of the climate. Lorenz (1968, 1970) discusses implications for the climate system if the governing equations allow more than one stable solution. While multiple equilibria have often been observed in simple models of the Earth system as, for example, in studies on multiple states of the THC (e.g. Stommel, 1961; Marotzke & Willebrand, 1991), on vegetation cover (e.g. Claussen, 1998), or on the ice–albedo feedback (e.g. Budyko, 1969; Sellers, 1969), their existence has not been demonstrated in complex atmosphere–ocean general circulation models (with the exception of a recent study by Ferreira *et al.*, 2011). So far they are not well understood and the question remains whether they even exist.

Oscillations in the climate system can be observed on many time scales and are often caused by internal feedback processes, which are still not completely determined. Examples for such internal climate oscillations are, amongst others, the AMO (Atlantic Multidecadal Oscillation, Jungclaus *et al.*, 2005), ENSO (El Niño–Southern Oscillation, Neelin *et al.*, 1998), the QBO (Quasi-Biennial Oscillation, Wang *et al.*, 1995). Understanding feedback mechanisms within the climate system is essential when dealing with climate variations on long time scales.

There are different approaches to address these (and many more) open questions in climate research. One possibility is to achieve higher levels of complexity and resolution in climate models or to further improve observational techniques. A more detailed description of the climate state can indeed help to better explain climate phenomena and to make better predictions. However, for understanding basic climate processes, this approach is not always the most suitable and, for example, Held (2005) discusses the gap between simulation and understanding in climate modeling.

Another approach refrains from applying increasingly complex techniques and does not aim at describing the climate state as realistically as possible, but is rather directed at understanding the underlying mechanisms. If the model is confined to the most elemental processes, fundamental characteristics of the coupled climate system become easier to identify. The philosophy behind this method is to first understand the basic and most fundamental processes, before including more complex phenomena into the model of the climate system. This is the approach chosen in this study by means of applying an aquaplanet concept. An aquaplanet is a planet, where the entire surface of the Earth is covered with an ocean with a flat bottom and without any geometrical constraints. Aquaplanets can be a very useful tool for analyzing the climate state in its most elemental form, representing only a crude approximation of the Earth but with the same governing processes.

The purpose of this work is to study different climate regimes and climate changes on long time scales, which are either internally generated or externally forced. Idealized topographical set-ups are applied, which create fundamentally different ocean circulation regimes and global climate conditions. The mean state and the variability of climate systems, in which complexities caused by land–sea configurations are reduced, are studied with a full general circulation model which represents the dynamics of the climate system. Long-term numerical simulations are conducted with a coupled global atmosphere–ocean–sea ice model of intermediate complexity (MIC) in various (expanded) aquaplanet configurations.

While state-of-the-art climate models are becoming increasingly complex and higher resolutions can be achieved with more computational resources, models of intermediate complexity still have several advantages over complex Earth system models (ESMs). Simpler models, which gradually reduce the climate system to the key mechanisms, are a helpful tool in fundamental climate research and are particularly suitable for hypothesis testing. Some applications are, for example, hysteresis experiments (e.g. Lucarini *et al.*, 2010), studies on the transient evolution of Earth's climate (e.g. Crucifix *et al.*, 2002; Weber *et al.*, 2004; Tuenter *et al.*, 2005), and the evolution of ice sheets (e.g. Loutre & Berger, 2000; Swingedouw *et al.*, 2008). Abrupt climate changes or different steady states of the thermohaline circulation (e.g. Rahmstorf *et al.*, 2005; Knorr & Lohmann, 2007) are problems often addressed with models of intermediate complexity. MICs describe the dynamics of atmosphere and ocean in less detail but still apply sophisticated parameterizations and explicitly resolve the geophysical fluid dynamics equations, though with a coarse resolution (for a more detailed description of MICs see for example Claussen *et al.* 2002 or Weber 2010). Most importantly for this study, general circulation models of reduced complexity and with a lower resolution are able to simulate long periods of time in relative short real time and are often applied for studies on slow climate variations on long-time scales.

Aquaplanets offer completely zonally symmetric boundary conditions, since they are entirely covered with an ocean surface and do not contain any land masses. They provide an ideal test environment, since many characteristics of the zonal mean climate of the Earth are hardly affected by orographic barriers or the presence of land masses. It is emphasized, however, that aquaplanets are neither meant to produce very "realistic" climates, nor are they supposed to represent a past, present, or future scenario of the Earth's climate, but basic mechanisms and feedbacks can be highlighted and explored in an aquaplanet environment. Without complex land–sea distributions, many climate features are easier to analyze and can be compared to theoretical studies and conceptual models.

In the past, the aquaplanet set-up has mostly been used with atmosphere-only models and prescribed sea surface temperature (SST) distributions. For example, Hess *et al.* (1993) simulate an aquaplanet with prescribed SSTs to analyze the sensitivity of the ITCZ to the latitudinal distribution of SSTs. Similar numerical experiments have been conducted by Chao & Chen (2004). Neale & Hoskins (2001b,a) describe an aquaplanet intercomparison project with different meridional SST profiles. Dahms *et al.* (2011) investigate ITCZ splitting and the influence of large-scale eddies on the zonal mean circulation in an aquaplanet environment with various prescribed SST distributions. The aim of these studies is to investigate convection and large-scale motions over a zonally uniform region. As the entire surface is covered with water and the SST is zonally uniform and symmetric about the equator, the occurrence of moist convection is equally likely in the longitudinal direction, which is the great advantage of an aquaplanet with prescribed SSTs.

However, an aquaplanet is still a rough approximation of the Earth, especially with an atmosphere-only model and constant SST distributions. The atmosphere is driven by the prescribed surface temperatures, while in reality the SST is affected by the atmospheric and oceanic circulation, the incoming and outgoing radiation, and the surface fluxes. It has to be acknowledged that the ocean plays an important role for the global climate system and in particular for the Earth's energy budget: It acts as a heat buffer to mitigate strong atmospheric temperature changes and it transports heat around the globe (Trenberth & Caron, 2001). Furthermore, it is assumed that changes in the thermohaline circulation of the ocean have greatly influenced the climate of the Earth in the past (e.g. Broecker *et al.*, 1985; McManus *et al.*, 2004). There are numerous studies on the effects of a changing ocean circulation, covering simulations under realistic settings (e.g. Bryan *et al.*, 1975; Houghton *et al.*, 2001) and rather idealized configurations (e.g. Bryan, 1986; Cox, 1989; Marotzke & Willebrand, 1991; Bjornsson & Toggweiler, 2001), which have shown that the ocean is capable of having a significant impact on the global climate state.

A coupled model approach is called for and the model needs to include three-dimensional oceanic and atmospheric flow. Ocean heat fluxes force the atmosphere and, in turn, the distribution of atmospheric energy (heat flux), moisture (freshwater flux), and momentum (wind stress) are the prevalent driving mechanisms for the ocean.

Pike (1971) started the line of research on aquaplanets with coupled models by adding a simple two-layer ocean model to a primitive equation atmospheric model. However, a fully coupled atmosphere–ocean general circulation model (AOGCM) was first applied to an aquaplanet by Smith *et al.* (2006). They use the aquaplanet set-up to investigate the impact of the ocean circulation on the ability to transport heat around the globe. In the resulting warm climates (considerably warmer than present-day observations) with shallow equator-to-pole temperature gradients, sea ice does not form at any time of the year.

A study by Marshall *et al.* (2007) followed, with subsequent work by Enderton & Marshall (2009) and Ferreira *et al.* (2010, 2011). Marshall *et al.* analyze the mean climate and the variability of an aquaplanet with a coupled AOGCM. The simulation leads to a climate with ice caps over the poles and strong meridional temperature gradients. Enderton & Marshall concentrate on different ocean settings, however, in their pure aquaplanet they find a similar climate as Marshall *et al.* The mean state of the aquaplanet simulations by Marshall *et al.* and Enderton & Marshall differ significantly from the results of Smith *et al.* Marshall *et al.* believe that differences in the ocean model formulation are the primary source for these discrepancies. Furthermore, Enderton &

Marshall show that the system of Smith *et al.* was not integrated out to equilibrium and that the presence of strong lateral diffusive fluxes in the ocean model caused unrealistically large meridional (diffusive) heat fluxes.

Ferreira *et al.* (2010, 2011), however, find that the aquaplanet exhibits multiple stable states. Besides the cold climate state with sea ice caps over the poles (presented in Marshall *et al.*, 2007), there is an ice-free warm solution (presented in Ferreira *et al.*, 2010). A snowball state is also observed, in which the entire surface of the planet is covered with sea ice (presented in the appendix of Ferreira *et al.*, 2011). Ferreira *et al.* (2011) find these multiple stable states in two fundamentally different configurations and conclude that the existence of multiple equilibria relies on rather robust dynamical features.

The aquaplanet environment is chosen to exclude external forcings and especially effects of orography. However, there are a series of aquaplanet studies with coupled models that include meridional barriers in the ocean and therefore topographical effects. One reason for this approach is to get stepwise closer to reality. The ocean circulation of an aquaplanet deviates greatly from the circulation in the Atlantic or Pacific Ocean. In the absence of zonal pressure gradients, zonally integrated meridional flow cannot be supported by geostrophy. By inserting a meridional barrier in the ocean, a closed basin is created and Sverdrup balance can be supported. Thus, the ocean circulation regime resembles that of our present-day climate (in the Atlantic or Pacific ocean basin) more closely.

For example Marotzke & Willebrand (1991), Toggweiler & Bjornsson (2000), and Hotinski & Toggweiler (2003) present coupled simulations with idealized ocean basin geometries, but employ energy balance models (EBMs) for the atmosphere with prescribed surface wind patterns. Marotzke & Willebrand only preserve the major geometrical features of the global ocean (ignoring the possible role of the Indian Ocean): two meridional ocean barriers create two ocean basins, which are connected in the southern ocean by a circumpolar channel (representing the Atlantic and Pacific ocean basin and the Antarctic Circumpolar Current, ACC) to study which fundamentally different patterns of the global thermohaline circulation may possibly be achieved. Marotzke & Willebrand observe four different stable steady states for the THC in their idealized ocean set-up. Toggweiler & Bjornsson use a highly idealized geometry to simulate the effect of the Drake Passage on the Earth's climate. They apply an aquaplanet configuration with small polar islands and a meridional barrier in the ocean that contains an opening near the south pole (representing the Drake Passage). Toggweiler & Bjornsson observe that a strong cooling effect occurs in the southern hemisphere when the passage is opened, which is caused by a cross-equatorial overturning circulation and westerly winds over the open channel. Hotinski & Toggweiler apply a similar land–sea set-up as Toggweiler & Bjornsson: an expanded aquaplanet containing two polar islands connected by a meridional barrier. In this case, the passage in the barrier is located in low latitudes simulating a circumglobal Tethyan or Panama gateway. This tropical ocean gateway induces high rates of wind-driven upwelling of cool water from the deep ocean.

Fully coupled atmosphere–ocean general circulation models (AOGCMs) are applied by Smith *et al.* (2006), Enderton & Marshall (2009), and Ferreira *et al.* (2010), who extend the pure aquaplanet set-up to an idealized land–sea configurations including meridional ocean barriers. Smith *et al.* insert a meridional barrier into their aquaplanet ocean and investigate the role of the ocean circulation in the coupled system, in particular the importance of geometrical constraints on the ability of the climate system to transport heat around the globe. The experimental set-up employed by Smith *et al.* includes an aquaplanet that contains a single closed meridional barrier from pole-to-pole ("RidgeWorld") and an idealized Drake Passage, i.e. an aquaplanet with a ridge that contains a passage in the southern ocean ("DrakeWorld"). They find that even though changes in the land–sea configuration cause regional climate deviations, there is hardly an impact on heat transports within the system. Enderton & Marshall apply different aquaplanet configurations to explore the degree to which the total meridional heat transport is sensitive to the details of its atmospheric and oceanic components: One configuration contains a barrier running continuously from pole-to-pole ("Ridge"), one has a barrier with a passage in the tropics ("EqPas") and one has a barrier with a passage at the south pole ("Drake"). The different set-ups result in completely different climate states, of which the "Drake" solution shows the closest resemblance to our present-day climate. Ferreira *et al.* insert a second barrier (with a passage in the southern ocean) into the "Drake" set-up ("Double–Drake"). They find that when moving from "Aqua" to "Ridge" to "Drake" to "Double–Drake", the energy transports become increasingly realistic.

The energy transport[1] from low to high latitudes warms the poles and cools the tropics and, hence, is a very important feature of the climate. Smith *et al.*, Enderton & Marshall, and Ferreira *et al.* concentrate on meridional energy transports and the results are discussed with regard to a study by Stone (1978). Stone provides a theoretical basis for the suggestion initially proposed by Bjerknes (1964) (and since supported by many subsequent studies, e.g. Manabe *et al.* 1975; Clement & Seager 1999; Winton 2003) that the sum of the oceanic and atmospheric meridional energy transports generally remains constant throughout any changes imposed on the system. Stone found that the controlling factors on the strength and structure of this transport are limited to the size of the Earth, the rotation rate, the axis tilt, the solar constant, and the mean hemispheric albedo. The highly idealized set-up of an aquaplanet and the set-ups of expanded aquaplanets including topographical constraints on the ocean circulation represent ideal test environments for this theory.

The ocean circulation regime greatly influences the strength and structure of the ocean heat transport (OHT). Deviations in the OHT create different meridional temperature gradients, which again have an impact on the atmospheric circulation. Besides the atmospheric and oceanic circulation and the energy budget and transports, main characteristics of different aquaplanet climate regimes can be studied, for example, by means of analyzing temperatures in atmosphere and ocean, the sea ice coverage, and

---

[1] Throughout this work the terms "energy transport" and "heat transport" are used synonymously, although it should be kept in mind that kinetic energy is negligible and not included in the total energy of atmosphere or ocean. In case of the ocean, the flux of potential energy and the pressure work term practically cancel each other because the ocean water is almost incompressible and, thus, the total energy transport in the ocean reduces to the transport of heat. However, as Warren (1999) points out, the term "heat flux" is misleading since heat is not a fluid property that can be advected by the circulation.

the hydrological cycle.

This work is partitioned into three studies, which aim to contribute to the following questions:

> *How do topographic boundaries define the circulation regime and the zonal mean climate state of atmosphere and ocean?*
>
> *What kind of internally generated long-term variability mechanisms exist and what are their underlying physical processes?*
>
> *Which processes are responsible for climate changes of the past, for example the onset of the Antarctic glaciation?*

1.1 Outline

The three studies deal with different climate states and long-term climate changes under idealized topographical boundary conditions. Each study is structured into a chapter of its own including an introduction, a description of the experimental design, and a summary and discussion of the results.

The thesis is structured into six chapters (including the introductory remarks in this chapter) containing the following:

- **Chapter 2 — The Coupled Model:** The coupled atmosphere–ocean–sea ice general circulation model applied in this study is described in chapter 2. For the atmosphere the Planet Simulator, a spectral model of intermediate complexity, is used. A short overview of the model dynamics and parameterizations of the Planet Simulator is given. Furthermore, the thermodynamic sea ice model is introduced. The Planet Simulator is coupled to the Hamburg Large Scale Geostrophic (LSG) ocean model. An introduction to the LSG model and a short description of the coupling between the atmospheric and oceanic model are provided. Information is given on how the aquaplanet set-up is realized in the coupled model.

- **Chapter 3 — Aquaplanets with Idealized Ocean Barriers:** The circulation regimes and zonal mean climate states of various aquaplanet configurations with idealized meridional barriers in the ocean are studied in chapter 3. Besides the pure aquaplanet, set-ups are applied with an ocean barrier that runs either continuously from pole-to-pole or leaves a passage in the tropics (simulating, though highly idealized, the isthmus of Panama) or in the southern ocean (creating an idealized Drake Passage). Furthermore, a configuration with two ocean barriers is used, creating two basins which resemble the Atlantic and Pacific. It is studied how a single topographic feature (an ocean barrier) completely alters the ocean circulation regime and, thus, the global climate. The zonal mean climate states are analyzed and intercompared. Moreover, the climate states are compared to results from previous studies to test the aquaplanet configuration of the coupled model.

- **Chapter 4 — Low-frequency Climate Variability:** The climate variability of the pure aquaplanet is analyzed in chapter 4. A very dominant low-frequency oscillation between warm, ice-free climate states and cold climates with high sea ice cover can be observed. All compartments of the aquaplanet climate system are included in the oscillation: atmosphere, ocean, and sea ice. This long-periodic oscillation is completely internally generated and all external forcings are kept constant throughout the integration. The low-frequency climate variability of the aquaplanet is studied in detail with various time series analysis techniques. Even though this aquaplanet climate oscillation cannot be transferred directly to a past or present climate phase of the Earth, a thorough analysis contributes to a better understanding of the variability of the coupled climate system on very long time scales.

- **Chapter 5 — The Onset of the Antarctic Glaciation:** An application of the aquaplanet concept to a past climate phase of the Earth is presented in chapter 5 in the study of the onset of the Antarctic glaciation. The coupled atmosphere–ocean–sea ice model is applied in idealized numerical sensitivity simulations testing three hypotheses concerning the triggering of the build-up of the Antarctic Ice Sheet (AIS): *(1)* declining atmospheric CO_2, *(2)* the opening of the Drake Passage, and *(3)* changing orbital parameters. To focus on the essentials, an expanded aquaplanet set-up is applied by including two topographical features in a planet covered with a single ocean: a circular continent at the south pole representing Antarctica and a meridional barrier in the ocean. The latter allows to mimic a closed or open Drake Passage. When all three forcings are included, temperatures decrease and snow accumulates, creating conditions for a glaciation of the southern polar continent. Furthermore, the relative importance of each possible forcing is explored.

- **Chapter 6 — Conclusion:** The three parts of this study (the chapters “Aquaplanets with Idealized Ocean Barriers”, “Low-frequency Climate Variability”, and “The Onset of the Antarctic Glaciation”) are summarized and discussed in chapter 6. Furthermore, the conclusions are evaluated in the context of previous studies and discrepancies between the findings as well as problems with the results are discussed. An outlook for possible future work is given.

The appendix contains supplementary information. Appendices A and B explain symbols and abbreviations used this work. A list of all figures can be found in appendix C. Statistical methods applied in this study are explained in appendix D. The computation of meridional energy transports is described in appendix E. Supplementary information about the LSG ocean model is given in appendix F. Appendix G explains how the coupled model can be run in an aquaplanet set-up.

2 The Coupled Model

> *"The atmosphere is neither a laboratory experiment nor a set of numbers in a computer, and we cannot turn it off and then set it in motion again to see whether a new climate develops."*
>
> — Edward N. Lorenz

This study is carried out with a coupled atmosphere–ocean–sea ice general circulation model. For the atmospheric part, the Planet Simulator (Fraedrich *et al.* 2005a; and for an update overview Fraedrich 2012) is employed. The Planet Simulator is coupled to the Hamburg Large Scale Geostrophic (LSG) ocean model (Maier-Reimer *et al.*, 1993). The coupled model includes a thermodynamic sea ice model.

2.1 The Planet Simulator

The Planet Simulator is an atmospheric general circulation model (AGCM) which has been developed at the University of Hamburg. In this section a short introduction to the dynamical core and the parameterizations of the Planet Simulator is given. The following information comes mostly from the model's manual by Lunkeit *et al.* (2011), where more details can be found. The Planet Simulator is an open source model and freely available (together with the model's documentation) at *http://www.mi.uni-hamburg.de/plasim.*

The Planet Simulator is a Model of Intermediate Complexity (MIC), which holds several advantages over more complex models. Less sophisticated models can more easily be applied for studies aiming at understanding climate phenomena by gradually simplifying the system to reveal key mechanisms. Furthermore, MICs are able to simulate long periods of time (millennia and longer) in relatively short real time and can be used with less powerful hardware. The Planet Simulator is portable to various platforms and the system is scalable with regard to the vertical and horizontal resolutions. The model is also able to simulate atmospheres of other planets and moons.

MICs, like the Planet Simulator, are applied in education and for gaining practice with climate models. Since the Planet Simulator is applied in an university environment, it has to fulfill several conditions:

- The code must be open access and freely available together with the software required to run it.
- The model should be user friendly and have a graphical user interface (GUI).
- It should be suitable for teaching project studies, i.e. students should be able to run the model without the help of technicians.

The dynamical core of the Planet Simulator consists of a general circulation model (GCM) based on the Portable University Model of the Atmosphere (PUMA, Fraedrich *et al.*, 2005b), which runs with linear processes, such as Newtonian cooling and Rayleigh friction. Though simple, PUMA has a wide spectrum of applications in fundamental research. Besides the atmospheric circulation, the Planet Simulator includes other compartments of the climate system, like an ocean with sea ice and a land surface with biosphere. The coupling to other compartments is visualized in figure 2.1.

2.1.1 Model Dynamics

The dynamical core is based on a dimensionless set of moist primitive equations, which are expressed in a spherical coordinate system (the (λ, μ, σ)-coordinates, Hoskins & Simmons 1975). In the vertical direction a terrain following σ-coordinate system is used, where σ represents the pressure normalized by the surface pressure ($\sigma = p/p_s$). In the σ-system the lower boundary (at $\sigma = 1$) exactly follows the orography. The horizontal coordinates are represented by the latitude, φ (with $\mu = \sin\varphi$), and the longitude, λ.

From the conservation of momentum, prognostic equations for the vertical component of the vorticity, ξ, and the horizontal divergence, D, are obtained (see equations 2.1 and 2.2). The equation of state is simplified by the hydrostatic approximation (equation 2.3). The continuity equation is derived from the conservation of mass (equation 2.4). The first law of thermodynamics requires the conservation of energy and yields to the thermodynamic equation (equation 2.5).

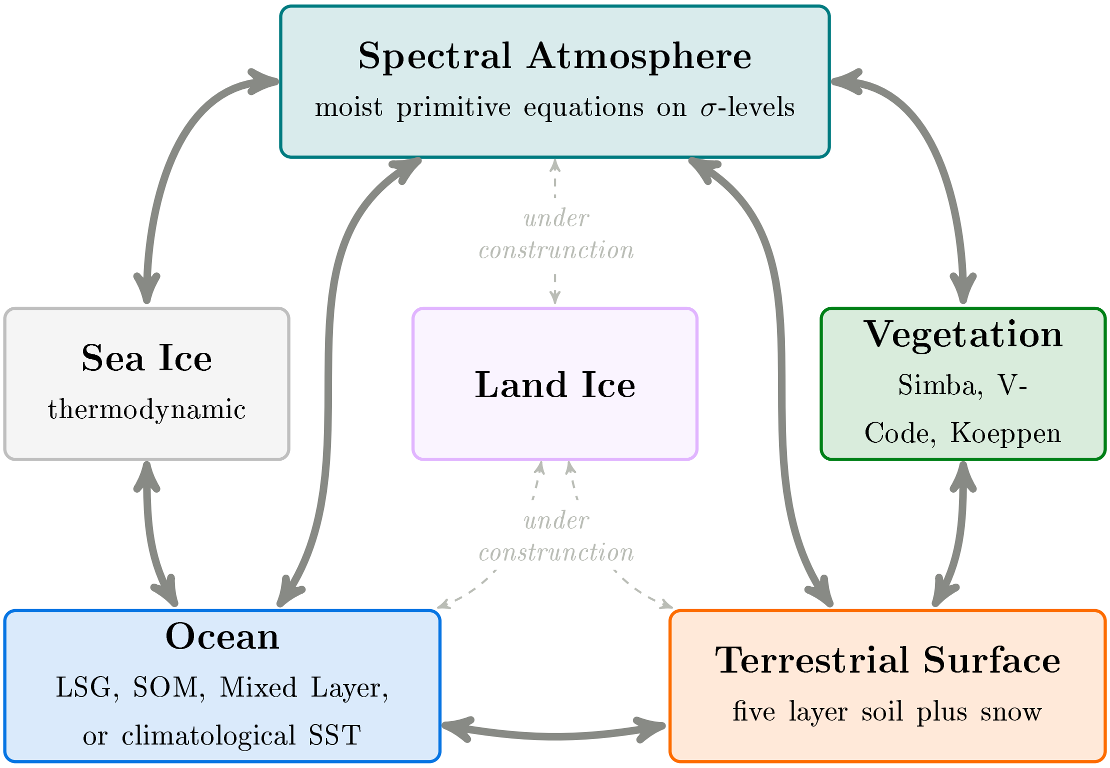

Figure 2.1: Schematic overview of the different compartments available for the coupled model

Conservation of momentum (vorticity and horizontal divergence equation):

$$\frac{\partial}{\partial t}(\xi + f) = \frac{1}{(1-\mu^2)}\frac{\partial F_v}{\partial \mu} + P_\xi \tag{2.1}$$

$$\frac{\partial D}{\partial t} = \frac{1}{(1-\mu^2)}\frac{\partial F_u}{\partial \lambda} + \frac{\partial F_v}{\partial \mu} - \nabla^2 E - \nabla^2 (\phi + T_0 \ln p_s) + P_D \tag{2.2}$$

Hydrostatic approximation (using the equation of state):

$$0 = \frac{\partial \phi}{\partial \ln \sigma} + T \tag{2.3}$$

Conservation of mass (continuity equation):

$$\frac{\partial \ln p_s}{\partial t} = -\int_0^1 A \, d\sigma \tag{2.4}$$

Conservation of energy (thermodynamic equation):

$$\frac{\partial T'}{\partial t} = F_T - \dot{\sigma}\frac{\partial T}{\partial \sigma} + \kappa W T + \frac{J}{c_p} + P_T \tag{2.5}$$

Turbulent flux divergences (Reynolds averaged) are included in equations (2.1) to (2.5) as parameterizations in the terms P_ξ, P_D, and P_T. The spherical form of the coordinate system yields a poleward convergence of the meridians which is included by re-expressing the zonal (u) and meridional (v) velocities: $U = u\cos(\varphi)$ and $V = v\cos(\varphi)$. f stands for the planetary vorticity in equation (2.1). In equation (2.2) the divergence, E, represents the kinetic energy per unit mass and ϕ the geopotential. The thermodynamic equation (2.5) is a prognostic equation for the temperature deviation T' from a constant reference temperature $T_0 = 250$ K for all σ levels: $T' = T - T_0$. The vertical velocity in the σ-system is:

$$\dot{\sigma} = \frac{d\sigma}{dt} \tag{2.6}$$

J stands for the diabatic heating per unit mass, c_p is the specific heat at constant pressure, and κ is the adiabatic coefficient. All other variables are explained in appendix A. Furthermore, the following notations are used in equations (2.1) to (2.5):

$$F_u = (\xi + f)\,V - \dot{\sigma}\frac{\partial U}{\partial \sigma} - T'\frac{\partial \ln p_s}{\partial \lambda}$$

$$F_v = -\,(\xi + f)\,U - \dot{\sigma}\frac{\partial V}{\partial \sigma} - \left(1 - \mu^2\right)T'\frac{\partial \ln p_s}{\partial \mu}$$

$$F_T = -\frac{1}{(1-\mu^2)}\frac{\partial\,(UT')}{\partial \lambda} - \frac{\partial\,(VT')}{\partial \mu} + DT'$$

$$E = \frac{U^2 + V^2}{2\,(1 - \mu^2)}$$

$$\dot{\sigma} = \sigma\int_0^1 A\ d\sigma - \int_0^\sigma A\ d\sigma$$

$$W = \frac{\omega}{p} = \vec{V}\cdot\nabla\ln p_s - \frac{1}{\sigma}\int_0^\sigma A\ d\sigma \qquad \text{with} \quad \omega = \frac{dp}{dt}$$

$$A = D + \vec{V}\cdot\nabla\ln p_s = \frac{1}{p_s}\nabla\cdot p_s\vec{V}$$

The fast gravity modes are linearized around a reference temperature profile (T_0). Equations (2.1) to (2.5) can be separated into fast linear gravity modes and the slower non-linear terms. The linear terms contain the effect of divergence (or gravity waves) on the surface pressure, the temperature tendency, and the geopotential.

The primitive equations are solved by the spectral transform method (Eliasen *et al.*, 1970; Orszag, 1970). This method uses an auxiliary grid in the physical space where point values of the dependent variables are computed. The prognostic variables (ξ, D, T, and $\ln p_s$) are represented in the horizontal by truncated series of spherical harmonics. The auxiliary grid in the physical space (Gaussian grid) is defined by equally spaced longitudes and Gaussian latitudes.

Vorticity, temperature, and divergence are calculated at full levels and the vertical velocity at half levels. For the hydrostatic approximation, an angular momentum conserving finite-difference scheme (Simmons & Burridge, 1981) is applied, which solves the equation at half levels.

The hydrostatic approximation filters vertical sound waves and the lower boundary condition in pressure or σ-coordinates (vanishing vertical velocity at the surface) suppresses horizontal sound waves. However, fast propagation of gravity waves strongly reduces the time step of explicit numerical schemes and, therefore, mode splitting is applied and an implicit scheme for the divergence is used. The vorticity equation is computed by an explicit scheme (the leap frog scheme) and the common Robert/Asselin time filter is employed (Haltiner & Williams, 1980).

2.1.2 Parameterizations

Processes, like boundary-layer fluxes and diffusion, radiation, and moist processes are unresolved but included as simplified parameterizations in the Planet Simulator.

Turbulent eddies are much smaller than the scales that can be resolved in a general circulation model like the Planet Simulator. The methods after Louis (1979) and Louis *et al.* (1982) are used to parameterize the vertical eddy fluxes of heat, momentum and moisture. The parameterization scheme for the surface fluxes is based on the Monin-Obukhov similarity theory (see Obukhov, 1946; Monin & Obukhov, 1954; Obukhov, 1971). In the planetary boundary layer, bulk formulas are used to parameterize fluxes of zonal and meridional momentum (wind stress) as well as sensible and latent heat: The fluxes are positive in downward direction (towards the surface) and negative in upward direction (away from the surface). The drag and the transfer coefficient for heat are calculated following the method described by Roeckner *et al.* (1992), which is based on the work of Louis (1979) and Louis *et al.* (1982).

Turbulent mixing is not resolved in the model, but represented by a vertical diffusion applied to the horizontal wind components u and v, the potential temperature, θ, and the specific humidity, q. The turbulent fluxes of zonal and meridional velocity, of heat, and of moisture are parameterized by a vertical diffusion along the vertical gradient with the exchange coefficients for momentum and heat, which are calculated with the mixing length approach as an extension of the similarity theory (see Roeckner *et al.*, 1992). Horizontal diffusion is computed in spectral space in analogy to the approach in the ECHAM-3 model (Roeckner *et al.*, 1992). The parameterization is based on the ideas of Laursen & Eliasen (1989).

The short-wave radiation scheme for the cloud-free atmosphere, which includes Rayleigh scattering, ozone absorption, and water vapor absorption, is based on the work of

Lacis & Hansen (1974). For high-, middle- and low-level clouds, albedos and transmissivities can be prescribed or parameterized following Stephens (1978) and Stephens *et al.* (1984). The long-wave radiation scheme for the cloud-free atmosphere depends on a broad band emissivity method (e.g. Manabe & Möller, 1961; Rodgers, 1967; Sasamori, 1968; Katayama, 1972; Boer *et al.*, 1984). Cloud flux emissivities can either be obtained by treating clouds as gray bodies or be derived from the cloud liquid water content (for example Stephens, 1984).

The ozone concentration in the radiation scheme of the Planet Simulator is prescribed. The model contains an idealized annual cycle of the ozone concentration (which may be switched off). Alternatively, a three dimensional ozone distribution can be externally provided.

The area of rising motion in moist convection processes is very small compared to the horizontal resolution of most GCMs. Therefore, cumulus convection needs to be parameterized, and (in the Planet Simulator) follows a Kuo-type convection scheme. In the Kuo-scheme (Kuo, 1965, 1974) convection is activated in a conditionally unstable layer between the pressure levels, if there is net convergence of moisture into the grid box.

Shallow convection is parameterized by vertical diffusion of moisture, potential temperature and, optionally, momentum (Tiedtke, 1983). The shallow convection scheme is only applied when the penetrative convection is not operating due to lack of moisture or (optional) if the unstable layer is located below a given threshold height (default is 700 hPa) and applied in the ten level resolution version of the model only. The effect of the parameterization of shallow convection on the model results is discussed for example in Dahms (2009).

If the air is supersaturated, large-scale condensation occurs. Storage of water in clouds is not considered, as condensed water falls out instantaneously as precipitation. Cloud cover and cloud liquid water content are diagnostic quantities, while the fractional cloud cover of a grid box is parameterized using the relative humidity for the stratiform clouds and the convective precipitation rate for the convective clouds (following the ideas of Slingo & Slingo, 1991).

Phase changes of convective or large-scale precipitation within the atmosphere are considered. Melting and freezing of precipitation depends on the respective temperature level (using 273.16 K as a threshold). Evaporation is parameterized in terms of the saturation deficit.

Layers, where $\partial\theta/\partial p > 0$, are called dry adiabatically unstable and dry convective adjustment is performed, so that the total sensible heat of the respective column is conserved. In dry convection it is assumed that the moisture is completely mixed by the convective process.

Some land surface properties are parameterized in the Planet Simulator. The parameterizations include calculations of temperatures for the surface and the soil, a soil hydrology and a river transport scheme. Albedo, roughness length, and the evaporation efficiency of the surface are provided. Some additional surface quantities need to be specified, like the land-sea mask or the orography. Since a coupling to a land ice model does not exist, glaciers are treated like land points, but with surface and soil characteristics appropriate for ice. A coupling of the Planet Simulator to a land ice model is presently under construction. A simple vegetation model (SimBA, Kleidon, 2006) may be applied.

Sea surface temperatures (SSTs), sea ice distributions, and surface temperatures over sea ice are provided by the ocean and sea ice modules. The prescribed surface albedo for open water is set to a default of 6.9 %. For sea ice surfaces the albedo depends on the surface temperature of the sea ice.

2.1.3 Mixed Layer Ocean Model

The sea surface temperature (SST) can either be prescribed to fixed values (for example in uncoupled aquaplanet simulations without a seasonal cycle, e.g. Dahms *et al.* 2011) or with a seasonal climatology. However, a slab ocean model is also available, which consists of a prognostic equation at each ocean point for the oceanic mixed-layer temperature. The default mixed-layer depth is 50 m. The net atmospheric heat flux into the mixed-layer ocean consists of the net solar and long-wave radiation and the sensible and latent heat fluxes. The heat flux from the deep ocean into the mixed-layer is either prescribed or comes from the coupled ocean model.

2.1.4 Thermodynamic Sea Ice Model

The thermodynamic sea ice model is based on the zero layer model of Semtner (1976). The model computes the thickness of sea ice from the thermodynamic balances at the top and the bottom of the ice. The zero layer assumes the temperature gradient in the ice to be linear and eliminates the capacity of ice to store heat. The freezing point is set to 271.25 K. The prognostic variables are the sea ice temperature, the ice thickness, and the ice concentration. Standard thermodynamic parameter values employed in the sea ice model can be found in the reference manual (table 7.1 in Lunkeit *et al.*, 2011).

It is assumed that melting of sea ice takes place in the atmosphere only, while freezing occurs at the lower side of the ice. Snow may accumulate on top of the sea ice. Snow cover affects the albedo and the heat conductivity. If there is sufficient snow to suppress the ice/snow interface below sea level, snow is converted into sea ice (mass conserving). If the surface temperatures rise above freezing point, first the snow and afterward the sea ice are melted.

2.2 The LSG Ocean Model

The Hamburg Large Scale Geostrophic Ocean General Circulation Model (LSG–OGCM) is based on the work of (Maier-Reimer *et al.*, 1993). Here, a short introduction into the model is given. The information comes mostly from the technical report describing the LSG (Maier-Reimer & Mikolajewicz, 1992), where more details can be found. However, many updates are now included in the LSG ocean model, which are not documented elsewhere and, thus, an updated model description can be found in appendix F. Furthermore, updated (but less detailed) model descriptions are presented, for example, by Prange *et al.* (2003) or Wenzel & Schröter (2007).

The LSG ocean model has evolved from an original concept of Hasselmann (1982), which is based on the observation that for a large-scale OGCM designed for climate studies, i.e. for long time scales, the relevant characteristic spatial scales are large compared with the internal Rossby radius throughout most of the ocean. Furthermore, characteristic time scales are large compared with the periods of gravity modes and barotropic Rossby wave modes.

2.2.1 Model Dynamics

The primitive equation ocean model integrates the momentum equations, including all terms except the non-linear advection of momentum, by an implicit time integration method that allows a time step of 10 days. The numerical scheme is unconditionally stable and can be applied uniformly to the entire globe, including equatorial and coastal current areas.

It is assumed that the spatial resolution of the model is large compared to the internal Rossby deformations radius (which is approximately 50 km). Therefore non-linear terms of the Navier-Stokes equation can be neglected. Furthermore, vertical friction is neglected and after applying the hydrostatic and the Boussinesq approximations, the three-dimensional momentum equation is reduced (see equations 2.7 to 2.9).

Conservation of momentum (Navier-Stokes equation):

$$\frac{\partial}{\partial t}u - fv + \frac{1}{a\sin\varphi}\frac{1}{\rho_0}\frac{\partial p}{\partial \lambda} = \frac{\tau^\lambda}{\rho_0} + A_h \triangle_h u \tag{2.7}$$

$$\frac{\partial}{\partial t}v - fu + \frac{1}{a}\frac{1}{\rho_0}\frac{\partial p}{\partial \varphi} = \frac{\tau^\varphi}{\rho_0} + A_h \triangle_h v \tag{2.8}$$

$$p = g\rho_0 \left(\zeta + \frac{1}{\rho_0} \int_0^z \rho z' dz' \right) \tag{2.9}$$

where

$$\frac{\partial u}{\partial z} = \frac{\tau^\lambda}{A_v} \qquad \text{and} \qquad \frac{\partial v}{\partial z} = \frac{\tau^\varphi}{A_v}$$

τ^λ denotes the zonal component of wind stress, while τ^φ is the meridional wind stress component. A_h is the coefficient of horizontal friction and A_v the coefficient of vertical friction. $\triangle_h$ stands for the horizontal Laplace operator. Other (more commonly used) variables are explained in appendix A.

Conservation of mass (continuity equation):

$$w_z + \frac{1}{a\cos\varphi}\left(\frac{\partial}{\partial\varphi}(v\cdot\cos\varphi) + \frac{\partial u}{\partial\lambda}\right) = 0 \tag{2.10}$$

Equations of state (the non-linear formula after UNESCO, 1981, is used):

$$\rho = \rho\,(S, T, p) \tag{2.11}$$

with the in-situ temperature, T, given as:

$$T = T\,(\theta, p) \tag{2.12}$$

An adaption of the tracer advection scheme by Farrow & Stevens (1995) for temperature and salinity has been implemented into the model, which uses a predictor–corrector method with a centered difference scheme for the predictor and a third-order QUICK scheme (Leonard, 1979) for the corrector stage. The QUICK scheme is less diffusive than the standard LSG upstream scheme and less dispersive than the common centered difference scheme. Explicit diffusion is necessary to ensure computational stability. Depth-dependent horizontal and vertical diffusivities are employed ranging from $10^7\text{cm}^2/\text{s}$ at the surface to $5\times10^6\text{cm}^2/\text{s}$ at the bottom, and from $0.6\,\text{cm}^2/\text{s}$ to $1.3\,\text{cm}^2/\text{s}$, respectively.

The free surface is treated prognostically. There is no rigid lid approximation. On the upper boundary (at $z = 0$) $\partial\zeta/\partial t = w$ is assumed. The only sources for heat (q_θ) and salt (q_S) are located at the sea surface.

The equations are divided into two coupled subsystem: the barotropic and the baroclinic part. The according sets of equations are listed in Maier-Reimer & Mikolajewicz (1992).

2.2.2 Model Grid and Resolution

The LSG ocean model is run with 22 vertical z-levels (thickness ranges from 50 m at the top to 1000 m at the bottom) on a semi-staggered grid type “E” (Arakawa & Lamb, 1977) with 72 × 72 horizontal grid points, which has a resolution of 3.5°. The grid of the LSG ocean model (subdivided into horizontal and vertical grid) is further explained in appendix F.

2.3 The Coupling

The coupling is conducted via the surface fluxes of heat, fresh water, and momentum. No flux correction (or flux adjustment) is applied. The interpolation between the atmospheric and the oceanic grid ensures global conservation. Atmospheric wind stress and fresh water flux (the sum of precipitation, evaporation, and continental runoff) are averaged over the coupling interval (one oceanic time step = 10 days) and then given to the ocean.

However, it appears that the coupling interval may be too long to keep the oceanic temperature constant during the atmospheric integration. Therefore, the uppermost 50 m of the oceanic column (the thickness of the uppermost layer in the LSG) serve as a mediator for the heat flux: During the atmospheric time steps, this part is treated as an oceanic mixed layer and its temperature (heat content) is changed at each time step according to the actual atmospheric heat fluxes (long- and short-wave radiation, as well as sensible and latent heat flux). In addition, the temperature is modified by an oceanic heat flux which is computed from the heating/cooling by all oceanic processes during the previous oceanic time step. After finishing the atmospheric part, the new temperatures (i.e. the new heat content) are provided to the ocean substituting the old ones and the LSG time step is performed. During this time step, the temperature change of the uppermost 50 m yields the oceanic heat flux to be used for the next atmospheric integration. Note that if no atmospheric heat flux was present during these next atmospheric steps, the mixed layer temperature would consistently obtain the actual LSG value.

The evolution of sea ice is computed by the thermodynamic sea ice within the atmospheric part of the integration using the same time step (and grid) as the atmosphere. The sea ice thickness is then given to the ocean and provides changes of salinity due to melting or freezing.

2.4 Aquaplanet Set-up

For the atmospheric model (the Planet Simulator) to be able to run in an aquaplanet mode, surface parameters need to be adapted. The land–sea mask has to be set to an ocean surface only and the orography is uniformly set to a height of 0 m. All simulations are initiated with the *Control* sea surface temperature profile from Neale & Hoskins (2001a).

The LSG ocean model is initialized with restart files. Normally, standard restart files are provided with an ocean circulation integrated out to equilibrium forced by a standard atmosphere. In the case of the aquaplanet, new restart files had to be created, in which no orographic boundaries exist and the ocean has a flat bottom. Furthermore, temperature and salinity distributions follow the Levitus profiles (Levitus, 1982) and all motion is set to zero.

The restart from a steady state causes a very long spin-up time of the ocean, however, in a motionless ocean it is possible to reinsert some topographic features, which is important for some of the experiments conducted in this study.

Moreover, a topography file for the LSG model, which is either set to ocean-only points or which includes idealized oceanic barriers, has to be created.

Namelists and how to create surface files for both the Planet Simulator and the LSG ocean model are further explained in appendix G.

For this study a T21 spectral resolution (approximately 5.6° on the corresponding Gaussian grid) with five non-equally spaced vertical σ-levels is used for the atmosphere.

The ocean model is run with 22 vertical z-levels with 72×72 horizontal grid points, providing a resolution of 3.5°.

3 Aquaplanets with Idealized Ocean Barriers

> *"Make everything as simple as possible, but not simpler."*
> — ALBERT EINSTEIN

3.1 Introduction

Many characteristics of the zonal mean climate of the Earth are hardly affected by the presence of land masses. Thus, zonally symmetric aquaplanets without any orographic constraints are a useful tool to study the climate in its most elemental form. The ocean circulation is, however, greatly altered by the absence of meridional boundaries and the reinsertion of a single meridional barrier changes the ocean circulation regime completely. Numerical simulations with idealized land–sea distributions may be used to study the most important features of the zonal mean states, though they are not meant to simulate the past, present, or future climate of the Earth.

The aim of this part of the study is to analyze how topographic features inserted in an aquaplanet ocean affect the circulation and, thus, the zonal mean climates. Different aquaplanet set-ups with meridional ocean barriers are applied to test the aquaplanet configuration, which in addition allows to compare the sensitivity of the model to previous studies.

The ocean acts as a heat buffer to mitigate strong temperature changes in the atmosphere. Furthermore, the ocean transports heat around the globe and, hence, plays an important role in the climate system of the Earth, especially for the energy budget

(Trenberth & Caron, 2001). Impacts of a changing ocean circulation on the global climate are studied, for example, by Bryan *et al.* (1975), Bryan (1986), Houghton *et al.* (2001), and Bjornsson & Toggweiler (2001), who show that the ocean does in fact have a great influence.

The different aquaplanet set-ups, which are applied in the coupled atmosphere–ocean model, are designed to cover a wide spectrum of highly idealized ocean circulation regimes. Meridional barriers are inserted into the aquaplanet ocean to alter the circulation and to create circulation regimes which resemble general features of present-day conditions: While the pure aquaplanet creates an almost completely zonally symmetric state, a meridional barrier leads to a closed basin circulation not unlike those found in the Atlantic or Pacific ocean basin. Furthermore, there are numerous ocean gateways, which had or have great influence on the ocean circulation during past or present climate phases of the Earth (e.g. Mikolajewicz & Maier-Reimer, 1993; von der Heydt & Dijkstra, 2006). Hence, gaps are inserted in the idealized ocean barriers to simulate ocean circulation regimes under the influence of the isthmus of Panama or the Drake Passage. The climate of the Earth is greatly affected by the different features of the Atlantic and Pacific ocean basins and, thus, another idealized set-up is analyzed, which contains two barriers.

Aquaplanets have a long history in applications with atmosphere-only models and fixed sea surface temperatures (for example Hess *et al.*, 1993; Chao & Chen, 2004; Neale & Hoskins, 2001b,a; Dahms *et al.*, 2011), and recently there are some studies on aquaplanets with coupled atmosphere–ocean general circulation models (AOGCMs), which also cover various configurations with idealized meridional ocean barriers, like the ones presented here. Smith *et al.* (2006) analyze the characteristics of the large-scale ocean circulation of three different aquaplanet configurations and their impacts on the global climate. The mean state and variability of the pure aquaplanet's climate is studied by Marshall *et al.* (2007). While focusing on meridional energy transports, Enderton & Marshall (2009) explore four different aquaplanet set-ups with meridional ocean barriers. Geometrical constraints on the ocean circulation are further studied by Ferreira *et al.* (2010), who analyze a simulation with multiple ocean barriers. Testing the ability of the coupled model (Planet Simulator & LSG, presented in chapter 2) to simulate aquaplanet climates, the zonal mean climate state of atmosphere and ocean is assessed and compared to the results of previous studies.

At first, the four set-ups *Aqua*, *Ridge*, *Panama*, and *Drake*, which are introduced in section 3.2, are explored and intercompared (in section 3.3). Afterwards one further ocean basin is created by means of introducing a second ocean barrier into the aquaplanet. The set-up of this *DDrake* experiment is also introduced in section 3.2 and the effect of the second ocean basin is studied in section 3.4. The results of all five simulations are discussed and compared to previous studies in section 3.5.

3.2 Experimental Design

Five different aquaplanets with idealized ocean barriers are introduced, which are supposed to create different ocean circulation regimes. The pure aquaplanet is compared to three expanded aquaplanets, in which a meridional boundary is inserted into the ocean that breaks the zonal symmetry of the aquaplanet set-up. The meridional barrier either runs continuously from pole-to-pole or leaves a passage either in the tropics or in the southern ocean. In another set-up, a second oceanic barrier is introduced into the system, which creates an additional ocean basin.

For the experiments all external forcings are kept constant throughout the entire integration period:

- The ocean has a flat bottom with a uniform depth of 5,500 m.
- The solar constant is fixed at 1,365 $\mathrm{W/m^2}$.
- The atmospheric CO_2 concentration is kept constant at 360 ppm.
- The simulations are carried out under perpetual equinoctial conditions to exclude the seasonal cycle. The annual cycle of atmospheric ozone is switched off.
- The integrations start from steady state.
- The simulations are run for 20,000 years since a very long spin-up time is needed for the ocean.

Time avarages are taken over the last 1,000 years of the integration period (i.e. the years 19,001 to 20,000) to ensure that the model has reached equilibrium and to obtain a robust average. Only for the pure aquaplanet a longer averaging period of 5,000 years (i.e. the years 15,001 to 20,000) is needed, since a long-periodic climate variability can be observed (which will be discussed in chapter 4).

The following set-ups are applied and analyzed in this chapter:

> ***Aqua*:** The pure aquaplanet has completely zonally and hemispherically symmetric boundary conditions. The entire surface of the planet is covered with one ocean, which has a flat bottom of uniform depth. There are no continents or orographic barriers. Since *Aqua* lacks any form of meridional ocean barriers, it cannot support zonally integrated meridional flow by geostrophy. The set-up of *Aqua* is displayed in figure 3.1a.
>
> ***Ridge*:** The introduction of a single idealized ocean barrier, which runs from pole-to-pole along one meridian, creates an (expanded) aquaplanet that is not zonally symmetric anymore, though symmetric about the equator. A single ocean basin is created by the closed barrier and, therefore, Sverdrup circulation can be supported. The set-up of *Ridge* is displayed in figure 3.1b.
>
> ***Panama*:** The expanded aquaplanet of this set-up contains the same ocean barrier as *Ridge*, but with a gap between 20°N and 20°S that allows zonal flow in the tropics but retains gyral flow in mid- and high latitudes. The passage in the tropics reminds of the isthmus of Panama (even though

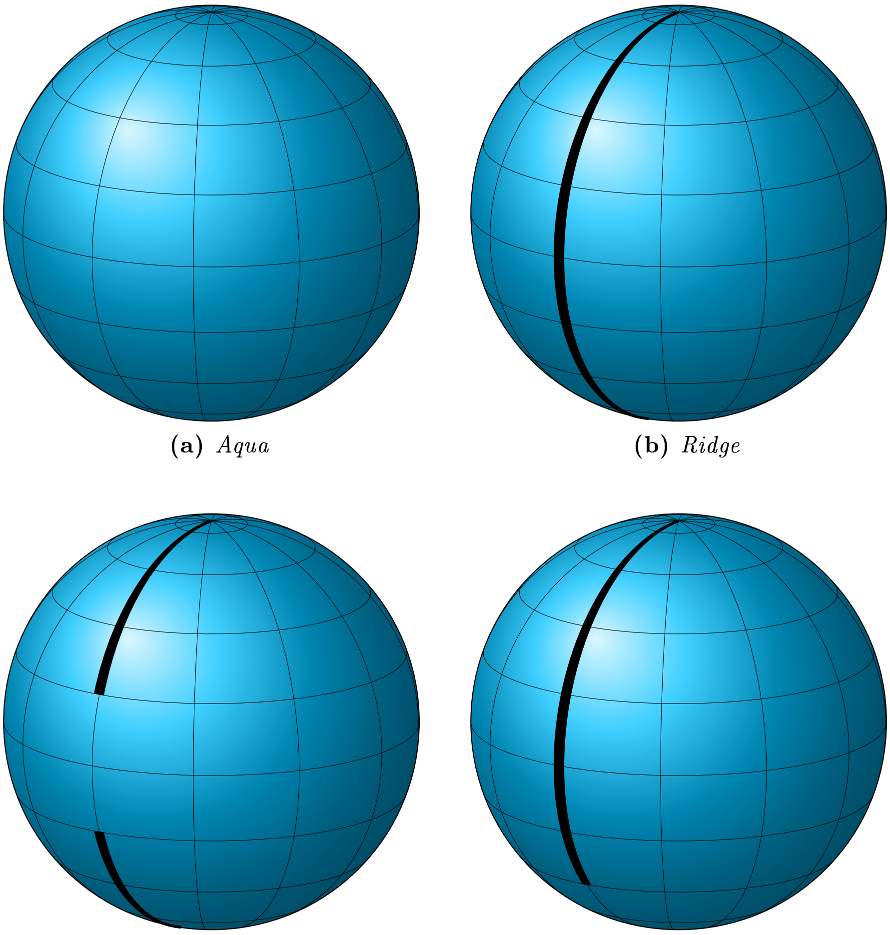
(a) *Aqua* (b) *Ridge*
(c) *Panama* (d) *Drake*

Figure 3.1: Set-up of aquaplanets with idealized meridional ocean barriers: *Aqua*, *Ridge*, *Panama*, and *Drake*

the gap is much bigger than in reality). Because of the meridional barrier, *Panama* is not zonally symmetric. Ideally, the symmetry about the equator should be conserved, however, in the LSG ocean model the number of grid points differs between the hemispheres and therefore *Panama* is only nearly symmetric about the equator. The set-up of *Panama* is displayed in figure 3.1c.

***Drake*:** The same ocean barrier as in the *Ridge* case now leaves a passage in the southern ocean poleward of 40°S and, thus, breaks the hemispherical symmetry of the other three set-ups. The passage in the southern ocean resembles the Drake Passage between Antarctica and South America (which, in reality, is more narrow). Geostrophic gradients and closed

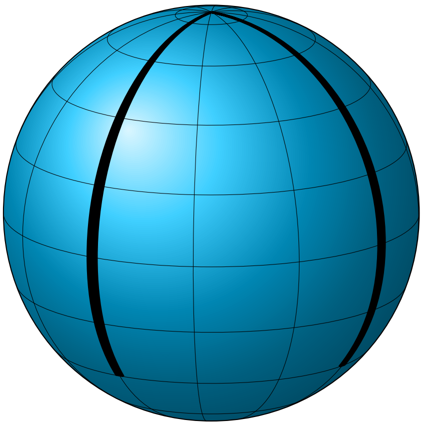

Figure 3.2: *DDrake* set-up: the expanded aquaplanet with two meridional ocean barriers

basin flow are supported north of 40°S, while circumpolar flow can take place in the southern ocean where zonal flow is unperturbed by orographic barriers. The *Drake* set-up is displayed in figure 3.1d.

***DDrake*:** A second oceanic barrier is included in *DDrake* to analyze the effect of a second ocean basin. The meridional barriers are exactly like the barrier in the *Drake* set-up: from the north pole down to 40°S. Therefore, the two ocean basins are connected in the southern ocean. The oceanic boundaries are 90° apart (at 90°E and 180°), thus creating ocean basins of different magnitudes. Though highly idealized, the larger and smaller ocean basins remind of the Pacific and Atlantic oceans, respectively, and will be referred to as *SB* (small basin) and *LB* (large basin). It is analyzed how the different basin sizes influence not only the ocean circulation but also the global-scale and local climate conditions. The set-up of *DDrake* is displayed in figure 3.2.

3.3 Aqua, Ridge, Panama, and Drake

The four different climate states of *Aqua*, *Ridge*, *Panama*, and *Drake* are studied and discussed here. In *Aqua*, which represents the pure aquaplanet set-up, orographic barriers exist neither in the ocean nor in the atmosphere. Consequently, the distributions of various atmospheric and oceanic fields are almost perfectly zonal. In *Ridge*, *Panama*, and *Drake* a single oceanic barrier changes the distribution of the variables and zonally asymmetric climates develop. The barriers of *Panama* and *Drake* are not closed but leave a passage in the tropics or at the south pole, respectively. Consequently, these two set-ups represent cases with regions that resemble an aquaplanet and regions which have features of closed basin circulations.

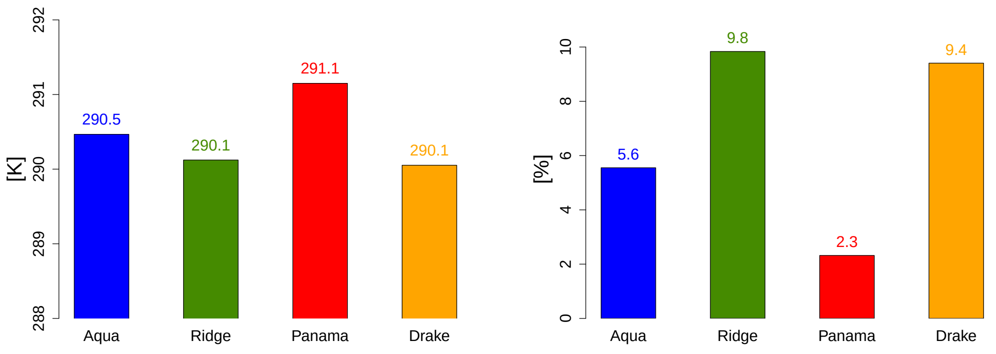

(a) global mean SST

(b) global mean sea ice cover

Figure 3.3: Global mean SST and sea ice cover (in % of global area) for *Aqua*, *Ridge*, *Panama*, and *Drake*

In the following, the different climate states of atmosphere and ocean are presented and discussed.

3.3.1 Temperature and Water Cycle

From the global mean sea surface temperatures (SSTs) and sea ice covers alone, it can already be deduced that an ocean barrier (with or without a passage in the tropics or at the south pole) can create very different climate states (see figure 3.3): The warmest climate can be observed in *Panama* with a global mean SST of 291.1 K. *Aqua* is colder with 290.5 K in the global mean, while *Ridge* and *Drake* both show equally the coldest global mean SST with 290.1 K. Sea ice is present in all four set-ups and varies in the global mean between only 2.3 % in *Panama* (i.e. $11.7{\times}10^6\,\mathrm{km}^2$ of the global area are covered with sea ice) and a maximum of 9.8 % ($50.0{\times}10^6\,\mathrm{km}^2$) sea ice cover in *Ridge*. *Drake* has only a slightly smaller sea ice covered area than *Ridge* ($47.9{\times}10^6\,\mathrm{km}^2$, i.e. 9.4 % of the global area), but the global mean sea ice cover of *Aqua* amounts only to 5.6 % ($28.6{\times}10^6\,\mathrm{km}^2$ of the global ocean).

The zonal mean SST and sea ice cover (figure 3.4) show further differences between the four climate states and provide more details than the global mean. *Aqua* shows the highest tropical surface temperatures of all four set-ups, but with a pronounced local minimum at the equator (which is caused by upwelling in the equatorial ocean). *Ridge* and *Drake* have tropical temperatures that are not quite as high as in *Aqua*, but substantially higher than in *Panama*, where zonal flow is unconstrained in the tropics and the equatorial SST minimum is strongest (the equatorial SST is almost 2–3 K colder than at 10°N/S). Upwelling at the equator is more pronounced when stronger zonal flow takes place.

In the mid- and higher latitudes of the northern hemisphere the four SST profiles are relatively similar but with the warmest surface temperatures in *Drake*. This can be explained by the zonal mean sea ice cover (figure 3.4b) of the northern hemisphere: Poleward of approximately 70°N, about 70 % of the area in *Aqua* and *Panama* is covered

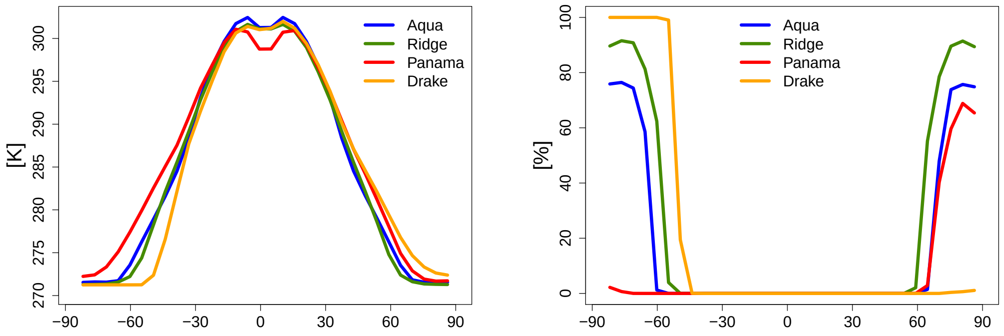

(a) zonal mean SST **(b)** zonal mean sea ice cover

Figure 3.4: Zonal mean SST and sea ice cover (in local area fraction) for *Aqua*, *Ridge*, *Panama*, and *Drake*

with sea ice. In *Ridge* there is even more sea ice, which extends down to 60°N. However, there is no sea ice present at the north pole of *Drake*.

In the southern hemisphere, *Panama* has no sea ice cover and consequently shows the warmest sea surface temperatures. As already noted in the description of the experimental set-up (chapter 3.2), *Panama* should be symmetric about the equator. However, since the number of grid points differs between the hemispheres in the ocean model, the set-up is not quite hemispherically symmetric. The consequence can be observed, for example, in the sea ice cover, which seems to be very sensitive to small deviations in the boundary conditions between the northern and southern hemisphere. The SSTs and the sea ice cover of *Aqua* and *Ridge* are not only very similar to each other (even though *Ridge* has slightly more ice and is colder), but also show an almost equatorial symmetric distribution of both parameters. *Drake* has very cold SSTs in the southern hemisphere and 100 % of the sea surface poleward of 45°S is covered with sea ice, where circumpolar flow can take place because of the passage in the oceanic barrier. The hemispheric asymmetry of *Drake* is, in contrast to *Panama*, not an artifact of the ocean model, but a consequence of the experimental set-up.

Zonal mean vertical profiles of atmospheric and oceanic temperatures (with a logarithmic vertical scale in the ocean) are displayed in figure 3.5. The specific moisture in the atmosphere and the salinity in the ocean are also shown as contour lines. The zonal mean atmospheric temperature and humidity fields of *Aqua* (figure 3.5a) and *Ridge* (figure 3.5b) resemble each other and are symmetric about the equator. Both set-ups have very cold and dry poles (which is due to the extensive sea ice cover), while the tropical air is very warm and moist, especially in the area of the intertropical convergence zone (ITCZ). The atmosphere of *Panama* (figure 3.5c) is very warm and moist, in particular at lower levels. The upper tropical troposphere is, however, colder and dryer than in the other realizations. The equatorial warm and moist zone is more spread out and is confined to the lower atmosphere. Heat from the low latitudes is effectively transported poleward and, thus, both poles of *Panama* are relatively warm. The most prominent characteristic of *Drake* (figure 3.5d) is the very cold and dry south pole. Strong equato-

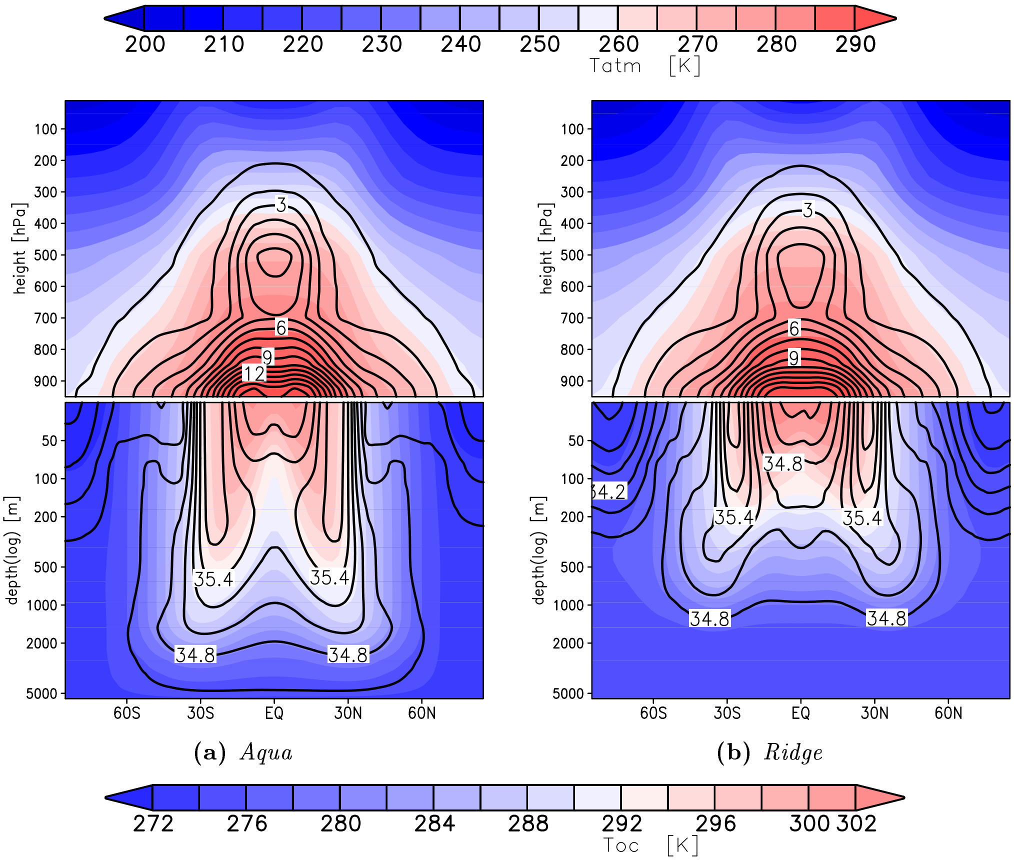

(a) *Aqua* **(b)** *Ridge*

Figure 3.5: Zonal mean temperature in atmosphere and ocean (shaded), and atmospheric specific moisture/oceanic salinity (contour line spacing: 1 g/kg for the specific moisture and 0.2 psu for the salinity) for *Aqua*, *Ridge*, *Panama*, and *Drake*

rial asymmetric conditions develop in *Drake* with a warm and moist north pole. In the tropics, the region of the ITCZ shows high temperatures and contains much moisture up to the upper troposphere.

The differences between the cases are stronger in the ocean than in the atmosphere. Even though *Aqua* and *Ridge* show very similar temperature and moisture structures, the zonal mean thermal and salinity patterns in the ocean differ greatly when a meridional ocean barrier is introduced into the system. Underneath the sea ice of *Aqua* (figure 3.5a), the poles are very cold and fresh. In the subtropics, pronounced warm and salty lenses form at the surface and reach down to a depth of almost 1,000 m. The salinity and the temperature gradients reach far down in *Aqua*, in contrast to the other set-ups, where the lower ocean is characterized by almost uniformly stratified water masses. The poles of *Ridge* (figure 3.5b) are not quite as cold, but fresher than in *Aqua*. The tropical area is also very warm and salty, however, compared to *Aqua*, higher temperatures and less salty waters close to the sea surface can be observed. Furthermore,

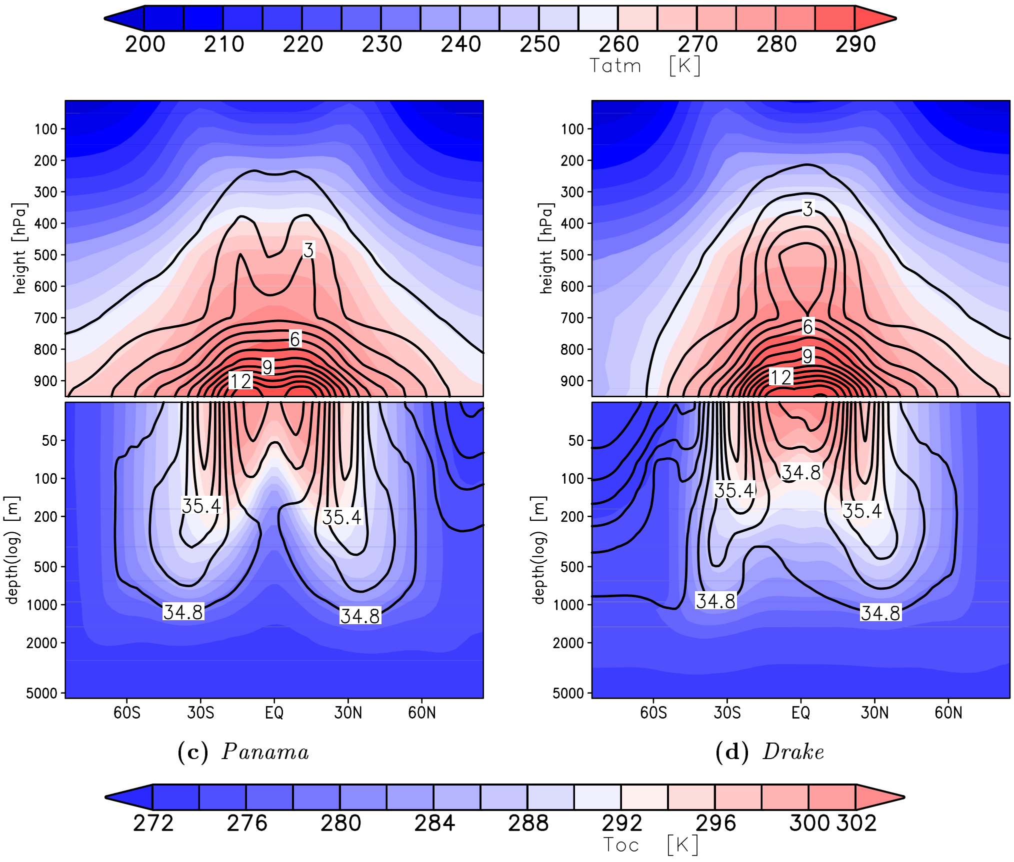

(c) *Panama* **(d)** *Drake*

Figure 3.5: continued

the warm and salty water masses are restricted to the upper ocean.

The most outstanding feature of the thermohaline structure of *Panama* (figure 3.5c) is the equatorial minimum in temperature and salinity (which is also present in the other realizations but most pronounced in *Panama*). Upwelling processes may be responsible for the fresher and colder equatorial water masses, which is more effective in *Panama*, where strong zonal flow develops in the tropics. In the subtropics salty and warm water masses can be observed. The poles of *Panama*, and especially the south pole which is completely ice-free, are much warmer and saltier than the ones of *Aqua* or *Ridge*. However, there is some intrusion of fresh water related to the sea ice at the north pole.

The south pole of *Drake* (figure 3.5d) is the coldest of all four set-ups. The different circulation pattern and the suppressed ocean heat transport (discussed in the following) are responsible for the very cold temperatures. Cold and fresh water reaches down to great depths. In contrast, the ice-free north pole is relatively warm and salty. Furthermore, the warm and salty lenses in the subtropics are not distributed symmetrically about the equator, since the one in the northern hemisphere is more pronounced.

The total precipitation (large scale plus convective) for *Aqua*, *Ridge*, *Panama*, and *Drake* is displayed in figure 3.6. The zonal mean total precipitation is shown in figure 3.7

together with the zonal mean evaporation and surface fresh water flux (precipitation minus evaporation).

The (time averaged) precipitation of *Aqua* (figures 3.6a and 3.7a) is completely zonally symmetric. The strongest precipitation takes place inside the ITCZ directly at the equator with approximately 2 m/a. Secondary peaks occur in the baroclinic zones of the mid-latitudes (with values up to 1.5 m/a). In the subtropics, and especially in the polar regions, the precipitation is relatively low.

The zonal mean precipitation of *Ridge* (figures 3.6b and 3.7b) resembles *Aqua*. The precipitation zones of the mid-latitudes are not quite as strong as in *Aqua* and the equatorial precipitation maximum is more peaked in *Ridge*. However, the distribution of precipitation in *Ridge* is not zonally symmetric. Even though the oceanic barriers do not extend into the atmosphere and there is no direct orographic forcing, the precipitation is greatly affected by the insertion of oceanic barriers. The local sea surface temperatures change and where warm water pools exist, greater upward surface heat fluxes are created, which influence the local precipitation rate. The warmer western boundary of the ocean basin experiences much more precipitation than the colder east side. The only exception are the poles, where more precipitation occurs over the eastern boundary of the ocean basin.

Poleward of 30°N/S the precipitation of *Panama* (figures 3.6c and 3.7c) is very similar to *Ridge*. However, the tropical precipitation is approximately zonally symmetric and greatly reduced compared to the other simulations (with a maximum of about 1.5 m/a). Furthermore, the equatorial precipitation maximum is spread out and a distinct single ITCZ cannot be observed. There is a hint of a double ITCZ with precipitation peaks on each side of the equator (between 5-10°N/S), but the horizontal resolution of the atmospheric model (T21) is too coarse to distinguish between a very broad equatorial precipitation band and a double ITCZ. The break down of a single ITCZ regime is often connected to weak temperature gradients in the low latitudes, like the ones observed in *Panama*.

The northern hemisphere of *Drake* (figures 3.6d and 3.7d) is very similar to *Ridge*, though with slightly higher precipitation in mid- and higher latitudes, which might be connected to higher surface temperatures and higher evaporation rates. Since *Drake* is not symmetric about the equator, conditions are different in the southern hemisphere: The zonal mean precipitation of the mid-latitudes is only slightly weaker than in the northern hemisphere, but poleward of 60°S, hardly any precipitation occurs over the sea ice covered ocean. The equatorial precipitation peak with almost 2 m/a is comparable to *Aqua*.

The highest evaporation occurs in the subtropics, where sea surface temperatures are high and the atmosphere is dry. At the equator a strong local minimum in the evaporation rates can be observed. In the ITCZ the air is very moist and surface winds are weak, which reduces the evaporation. Poleward of the subtropics, the evaporation efficiency weakens and vanishes (almost) completely at the poles.

At the equator there is a local minimum in evaporation and a maximum in precipitation. Hence, the tropical fresh water flux is positive (directed into the ocean). This is consistent with the fresh water masses which can be observed in the equatorial ocean (see figure 3.5). In the subtropics the evaporation reaches its maximum while the pre-

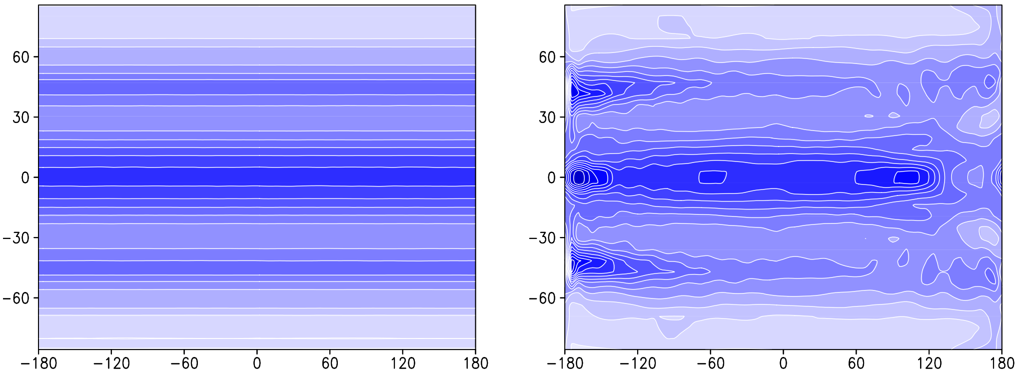

(a) *Aqua* **(b)** *Ridge*

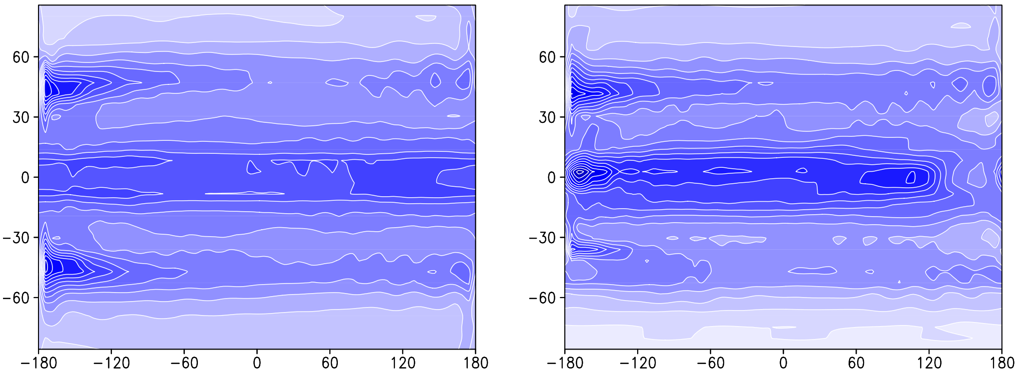

(c) *Panama* **(d)** *Drake*

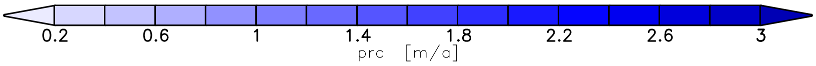

Figure 3.6: Total precipitation (large scale plus convective) for *Aqua*, *Ridge*, *Panama*, and *Drake*

cipitation rates are very low. Consequently, a negative fresh water flux (from the ocean into the atmosphere) can be observed, which is again consistent with the salty water masses in subtropical surface waters. The baroclinic precipitation zones dominate over the mid-latitude evaporation and the poles are mostly too cold for much evaporation to occur. Thus, poleward of approximately 40°N/S the fresh water flux is directed downward (positive).

Even though the four cases basically show the same characteristics, there are some differences in the fresh water cycles: *Aqua* (figure 3.7a) has great evaporation maxima in the subtropics (almost up to 2 m/a) and precipitation peaks in the tropics and mid-latitudes. Thus, the surface fresh water flux has relatively high minima and maxima, compared to the configurations which include an oceanic barrier. *Ridge* (figure 3.7b) has more moderate negative surface fresh water fluxes in the subtropics. The precipitation zones of the mid-latitudes are also weaker than the ones in *Aqua* and, consequently, the surface fresh water flux does not show local maxima in this area. In *Panama* (figure 3.7c)

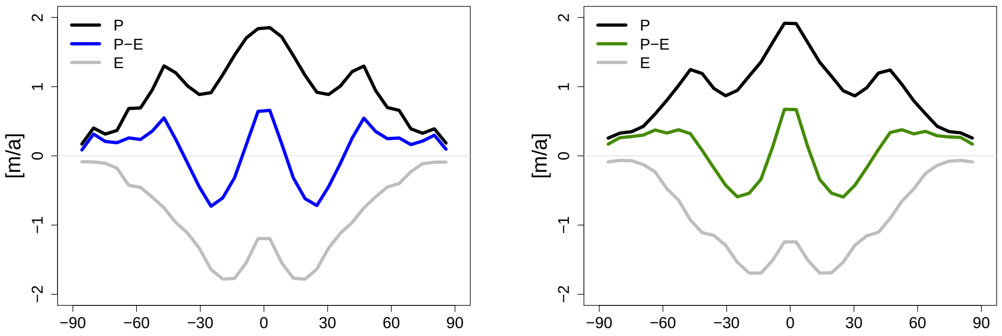

(a) *Aqua* **(b)** *Ridge*

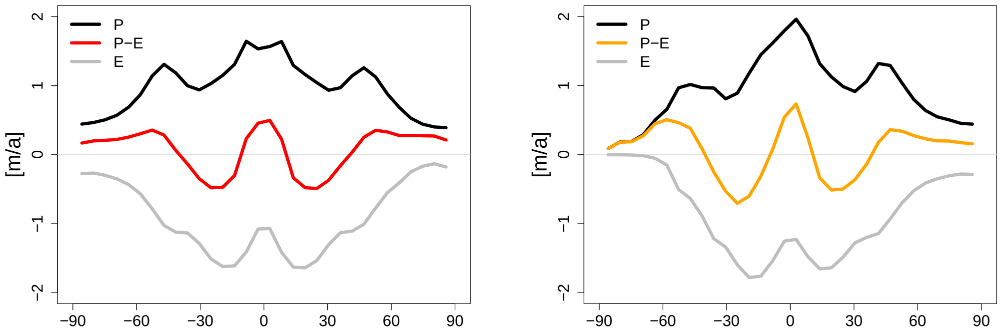

(c) *Panama* **(d)** *Drake*

Figure 3.7: Zonal mean precipitation (P), evaporation (E), and surface fresh water flux: precipitation minus evaporation ($P - E$) for *Aqua*, *Ridge*, *Panama*, and *Drake*

the precipitation and evaporation (and consequently the surface fresh water flux) peaks are less pronounced than in the other cases. The poles of *Panama* are relatively warm and precipitation as well as evaporation occur in the order of 0.2 m/a to 0.4 m/a. While the surface fresh water flux of the northern hemisphere of *Drake* (figure 3.7d) is very similar to the one in *Ridge*, the subtropical minimum in the southern hemisphere is stronger by about 0.2 m/a due to enhanced evaporation. Furthermore, a local (positive) peak can be observed in the southern mid-latitudes, which is caused by the substantially reduced evaporation over the southern ocean.

The zonal mean vertically integrated meridional transport of atmospheric water vapor for all four cases is shown in figure 3.8. The total transport can be subdivided into the transport conducted by the atmospheric mean circulation and the transport which is achieved by large-scale atmospheric eddies. The eddy-transport can be further partitioned into transport by transient and by stationary eddies. However, since there are no stationary eddies on the zonally symmetric aquaplanet (*Aqua*) and they are negligibly small on the almost zonally symmetric aquaplanet-like cases (*Ridge*, *Panama*, and *Drake*), both transports are displayed together but can be understood as the transient eddy-transport. The atmospheric water vapor transport is calculated in an analogous manner as the atmospheric energy transport, which is explained in appendix E.

In the tropics, approximately between 20°N and 20°S, the moisture transport is directed equatorward and conducted by the mean circulation of the atmosphere. The strongest water vapor transport, however, takes place in the mid-latitudes. Poleward of 20°N/S the entire moisture transport is directed toward the poles and is mostly achieved by atmospheric eddies. Thus, moisture convergence is created at the equator inside the ITCZ and moisture divergence takes place in the subtropics.

Even though the main characteristics of the atmospheric moisture transport are the same in all four set-ups, significant differences (especially in the magnitudes) still occur: *Aqua* (figure 3.8a) shows very high peak values in the equatorward (close to $7{\times}10^8$ kg/s) and poleward (over $10{\times}10^8$ kg/s) transport. Just as in *Ridge* (figure 3.8b), the transport is distributed symmetrically about the equator. *Ridge* shows generally smaller moisture transports than *Aqua* (peak values are about $1{\times}10^8$ kg/s weaker), but at high latitudes the moisture transport of *Ridge* exceeds the one of *Aqua*. The weakest moisture transport can be observed in *Panama* (figure 3.8c). The tropical equatorward transport hardly exceeds $5{\times}10^8$ kg/s and the poleward transport of the mid-latitudes only reaches maxima of about $8{\times}10^8$ kg/s. However, the transport of moisture in the high latitudes is not reduced. The northern hemisphere of *Drake* (figure 3.8d) with the ice-free warm pole conducts relatively small amounts of water vapor transport (comparable to the ones from *Panama*). However, the southern hemisphere with the cold sea ice covered pole shows the strongest transports of all four cases with equatorward transports of almost $8{\times}10^8$ kg/s and poleward transports of close to $11{\times}10^8$ kg/s. Overall, when sea ice covers the poles and a strong equator-to-pole temperature gradient can be observed, the atmospheric circulation strengthens and a stronger moisture transport takes place.

Figure 3.9 shows the atmospheric zonal mean potential and moist potential temperature. In all set-ups, the tropical temperature gradient is very weak at all levels. A broad baroclinic zone extends from the subtropics deep into the mid-latitudes, while the poles again show a weaker temperature gradient. Very moist air in the inner tropics alters the moist potential temperature throughout the entire troposphere.

The dry and moist potential temperature profiles of *Aqua* (figure 3.9a) and *Ridge* (figure 3.9b) hardly differ. In the tropics very moist air can be observed up to the upper troposphere, especially in *Aqua*. The sea ice covered poles of both set-ups are dry and, therefore, the moist and dry potential temperature profiles do not differ significantly. In *Panama* (figure 3.9c), the baroclinic zones in the mid-latitudes are not as strong as in the other three configurations. The poles are warmer (and more moist) and the tropics slightly colder (and dryer), in particular at higher levels. Since a double or very broad ITCZ develops in *Panama*, the moisture is not concentrated at the equator. In the tropics, the potential temperature distribution of *Drake* (figure 3.9d) is very similar to the one of *Ridge*. The sea ice covered south pole of *Drake* is, however, even colder and dryer, while the north pole shows warmer temperatures and contains more moisture.

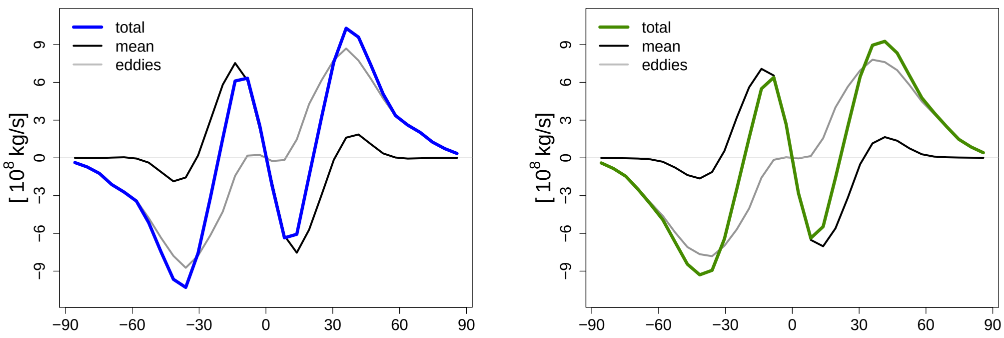

(a) *Aqua* **(b)** *Ridge*

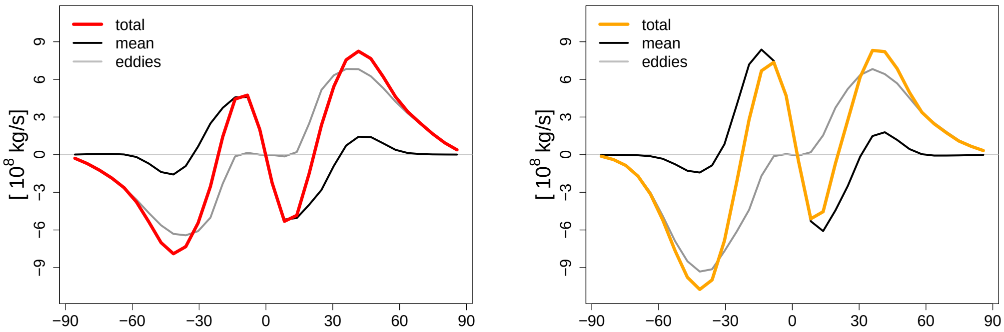

(c) *Panama* **(d)** *Drake*

Figure 3.8: Zonal mean vertically integrated meridional atmospheric moisture transport (total transport, transport by the mean circulation, and eddy-transport) for *Aqua*, *Ridge*, *Panama*, and *Drake*

3.3.2 Circulation

After the temperature, moisture, and salinity structures of the four aquaplanet climates, the circulation of atmosphere and ocean is now studied. The zonal mean circulation of atmosphere and ocean of the four set-ups is displayed in figure 3.10. The shaded background depicts the zonal mean zonal wind or zonal velocity of ocean currents and the contour lines show the mass stream function of the atmosphere or the meridional overturning circulation (MOC) of the ocean.

The structure of the atmospheric circulation is very similar in all four cases. In the tropics, direct Hadley circulation cells can be observed, which are symmetric about the equator (in *Aqua*, *Ridge*, and *Panama*) and are in magnitude comparable to present-day annual mean observations (e.g. Peixoto & Oort, 1992). The Hadley cells of *Aqua* (figure 3.10a) and *Ridge* (figure 3.10b) have maxima of 40×10^9 kg/s (the atmospheric stream function in 10^9 kg/s numerically represents about the same mass transport as an oceanic volume transport in Sverdrups; Czaja & Marshall 2006). The Hadley circulation of *Panama* (figure 3.10c) is much weaker with maxima of $20-30\times10^9$ kg/s. This is

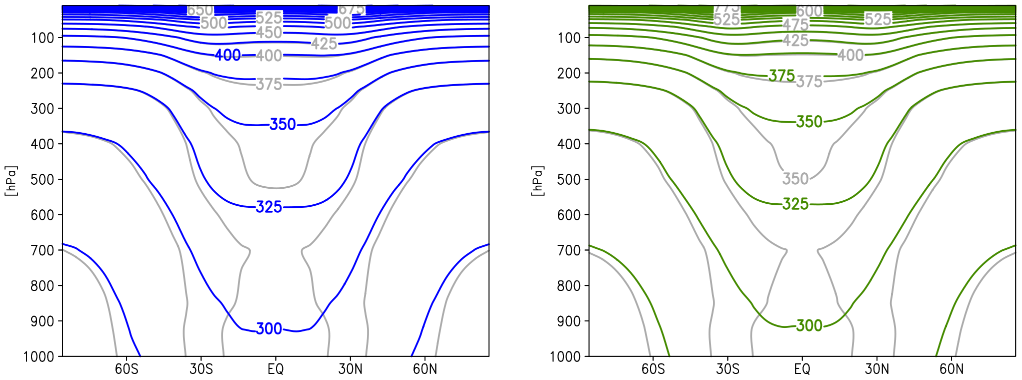

(a) *Aqua* **(b)** *Ridge*

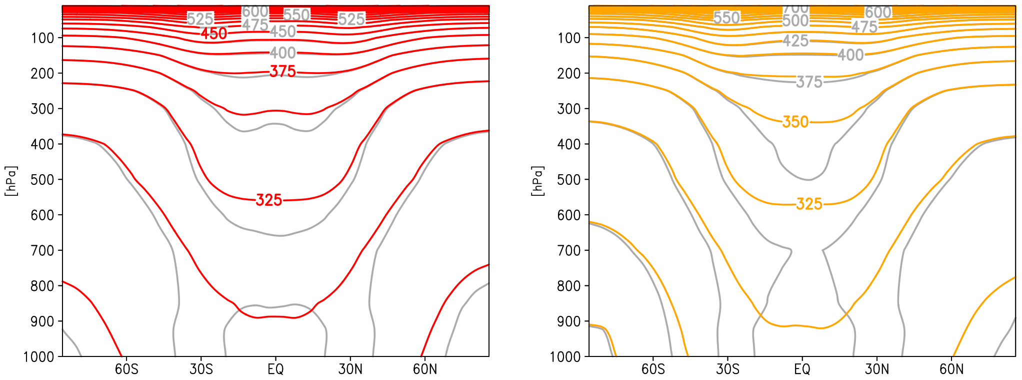

(c) *Panama* **(d)** *Drake*

Figure 3.9: Zonal mean atmospheric potential and moist potential temperature (dry potential temperature: colored lines; moist potential temperature: gray lines) for *Aqua*, *Ridge*, *Panama*, and *Drake*

not surprising, since the strength of the Hadley circulation depends on the meridional temperature gradient (see for example Held & Hou, 1980), which is weaker in *Panama*. The Hadley cells of *Drake* (figure 3.10d) are not hemispherically symmetric, which can also be explained by the meridional temperature gradient: In the southern hemisphere, there is a very strong temperature difference between the tropics and the sea ice covered polar ocean and a maximum Hadley circulation of 50×10^9 kg/s can be observed, while the ice-free north pole creates weak temperature gradients and a weaker Hadley circulation (up to 30×10^9 kg/s). In the mid-latitudes, indirect Ferrel cells exist (maxima of 20×10^9 kg/s), which also depend on the meridional temperature gradient (the weakest Ferrel cells can be found in *Panama*).

The mid-latitudes are characterized by westerly winds with a maximum in the upper atmosphere: the subtropical jet streams. As the subtropical jet streams are related to the temperature gradients, *Panama* shows the weakest velocities and the southern hemisphere of *Drake* the strongest. At the poles and at the equator, easterly winds prevail. In *Panama* the tropical easterly surface winds are not located directly at the

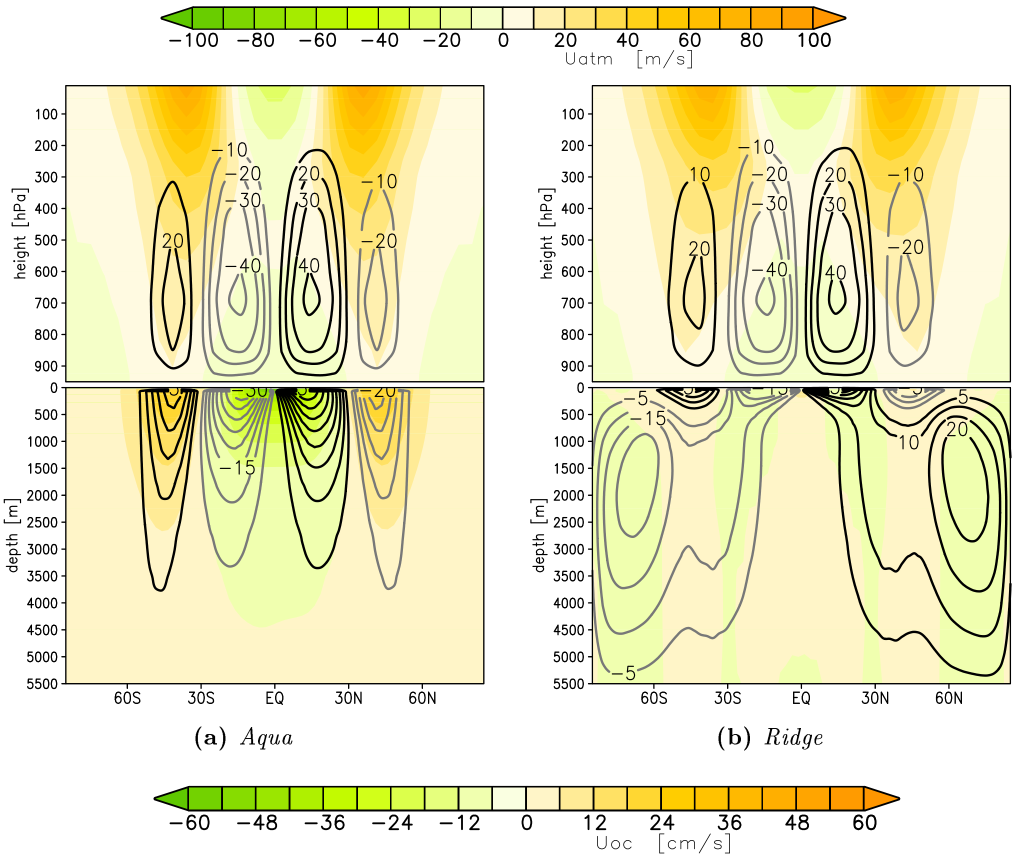

(a) *Aqua* **(b)** *Ridge*

Figure 3.10: Zonal mean zonal wind/ocean currents (shading) and atmospheric stream function/MOC (contour lines in 10^9 kg/s for the atmospheric stream function and in Sv for the MOC) for *Aqua*, *Ridge*, *Panama*, and *Drake*

equator but shifted north- and southward, which might be related to the (possible) ITCZ splitting.

The MOC in *Aqua* (figure 3.10a) consists of two Ekman cells in each hemisphere that stretch far down. The oceanic circulation cells mirror the Hadley and Ferrel circulations: strong tropical and weaker extra-tropical cells that have the same circulation sense as their atmospheric counterparts. In *Aqua* there are no zonal pressure gradients and, thus, mean meridional flow is not supported by geostrophy. Zonal wind stress and bottom friction are left to balance each other (in an inviscid fluid).

In the cases with a meridional ocean barrier geostrophic flow is supported at the latitudes where a closed basin structure exists. The MOC in *Ridge* (figure 3.10b) gives a very different picture from that of *Aqua*. There are also tropical and extra-tropical cells in each hemisphere, however, the subtropical cells are very small and confined to the upper ocean, while the tropical cells reach down to the sea floor where they stretch poleward. The MOC in *Panama* (figure 3.10c) resembles the one in *Ridge*, but the

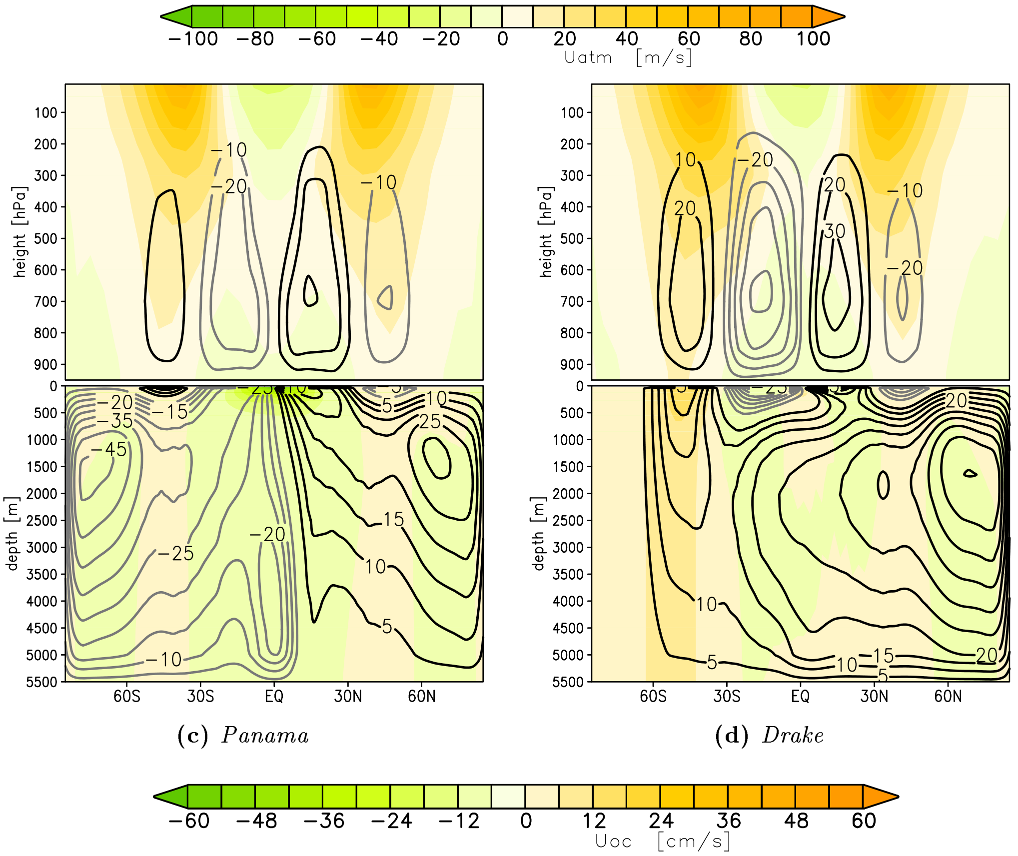

(c) *Panama*

(d) *Drake*

Figure 3.10: continued

circulation is much stronger and the tropical cells fill almost the entire ocean basin (in each hemisphere), except for a very small area close the sea surface in the mid-latitudes, where the extra-tropical cells are located. Again, a hemispherical asymmetry occurs in *Panama*, since the southern cell is stronger than the northern cell. A very small asymmetry in the boundary conditions is sufficient to alter the oceanic circulation and to create hemispherically asymmetric cells. The northern hemisphere of *Drake* (figure 3.10d) shows a MOC, which resembles the one from *Panama* or *Ridge*, but with stronger circulation in the polar ocean. In the southern hemisphere, the tropical cell is very weak and the extra-tropical cell, in contrast, is stronger and reaches farther down. The extra-tropical cell of the southern hemisphere is connected to the tropical cell of the northern hemisphere and, thus, cross-equatorial transport takes place in *Drake*.

In the area of the tropical cells, the zonal oceanic velocity of *Aqua* is directed eastward and in the mid-latitudes westward zonal velocity prevails. In *Ridge*, the zonal mean zonal velocity is rather small throughout all latitudes, since the barrier prevents circumglobal flow. The zonal velocity in *Panama* is restrained by the meridional ocean barrier and is therefore very weak, except for the equatorial region where a passage in the barrier allows stronger easterly currents. In *Drake* the zonal velocity is also very small, except

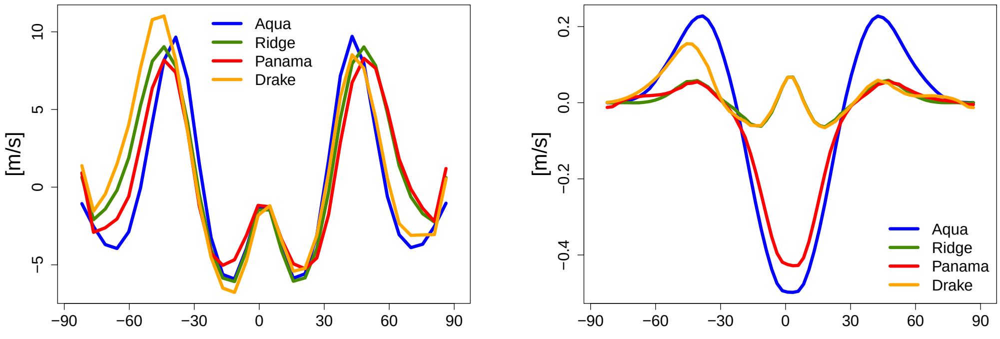

(a) zonal surface wind (atmosphere) **(b)** zonal surface currents (ocean)

Figure 3.11: Zonal mean zonal surface winds (at 925 hPa) and currents (at a depth of 25 m) for *Aqua*, *Ridge*, *Panama*, and *Drake*

for the region between 40°S and 60°S, where strong westerly currents can be observed.

The atmosphere and ocean are connected via the sea surface. Surface winds in the atmosphere force the ocean surface currents and the ocean circulation of the pure aquaplanet, *Aqua*, is even solely wind driven. Zonal mean zonal surface winds and currents are displayed in figure 3.11.

The zonal mean zonal surface winds at 925 hPa are displayed in figure 3.11a: Easterly winds prevail in the tropics, though directly at the equator the wind speed is very low. Strong westerly surface winds are located in the mid-latitudes (up to 10 m/s) and at high latitudes the predominant wind pattern is again easterly. *Aqua* and *Ridge* have almost identical surface wind structures, however, the easterly velocities at the poles are much weaker in *Ridge*. The surface winds of *Panama* are weaker than in *Aqua* over large regions. In the northern hemisphere, *Drake* is very similar to *Aqua*, but in the southern hemisphere the velocities are stronger except for the weak polar easterlies.

The differences in the ocean surface currents (at a depth of 25 m, figure 3.11b) are very pronounced: In the case of unrestrained flow at the equator (in *Aqua* and in *Panama*), strong easterly velocities (close to 0.5 m/s) can be observed at the sea surface, in contrast to *Ridge* and *Drake*, where the ocean barrier prevents strong tropical zonal currents. *Aqua*, and to a lesser extent *Drake* in the southern hemisphere, show strong mid-latitude westerly currents (approximately 0.2 m/s in *Aqua* and over 0.1 m/s in *Drake*). In *Ridge*, *Panama*, and in the northern hemisphere of *Drake* the currents are also westerly but very weak.

Figure 3.12 shows the horizontal barotropic stream function (note the different contour intervals in areas with open and closed ocean barriers) and the deviation of the sea surface temperature from its zonal average. In *Aqua* (figure 3.12a) hardly any zonal SST deviations can be observed. *Ridge* (figure 3.12b), *Panama* (figure 3.12c) and *Drake* northward of 40°S (figure 3.12d) reveal zonal SST deviations, in which warmer surface waters are located at the western boundary of the ocean basin, while the eastern boundary is much colder. The only exception is the polar ocean, which is warmer close to the eastern side of the basin. In the mid-latitudes the warm/cold contrast between west and east is particularly pronounced. In *Panama* the equatorial ocean has weaker zonal SST gradients because of the missing oceanic barrier. In *Drake* deviations occur at high latitudes: In the northern hemisphere, the polar ocean is warm close to both sides of the basin boundary and colder in the middle of the basin. Poleward of 40°S hardly any zonal SST deviations occur.

The barotropic stream function (depth-integrated flow) is directly related to the pattern of surface wind stress. In *Aqua* strong depth-integrated zonal flow develops. The closed ocean basin of *Ridge* favors a gyral structure, which is analogous to zonally bounded ocean basin circulation from present-day observations, including subtropical and subpolar gyres. *Panama* and *Drake* also show gyres in areas with the barrier, but strong zonal flow in regions where the passage is located.

3.3.3 Energy

In the four aquaplanet set-ups, there is no seasonality considered. The insolation is therefore always the greatest directly at the equator and decreases poleward. The atmospheric energy budget (E_{total}) is calculated by subtracting the budget at the sea surface (E_{srf}) from the budget at the top of the atmosphere (E_{TOA}) (equation 3.1). At the top of the atmosphere, only in- and outgoing long- ($LW^{\uparrow}_{TOA}$) and shortwave ($SW^{\downarrow}_{TOA}$) radiation contribute to the energy budget (equation 3.2). At the sea surface, additional sensible ($SH^{\uparrow}_{srf}$) and latent ($LH^{\uparrow}_{srf}$) heat fluxes need to be considered next to the long- ($LW^{\uparrow}_{srf}$) and shortwave ($SW^{\downarrow}_{srf}$) radiation (equation 3.3). Downward fluxes are defined to be positive.

$$E_{total} = E_{TOA} - E_{srf} \tag{3.1}$$

$$E_{TOA} = SW^{\downarrow}_{TOA} + LW^{\uparrow}_{TOA} \tag{3.2}$$

$$E_{srf} = SW^{\downarrow}_{srf} + LW^{\uparrow}_{srf} + LH^{\uparrow}_{srf} + SH^{\uparrow}_{srf} \tag{3.3}$$

The zonal mean total energy budgets, as well as the budgets at the TOA and at the surface, and the surface albedo, are displayed in figure 3.13. The total energy budget in all four cases is almost balanced directly at the equator and positive in the entire tropics. Poleward of approximately 20°N/S, where the maxima are located, the total atmospheric energy budgets decrease and become negative in mid- and higher latitudes.

Differences in the total energy budgets occur at the equator, where the ITCZ structure mostly determines the budget. The energy balance at the TOA, E_{TOA}, shows in the tropics maximum values of $50\,\mathrm{W/m^2}$, however, while *Aqua* (figure 3.13a) is almost balanced at the equator and *Ridge* (figure 3.13b) and *Drake* (figure 3.13d) show a (small) energy surplus, the (possible) double ITCZ structure of *Panama* (figure 3.13c) alters the surface energy budget, E_{srf}, and causes an energy deficit.

Outgoing longwave radiation depends on the temperature of the atmosphere and consequently (in the high latitudes) on the sea ice coverage. Poleward of the subtropics E_{TOA} shows an energy deficit in all four cases and the amplitude of the deficit is directly (and inversely) related to the sea ice cover: In *Panama* and the northern hemisphere of

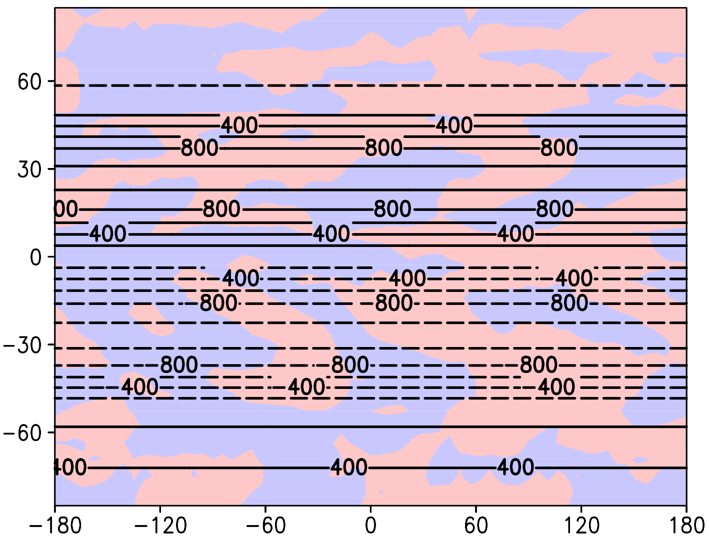

(a) *Aqua*

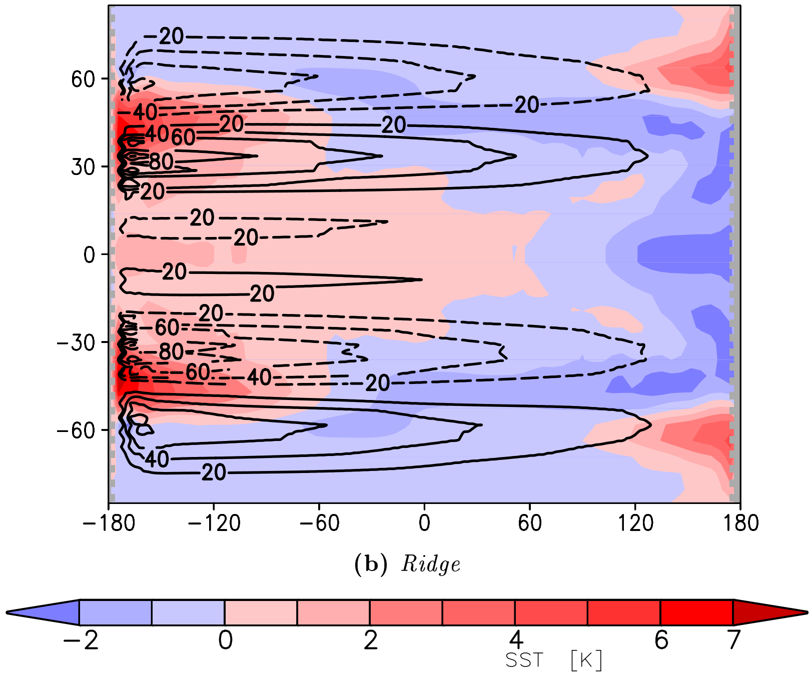

(b) *Ridge*

Figure 3.12: Barotropic horizontal stream function of the ocean (different contour intervals: 200 Sv in *Aqua*, between 20°N/S in *Panama*, and southward of 40°S in *Drake*; 20 Sv in *Ridge* and northward of 40°S in *Drake*; 60 Sv poleward of 20°N/S in *Panama*) and deviations from the zonal mean SST for *Aqua*, *Ridge*, *Panama*, and *Drake*

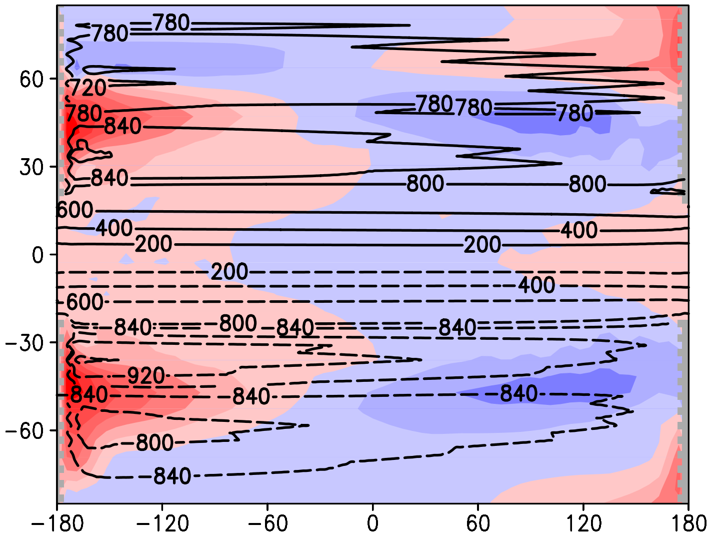

(c) *Panama*

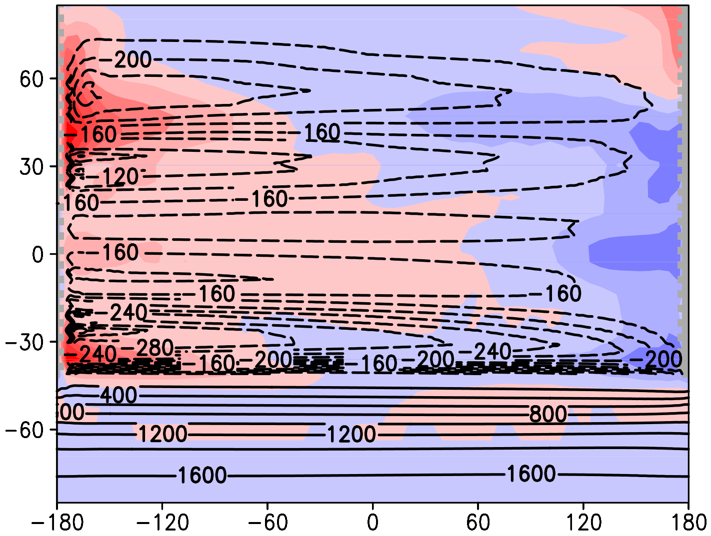

(d) *Drake*

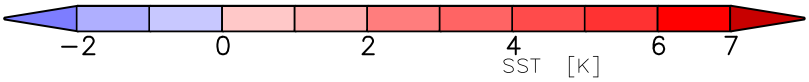

Figure 3.12: continued

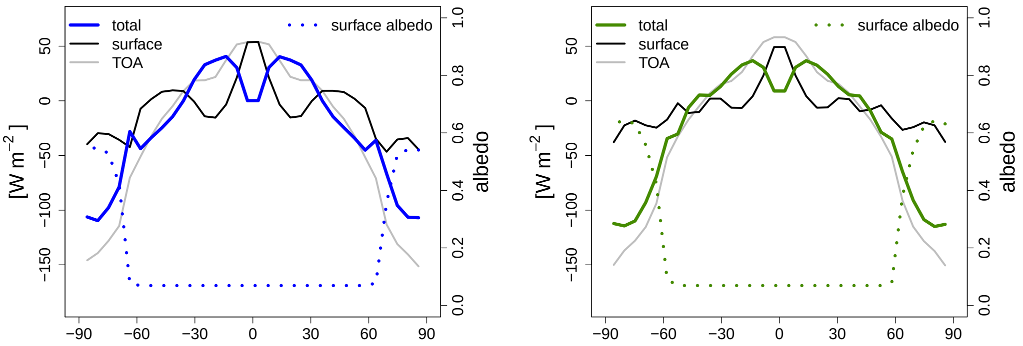

(a) *Aqua* **(b)** *Ridge*

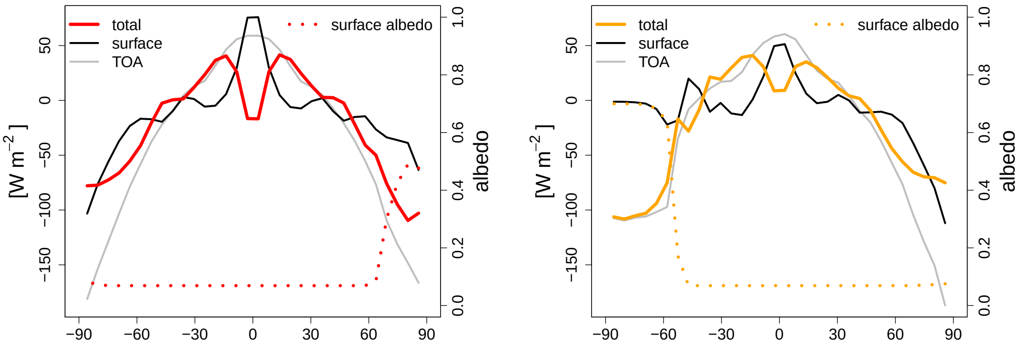

(c) *Panama* **(d)** *Drake*

Figure 3.13: Zonal mean atmospheric energy budget (total, at the TOA, and at the surface) and surface albedo for *Aqua*, *Ridge*, *Panama*, and *Drake*

Drake, the poles are warmer and, therefore, the energy deficit at the TOA is greater than in the other set-ups. E_{srf} also depends on the sea ice cover, via the albedo, temperature, and sensible and latent heat flux. If there is almost complete sea ice cover over the poles, like in *Aqua*, *Ridge*, and the southern hemisphere of *Drake*, the surface energy budget is almost balanced, while a strong deficit can be observed over open waters.

The surface albedo on the aquaplanets is directly related to the sea ice cover, since the entire surface of the planet is either covered with open water, which is dark and has a very low albedo (6.9 %), or sea ice with an albedo of 70 % (in our model set-up).

In all four set-ups, there is an energy net surplus in the tropics and a deficit at high latitudes. In order to maintain equilibrium, energy needs to be transported poleward. This transport is conducted by the atmospheric and oceanic circulation. The total energy transport and the partitioning into atmospheric and oceanic transport are presented in figure 3.14. The computation of energy transports is further described in appendix E.

The total transports are almost exactly the same in all four aquaplanet configurations, even though very different climates states emerge from the set-ups. This is not surprising, since after the concept of Stone (1978), the sum of the oceanic and at-

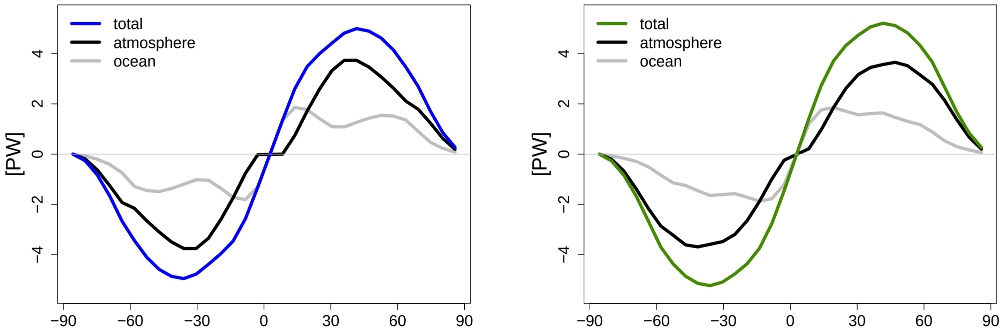

(a) *Aqua* **(b)** *Ridge*

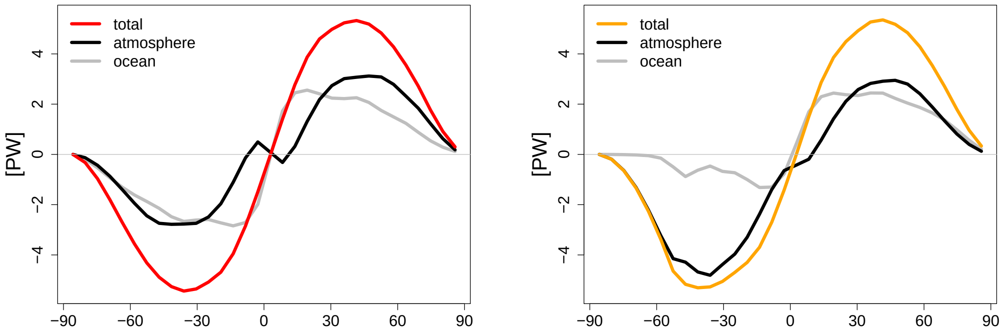

(c) *Panama* **(d)** *Drake*

Figure 3.14: Zonal mean vertically integrated meridional energy transport (total, atmospheric, and oceanic) for *Aqua*, *Ridge*, *Panama*, and *Drake*

mospheric meridional energy transports remains mostly constant throughout changes imposed on the climate system. While the total transports hardly differ, the partition into atmospheric and oceanic heat transports may change with the circulation regime. In the deep tropics the atmosphere has little or no contribution to the poleward energy transport. This feature is most pronounced in *Panama* (figure 3.14c) and the northern hemisphere of *Drake* (figure 3.14d), where the tropical ocean heat transport (OHT) is very strong (up to 3 PW) and the atmospheric energy transport in the deep tropics is directed equatorward. Poleward of approximately 10°N/S to 20°N/S, the OHT decreases and the atmospheric transport gains in importance. In *Aqua* (figure 3.14a), *Ridge* (figure 3.14b), and in the southern hemisphere of *Drake*, the atmospheric transport is great (with a maximum between 4 PW and 5 PW). However, the OHT is still considerable and, in *Aqua*, shows a secondary peak at approximately 70°. In *Ridge*, where a secondary peak does not occur, the OHT still exceeds 1 PW up to 70°N/S. In the southern hemisphere of *Drake*, the OHT is very weak compared to the other setups and vanishes completely poleward of 60°S. In the realizations with relatively warm poles (*Panama* and the northern hemisphere of *Drake*), the OHT is very large and the atmospheric energy transport, which is forced by the meridional temperature gradient,

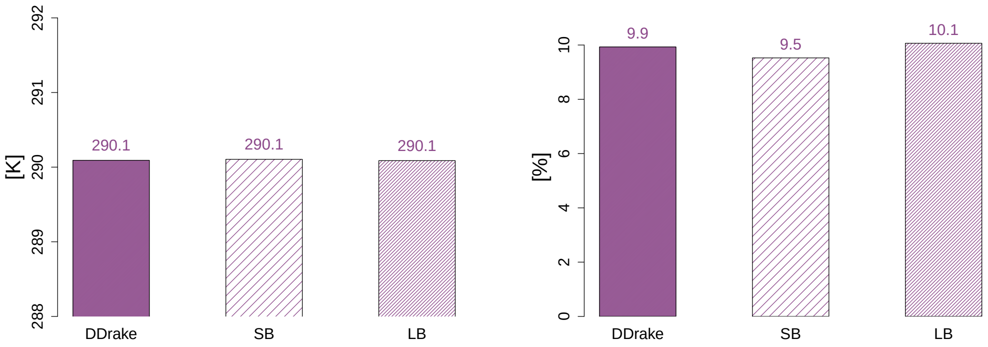

(a) global mean SST

(b) global mean sea ice cover (in % of global area)

Figure 3.15: Global and basin mean SST and sea ice cover for *DDrake*

is rather weak (both are of the same order of magnitude, i.e. between 2 PW and 3 PW).

3.4 DDrake

In the next step, the *DDrake* case, a second barrier is introduced into the system. Both ocean barriers have the same structure as the one in the *Drake* set-up from the previous section (3.3). Consequently, in *DDrake* two ocean basins are constructed instead of one, which are connected in the southern ocean. The zonal mean climate on a global scale is studied as well as zonal averages over the individual ocean basins, since one basin is substantially larger than the other.

3.4.1 Temperature and Water Cycle

The global mean sea surface temperatures (SSTs) and sea ice covers for *Aqua*, *Ridge*, *Panama*, and *Drake* (figure 3.3) instantly revealed that very different climate regimes emerge from the various ocean circulation regimes. However, for the *DDrake* simulation, the global and zonal averages of SST and sea ice cover (figures 3.15 and 3.16) are very similar to *Drake* (compare to figures 3.3 and 3.4), even though a second ocean basin is created.

The global mean SST for *DDrake*, as well as the SST averaged over each basin, is exactly the same as for *Drake* (i.e. 290.1 K, figure 3.15a). While in *Drake* $47.9\times10^6\,\mathrm{km}^2$ are covered with sea ice (9.4 % of the global mean area), *DDrake* has a slightly greater sea ice covered area with $50.5\times10^6\,\mathrm{km}^2$ (9.9 % of the global area, figure 3.15b). The smaller basin, *SB*, has less sea ice cover (9.5 % of the surface area) than the larger ocean basin, *LB* (10.1 % of the area).

In the zonal mean, the three SST profiles (zonal averages over the entire ocean of *DDrake* and zonal averages over the small basin, *SB*, and the large basin, *LB*) are almost identical (see figure 3.16a). Just as in *Drake*, very cold temperatures can be observed

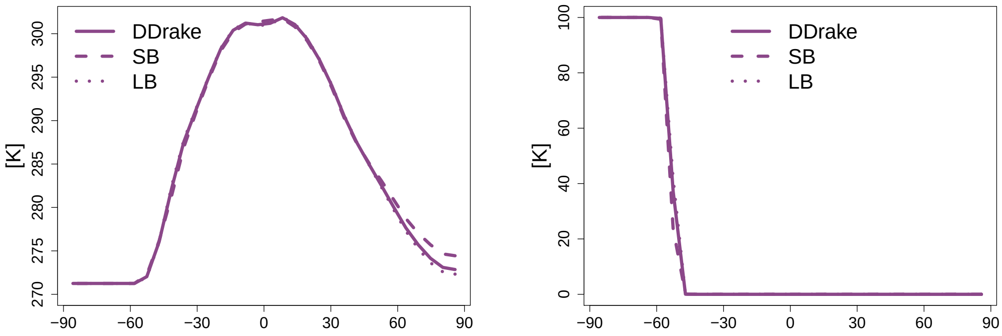

(a) zonal mean SST

(b) zonal mean sea ice cover (local area fraction)

Figure 3.16: Zonal mean SST and sea ice cover for *DDrake*

at the south pole, while the tropical maximum exceeds 300 K. A local minimum in the tropical temperature profiles occurs directly at the equator, but is absent in *SB*. The very cold temperatures at the south pole are related to the high sea ice cover in both basins (figure 3.16b). The sea ice cover is confined to the south pole while the north pole is completely ice-free. Consequently, the north pole is significantly warmer than the south pole and, while all SSTs are above freezing level, *SB* is about 2–3 K warmer than *LB*.

Figure 3.17 shows the zonal mean temperatures for atmosphere and ocean, as well as specific moisture of the atmosphere and salinity of the ocean. Zonal means for *DDrake* and for the basins *SB* and *LB* are displayed. In the atmosphere, the differences between *DDrake* and *Drake* (compare to figure 3.5d) are very small: The south pole is cold and dry, even at great heights, while the north pole is relatively warm and moist. The tropical zone of high moisture and warm temperatures is concentrated at the equator. Hardly any differences in atmospheric temperature and moisture distribution between *SB* and *LB* can be detected.

The thermohaline structure of the *DDrake* ocean is, overall, also all very similar to *Drake*, but some discrepancies between the different ocean basins occur. In all cases, the northern hemisphere is relatively warm, while the southern ocean is very cold poleward of the passage (40°S). However, it can be observed that in the northern polar ocean and in the deep ocean *SB* is colder than *LB*. The salinity is also generally higher in *SB* than in *LB*.

Figure 3.18 displays the total precipitation. The most precipitation occurs over the western sides of the ocean basins, while the eastern sides are dryer, which is related to warmer SSTs regions at the western boundaries of ocean basins (compare to figure 3.6). Tropical precipitation areas, as well as the precipitation regions of the baroclinic zones in the mid-latitudes, are well developed, but interrupted by the two ocean barriers of *DDrake*, even though they do not stretch into the atmosphere. However, they create areas of colder surface waters and, hence, less evaporation and heat fluxes over the eastern sides of the ocean basins.

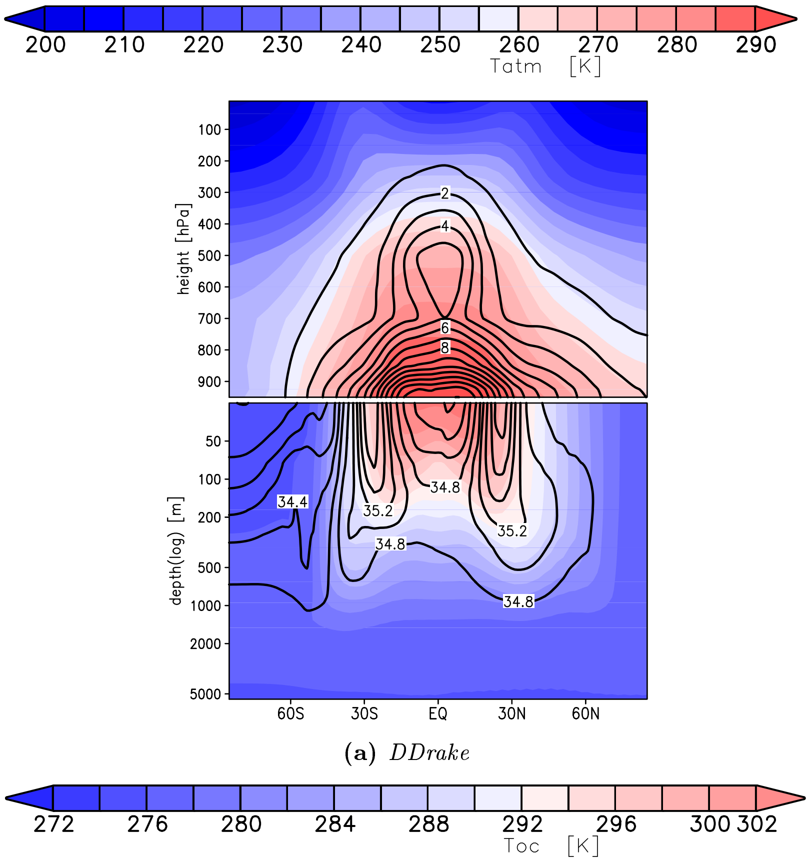

(a) *DDrake*

Figure 3.17: Zonal mean temperature in atmosphere and ocean (shaded), and atmospheric specific moisture/oceanic salinity (contour line spacing: 1 g/kg for the specific moisture and 0.2 psu for the salinity) for *DDrake*

The zonal mean precipitation, evaporation, and surface fresh water fluxes (figure 3.19) show the same structure as *Drake* (see figure 3.7d), with a strong equatorial precipitation peak, dry southern high latitudes, where neither much precipitation nor evaporation occurs and northern mid- and high latitudes that have warmer SSTs which favor higher precipitation as well as evaporation rates. Differences occur for *SB*, where precipitation rates are weaker over great areas. In the northern hemispheric mid-latitudes precipitation rates of *SB* are slightly stronger, but at the same time evaporation is greater and, thus, the surface fresh water flux is smaller at all latitudes. This explains the higher salinity concentrations in *SB* compared to *LB* (in figure 3.17).

Atmospheric water vapor transports for *DDrake* are displayed in figure 3.20. Moisture is transported equatorward inside the tropics, but poleward of 30°N/S the atmosphere transports water vapor toward the poles. Consequently, moisture convergence occurs at the equator and divergence in the subtropics. The vast amount of water vapor transport inside the tropics is achieved by the atmospheric mean circulation, while atmospheric

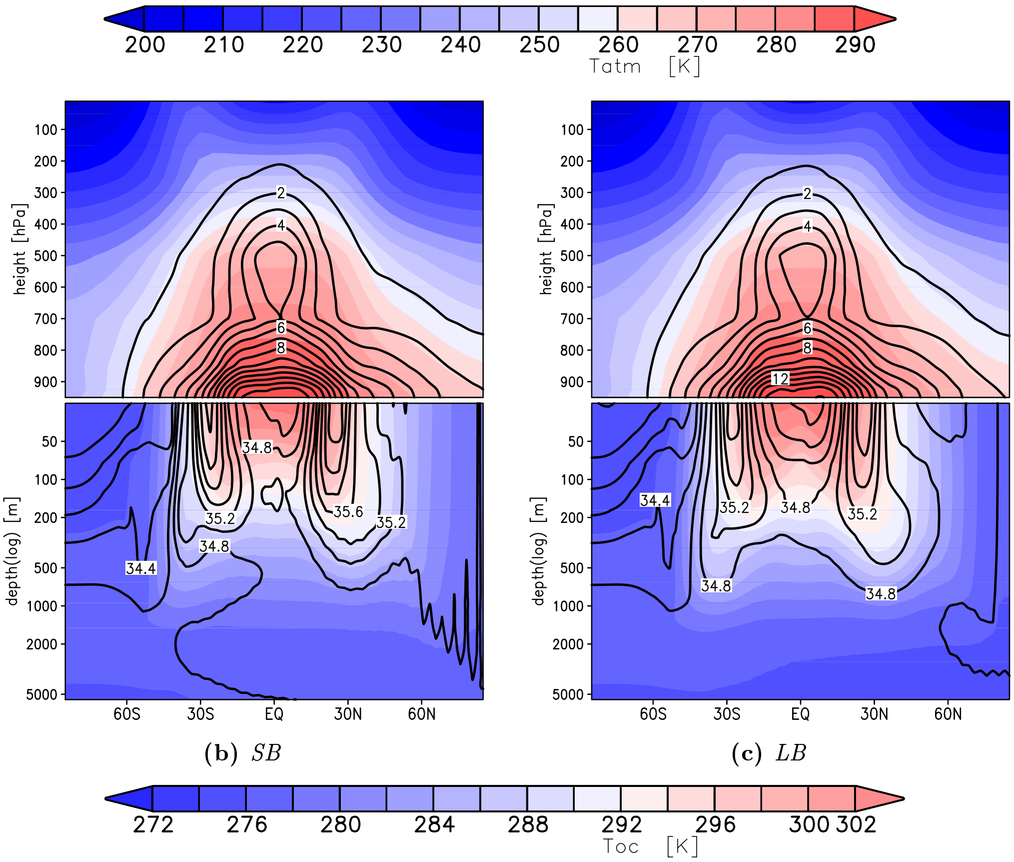

(b) *SB*

(c) *LB*

Figure 3.17: continued

eddies (mostly transient eddy-fields, since stationary eddies are negligible small in the absence of land masses) conduct almost the entire water vapor transport of the mid-latitudes. The moisture transport of the southern hemisphere (both tropical and extra-tropical) is greater than the transport northward of the equator. This is related to the different strengths of the atmospheric circulation cells in each hemisphere which is discussed in section 3.4.2. The meridional water vapor transport zonally averaged over the individual basins of *DDrake* is also shown in figure 3.20. The equatorward moisture transport of the tropics is stronger in *SB*, while the extra-tropical poleward water vapor transport of *LB* is greater.

The zonal mean dry and moist potential temperature distribution of *DDrake* (displayed in figure 3.21) is very similar to *Drake* (compare to figure 3.9d). While the tropical temperature gradient is very weak, a broad baroclinic zone extends from the subtropics into the mid-latitudes. The moist potential temperature profile differs most strongly from the dry potential temperature profile in the tropics, since this is the area with the greatest moisture content. The relatively warm and moist north pole shows different potential temperature profiles throughout the entire troposphere than the sea ice covered south pole, which is very cold and dry at all levels. Some deviations of the

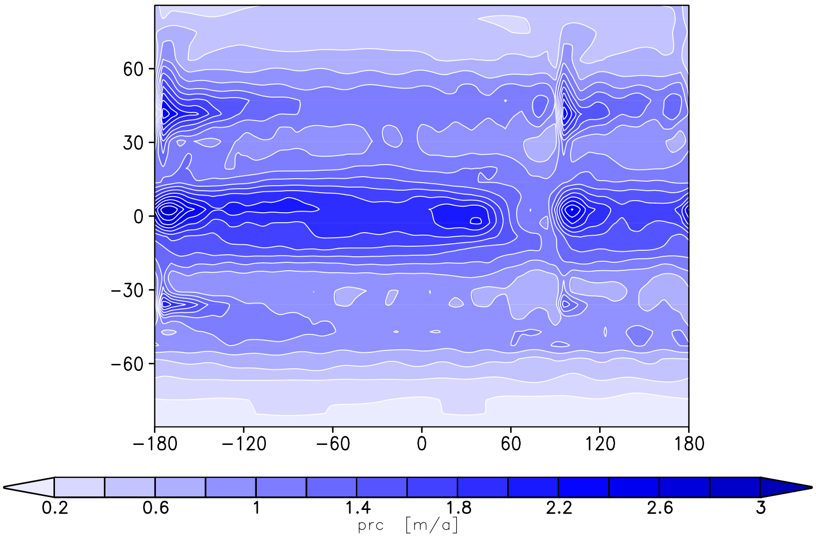

Figure 3.18: Total precipitation (large scale plus convective) for *DDrake*

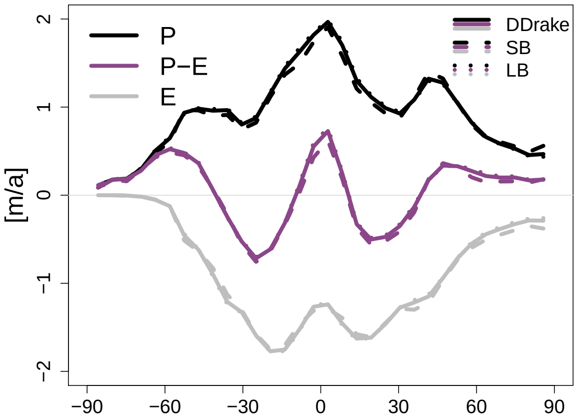

Figure 3.19: Zonal mean precipitation (P), evaporation (E), and surface fresh water flux: precipitation minus evaporation ($P - E$) for *DDrake*

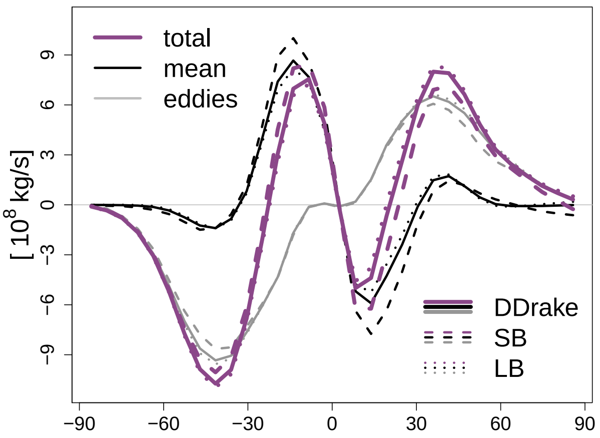

Figure 3.20: Zonal mean vertically integrated meridional atmospheric moisture transport (total transport, transport by the mean circulation, and eddy-transport) for *DDrake*

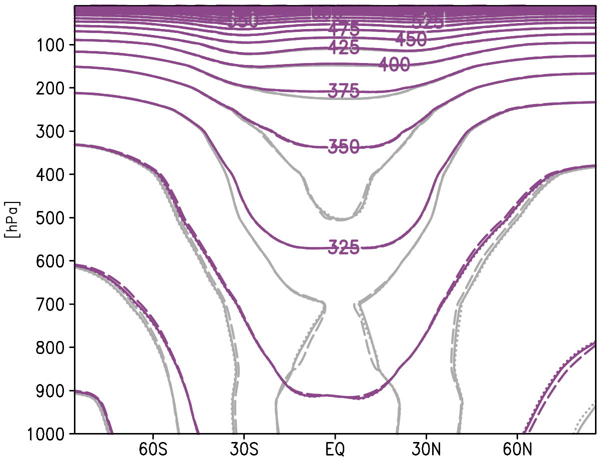

Figure 3.21: Zonal mean atmospheric potential and moist potential (gray) temperature (*DDrake*: solid lines, *SB*: dashed lines, *LB*: dotted lines) for *DDrake*

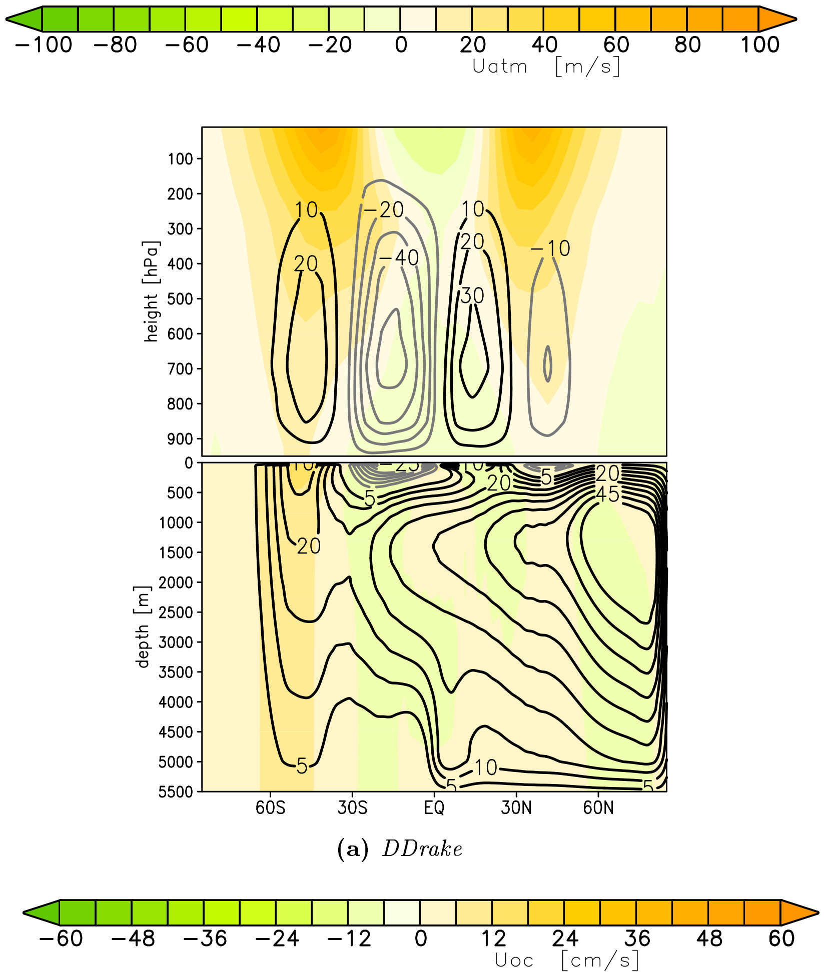

(a) *DDrake*

Figure 3.22: Zonal mean zonal wind/ocean currents (shading) and atmospheric stream function/MOC (contour lines in 10^9kg/s for the atmospheric stream function and in Sv for the MOC) for *DDrake*

individual basins can be detected: the north pole is warmer in *LB* and the tropical air is dryer in *SB*.

3.4.2 Circulation

Figure 3.22a shows the atmospheric and oceanic circulation of *DDrake*. Since the meridional temperature gradient is similar, the atmospheric stream function has the same pattern as the one from *Drake* (see figure 3.10d): The southern Hadley cell is much stronger (50×10^9 kg/s in the maximum) and larger than in the northern hemisphere (with a maximum of 30×10^9 kg/s). The southern Ferrel cell is also stronger (with a maximum of 20×10^9 kg/s). Furthermore, the subtropical jet stream in the southern

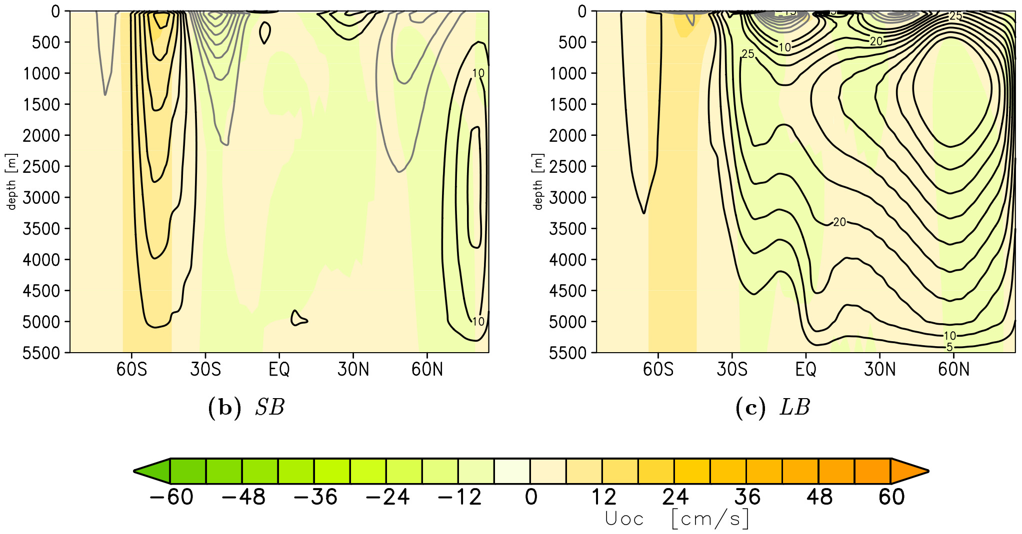

(b) *SB*

(c) *LB*

Figure 3.22: continued

hemisphere has higher velocities. Polar easterlies can only be observed over the north pole. In the tropics easterly winds prevail at all levels.

The strength and overall pattern of the MOC in *DDrake* (figure 3.22a) show similar features as in *Drake* (compare to figure 3.10d): There is also a great interhemispheric cell that stretches over almost the entire global ocean (except the deep southern ocean). In *SB* (figure 3.22b) there is a strong sinking region in the area of the passage (in the southern ocean). There is no interhemispheric cell so little cross-equatorial transport can take place in the small basin of *DDrake*. In contrast, in *LB* (figure 3.22c) there is a large cell stretching from the north pole to approximately 30°S. However, in the southern ocean the large basin shows only very weak overturning circulation.

The zonal mean zonal surface winds averaged over the global ocean and over each basin (at 925 hPa) are depicted in figure 3.23a. The most pronounced feature is the hemispherical asymmetry in *DDrake*: The southern hemispheric tropical surface easterlies and mid-latitude westerlies are much stronger than their counterparts in the northern hemisphere, which is related to the greater equator-to-pole temperature gradients. The only exception is the polar region of surface easterly winds, which is very pronounced in the northern hemisphere, but does not exist in the southern high latitudes. Close to the equator, the surface easterlies over *SB* are weaker than over the other basins. However, in the northern mid-latitudes the west wind zone close to the surface is stronger over *SB* than over *LB*.

The zonal mean zonal surface currents of the ocean (at a depth of 25 m, in figure 3.23b) show a similar picture as the surface winds: A strong westerly current (up to 0.15 m/s) develops at approximately 60°S, where the passage in the barrier allows circumpolar flow. Tropical easterlies are approximately of equal strength in both hemispheres, but the westerly currents in the northern mid-latitudes are very weak. The zonal ocean velocity strongly depends on the basin size, since stronger velocities develop in a greater

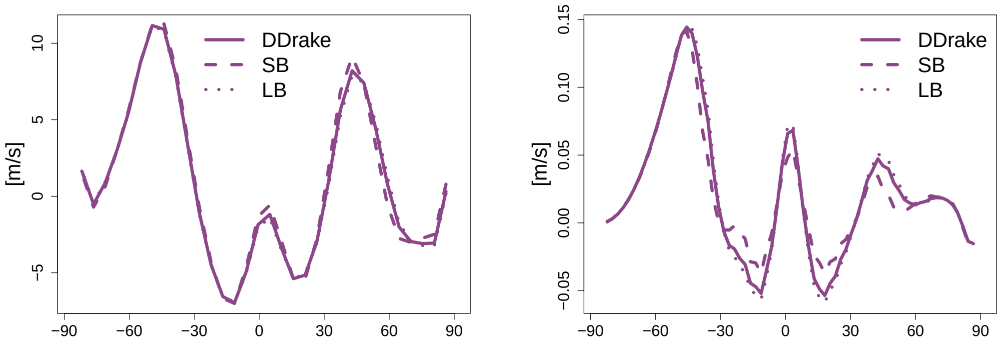

(a) zonal surface wind (atmosphere)

(b) zonal surface currents (ocean)

Figure 3.23: Zonal mean zonal surface winds (at 925 hPa) and currents (at a depth of 25 m) for *DDrake*

basins: the weakest velocities can be observed in *SB* and the strongest zonal ocean currents in *LB*.

The size of the ocean basin is essential when dealing with the structure of the barotropic horizontal stream function, i.e. the depth-integrated ocean flow, as shown (together with zonal SST deviations) in figure 3.24. Northward of the passage at 40°S gyral structures develop in each basin, however, stronger gyres can be observed in larger basins. While in the northern hemisphere of *LB* very pronounced subpolar and subtropical gyres exist, the gyres of *SB* are much weaker. The southern hemisphere also shows subtropical gyres but poleward of 40°S strong circumpolar zonal flow develops.

The zonal SST deviations reveal warmer ocean surfaces at the western sides of the basins and colder SSTs at the eastern sides. Only the polar ocean is warm close to both sides of the boundary and colder in the middle of the basin. Poleward of the passage, hardly any zonal SST deviations occur.

3.4.3 Energy

The energy budget for *DDrake* is calculated in accordance with equations (3.1) to (3.3) from the previous section. Figure 3.25 shows the zonal averages of the total energy budgets for *DDrake*, *SB*, and *LB*, as well as the balances at the top of the atmosphere (TOA) and at the surface. Zonal mean surface albedos are also displayed.

The total energy budget of *DDrake* strongly resembles the budget of *Drake* (see figure 3.13d). Most notably, an asymmetry between the north and south pole occurs, since the north pole is much warmer. Thus, more longwave radiation leaves the atmosphere and the energy budget at the TOA is highly negative. At the south pole the energy balance at the TOA also shows a deficit, but the surface budget is almost balanced because of the sea ice cover, which causes a high reflection rate of incoming shortwave radiation but also inhibits great amounts of outgoing longwave radiation, sensible or latent heat fluxes.

Main differences between the energy budgets of *SB* and *LB* occur at low latitudes and

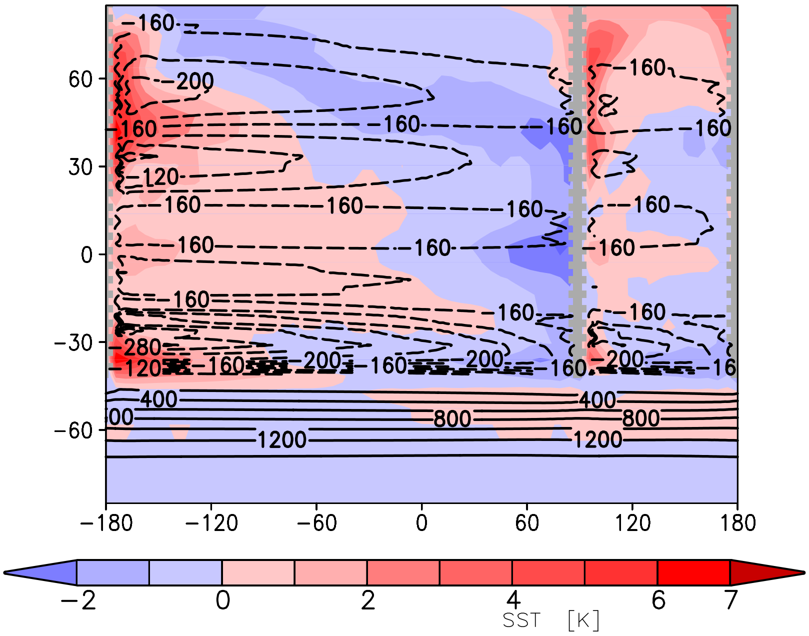

Figure 3.24: Barotropic horizontal stream function of the ocean (different contour intervals: 200 Sv southward of 40°S and 20 Sv northward of 40°S) and deviations from zonal mean SST for *DDrake*

at the north pole. The total energy budget of the subtropics in *SB* is smaller, but the local equatorial minimum is also less pronounced, which is mostly caused by differences in the surface energy budget. At northern high latitudes the total energy budget of *SB* is less negative than over *LB*. Again, the differences are located in the surface energy budget, since the SSTs of *LB* are slightly cooler than of *SB* (see figure 3.16a).

The zonal mean vertically integrated meridional heat transport of *DDrake* is displayed in figure 3.26a. The total meridional heat transport as well as the atmospheric and the oceanic transport strongly resemble the transports of *Drake* (compare to figure 3.14d). The atmospheric transport dominates in the southern hemisphere, where the ocean heat transport is rather weak. In the northern hemisphere, the OHT gains in importance and both atmospheric and oceanic heat transport are of similar magnitude.

Figures 3.26b and 3.26c additionally show the atmospheric and the oceanic heat transports of the individual basins of *DDrake*. Only latitudes between 40°S and 90°N are shown, since this is the area where the ocean barrier is closed. In *SB* the northern hemispheric OHT is very large (approximately 3.5 PW at the maximum) and even exceeds the atmospheric energy transport, which is rather weak in the northern hemisphere and equatorward of 15°N the atmospheric energy transport of *SB* is directed southward. However, in the southern hemisphere the picture is reversed: the OHT of *SB* is very weak and equatorward of 10°S still directed northward, while the atmospheric energy transport is rather strong. Heat transports in *LB* differ from the transports of *SB*. Most notably, the OHT has its zero-crossing at the equator, i.e. all oceanic heat transports are directed poleward, and the atmospheric transport of *LB* changes its sign almost

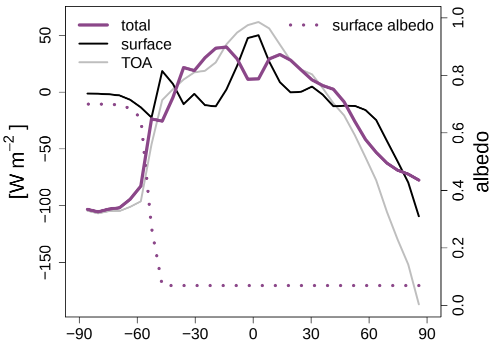

(a) *DDrake*

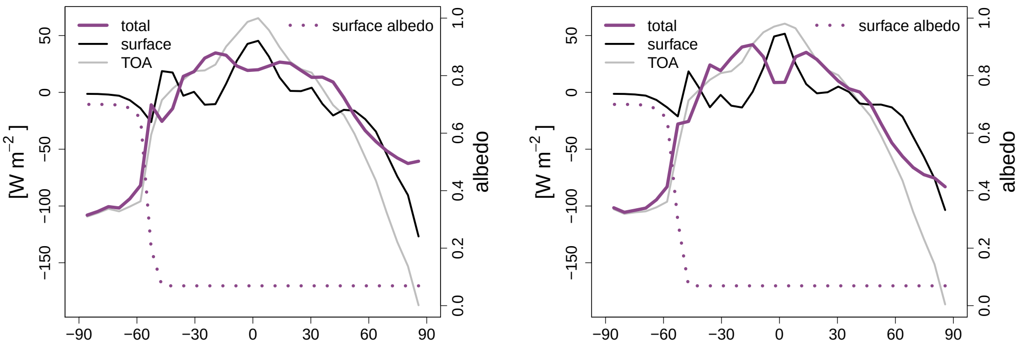

(b) *SB* **(c)** *LB*

Figure 3.25: Zonal mean atmospheric energy budget (total, at the TOA, and at the surface) and surface albedo for *DDrake*

directly at the equator (at approximately 5°N).

3.5 Summary and Discussion

Different idealized set-ups, which vary between a pure aquaplanet and expanded aquaplanets that contain one or two meridional ocean barriers, are studied with a coupled model to cover a wide spectrum of ocean circulation regimes. While *Aqua* allows unconstrained zonal flow, *Ridge* creates a single closed ocean basin. The settings of *Panama* and *Drake* also include closed basin circulation, but allow circumglobal flow in the tropics and in the southern ocean, respectively. *DDrake* contains two ocean basins with different dimensions, which are connected in the southern ocean. The climatic impacts of these fundamentally different ocean circulation regimes are analyzed and intercompared.

There are few previous aquaplanet simulations with coupled atmosphere–ocean general circulation models, but (for example) studies by Smith *et al.* (2006), Marshall *et al.* (2007), Enderton & Marshall (2009), and Ferreira *et al.* (2010) exist: Marshall *et al.*

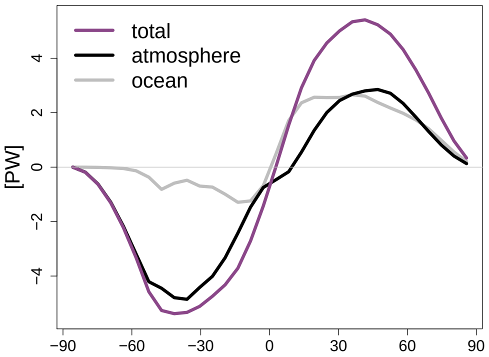

(a) total, atmosphere & ocean (*DDrake*)

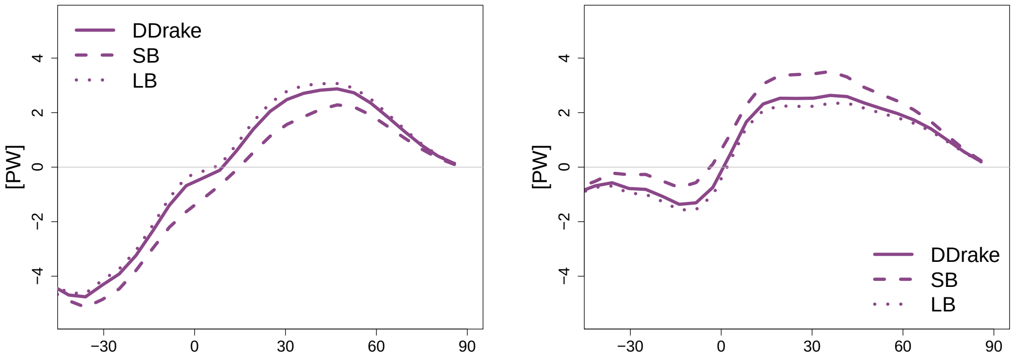

(b) atmosphere (*DDrake*, *SB* & *LB*)   **(c)** ocean (*DDrake*, *SB* & *LB*)

Figure 3.26: Zonal mean vertically integrated meridional energy transport: (a): total, atmospheric, and oceanic transport for *DDrake*; (b) & (c): atmospheric and oceanic transport of the individual basins of *DDrake*

simulate a pure aquaplanet only. An aquaplanet, like *Aqua*, is also analyzed by Smith *et al.*, who furthermore study set-ups, which strongly resemble *Ridge* and *Drake*. Four cases, like *Aqua*, *Ridge*, *Panama*, and *Drake*, are studied by Enderton & Marshall, who focus on meridional energy transports in different circulation regimes. A *DDrake* set-up is analyzed by Ferreira *et al.* (together with cases resembling *Aqua*, *Ridge*, and *Drake*). However, it should be noted that Marshall *et al.*, Enderton & Marshall, and Ferreira *et al.* apply the same model and, for the most part, use the same experimental design.

The ocean circulation of the pure aquaplanet, *Aqua*, differs strongly from the other set-ups with meridional ocean barriers, but the other two aquaplanet simulations (by Smith *et al.* and the set-up described by Marshall *et al.* and Enderton & Marshall) develop ocean circulation regimes, which are very similar to *Aqua*. The ocean flow is predominantly zonal and reflects the sense of the surface winds: easterlies in the tropics and westerlies and the mid-latitudes. The meridional overturning circulation consists of two Ekman cells in each hemisphere with Ekman pumping centered on 30°N/S and upwelling at the equator. There are no zonal pressure gradients and mean meridional flow is not supported by geostrophy. Hence, Sverdrup balance is not possible in *Aqua*.

When comparing the results of Marshall *et al.* to the climate state of *Aqua*, the distribution of the potential temperature in atmosphere and ocean, as well as moisture and salinity patterns resemble each other. In contrast to the aquaplanet climate of Smith *et al.*, which is very warm and completely ice-free, sea ice covers the poles and reach down to the mid-latitudes (to 55°N/S in the aquaplanet of Marshall *et al.* and to 65°N/S in *Aqua*). The Hadley and Ferrel cells of the aquaplanet by Marshall *et al.* are stronger than in *Aqua*, which is related to a slightly stronger meridional temperature gradient.

Even though *Aqua* differs most strongly in its ocean circulation from the other cases with closed basin circulation, the mean climate states of *Aqua* and *Ridge* are similar: Both result in climate states that are hemispherically symmetric. Sea ice covers the poles and causes strong meridional temperature gradients. Consequently, the atmospheric circulation (Hadley and Ferrel cells) are relatively strong. A single equatorial precipitation peak can be observed in the zonal mean. However, as already observed by Smith *et al.*, the scenarios with an ocean barrier have significantly different rainfall patterns than the zonally symmetric structure of the aquaplanet, despite a lack of direct orographic forcing. A pool of warm water and strong boundary currents, which transport warm water poleward, develop at the western side of the ocean basin and influence surface heat fluxes and, thus, the precipitation rates.

Aqua and *Ridge* differ mostly in the ocean: Just like in *Ridge* and in contrast to *Aqua*, the set-ups with a closed barrier by Smith *et al.* and Enderton & Marshall are able to support zonally integrated geostrophic meridional flow. Thus, a deep hemispherically symmetric MOC pattern develops in *Ridge* with sinking regions at both poles and upwelling at the equator. The ocean of *Ridge* is fresher, especially at the poles which is related to a higher sea ice cover, while the deep ocean of *Aqua* is colder and contains more salt. The zonal ocean currents of *Aqua* are much stronger than in *Ridge*, where the barrier prevents circumglobal flow.

There are great differences between the climates of *Ridge* and the closed barrier set-up of Enderton & Marshall. In this study *Ridge* has the highest sea ice cover of all four cases (in the global mean) and accordingly a relatively cold climate with a great equator-to-pole temperature gradient, but there is no sea ice at all in the closed barrier set-up of Enderton & Marshall, which has a warm climate with a rather weak meridional temperature gradient. However, the ocean circulation patterns of *Ridge*, i.e. the depth-integrated flow and the MOC, still strongly resemble the closed basin circulation set-up of Enderton & Marshall.

In *Panama* very similar climates to the according set-up by Enderton & Marshall are found. Most importantly, the lack of zonal pressure gradients in the tropics creates strong zonal flow at low latitudes. Very warm temperatures develop in *Panama* and hardly any sea ice forms at the relatively warm and moist poles, which also show higher salinity concentrations. The equatorial precipitation zone is very spread out, i.e. there is a hint of a double ITCZ, which is created when tropical temperature gradients are weak (see for example Dahms *et al.*, 2011). However, the horizontal resolution of the model is very coarse and it cannot be conclusively determined if indeed a double ITCZ or a very broad tropical precipitation zone exists. Furthermore, the flat meridional temperature gradient causes weak Hadley and Ferrel cells and reduces zonal winds.

Drake has a passage in the southern hemisphere and, thus, a hemispherically asymmetric climate state. The southern hemisphere is very cold with extensive sea ice cover and dry air over the poles, which goes along fresh water intrusion in the polar ocean. A great equator-to-pole temperature gradient creates a very strong Hadley cell in combination with a strong subtropical jet. The northern hemisphere is, in contrast, very warm and ice-free. The air is moist and the polar ocean is warmer and contains more salt. The meridional temperature gradient is weaker and, hence, the atmospheric Hadley cell is not as strong as in the southern hemisphere.

The set-up with circumpolar flow in the southern ocean of Enderton & Marshall resembles the aquaplanet in the southern hemisphere and the closed barrier case in the northern hemisphere. This is consistent with the *Drake* set-up of this study, even though the resulting climate in the northern hemisphere resembles *Panama* more closely than *Ridge* because of the ice-free poles. The MOC of the *Drake* set-up by Smith *et al.* resembles the closed basin flow more strongly than in this study, where a great interhemispheric cell is created.

The cases from Smith *et al.*, which resemble *Ridge* and *Drake*, develop a similar horizontal ocean circulation with subpolar and subtropical gyres as in *Ridge* and a gyral structure combined with the circumpolar flow in the southern ocean as in *Drake*. However, the depth-integrated flow is slightly stronger in *Ridge* and *Drake* than in the experiments by Smith *et al.*

The zonal mean climate of *DDrake* is very similar to the zonally averaged climate state of *Drake*, which is consistent with the results of Ferreira *et al.*, who observe that on a global scale the climates are very similar independent from inserting one or two ocean barriers in the aquaplanet ocean: Both *Drake* and *DDrake* have sea ice covered south poles and ice-free north poles, stronger atmospheric circulation in the southern hemisphere (where the meridional temperature gradient is greater), the MOC has two shallow wind-driven cells and a clockwise interhemispheric circulation extending from deep sinking regions at the north pole southward (to 50°S in Ferreira *et al.* and to 60°S in *Drake* and *DDrake* of this study).

However, the regional climates of *Drake* and *DDrake* differ significantly. Just like in the results of Ferreira *et al.*, the *DDrake* simulation reveals that the smaller and larger basin (*SB* and *LB*) have characteristics, which resemble the Atlantic and Pacific oceans, respectively: *SB* is warmer and saltier than *LB* and in *SB* the northward OHT is much stronger.

The main characteristics of the *DDrake* simulation compare very well to the results of Ferreira *et al.*, however, there are some significant differences: The small basin of Ferreira *et al.* is dominated by a deep-reaching clockwise cell that extends from the north pole to the southern margin, while the MOC of *SB* is characterized by two deep cells which are confined to higher latitudes. Furthermore, the OHT in the small basin by Ferreira *et al.* is northward everywhere, while *SB* shows a strong northward OHT only in the northern hemisphere (and generally a weak but southward OHT in the southern hemisphere).

Marotzke & Willebrand (1991) also simulate an idealized configuration of the world ocean, which resembles the *DDrake* set-up. However, in the set-up by Marotzke & Willebrand, both basins are of equal size and they apply an ocean model which is driven by wind forcing, by restoring sea surface temperatures to prescribed values, and specified freshwater fluxes in the surface salinity budget. They find multiple steady states, which are characterized by deep-water formation in different basins.

A *DDrake* case with ocean basins of equal size has also been simulated with the Planet Simulator–LSG AOGCM. However, the case is not presented here, since the results are identical with the *DDrake* simulation from this study (on a global scale and the individual basins hardly differ from the global scale results). Multiple steady states do no occur.

Overall, the coupled atmosphere–ocean model (PlaSim & LSG) is able to simulate different aquaplanet configurations and produce results, which are consistent with previous studies. There are some differences, which are mainly connected to the sea ice cover and the resulting meridional temperature gradient. *Ridge* is the case, where discrepancies to previous studies are the greatest. However, the ocean circulation regimes are still relatively similar.

The total energy transport of the coupled system for all cases is not only very similar to other aquaplanet simulations, but also to observations (see for example Peixoto & Oort, 1992). This is expected because Bjerknes (1964) and Stone (1978) explain that the sum of the oceanic and atmospheric meridional energy transports remains mostly constant throughout changes imposed on the climate system. Stone (1978) found that the controlling factors on the strength and form of the total meridional energy transport are limited to size, rotation rate, and axis tilt of the Earth, the solar constant, and the mean hemispheric albedo. He suggested that this concept should hold even under unusual conditions or scenarios, which is supported by the great idealizations of different ocean circulation regimes from this study. However, as shown in *Aqua*, *Ridge*, *Panama*, *Drake*, and *DDrake*, the partition of the heat transport between atmosphere and ocean may change.

Czaja & Marshall (2006) note that the partition of heat transport between atmosphere and ocean in the aquaplanet simulation is remarkably similar to that of the present climate: the atmosphere dominates in mid- to high latitudes and the ocean dominates in the tropics.

The total heat transport of *Aqua* is slightly smaller than the one from the Marshall *et al.* simulation, however, the oceanic heat transport also dominates in the tropics and the atmospheric transport everywhere else. It should be noted, however, that the oceanic heat transport (OHT) differs from the observed OHT as well as from the one seen in the aquaplanet of Marshall *et al.* and Enderton & Marshall, which peaks at typically 2 PW around 20°N/S and is already very weak at 60°N/S. The maximum of *Aqua* is also approximately 2 PW and located around 20°N/S, but there is still a very strong OHT of over 1 PW up to approximately 75°N/S. While the OHT in *Aqua* shows the peak convergence poleward of 70°N/S, the maximum convergence in observation and in Enderton & Marshall is located in the mid-latitudes. Consequently, in *Aqua* the OHT carries much more heat into high latitudes, which affects the partition between atmosphere and ocean.

When interpreting and comparing results, it has to be kept in mind, that different model set-ups are applied. Smith *et al.* also applies a model of relatively low resolution and medium complexity, however, orbital parameters are set to present-day values, in contrast to this study, where perpetual equinoctial conditions are used. Marshall *et al.*, Enderton & Marshall, and Ferreira *et al.* also use present-day orbital parameters, but in a model with higher resolution. The depth of the ocean is similar with 5,200 m (compared to 5,500 m in this set-up).

4 Low-frequency Climate Variability

> *"The most exciting phrase to hear in science, the one that heralds new discoveries, is not 'Eureka!' but 'That's funny...' "*
>
> — ISAAC ASIMOV

4.1 Introduction

The variability of the climate of the aquaplanet (*Aqua*, see chapter 3) is analyzed[2]. An aquaplanet is a planet, where the entire surface of the earth is covered by one ocean with a flat bottom and without any geometrical constraints. Without complex land–sea configurations, many features of the climate are easier to analyze and can be compared to theoretical studies and conceptual models. Furthermore, many characteristics of the zonal mean climate state of the Earth are hardly influenced by topographic features, like continents. Aquaplanets are, therefore, an idealized test environment, in which basic mechanisms and feedbacks can be highlighted and explored.

The aim of this study is to analyze the variability of a coupled atmosphere–ocean climate system, in which complexities caused by land–sea configurations are eliminated, but with a full general circulation model (GCM) which represents the dynamics of the climate system. A purely internally forced climate variability is assessed, as all external forcings are kept constant throughout the entire integration.

---

[2] Some of the results of this chapter are also presented in Dahms *et al.* (2012a).

Past applications of aquaplanets are mostly connected to atmosphere-only models and fixed sea surface temperatures (for example Hess *et al.*, 1993; Chao & Chen, 2004; Neale & Hoskins, 2001b,a; Dahms *et al.*, 2011), however, some studies on aquaplanets with coupled atmosphere–ocean general circulation models (AOGCMs) exist. A pure aquaplanet, like the one studied here, has also been simulated by Smith *et al.* (2006), Marshall *et al.* (2007), Enderton & Marshall (2009), and Ferreira *et al.* (2010, 2011).

Smith *et al.* explore the role of the ocean circulation in transporting heat around the globe in a coupled system in an aquaplanet configuration. The resulting climate is very warm (much warmer than the present-day climate) and contains a weak equator-to-pole temperature gradient. Marshall *et al.* analyze the mean climate and the variability of an aquaplanet. In contrast to Smith *et al.*, they find a rather cold climate with ice caps over the poles and strong meridional temperature gradients. Enderton & Marshall, who apply the same model as Marshall *et al.*, concentrate on the meridional heat transport. Ferreira *et al.* find multiple stable states in the aquaplanet simulated with a coupled model: a cold state (presented in Marshall *et al.*, 2007), an ice-free warm solution (presented in Ferreira *et al.*, 2010), and a snowball state (presented in the appendix of Ferreira *et al.*, 2011).

Even though coupled aquaplanet experiments and their multiple equilibria have been analyzed before, there are some major new aspects in the simulation presented in this study. A general circulation model of intermediate complexity is applied, which is, hence, able to simulate very long periods of time. In contrast to Ferreira *et al.* multiple equilibria are not observed, but a very dominant low-frequency oscillation between cold and warm climate states develops in the long-term integration. All compartments of the coupled system are included: atmosphere, ocean, and sea ice. Such an oscillation in an aquaplanet set-up has not been reported before.

The experimental design and the data analysis methods are introduced in section 4.2. Time series of various fields are presented in section 4.3 to visualize the variability of the aquaplanet climate. In section 4.4 mean climate states of extreme *cold* and *warm* time periods are presented and compared. Two different methods are used to obtain a deeper understanding for the nature of the low-frequency variability and to gain insight into the physical mechanisms behind this process. In section 4.5 empirical orthogonal function (EOF) analyses are applied to the individual atmospheric and oceanic fields. To complement the EOF analysis, which finds orthogonal patterns that maximize explained variance, but does not necessarily find dynamically significant components, a composite life cycle of the low-frequency oscillation is computed and presented in section 4.6. In section 4.7 the results are discussed.

4.2 Experimental Design and Time Series Analysis Methods

An aquaplanet is completely covered by an ocean. There are no land masses, and no topographical constraints on the atmospheric or oceanic circulation and, hence, the boundary conditions of the aquaplanet are completely zonally symmetric and symmetric about the equator.

The pure aquaplanet, *Aqua*, has been introduced in chapter 3, where the zonal mean state has been studied. However, a long-periodic climate oscillation occurs in the aquaplanet, which is analyzed here. The simulation from the previous chapter is used and all parameters are the same as in *Aqua* (the set-up is displayed in figure 3.1a), where all external forcings are kept constant throughout the entire integration:

- The ocean has a flat bottom with a uniform depth of 5,500 m.
- The solar constant is fixed at 1,365 W/m^2.
- The atmospheric CO_2 concentration is kept constant at 360 ppm.
- The simulation is carried out under perpetual equinoctial conditions to exclude the seasonal cycle. The seasonal cycle of atmospheric ozone is switched off.
- The integration starts from steady state.
- The simulation is run for 20,000 years since a very long spin-up time is needed for the ocean.

The following time series analysis methods are applied to analyze the low-frequency climate oscillation and to understand the processes and physical mechanisms behind this long-periodic variability pattern:

> **Time Series:** To visualize the oscillation, time series over 10,000 years are displayed (the years 10,001 to 20,000). The beginning of the time series might still contain some spin-up effects, however, they are minor compared to the amplitude of the oscillation.
>
> ***Cold* and *Warm* Climates:** 100-year averages over extreme *cold* and *warm* phases are taken to analyze the different climate states. Since the variability is very high, a long averaging period is necessary to capture the mean state. However, 100 years is approximately the longest time that the climate remains relatively constant in a climate state. How the *cold* and *warm* time periods are chosen is further explained in section 4.4
>
> **EOF Analysis:** An empirical orthogonal function (EOF) analysis is applied to the individual yearly averaged and zonal mean atmospheric and oceanic fields. For the EOF analysis, time series of 5,000 years (the years 15,001 to 20,000) are used to obtain sufficient cycles of the low-frequency oscillation, but to still avoid as much spin-up effects as possible. EOFs are explained, for example, in von Storch & Zwiers (1999, chapter 13). Furthermore, a short overview of the EOF analysis is given in appendix D.
>
> **Lead–Lag Correlations:** Lead–lag correlations (see appendix D) are computed between the first principal component (PC 1) of the meridional overturning circulation (MOC, as a reference variable) and other relevant

PCs of atmospheric and oceanic fields to find the sequential arrangement of the oscillation and the interrelationships between variability patterns. Time series of 5,000 years (the years 15,001 to 20,000) are also used for this analysis.

Composite Life Cycle: A composite life cycle of the low-frequency oscillation is constructed to find relations and feedbacks between the variability of atmospheric and oceanic fields with the MOC as a reference variable. A 101-year running mean of the time series of PC 1 of the MOC is computed and local maxima are identified. With the mean distance between the peaks, six single oscillation cycles centered around the maxima are chosen. Composites are computed for the years, when the cycle is at its minimum, at its zero-crossing and increasing, at its maximum, and at its zero-crossing and decreasing.

4.3 Time Series

Time series of various atmospheric and oceanic fields are displayed to get a first insight into the climate variability of the aquaplanet. As discussed in section 4.2, the spin-up time of the ocean model is very long and, therefore, not the entire time series can be used for analysis. Time series of the years 10,001 to 20,000 are presented. The beginning of the time series might still contain some spin-up phenomena, however, the climate of the aquaplanet does not exhibit any significant trends after the first 10,000 years of integration, though variability over a broad range of time scales can be observed.

Figure 4.1a presents time series of the global mean sea surface temperature (SST) and the global mean sea ice cover. Furthermore, time series of the meridional overturning circulation in the ocean are shown in figure 4.1b (the northern hemisphere is chosen as an example). Depicted are the maxima (positive or negative, depending of the sense of the circulation) of the yearly averaged strengths of the tropical and extra-tropical cell and the according 101-year running means (see appendix D for a short explanation of moving averages) to filter contributions of decadal variability (see for example Zhu *et al.*, 2006). Both figures reveal a very dominant low-frequency climate oscillation.

The global mean sea ice cover oscillates between states without any sea ice at all and peak values of approximately 10 % of the global area. The according global mean SST time series varies with a difference between cold and warm temperature extremes of up to 1 K. The period of the oscillation can be obtained from the spectra of the time series in figure 4.1c. Both spectra (of the global mean SST and of the sea ice) show a distinct peak close to 700 years.

The MOC also oscillates between stronger and weaker states. The amplitude of the oscillation is slightly stronger for the tropical than for the extra-tropical cell (approximately 2–3 Sv compared to 1–2 Sv for the 101-year running means). The oscillation is in both hemispheres in phase, though only the nothern hemisphere is displayed in figure 4.1b. The period of the low-frequency oscillation (also approximately 700 years) can be obtained from the spectra in figure 4.1d.

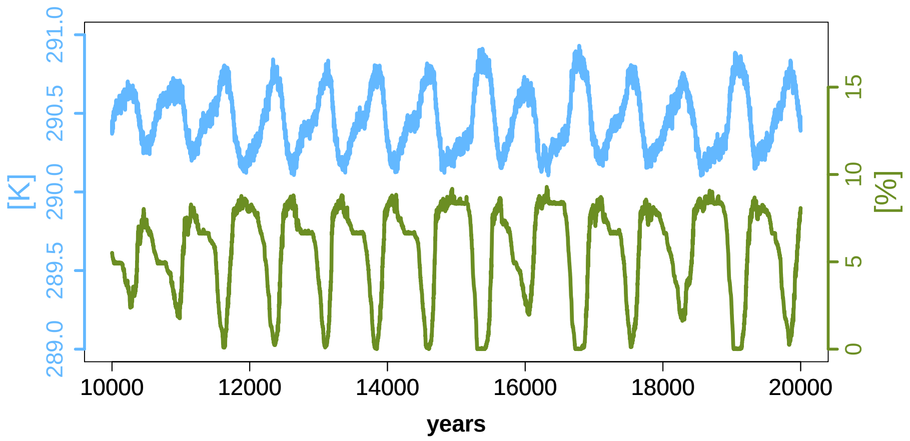

(a) global mean SST (light blue) and sea ice cover (green, in % of global area)

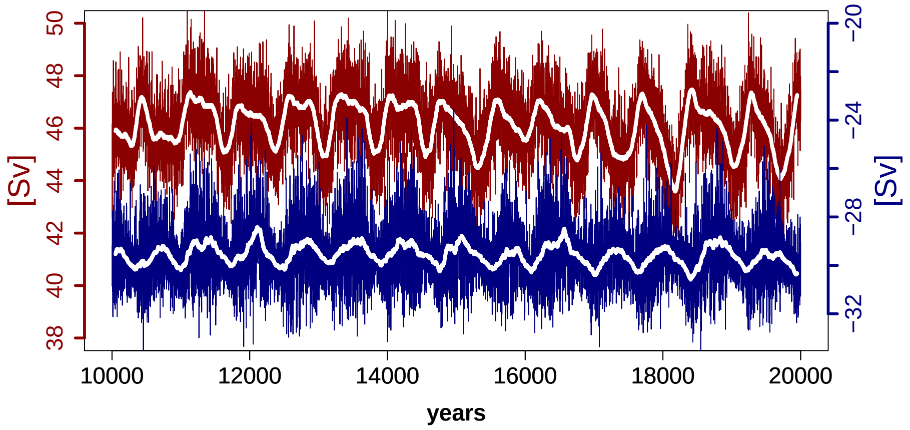

(b) maximum MOC

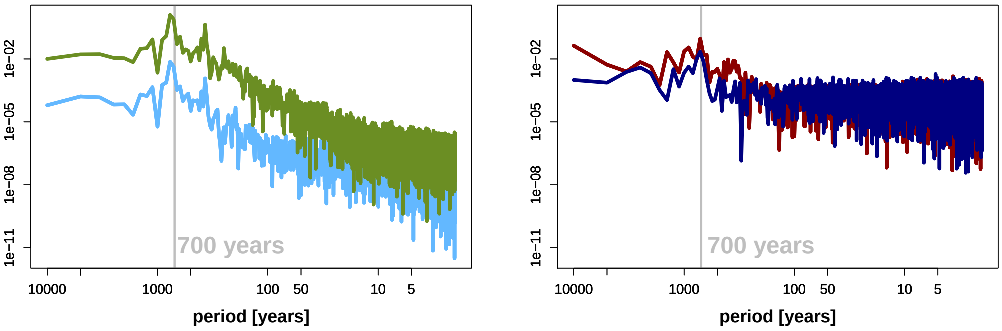

(c) spectra of global mean SST and sea ice cover

(d) spectra of maximum MOC

Figure 4.1: (a-b) Time series and (c-d) spectra of global mean SST (light blue), global mean sea ice cover (green), and maximum of MOC (dark red: tropical cell, dark blue: extra-tropical cell)

The analysis of the nature of this internally forced low-frequency oscillation is the objective of this chapter. As a consequence of the long-periodic variability, two fundamentally different climate regimes alternate on the aquaplanet. Warmer climate periods, without sea ice at the poles, go along with a weaker meridional overturning circulation, while colder climates, which include sea ice cover down to the mid-latitudes, exhibit a stronger MOC. The mean state of the aquaplanet (averaged over the last 5,000 years of the integration period) has been introduced in the previous chapter (*Aqua* in chapter 3). Differences between *warm* and *cold* climate states will be analyzed in the following section. Variability on smaller time scales, which also exists, is not part of this discussion.

4.4 Cold and Warm Climates

The time series in figure 4.1 have revealed that the variability of atmospheric and oceanic fields of the aquaplanet is very high. To further analyze the mean climate of the aquaplanet under this aspect, time periods from extreme cold and warm states are chosen and averages are taken. These *cold* and *warm* climate states are presented and intercompared.

The long-term mean state of the aquaplanet, which is not presented again (for references see chapter 3), is not necessarily located exactly halfway between *cold* and *warm* states. The entire period over the last 5,000 years is averaged for the long-term mean, while *cold* and *warm* climates are averaged each over 100 years of extreme phases. Since the variability is high, a long averaging period is necessary, however, 100 years is approximately the longest time that the climate remains relatively constant before cooling or warming again.

Various atmospheric and oceanic fields take part in the low-frequency oscillation, but the global mean SST and the according global mean sea ice cover are taken as reference variables and, thus, the climate phases are called *cold* and *warm* states. Figure 4.2 shows the last 1,500 years of the time series from figure 4.1, i.e. global mean SST, global mean sea ice cover, and maxima of both MOC cells. The *cold* and *warm* phases, which have been chosen to represent 100 years of extreme climate phases, are highlighted in each time series. The time periods (the years 18,701 to 18,800 for the *cold* period and the years 19,051 to 19,150 for the *warm* period) do not exactly capture an extreme phase for all atmospheric and oceanic fields. This is caused by a time lag in the oscillation cycles between the different climate variables, which is discussed further is section 4.5. However, the *cold* and *warm* phases still show fundamentally different states of the aquaplanet climate.

4.4.1 Temperature and Water Cycle

The main differences between the *cold* and *warm* climate states are displayed in figure 4.3, where the zonal mean sea surface temperatures and the zonal mean sea ice covers are shown. On the aquaplanet, the SST distribution is zonally symmetric and symmetric about the equator. Tropical surface temperatures reach values up to 30 °C. An equatorial minimum, caused by upwelling processes, can be observed in both *warm*

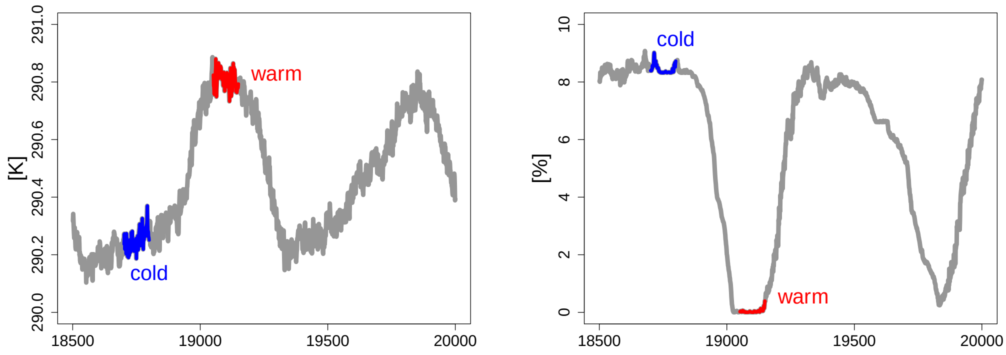

(a) SST

(b) sea ice cover

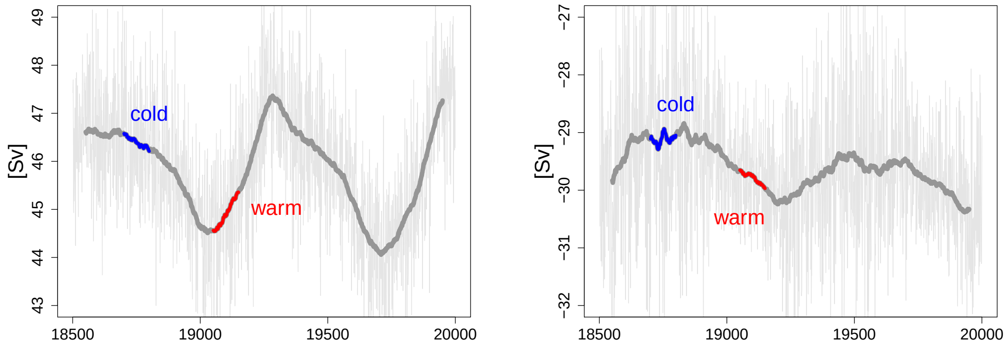

(c) MOC (tropical cell)

(d) MOC (extra-tropical cell)

Figure 4.2: Time series of SST, sea ice cover, and MOC (tropical and extra-tropical cell) with *cold* and *warm* periods highlighted

and *cold* climate phases. Poleward of the subtropics, the *warm* SSTs become higher than the SSTs from the *cold* climate state. The greatest deviations occur at the poles, where low SSTs in the *cold* climate are related to high sea ice cover (the SSTs are temperatures of the ocean surface below the sea ice), while higher temperatures in mid- and high latitudes result in ice-free poles during *warm* climate phases. The alternation between climate phases with poles, which are completely covered with sea ice and climates without any sea ice at all, is one of the most fundamental differences between the *cold* and the *warm* climate state. In the global mean, the SST differences amount to almost 1 K.

Figure 4.4 shows the zonal mean temperature (figure 4.4a) and specific humidity (figure 4.4b) of the atmosphere as well as the zonal mean potential temperature (figure 4.4c) and salinity (figure 4.4d) of the ocean. At high latitudes atmospheric temperature differences between *cold* and *warm* states are particularly pronounced. Over the sea ice covered poles the atmosphere is much colder (up to 10 K in the lower and middle troposphere) and dryer (approximately 1 g/kg) than over the open waters in the *warm* climate state. In lower latitudes, temperature differences between *cold* and *warm* climate phases cannot be detected, while the tropical upper troposphere contains slightly

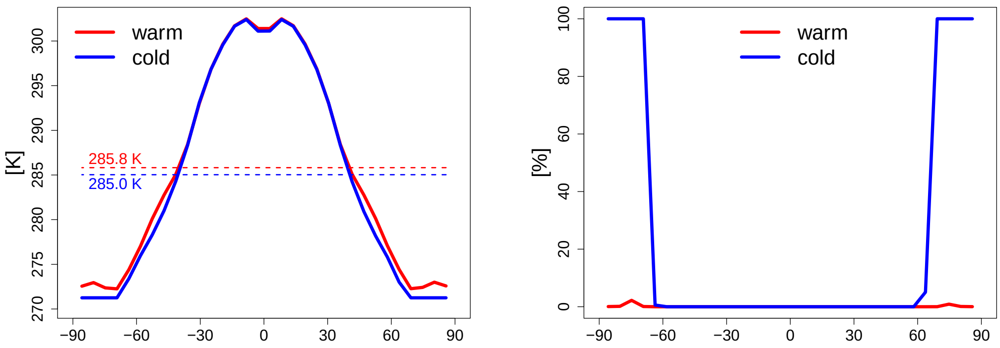

(a) SST **(b)** sea ice cover

Figure 4.3: Zonal mean SST (global mean values are indicated with dashed lines) and sea ice cover (local area fraction) for *cold* and *warm* climate states

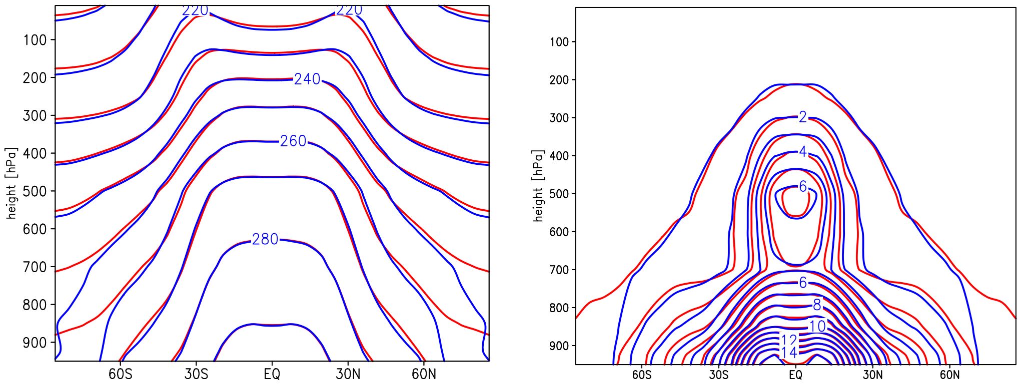

(a) temperature (atmosphere) **(b)** specific humidity (atmosphere)

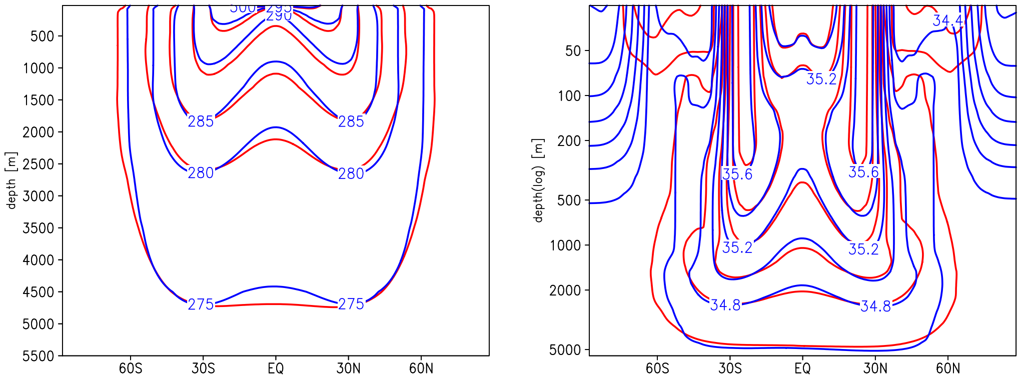

(c) temperature (ocean) **(d)** salinity (ocean)

Figure 4.4: Zonal mean atmospheric and oceanic temperature (in K) as well as specific humidity (in g/kg) and salinity (in psu, note the logarithmic scale on the vertical axis) for *cold* (blue) and *warm* (red) climate states

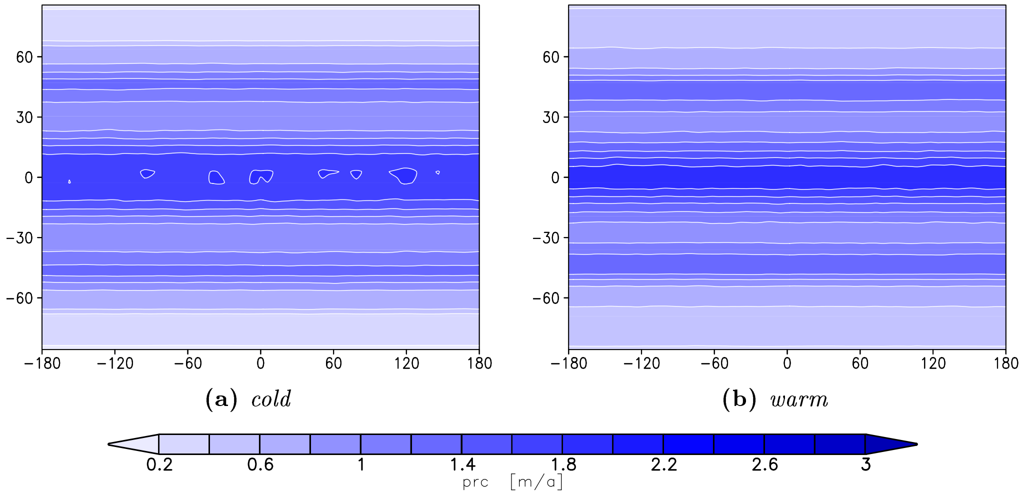

(a) *cold* **(b)** *warm*

Figure 4.5: Total precipitation (large scale plus convective) for *cold* and *warm* climate states

more moisture during *cold* phases.

Temperature differences in the ocean can be observed at all depths, since the ocean is warmer almost everywhere during the periods without sea ice. The salinity fields correspond to the fresh water fluxes at the sea surface. Where evaporation exceeds precipitation (see figure 4.6), areas of high salinity develop. In the tropics (high moisture and excess of precipitation) and at high latitudes (low moisture and little evaporation) the salinity fields exhibit minima. Fresh water is located underneath the ice in the *cold* state, which stabilizes the temperature inversion in this area. In the *warm* climate state the polar ocean is more salty, though the rest of the ocean shows a salinity distribution which resembles the *cold* state.

The total precipitation (large scale plus convective precipitation) is displayed in figure 4.5. The distribution of precipitation on the aquaplanet is completely zonally symmetric in both *warm* and *cold* climates. Zonal means of the precipitation, the evaporation, and the surface fresh water flux (precipitation minus evaporation) are displayed in figure 4.6. The precipitation peaks at the equator inside the intertropical convergence zone (ITCZ) with approximately 2 m/a during the *warm* phases (figures 4.5b and 4.6b), since the atmospheric mean circulation in the tropics transports moisture toward the equator (atmospheric transports of water vapor are displayed in figure 4.7). During *cold* periods (figures 4.5a and 4.6a), the tropical precipitation zone is more spread out and the maximum is slightly weaker (approximately 1.6 to 1.8 m/a). Secondary peaks occur in the baroclinic zones of the mid-latitudes with values between 1.2 m/a (in *cold* climates) and 1.3 m/a (in *warm* climates). In the subtropics and especially in the polar regions precipitation rates are small. Over sea ice covered poles, the air is very dry and there is hardly any precipitation, but in warmer climates the polar air contains more moisture and the precipitation rate is slightly higher.

Tropical evaporation is hardly stronger in *warm* climates, but the higher equatorial

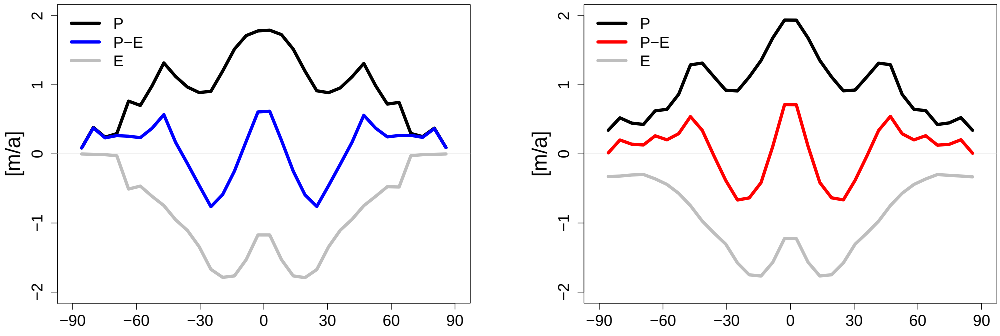

(**a**) *cold* (**b**) *warm*

Figure 4.6: Zonal mean precipitation (P), evaporation (E), and surface fresh water flux, i.e. precipitation minus evaporation ($P - E$) for *cold* and *warm* climate states

precipitation peak is caused by a net increase in water vapor convergence at the equator (which can also be seen in the $P - E$ budget). The differences between *cold* and *warm* climate phases in the equatorial moisture convergence (figure 4.7) are very small, but are still able to alter the tropical precipitation rates. For the total freshwater budget (precipitation minus evaporation) the *cold*/*warm* differences in precipitation and evaporation partly compensate each other. For the evaporation rates, only at the poles large discrepancies (approximately 0.3 m/a) can be observed as the evaporation goes to zero when sea ice covers the ocean surface.

The zonally averaged vertically integrated meridional transport of atmospheric water vapor (figure 4.7) can be subdivided into the transport conducted by the mean circulation and the eddy-transport (transient eddies only, since stationary eddies can be neglected on a zonally symmetric aquaplanet). In *warm* climates slightly more water vapor is transported equatorward than during *cold* phases. This transport is mostly conducted by the mean circulation of the atmosphere. In mid- and high latitudes, more moisture is transported poleward during *cold* climate states, which is mostly achieved by large-scale atmospheric eddies. The computation of the atmospheric moisture transport is very similar to the calculation of the atmospheric energy transport, which is introduced in appendix E.

The atmospheric potential and moist potential temperature for *cold* and *warm* climate periods is shown in figure 4.8. The meridional tropical temperature gradient is very weak and deviations between the different climate phases cannot be detected. The broad baroclinic zone, which extends from the subtropics into the mid-latitudes, is also very similar in both *cold* and *warm* climates. The poles show a weaker temperature gradient and there the most pronounced differences between the two climate states can be observed: The air above sea ice covered poles is much colder and dryer than over open polar waters.

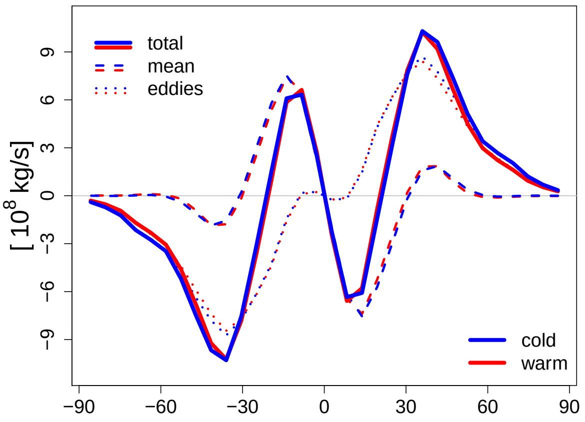

Figure 4.7: Zonal mean vertically integrated meridional transport of atmospheric moisture during *cold* and *warm* climate phases

4.4.2 Circulation

The atmospheric circulation can be described with the zonal mean mass stream function (figure 4.9a). Hadley and Ferrel cells develop in both hemispheres symmetric about the equator. The Hadley cells have a maximum strength of about 40×10^9 kg/s (the atmospheric stream function in 10^9kg/s represents numerically about the same mass transport as an oceanic volume transport in Sverdrups; see Czaja & Marshall 2006), which is comparable to annual mean present-day observations (for example Peixoto & Oort, 1992). The indirect Ferrel cells in the mid-latitudes show approximately half the strength of the tropical Hadley cells with maxima of approximately 20×10^9 kg/s.

The strength and structure of the Hadley cells are strongly connected to the equator-to-pole temperature gradient, which can be explained, for example, by the model of Held & Hou (1980). When the poles are covered with sea ice, the meridional temperature contrasts are higher and the atmospheric overturning circulation is stronger than during *warm* climate phases. In *cold* climate periods, an equatorward shift in both Hadley and Ferrel cells can be observed.

The west-wind zones of the mid-latitudes are very pronounced in both climate states (see figure 4.9b). Subtropical jets develop at the upper poleward edge of the Hadley cells. Tropical easterly winds can be observed in the upper atmosphere. Surface easterly winds (as depicted in figure 4.10) are too weak to be captured in this plot (for a contour interval of 10 cm/s). Just as the Hadley cells, the subtropical westerly jets in the upper troposphere show higher velocities and are shifted poleward during *cold* periods.

Circulation in the ocean (figure 4.9c) takes place in meridional overturning cells. As meridional boundaries are missing in the aquaplanet set-up, Sverdrup balance is not possible and there are no geostrophically balanced meridional overturning cells. There is Ekman pumping in the subtropics and upwelling in a narrow band around the equator, which leads to Eulerian mean overturning cells in the tropics that reach down almost to the bottom of the ocean. The Eulerian flow is confined to the top and bottom Ekman

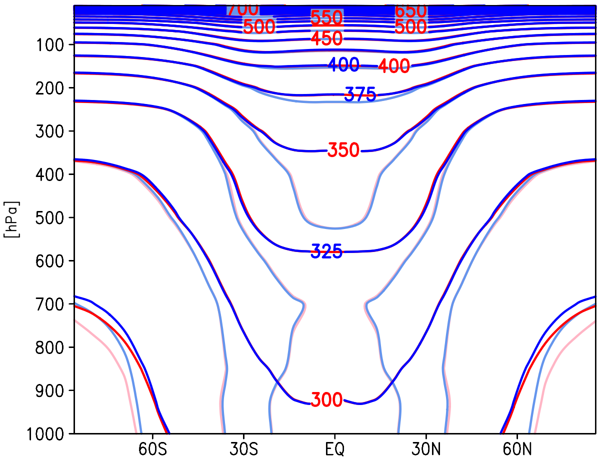

Figure 4.8: Zonal mean atmospheric potential (*cold* climate: blue lines; *warm* climate: red lines) and moist potential (*cold* climate: light blue; *warm* climate: light red) temperature

layer, but mid-depth meridional (ageostrophic) currents are supported by diffusivity. The cells in the ocean show similar patterns and have the same circulation sense as the cells in the atmosphere. During *cold* climate states, the meridional overturning cells have greater strengths (up to 5 Sv higher), especially in the deep ocean. In *warm* climate phases without sea ice, a small and weak overturning cell develops at each pole. This circulation pattern is absent during *cold* climate phases.

The currents in the ocean (figure 4.9d) are predominantly zonal and forced by the overlying wind pattern of the atmosphere. There is westward flow in the tropics and eastward flow in the mid-latitudes. The zonal ocean currents are stronger during *cold* climate periods, when velocities are almost 5 cm/s higher.

The zonal surface wind (at 925 hPa, displayed in figure 4.10a), which forces the MOC over the surface wind stress, also changes with the climate regimes. Only in the deep tropics, where (weak) easterly surface winds prevail, the zonal mean profiles are identical during *cold* and *warm* states. Poleward of approximately 10°N/S, stronger easterlies develop during *cold* climate phases (with a maximum of approximately 6 m/s). The strongest westerly wind occurs in the mid-latitudes (with peak values of almost 10 m/s), where a poleward shift of the peak winds can be observed during *cold* states. The greatest differences exist at high latitudes: during *warm* climate phases the easterly winds are much stronger than over the sea ice covered poles.

The zonal surface currents in the ocean (at a depth of 25 m, displayed in figure 4.10b) are the strongest in the tropics, where they are predominantly easterly. During *warm* climate periods, these tropical currents are slightly stronger than during *cold* phases and show a maximum of 0.5 m/s. In the mid-latitudes the ocean currents are westerly and become stronger during *cold* periods (with maxima exceeding 0.2 m/s). Only at the very high latitudes the situation reverses again: directly below the sea ice the ocean currents are weaker than in open polar waters.

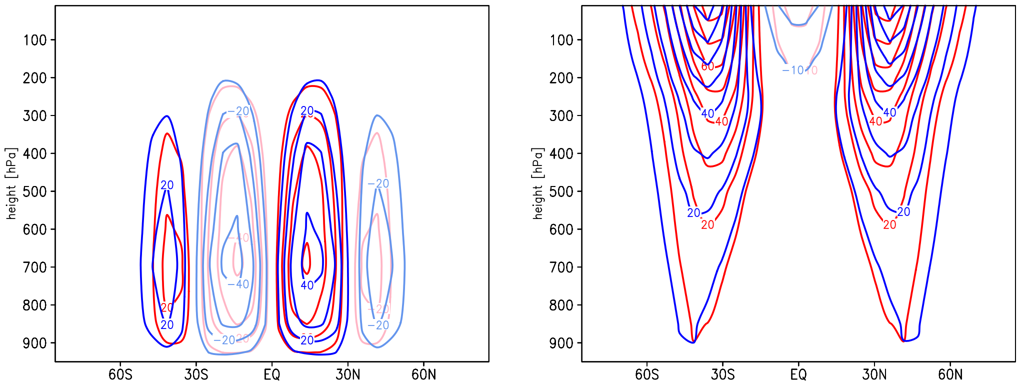

(a) stream function (atmosphere)

(b) zonal wind (atmosphere)

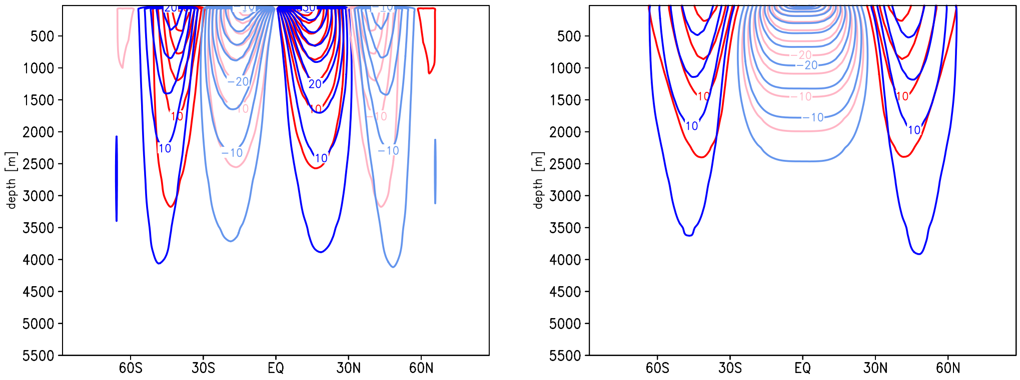

(c) MOC (ocean)

(d) zonal velocity (ocean)

Figure 4.9: Zonal mean meridional overturning circulation in atmosphere (in 10^9 kg/s) and ocean (in Sv) and zonal mean atmospheric zonal wind (in m/s) and oceanic zonal flow (in cm/s) for *cold* (blue/light blue for negative values) and *warm* (red/light red for negative values) climates

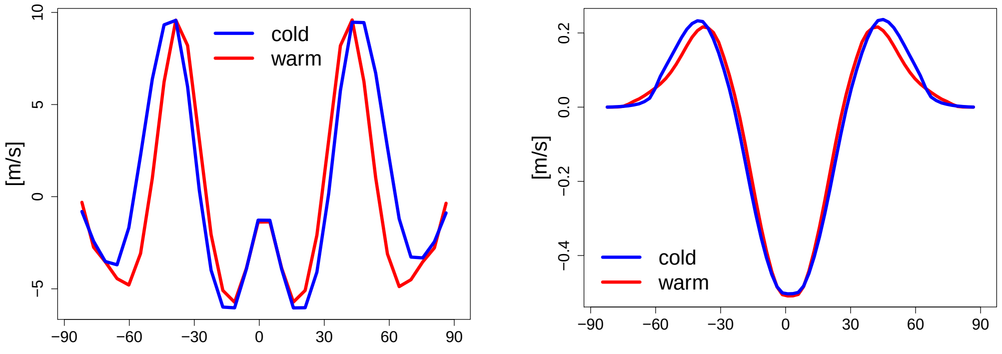

(a) zonal surface winds (atmosphere)

(b) zonal surface currents (ocean)

Figure 4.10: Zonal mean zonal surface winds and currents for *cold* and *warm* climate states

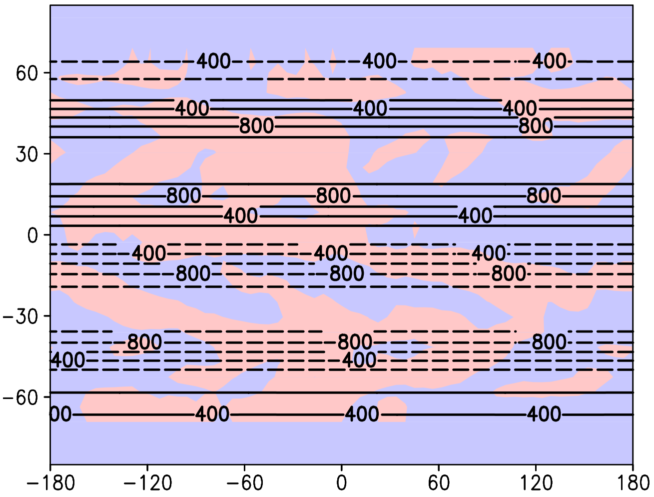

(a) *cold*

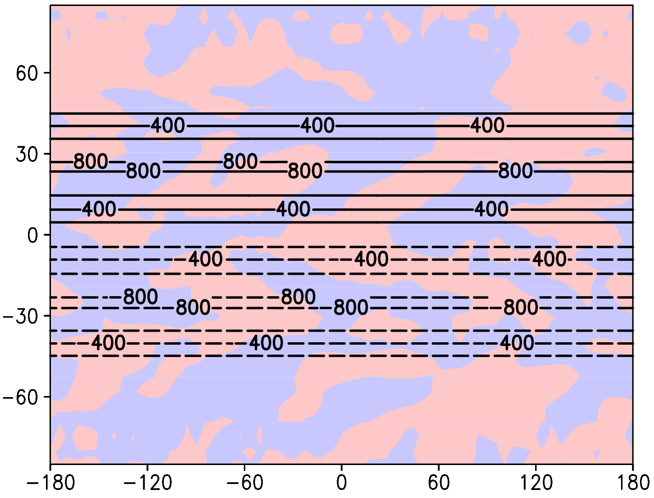

(b) *warm*

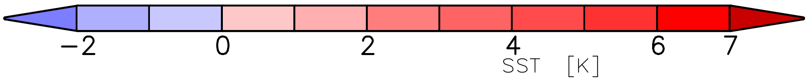

Figure 4.11: Barotropic horizontal stream function (contour intervals: 200 Sv) and deviations from zonal mean SST for *cold* and *warm* climate states

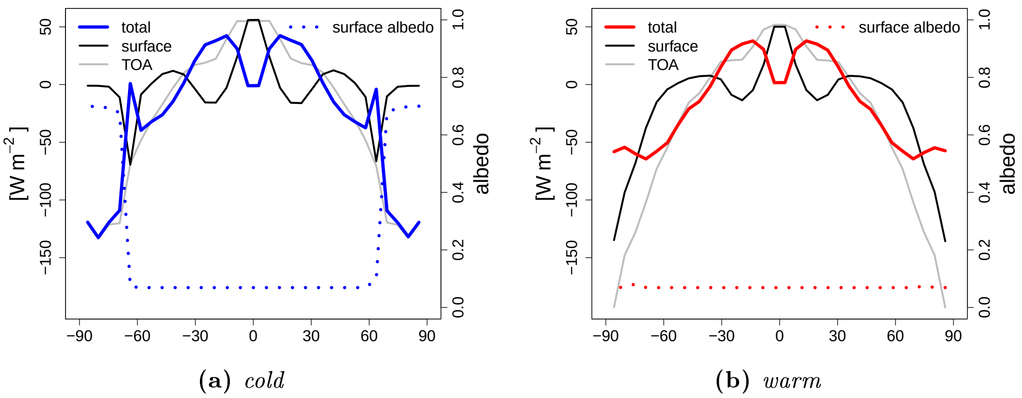

(a) *cold* **(b)** *warm*

Figure 4.12: Zonal mean atmospheric energy budget (total (TOA − surface), at the top of the atmosphere (TOA), and at the surface) as well as the surface albedo for *cold* and *warm* climate states

Figure 4.11 shows the horizontal barotropic stream function and the deviation of the sea surface temperature from its zonal average for both *cold* (figure 4.11a) and *warm* (figure 4.11b) climate states. The aquaplanet climate shows strong depth-integrated zonal flow and hardly any zonal SST deviations. The zonal flow is notably stronger during *cold* climate states. Furthermore, during *warm* periods, the flow is more confined to lower and mid-latitudes without stretching into higher latitudes.

4.4.3 Energy

The zonal mean atmospheric energy budget of the aquaplanet is comparable to observations of the present-day climate (e.g. Peixoto & Oort, 1992). The total atmospheric energy budgets in *cold* (figure 4.12a) and *warm* (figure 4.12b) climate states (computed following equations 3.1 to 3.3 from chapter 3) differ most strongly poleward of 60°N/S (figure 4.12). The differences are mainly caused by changes in the sea ice cover over the poles via the surface albedo (also shown in figure 4.12). Furthermore, the sea ice cover in *cold* climate states causes colder ocean surfaces and consequently less outgoing longwave radiation. Thus, the energy budgets at the surface and at the top of the atmosphere (TOA) are less negative at the sea ice covered poles than over open polar oceans. The polar energy deficit is, therefore, much greater in *cold* than in *warm* climate states.

The energy surplus in the tropics has to be transported poleward to maintain equilibrium. The zonal mean vertically integrated meridional transport of energy is displayed in figure 4.13a, as well as the division of the transport between atmosphere and ocean. The computation of energy transports is explained in appendix E. The atmospheric transport is greater than the oceanic transport almost everywhere poleward of 10°N/S, even though the contribution from the ocean is still considerable.

Since neither size of the planet, rotation rate, axis tilt, nor the solar constant changes, and differences in mean hemispheric albedo are minor, the sum of the oceanic and atmospheric meridional energy transports remain constant throughout the different climate

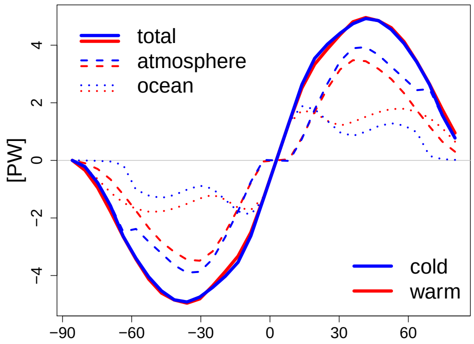

(a) energy transport (total, atmosphere, & ocean)

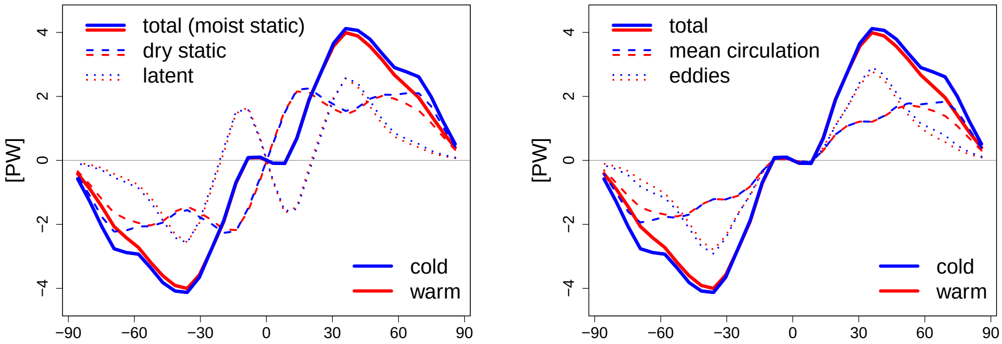

(b) atmospheric transport (total, dry static, & latent)

(c) atmospheric transport (total, mean circulation, & eddies)

Figure 4.13: Zonal mean vertically integrated meridional transport of energy: (a) total transport (atmospheric and oceanic), and the atmospheric transport divided into (b) dry static and latent energy, and (c) transport by the mean circulation and eddy-transport in *cold* and *warm* climate phases

states (after the concept of Stone, 1978, see chapter 1). While the total transport is almost identical in both *cold* and *warm* climate regimes, the partition between oceanic and atmospheric transport is rather different. In the tropics both climate phases show similar patterns, but in mid- and high latitudes the sea ice coverage is reflected in the poleward transport of energy. The meridional temperature gradient is smaller during *warm* climate phases and the transport in the atmosphere is, therefore, weaker. In contrast, the ocean heat transport (OHT) gains in strength and is even greater than the atmospheric transport poleward of 60°N/S. When sea ice covers the poles, the OHT is weaker everywhere and vanishes completely at high latitudes. There the atmosphere takes over, which conducts more meridional heat transport in *cold* than during *warm* climate phases. The phenomenon, that the oceanic heat transport gets stronger at times when the MOC is weaker, will be further discussed in section 4.6.

The atmospheric transport of moist static energy can be split into the transport of dry static and latent energy, which is shown in figure 4.13b. At low latitudes equatorward latent energy transport and poleward dry static energy transport counteract, reducing the total atmospheric transport to almost zero. The latent energy transport, which changes direction poleward of approximately 25°N/S, is at mid- and high latitudes slightly weaker in the *warm* case. However, the latent energy transport does not change as strongly with the different climate regimes as the dry static energy transport, which is much stronger at high latitudes during *cold* phases. The great differences between the climate regimes, which can be observed at high latitudes in the total atmospheric energy transport, are mainly caused by the transport of dry static energy.

The transport mechanisms in the atmosphere (of total, latent, or dry static energy) can further be partitioned into transports by the mean circulation and by transient eddies (stationary eddies can be neglected on the zonally symmetric aquaplanet) as displayed in figure 4.13c. In the deep tropics, both mean circulation and transient eddies are not active in the meridional heat transport. The eddy-transport exhibits a maximum at approximately 35°N/S, while the mean circulation transports about 1–2 PW of energy poleward throughout the low and mid-latitudes. In high latitudes the energy transport by the mean circulation exceeds the eddy transport. While the atmospheric eddy-transport is very similar for *cold* and *warm* climates at all latitudes (slightly stronger in the *cold* case), the differences at high latitudes are caused by the mean circulation, which shows a higher transport when sea ice covers the poles.

4.5 EOF Analysis

The low-frequency oscillation (displayed in the time series in figure 4.1) will be further analyzed and discussed here. EOF analysis is used to filter the noise by retaining the dominant variability patterns and the according temporal structures (PCs) only. The EOF analysis is applied to individual yearly averaged and zonal mean atmospheric and oceanic fields. Lag correlations between the principal components are computed, which capture temporal evolution and interrelations between the variability patterns of the atmospheric and oceanic fields.

4.5.1 Individual EOF Analysis

The low-frequency variability is illustrated by empirical orthogonal functions of various atmospheric and oceanic fields. The oscillation is defined by spatial patterns (EOFs) with pronounced positive and negative anomalies that are symmetric about the equator and by the associated principal components oscillating with a period of approximately 700 years.

The first EOF is sufficient to explain the low-frequency oscillation in most cases. However, there are some exceptions, in which the second EOF needs to be retained for the analysis of the low-frequency variability. Thus, the first two EOFs and PCs are presented for all cases to decide whether only the first or both EOFs fulfill the following criteria:

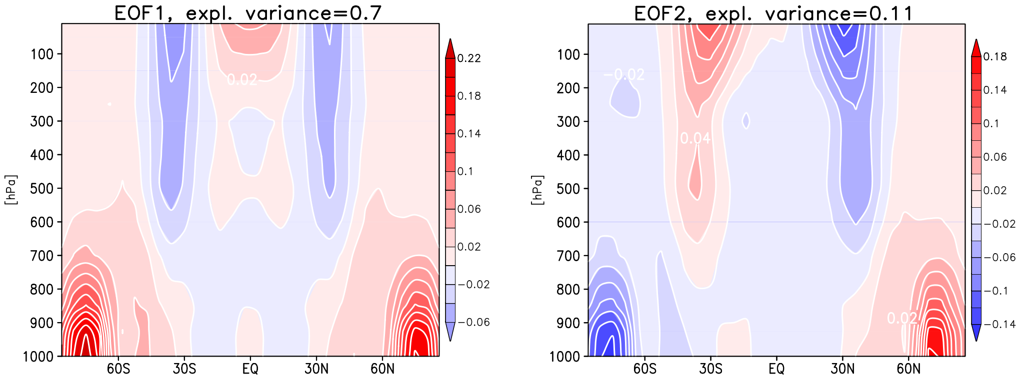

(a) EOF 1 (b) EOF 2

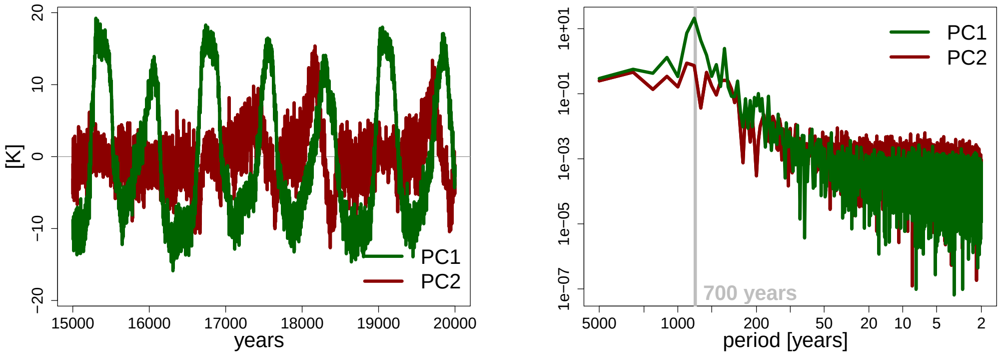

(c) PC 1 & 2 (time series) (d) PC 1 & 2 (spectra)

Figure 4.14: EOF 1 & 2 and PC 1 & 2 (time series and spectra) of the atmospheric temperature

- the principal component oscillates with a period of approximately 700 years and
- the spatial pattern (EOF) is distributed symmetrically about the equator.

In figure 4.14 the first two EOFs of the atmospheric temperature are displayed together with time series of PC 1 and PC 2. Furthermore, spectra of the time series are shown to find the period of the oscillation cycle (if any). While EOF 1 (figure 4.14a) shows a pattern, which is symmetric about the equator, and PC 1 (figure 4.14c) oscillates with a period of 700 years, the second EOF does not take part in the low-frequency oscillation. EOF 2 (figure 4.14a) is anti-symmetric about the equator and the spectrum of PC 2 (figure 4.14d) does not show a distinct peak. EOF 1 explains 70 % of the temperature's variability and shows very strong anomalies over the poles, which are mainly caused by a change in the sea ice cover. In the upper subtropical atmosphere opposite temperature deviations occur (i.e. warm anomalies in the upper subtropics go along with cold poles and vice versa).

The atmospheric specific moisture (figure 4.15) is closely coupled to the atmospheric temperature distribution. The first EOF, which explains 63 % of the moisture's variability, clearly shows an anomaly pattern symmetric about the equator (figure 4.15a).

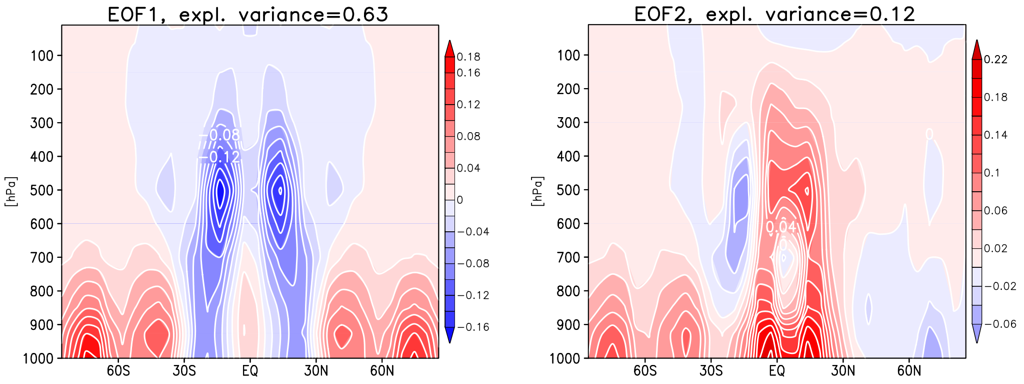

(a) EOF 1 **(b)** EOF 2

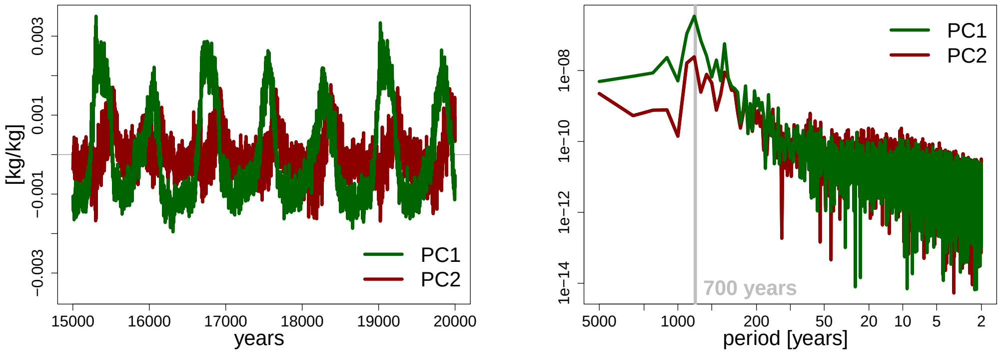

(c) PC 1 & 2 (time series) **(d)** PC 1 & 2 (spectra)

Figure 4.15: EOF 1 & 2 and PC 1 & 2 (time series and spectra) of the atmospheric specific moisture

When tropics and subtropics have a moist anomaly throughout the troposphere, middle and especially high latitudes are dryer in the lower part of the troposphere, and vice versa. The according PC 1 (figure 4.15c) oscillates with a period of 700 years, as a distinct peak in the spectrum (figure 4.15d) reveals. EOF 2 (figure 4.15b), which explains 12 % of the variability, is hemispherically symmetric only in lower latitudes, but (strong) south polar anomalies, which have the same sign as the tropical pattern, are connected to (weak) opposite north polar anomalies. The spectrum of PC 2 does not show a strong peak at 700 years, but a local maximum can be observed. The second mode seems to be partly influenced by the low-frequency oscillation, however, since both characteristics necessary for retaining the mode are not explicitly pronounced, EOF 2 of the atmospheric specific moisture will not be further considered for the low-frequency oscillation.

For the zonal wind of the atmosphere (figure 4.16) only the first EOF (which explains 78 % of the variability) is retained, since the second EOF (figure 4.16b) shows an anti-symmetric pattern about the equator and the according principal component does not vary on a 700-year time scale. EOF 1 (figure 4.16a), in contrast, is completely symmetric

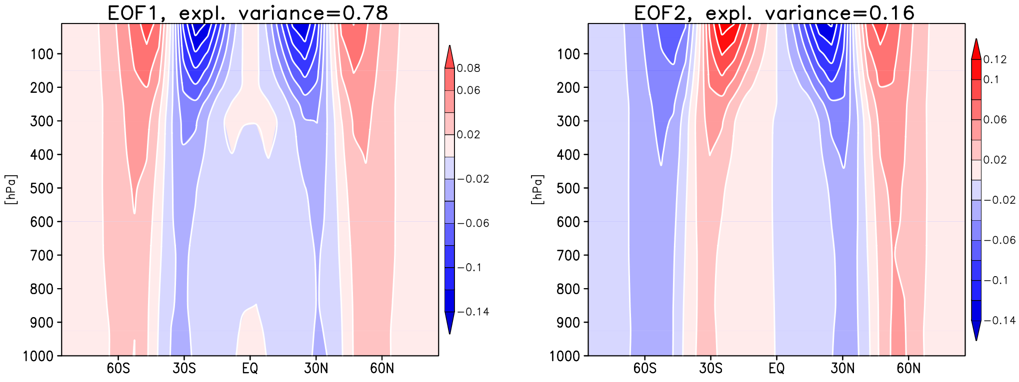

(a) EOF 1 **(b)** EOF 2

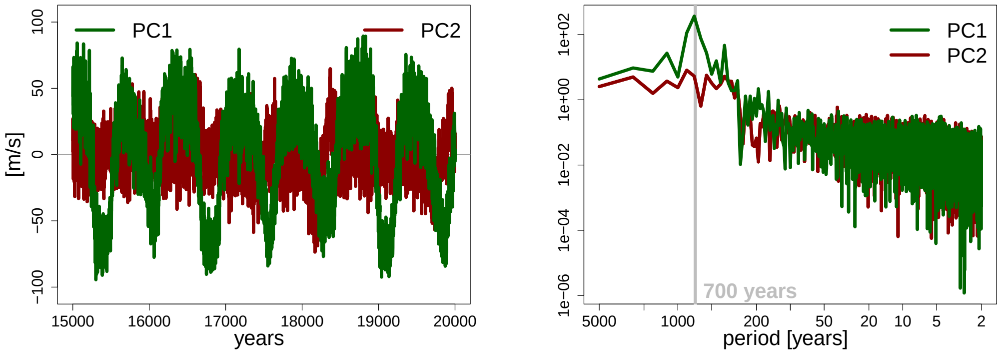

(c) PC 1 & 2 (time series) **(d)** PC 1 & 2 (spectra)

Figure 4.16: EOF 1 & 2 and PC 1 & 2 (time series and spectra) of the atmospheric zonal wind

about the equator. Most notably, an equator-/poleward shift of the subtropical jet streams can be observed, which is consistent with temperature anomalies in the upper subtropical atmosphere. PC 1 shows high variability on many time scales (figure 4.16c), but the low-frequency oscillation with a period around 700 years is most prominent (figure 4.16d).

The EOFs of the atmospheric stream functions are presented in figure 4.17. The sign of the stream function changes with the hemisphere and, therefore, EOF 1 (figure 4.17a) is symmetric about the equator, while EOF 2 (figure 4.17b) shows an anti-symmetric pattern. Furthermore, only PC 1 oscillates on long-periodic time scales (figures 4.17c and 4.17d). EOF 1 explains 64 % of the variability of the atmospheric stream function, which varies mostly in strength. Hadley and Ferrel cells are in phase in the low-frequency oscillation, i.e. when the Hadley circulation gets stronger so does the Ferrel circulation, and vice versa. There is a small exception in a narrow region at the equator, where the Hadley cells get weaker/stronger when the circulation is strengthening/weakening everywhere else, but this can be explained with a pole-/equatorward shift of the Hadley cells. The varying strength of the Hadley cells is consistent with the temperature anomalies

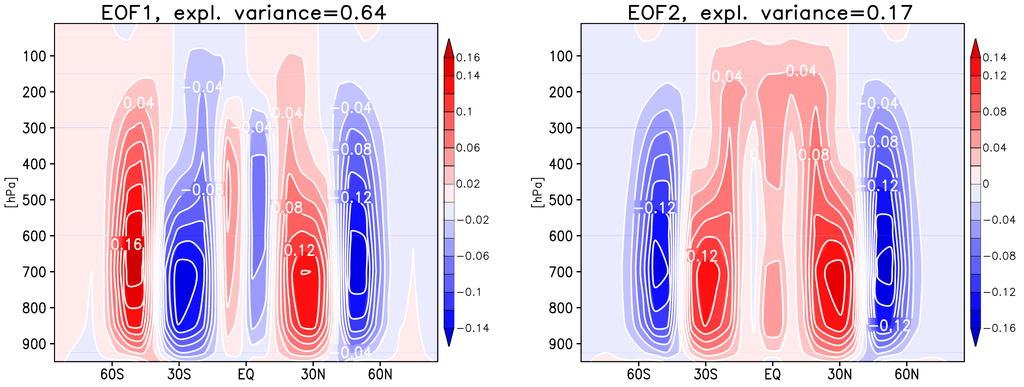

(a) EOF 1 **(b)** EOF 2

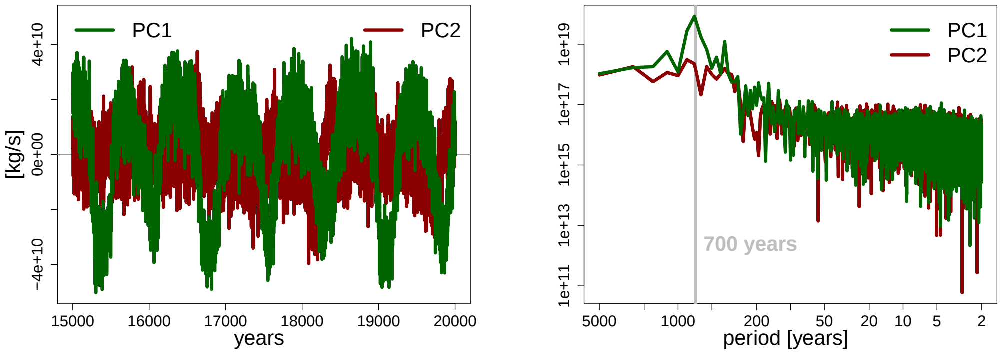

(c) PC 1 & 2 (time series) **(d)** PC 1 & 2 (spectra)

Figure 4.17: EOF 1 & 2 and PC 1 & 2 (time series and spectra) of the atmospheric stream function

in the upper tropics and the shift of the subtropical jets.

The second EOF of the oceanic temperature field (figure 4.18) most clearly fulfills the conditions for retaining the mode for the analysis of the low-frequency oscillation. Not only the pattern of EOF 1 (figure 4.18a) is distributed symmetric about the equator, but also EOF 2 (figure 4.18b) is almost completely hemispherically symmetric. Furthermore, both PCs reveal in their time series (figure 4.18c) and their spectra (figure 4.18d) the long-periodic oscillation. The oceanic temperature anomaly field shows a propagating signal and the second EOF needs to be included to represent the low-frequency oscillation. Combined EOF 1 and EOF 2 explain more than 90% of the variability of the ocean's temperature. For a propagating signal usually both EOFs capture a similar amount of variance, however, in this case the larger contribution still comes from the first EOF (67 %, compared to 25 % explained variability of the second EOF).

PC 1 and PC 2 are approximately 90° out of phase. When the first mode dominates, strong temperature anomalies are located at upper layers, especially in tropical regions. Close to the sea floor, at the poles, and in the mid-latitude middle ocean, temperature deviations with an opposed sign prevail. The contributions from EOF 2 show ocean

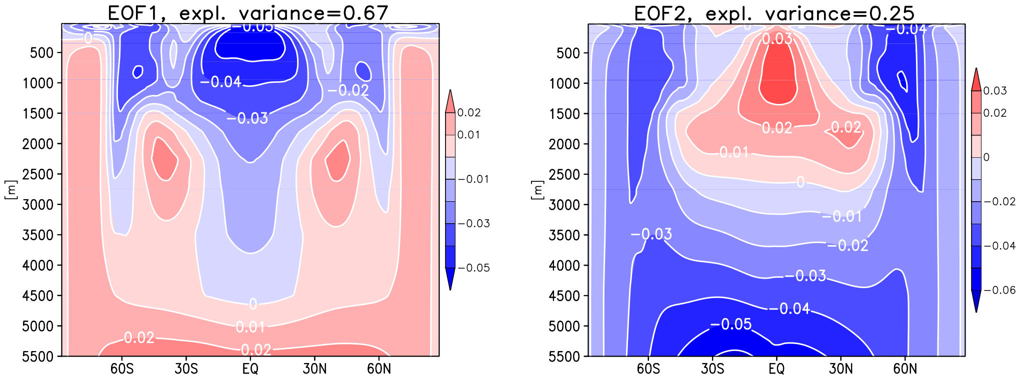

(a) EOF 1 **(b)** EOF 2

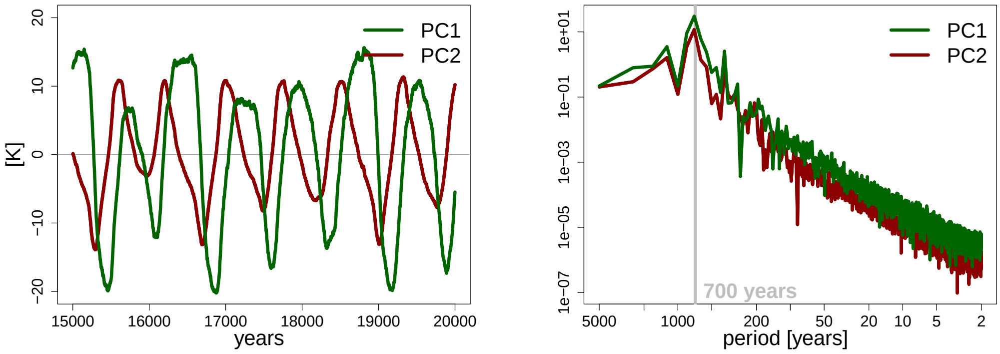

(c) PC 1 & 2 (time series) **(d)** PC 1 & 2 (spectra)

Figure 4.18: EOF 1 & 2 and PC 1 & 2 (time series and spectra) of the oceanic temperature

temperatures, which are colder/warmer almost everywhere except for the tropical upper and middle ocean.

EOF 1 and EOF 2 of the salinity are displayed in figure 4.19 (with a logarithmic z-axis, since most of the variability occurs in the upper ocean layers). Even though the spectrum of PC 2 (figure 4.19d) shows a local maximum close to a period of 700 years, the second mode is not considered for the low-frequency oscillation. The time series (figure 4.19c) reveals that the variability of PC 2 is very irregular and the spatial pattern (figure 4.19b) is not symmetric about the equator. The first EOF (figure 4.19a) explains 68 % of the salinity variance. Salinity anomalies are dominant close to the sea surface, where strong negative/positive anomalies at the poles go along with (smaller) positive/negative anomalies between approximately 30° and 60° north and south. The equatorial ocean shows weak salinity anomalies with the same sign as the strong polar anomalies.

The EOFs of the zonal velocity of ocean currents are presented in figure 4.20. The first EOF (figure 4.20a) displays a hemispherically symmetric anomaly pattern with a change in sign between tropics and extra-tropics: weaker easterly flow in the tropics goes along with an reduced westerly flow in the extra-tropics and vice versa. PC 1 follows

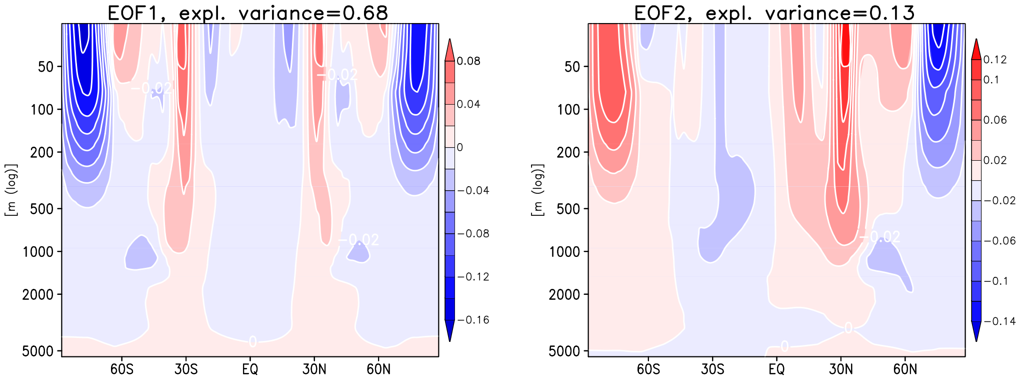

(a) EOF 1 **(b)** EOF 2

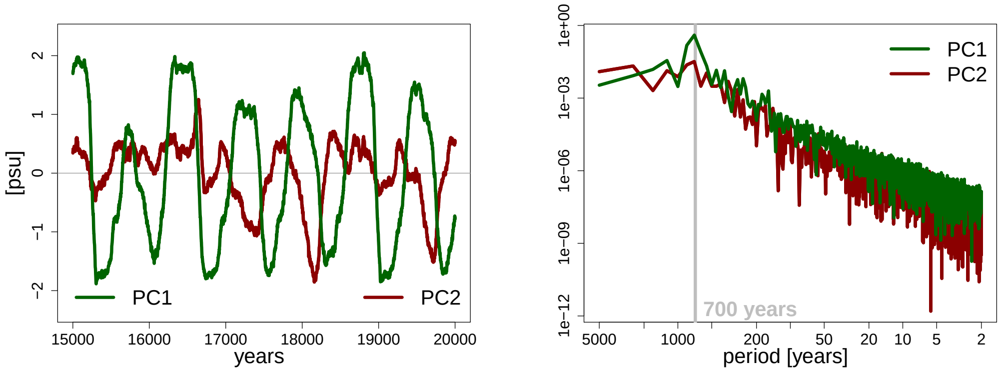

(c) PC 1 & 2 (time series) **(d)** PC 1 & 2 (spectra)

Figure 4.19: EOF 1 & 2 (with a logarithmic z-axis) and PC 1 & 2 (time series and spectra) of the salinity

the dominant low-frequency oscillation with a period close to 700 years (figure 4.20d), even though fluctuation on short time scales are also significant (figure 4.20c).

EOF 2 (figure 4.20b) is not completely symmetric about the equator, however, the zonal current anomaly pattern is hemispherically symmetric over great areas and PC 2 shows a distinct multi-centennial oscillation with a period of 700 years. Furthermore, PC 1 and PC 2 seem to be approximately 90° out of phase. Even though the propagating anomaly pattern cannot be distinguished as clearly as for the oceanic temperature anomaly field, the second mode of the oceanic zonal velocity needs to be retained for the representation of the low-frequency oscillation. However, it should be noted that the explained variance for the first EOF is much higher (70 %) than for EOF 2 (15 %).

64 % of the MOC's variability (figure 4.21) is explained by its first EOF. Even though the time evolution (PC 1) shows great short term variability (figure 4.21c), a dominant oscillation period appears at approximately 700 years (figure 4.21d). The anomalies of the first mode (figure 4.21a) of the ocean circulation have a pattern symmetric about the equator (the sign of the circulation changes from the southern to the northern hemisphere). Furthermore, the sign of the tropical and extra-tropical circulation cells

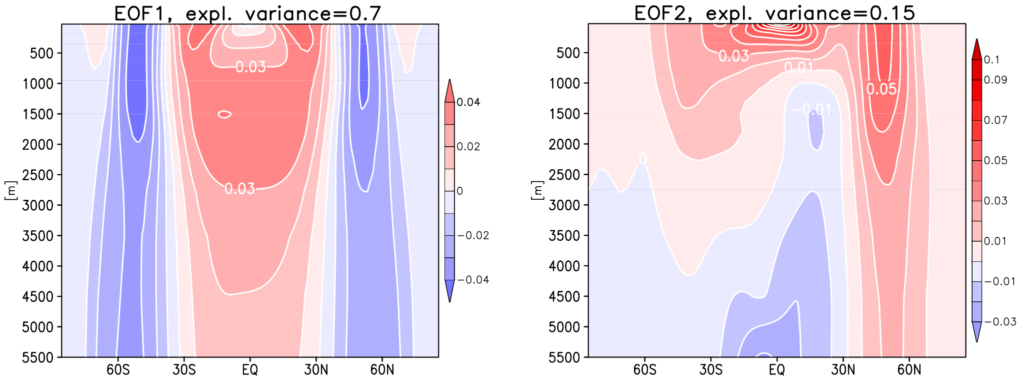

(a) EOF 1 **(b)** EOF 2

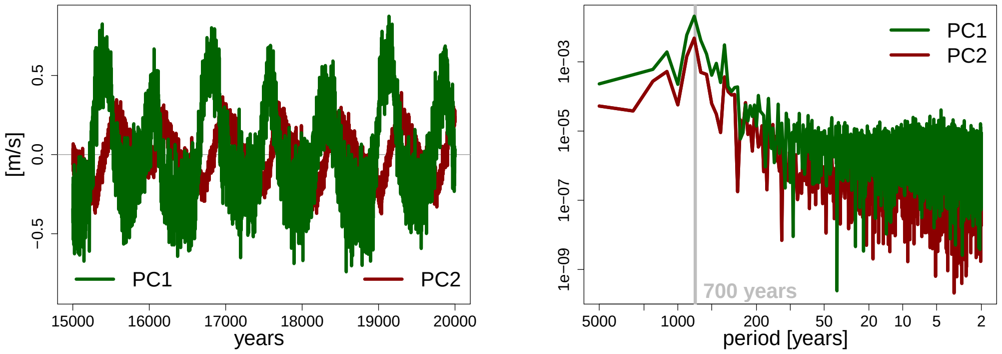

(c) PC 1 & 2 (time series) **(d)** PC 1 & 2 (spectra)

Figure 4.20: EOF 1 & 2 and PC 1 & 2 (time series and spectra) of the oceanic zonal velocity

are opposite, i.e. when both tropical overturning cells get stronger, the extra-tropical circulation also strengthens and vice versa. The second EOF (figure 4.21b) is completely anti-symmetric about the equator (note the sign change with the hemisphere) and PC 2 does not show an oscillatory pattern with a preferred multi-centennial period.

The sea surface has an important role as the interface between atmosphere and ocean. The first EOFs of the zonal mean sea surface temperature and the sea ice thickness (figure 4.22) explain much of the variability of the system (71% and 72%, respectively). EOF 1 of the SST (figure 4.22a) shows the highest variability in mid- and higher latitudes, but in the tropics and subtropics the surface temperature hardly varies at all. Even though PC 2 also oscillates with a 700-year-period and is approximately in quadrature with PC 1 (figures 4.22c and 4.22e), EOF 2 shows a sea surface temperature variability pattern, which is anti-symmetric about the equator. Thus, the second mode of the SST will not be considered for the analysis of the low-frequency oscillation. EOF 1 of the sea ice thickness (figure 4.22b) alternates between high sea ice and open waters at the poles with a period of approximately 700 years (figures 4.22d and 4.22f). EOF 2 does not take part in the low-frequency oscillation.

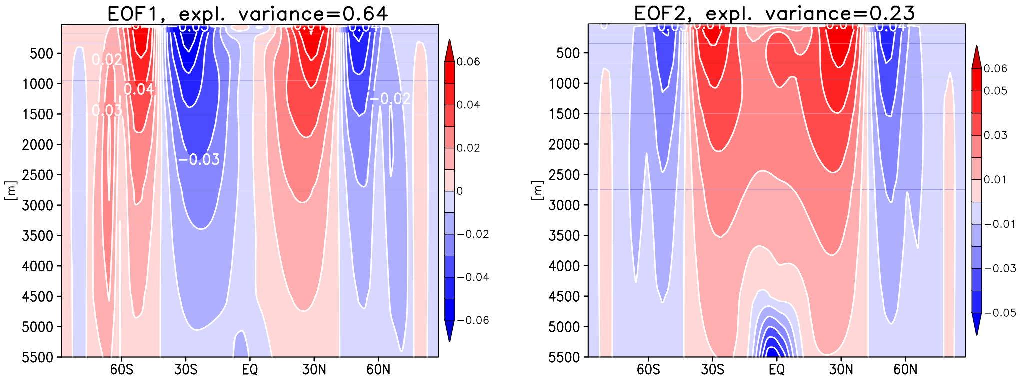

(a) EOF 1 **(b)** EOF 2

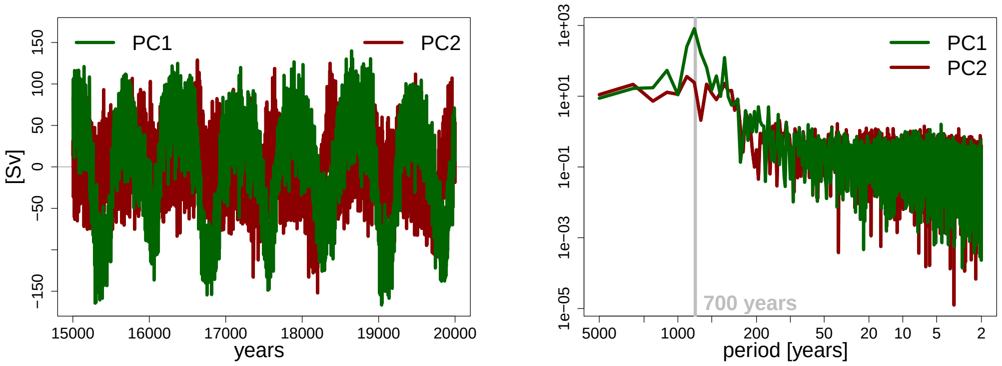

(c) PC 1 & 2 (time series) **(d)** PC 1 & 2 (spectra)

Figure 4.21: EOF 1 & 2 and PC 1 & 2 (time series and spectra) of the MOC

4.5.2 Lead–Lag Correlations

The sequential arrangement of the oscillation and the interrelationships between the variability patterns of atmospheric and oceanic fields is determined by lead–lag correlations between PC 1 of the MOC and the other relevant PCs, i.e. PCs 1 of the atmospheric temperature, specific humidity, zonal wind, and stream function, PCs 1 and PCs 2 of the oceanic temperature and zonal ocean currents, PCs 1 of oceanic salinity and MOC (autocorrelation), and PCs 1 of SST and sea ice thickness.

For the computation of lead–lag correlations, the MOC is used as a reference variable for the low-frequency oscillation. In section 4.4, the temperature was used to differentiate between *cold* and *warm* climates. However, since the first EOF is not sufficient to explain the temperature variability of the ocean and EOF 2 has to be retained, the meridional overturning circulation, in which the long-periodic oscillation is explained by EOF 1 alone, is now used as a representative variable.

Since the low-frequency variability is a cyclic process, it is not possible to determine which field starts the oscillation, but the lead–lag correlation plots (figure 4.23) reveal a temporal sequence of the oscillation cycle. The definition is used that for negative lag

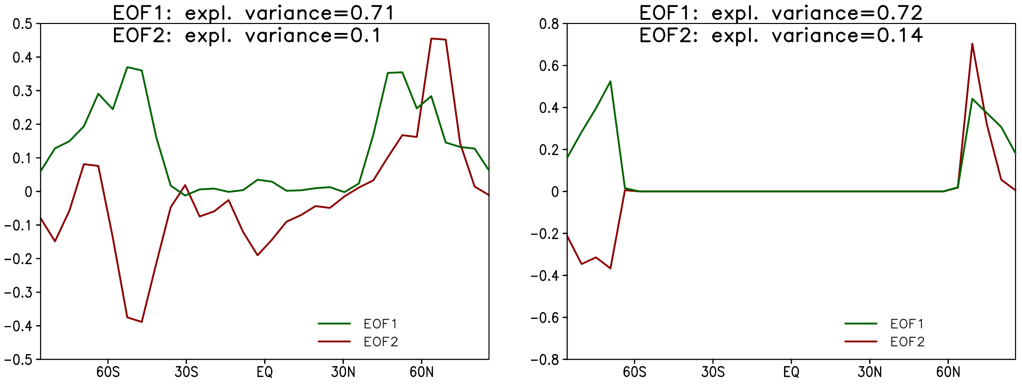

(a) SST (EOF 1 & 2) **(b)** sea ice thickness (EOF 1 & 2)

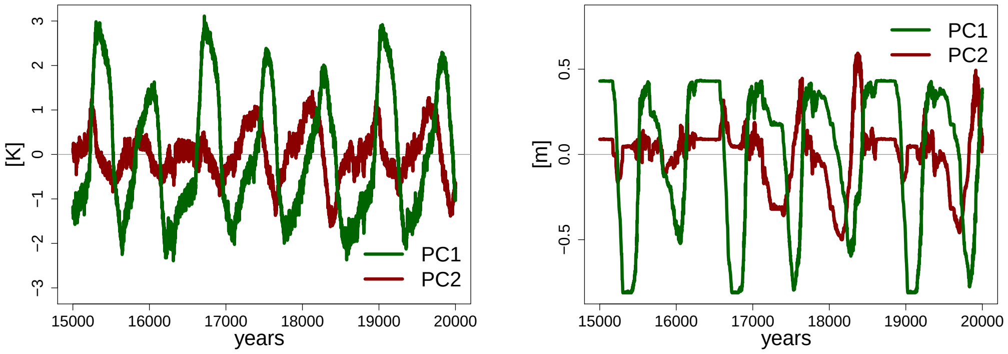

(c) SST (time series of PC 1 & 2) **(d)** sea ice thickness (time series of PC 1 & 2)

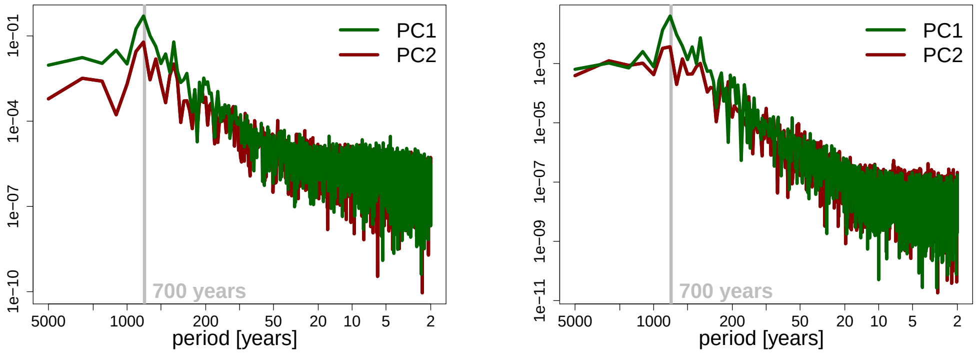

(e) SST (spectra of PC 1 & 2) **(f)** sea ice thickness (spectra of PC 1 & 2)

Figure 4.22: EOF 1 & 2 and PC 1 & 2 (time series and spectra) of the SST and sea ice thickness

times the variability of the MOC leads (without implying that the MOC is the cause), while positive lag times denote that the MOC lags behind.

The lead–lag correlations for the atmospheric fields (temperature, T, specific moisture, Q, zonal wind, U, and stream function) are displayed in figure 4.23a. PC 1 of the atmospheric stream function is in phase and very strongly correlated to the first mode of the MOC, especially with a lag up to ±100 years. The correlation with the zonal wind is also very high, but the MOC variability slightly leads the variability of the zonal wind. The oscillations of the atmospheric temperature and moisture are in phase with the oscillation of the MOC, but anti-correlated: at zero-lag the correlations are highly negative, i.e. higher temperatures (including moist air) occur simultaneously with a weaker MOC and vice versa.

Figure 4.23b shows the lead–lag correlations for the PCs of the oceanic fields (temperature, T, zonal velocity, U, salinity, S, and MOC). The autocorrelation function for the MOC is strong, in particular for a lag up to ±100 years. PC 1 of the salinity field is also strongly correlated to the MOC variability, but lags behind with approximately 50 years. For the oceanic temperature, lag correlations with PC 1 and PC 2 are computed and both show strong correlations to the first mode of the MOC. The MOC variation is approximately 50 years ahead of PC 1 of the oceanic temperature anomaly, while PC 2 leads the MOC variation (with 50–100 years). Lag correlations with PC 1 and PC 2 are also computed for the oceanic zonal velocity, as both may be relevant for the low-frequency oscillation. PC 1 of the zonal velocity is, at zero-lag, strongly correlated to the long-periodic variability of the MOC, but the MOC variability leads. PC 2 of the zonal velocity is approximately in quadrature with the PC 1 of the MOC, i.e. it leads the MOC variability by about 150 years.

The lag correlations for the sea surface variables (sea surface temperature, SST and sea ice thickness) are shown in figure 4.23c. PC 1 of the sea ice thickness is strongly correlated to the low-frequency variability, however, lagging behind the MOC oscillation (approximately 50–100 years). The SST is anti-correlated, but leads the MOC variability by approximately 20–50 years.

4.6 Composite Life Cycle

After the mathematical–statistical analysis of the low-frequency variability, a second method is used to complement the EOF analysis: a physical description in form of a composite life cycle of the low-frequency oscillation is computed to find relations and feedbacks between the variabilities of atmospheric and oceanic fields. The composite life cycle of the oscillation is constructed based on the meridional overturning circulation as a representative variable for the low-frequency oscillation.

Local maxima in the time series of the first principal component of the MOC (101-year running mean of figure 4.21c) are identified and the mean distance between the peaks is computed. With the length of the mean distance, each single oscillation cycle centered around the maximum is chosen. To create an ensemble all six cycles are plotted together in figure 4.24a. The ensemble mean (black line) is computed as well as the standard deviation (shaded area). The same analysis is repeated centered around the local minima

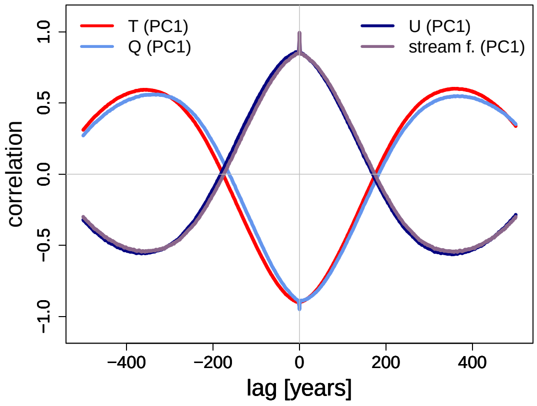

(a) atmosphere

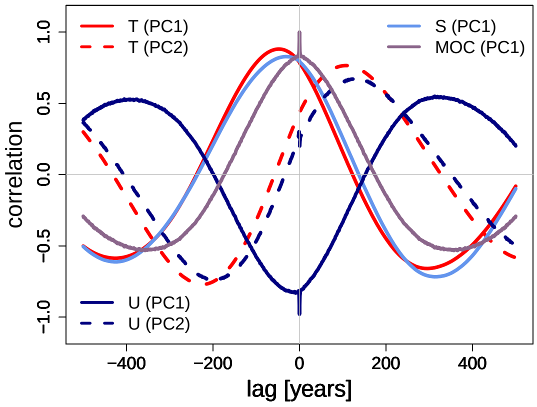

(b) ocean

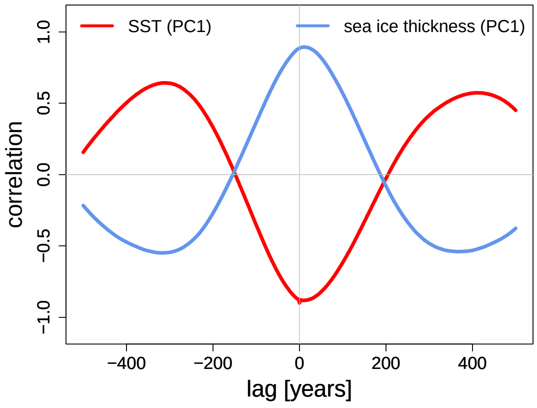

(c) sea surface

Figure 4.23: Lag correlations between PC 1 of the MOC and PCs of (a) atmospheric, (b) oceanic, and (c) sea surface fields

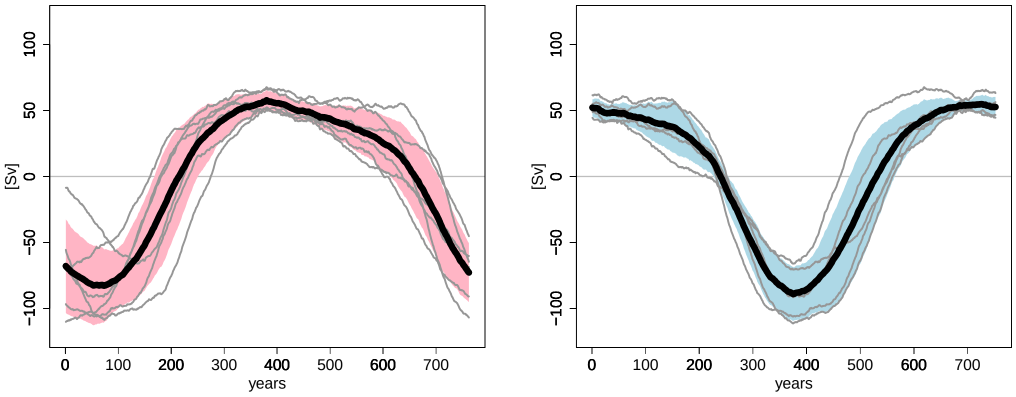

(a) centered around maxima **(b)** centered around minima

Figure 4.24: Composite cycle of the oscillation of PC 1 of the MOC centered around the maxima and minima (single oscillation cycles: gray lines; ensemble mean, i.e. composite life cycle: black line; standard deviation: shaded area)

of PC 1 of the meridional overturning circulation and depicted in figure 4.24b.

Both composites (figure 4.24) show very similar life cycles, independent from being centered around the maxima or minima. The weak MOC phase of the cycle is more pronounced, i.e. PC 1 reaches greater negative than positive values. However, the time that the principal component spends in the negative area is shorter. The maximum phase of the MOC is weaker but lasts longer. The time between the minimum and the zero-crossing when PC 1 is increasing (ca. 150 years) is shorter than the time between the maximum and the decreasing zero-crossing (ca. 250 years). The system recovers much faster from a weaker MOC state and remains longer in a stronger MOC phase.

To give an overview of the state of the coupled climate system during the life cycle of the oscillation, deviations from the climatological mean atmospheric and oceanic fields are shown for four states of the MOC cycle:

1. *PC 1 is at its minimum (figure 4.25),*
2. *PC 1 is at its zero-crossing and increasing (figure 4.26),*
3. *PC 1 is at its maximum (figure 4.27), and*
4. *PC 1 is at its zero-crossing and decreasing (figure 4.28).*

Deviations from the mean are taken and averaged over all years with minima, maxima and the increasing and decreasing zero-crossings. The atmospheric temperature, stream function, zonal wind, specific humidity, and zonal wind stress, the oceanic temperature, MOC, zonal velocity, and salinity, the total, atmospheric, and oceanic meridional heat transport, the sea surface temperature, and the sea ice thickness are presented in the following.

4.6.1 Minimum

The state of atmosphere, ocean, and sea surface is studied when the MOC is at its minimum state, which is displayed in figure 4.25:

- The MOC cells in the ocean (both tropical and extra-tropical) are in their weakest states (see figure 4.25e).
- The ocean circulation is driven by the surface wind stress (figure 4.25i), which is (especially in the mid-latitudes) strongly reduced.
- Hence, the zonal velocity in the ocean (figure 4.25f), which is led by the MOC variability (at least PC 1 of the zonal ocean velocity), shows weaker currents in both tropics and extra-tropics.
- The EOF 1 pattern of the oceanic temperature (figure 4.25d) follows the MOC variability with a lag of approximately 50 to 100 years. Strong warm anomalies (up to 1 K) can be observed in the upper and middle ocean and cold anomalies are located at the poles and in the mid-latitude middle ocean.
- Since the surface wind stress forces the oceanic circulation, the atmospheric stream function and wind anomalies precede the MOC variability, but the time lag is very small (see figure 4.23a). Both Hadley and Ferrel cells (figure 4.25b) are weaker when the MOC is weak (reduced by more than 5×10^9 kg/s at the maximum). The exception in the deep tropics is caused by an equatorward shift of the Hadley cells.
- Accordingly, the easterly winds (figure 4.25c) in the tropics are weaker and subtropical jets are closer to the equator.
- A weaker MOC is connected to warm atmospheric temperature anomalies at high latitudes and a slight cold anomaly in the upper tropical atmosphere (see figure 4.25a).
- The atmospheric specific moisture field (figure 4.25g) is strongly connected to the temperature distribution. Consequently, very moist air can be observed over the poles, while dry anomalies are located at low latitudes.
- Furthermore, the polar ocean is more salty (more than 0.6 psu, see figure 4.25j).
- The salt anomaly is related to the absence of sea ice (figure 4.25l).
- The total heat transport (atmosphere and ocean, figure 4.25h) is reduced in the tropics, but slightly stronger at high latitudes. The differences amount to 0.1 PW. This is is mainly due to the ocean heat transport, which changes more strongly than the atmospheric transport. The change in the OHT (up to 0.7 PW at high latitudes) can be explained with the MOC anomalies. In the climatological mean (figure 4.9c), the tropical cells have upward branches in the equatorial region and downward motion in the mid-latitudes. The extra-tropical cells also show downward motion in the mid-latitudes and upward branches at the poles. This

results in poleward surface flow in the tropics and equatorward surface flow in the extra-tropics. With a weaker MOC, there is now an equatorward anomaly in the tropics (which weakens the poleward heat transport) and a poleward anomaly in the extra-tropics (which strengthens the heat transport in this area). However, this only applies to the surface flow. For the vertically integrated heat transport in the ocean, the circulation sense and the thermal stratification are also of importance. In this case the temperature at the poles increase from bottom to top. In combination with an anti-clockwise extra-tropical cell (northern hemisphere), stronger northward heat transport results. It has to be kept in mind, however, that at very high latitudes the MOC cannot be responsible for the changes in the heat transport, because the circulation is very weak in this area and much of the OHT in the model is diffusive rather than advective.

- Nevertheless, the increased heat transport at higher latitudes causes warm anomalies in the mid- and high latitude SSTs (figure 4.25k).

4.6.2 Increasing

The climate state, when the MOC is increasing and PC 1 is at its zero-crossing (figure 4.26), is presented in the following:

- The MOC (figure 4.26e) is recovering from its minimum state. PC 1 is almost zero, but there are still some anomalies in the zonal mean field, which are caused by higher modes of variability and are small (for most areas less than 1 Sv).
- The wind stress anomalies (figure 4.26i) are very small and constricted to high latitudes, which goes along with the MOC variability.
- The tropical easterly velocity in the ocean (figure 4.26f) is much weaker than its climatological mean but the westerly currents in the mid-latitudes are stronger in the upper ocean. Close to the sea floor the opposite can be observed: stronger easterly currents in the tropics and weaker westerlies in the (southern hemisphere) mid-latitudes.
- The oceanic temperature anomaly field (figure 4.26d) at the zero-crossing of PC 1 of the MOC strongly resembles the second EOF, since the first and second PC are approximately 90° out of phase. The cold bottom temperature anomaly (from the previous step) has propagated upward to fill almost the entire ocean. Only the tropics still show a warmer area close to the sea surface, where temperature maxima have shifted from the high latitudes toward the equator.
- The atmospheric fields, stream function (figure 4.26b), zonal wind (figure 4.26c), temperature (figure 4.26a), and moisture (figure 4.26g) are, at zero-lag, strongly correlated to the MOC and therefore show hardly any deviations from their climatological means. The warm and moist anomalies over the poles have disappeared but the tropics contain slightly more moisture than in the mean.

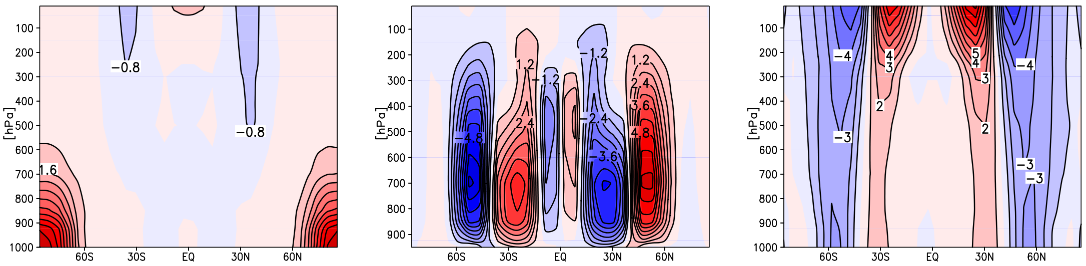

(a) atm. temperature (K)

(b) atm. stream function (10^9kg/s)

(c) atm. zonal wind (m/s)

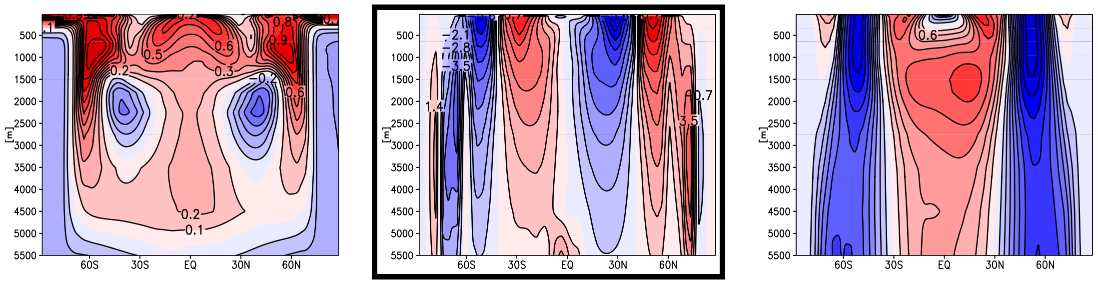

(d) oc. temperature (K)

(e) **oc. MOC** (Sv)

(f) oc. zonal velocity (cm/s)

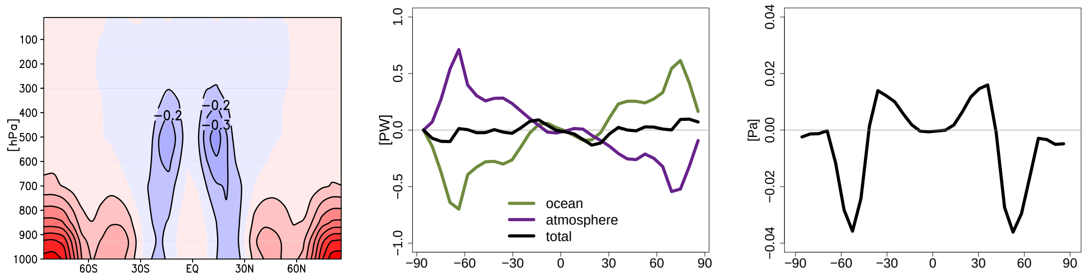

(g) atm. specific moisture (kg/kg)

(h) heat transport (PW)

(i) zonal wind stress (Pa)

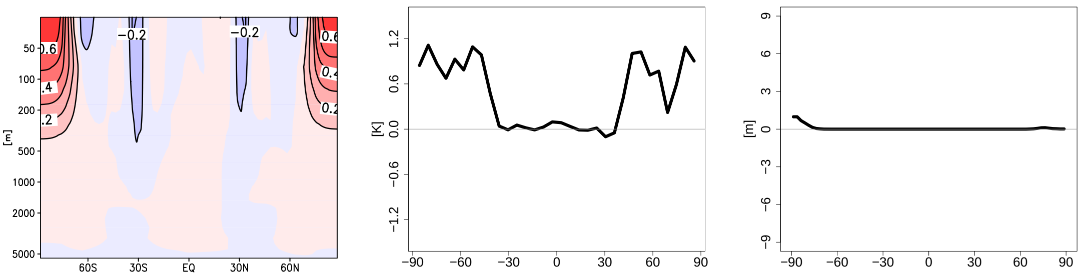

(j) oc. salinity (psu)

(k) SST (K)

(l) sea ice thickness (m)

Figure 4.25: Deviations from the mean oceanic and atmospheric fields when PC 1 of the MOC is at its minimum (note that for the sea ice thickness, absolute values are shown and the salinity has a logarithmic z-axis)

- At the poles, the positive salt anomaly still exist (see figure 4.26j).
- Sea ice (figure 4.26l) is slowly growing but, since it lags behind the MOC variability, hardly any sea ice has formed at this time.
- At all latitudes the total heat transport (figure 4.26h) is stronger than in the climatological mean, which is mainly caused by an enhanced ocean heat transport (0.25 PW at the maximum).
- The SST variability (figure 4.26k) is in phase with the variation of the MOC and negative temperature anomalies can be observed at the poles.

4.6.3 Maximum

The atmospheric and oceanic fields are analyzed when the MOC is at its maximum (figure 4.27):

- The MOC (figure 4.27e) strengthens in all cells, especially close to the sea surface and at higher latitudes.
- Thus, the zonal surface wind stress (figure 4.27i), which forces the MOC, shows positive anomalies, especially in the mid-latitudes.
- Accordingly, the mid-latitude westerly and the tropical easterly ocean currents (figure 4.27f) are much stronger than usual. Only close to the sea surface at the equator there is a westerly anomaly in the otherwise easterly flow.
- The cold temperatures in the ocean still propagate upward and fill almost the entire upper ocean. Warm exceptions occur at the poles below 500 m and in the mid-latitudes around a depth of 2500 m (see figure 4.27d).
- When the MOC is at its maximum, stronger circulation in both Hadley and Ferrel cells (figure 4.27b) can be observed. Close to the equator the Hadley cells experience a poleward displacement.
- The zonal wind (figure 4.27c) shows mid-latitude westerly wind anomalies and subtropical jets, that are displaced poleward.
- The atmosphere is colder than in the climatological mean. This is particularly pronounced over the poles (see figure 4.27a).
- At the same time, the atmosphere above the poles is very dry (figure 4.27g).
- At the poles very high sea ice (figure 4.27l) goes along with negative salt anomalies (almost 0.5 psu, figure 4.27j).
- The total meridional energy transport (figure 4.27h) is weaker at mid- and high latitudes (up to 0.6 PW), which is due to a decreased oceanic transport, that cannot be completely compensated by the stronger atmospheric energy transport.

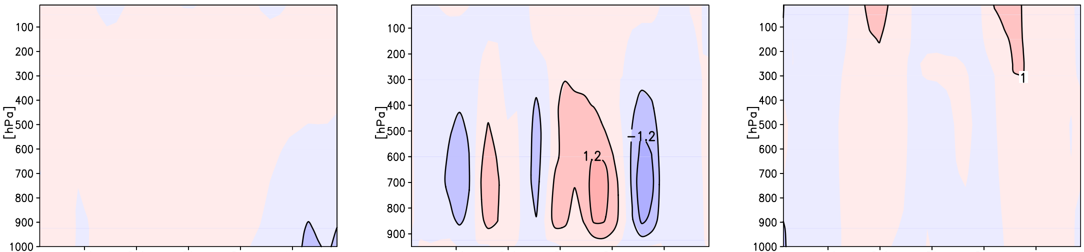

(a) atm. temperature (K)

(b) atm. stream function (10^9kg/s)

(c) atm. zonal wind (m/s)

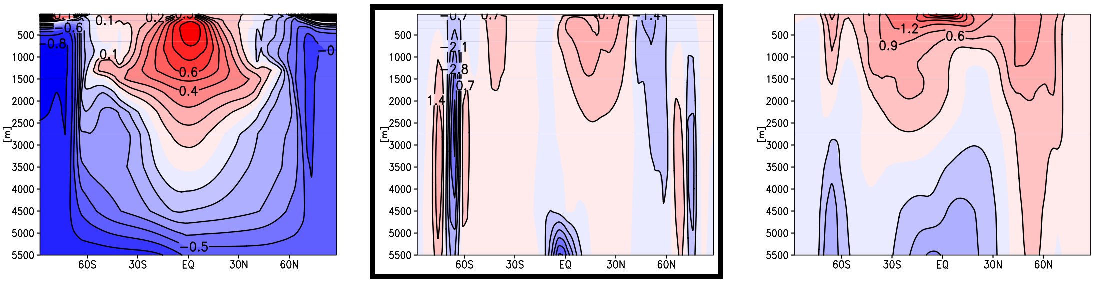

(d) oc. temperature (K)

(e) **oc. MOC** (Sv)

(f) oc. zonal velocity (cm/s)

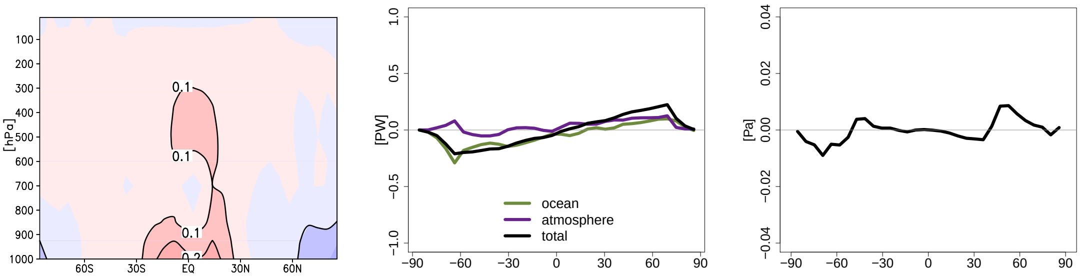

(g) atm. specific moisture (kg/kg)

(h) heat transport (PW)

(i) zonal wind stress (Pa)

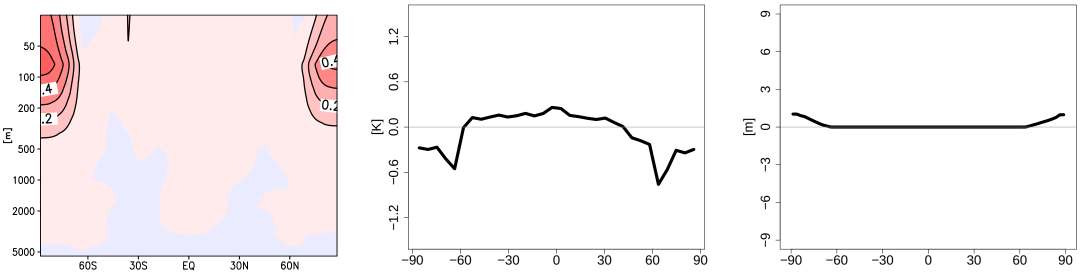

(j) oc. salinity (psu)

(k) SST (K)

(l) sea ice thickness (m)

Figure 4.26: Deviations from the mean oceanic and atmospheric fields when PC 1 of the MOC is at its zero-crossing and increasing (note that for the sea ice thickness, absolute values are shown and the salinity has a logarithmic z-axis)

- Because of the decreased ocean heat transport, the high latitude sea surface temperatures (figure 4.27k) are colder.

4.6.4 Decreasing

Figure 4.28 shows the climate state, when the MOC is decreasing and the first PC is at its zero-crossing:

- The strength of the MOC (figure 4.28e) is decreasing. As PC 1 is almost zero, there are no contributions from the low-frequency variability mode in the MOC anomaly field, but small hemispherically asymmetric anomalies are caused by higher order variability patterns.
- In accordance with the pattern of the MOC variability, the zonal wind stress (figure 4.28i) shows small deviations from its climatological average (in the southern hemisphere only).
- For the oceanic zonal velocity (figure 4.28f) the second EOF is dominant at times when PC 1 is zero and deviations from the mean are high (up to 1 cm/s). Stronger tropical easterlies and mid-latitude westerlies (in the southern hemisphere) are observed.
- The polar warm oceanic temperature anomalies (from the previous step) have highly intensified, spread across the sea floor and are now connected to the mid-ocean warm areas. However, the surface waters at the poles and the upper tropical ocean are still substantially colder than in the climatological mean (see figure 4.28d).
- Atmospheric stream function (figure 4.28b), zonal wind (figure 4.28c), temperature (figure 4.28a), and moisture (figure 4.28g) hardly deviate from their climatological means. The anomalies that still exist are very small and approximately anti-symmetric about the equator, which is not a feature of the analyzed low-frequency oscillation.
- In the polar ocean fresh water anomalies (figure 4.28j) can be observed, which are, however, weaker than in the previous step.
- This is connected to the fact that the sea ice (figure 4.28l) is still almost as high as to the time, when the MOC was at its maximum, but the sea surface temperatures (figure 4.28k) have risen and, at the ice edge, the ocean surface is already warmer than in the mean.
- The meridional heat transport (figure 4.28h) only shows very small anomalies (less than 0.1 PW even at the maximum), that are approximately anti-symmetric about the equator.

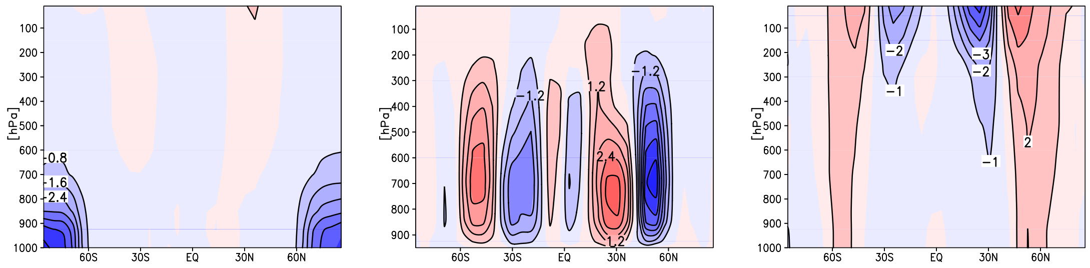

(a) atm. temperature (K) **(b)** atm. stream function (10^9kg/s) **(c)** atm. zonal wind (m/s)

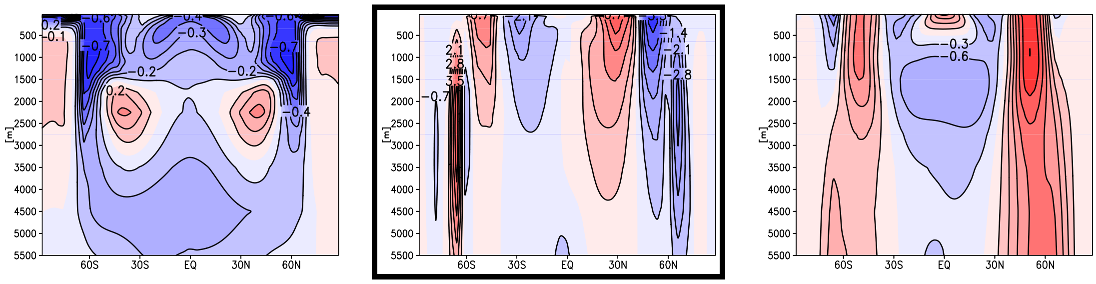

(d) oc. temperature (K) **(e) oc. MOC** (Sv) **(f)** oc. zonal velocity (cm/s)

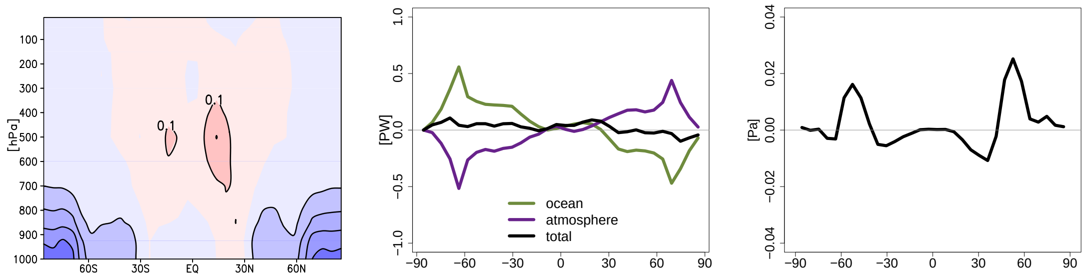

(g) atm. specific moisture (kg/kg) **(h)** heat transport (PW) **(i)** zonal wind stress (Pa)

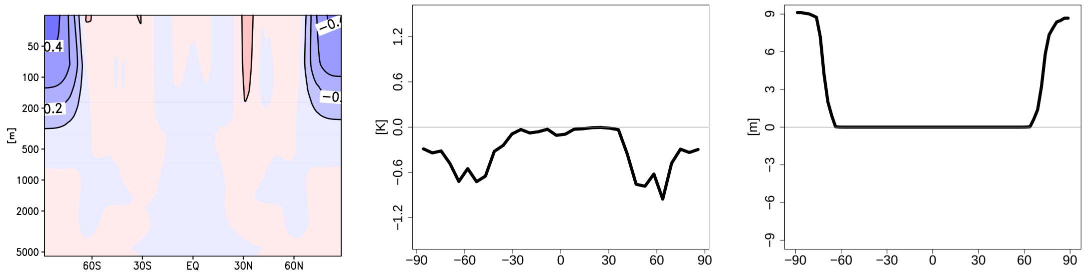

(j) oc. salinity (psu) **(k)** SST (K) **(l)** sea ice thickness (m)

Figure 4.27: Deviations from the mean oceanic and atmospheric fields when PC 1 of the MOC is at its maximum (note that for the sea ice thickness, absolute values are shown and the salinity has a logarithmic z-axis)

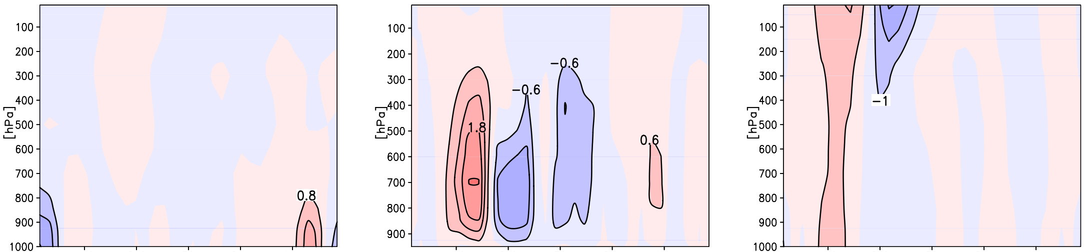

(a) atm. temperature (K)

(b) atm. stream function (10^9kg/s)

(c) atm. zonal wind (m/s)

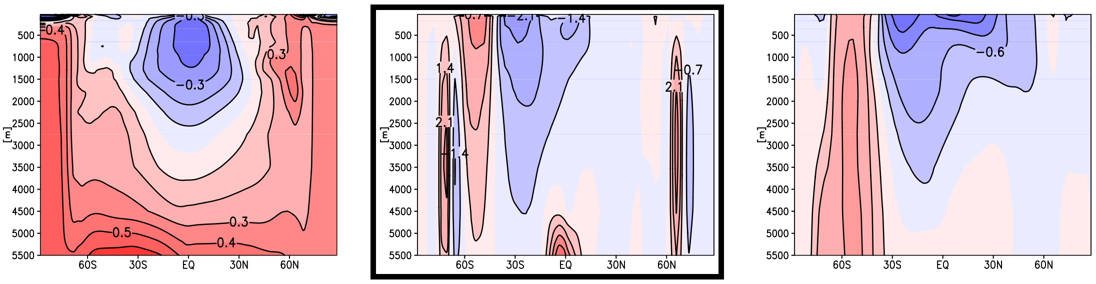

(d) oc. temperature (K)

(e) **oc. MOC** (Sv)

(f) oc. zonal velocity (cm/s)

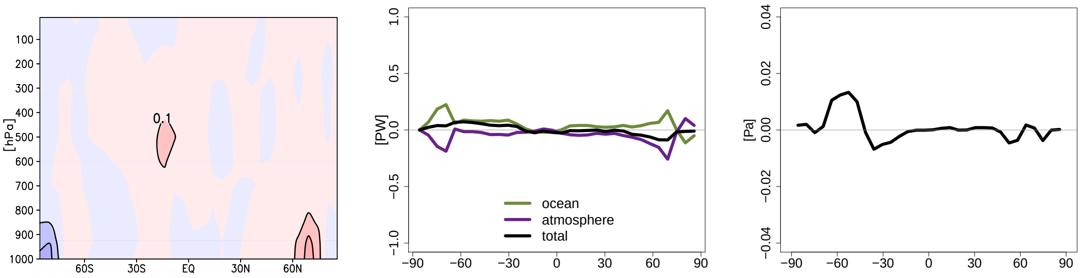

(g) atm. specific moisture (kg/kg)

(h) heat transport (PW)

(i) zonal wind stress (Pa)

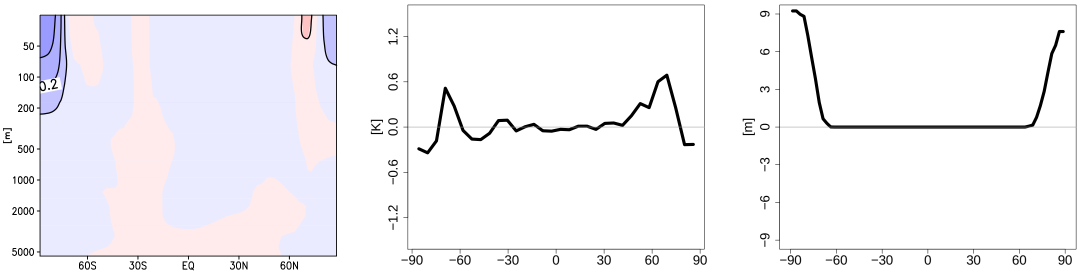

(j) oc. salinity (psu)

(k) SST (K)

(l) sea ice thickness (m)

Figure 4.28: Deviations from the mean oceanic and atmospheric fields when PC 1 of the MOC is at its zero-crossing and decreasing (note that for the sea ice thickness, absolute values are shown and the salinity has a logarithmic z-axis)

4.7 Summary and Discussion

Long-term variability of the aquaplanet climate system is studied. Long-periodic variations are analyzed and a low-frequency oscillation between colder and warmer climate states is found to be the main characteristic of the aquaplanet climate. This oscillation is completely based on internal variability mechanisms as all external forcings remain constant throughout the entire integration.

The low-frequency oscillation has a period of approximately 700 years. It affects all compartments of the aquaplanet climate system, i.e. atmosphere, ocean, and sea ice, and is in both hemispheres in phase. Warmer climate periods without sea ice cover over the poles go along with a weaker meridional overturning circulation in the ocean. Colder climates with a stronger MOC include sea ice cover down to the mid-latitudes.

A comparison between the mean states of *cold* and *warm* climate phases and time series analysis techniques, like EOF analysis and a composite life cycle, give a detailed picture of the low-frequency oscillation. The life cycle is defined by the variations of the meridional overturning circulation and a schematic plot is displayed in figure 4.29. Characteristically, the minimum of the cycle is more pronounced than the maximum, but the climate state spends more time in the maximum phase, i.e. the system recovers faster from a weak MOC state and remains longer in a strong MOC phase.

When the MOC is at its weakest state, warmer temperatures prevail and the poles are completely ice-free. The atmospheric circulation becomes weaker and the subtropical jets are closer to the equator. Relatively warm air above the poles contains more moisture and the salinity in the upper polar oceans is considerably higher without sea ice. The oceanic heat transport is stronger poleward of a narrow equatorial region. Warm temperature anomalies can be observed in the upper and middle ocean. Areas with colder waters are located at the sea floor and at the poles below the surface. During the maximum state of the MOC, the deviations from the climatological average are reversed with ice covered polar oceans.

While the total meridional heat transport (atmosphere and ocean) is almost identical in both warm and cold climates, the partition between oceanic and atmospheric transport is rather different. If sea ice covers the poles, the oceanic transport is almost zero below the ice cover, however, the atmospheric transport becomes stronger with the increased meridional temperature gradient and vice versa during warm climate phases.

The transitions between cold and warm states are characterized by climate phases which are close to the climatological average. It takes approximately 150 years for the MOC to recover from its weakest state. At this time, only small deviations from the mean can be observed: The sea surface temperature at the poles shows cold anomalies, but sea ice has not formed yet. The salinity has positive anomalies in the polar ocean and the (oceanic) poleward heat transport is still greater than in the mean. The ocean currents are stronger at the surface at high latitudes and close to the sea floor in the tropics. Weaker zonal currents exist in the tropical surface waters and in some areas at the lower high-latitude ocean. The cold ocean temperature anomalies have spread from the sea bottom upward so that the entire ocean is colder, apart from an area at the upper equatorial ocean, which shows warm anomalies.

The MOC spends a long time in its strong state, but approximately 300 years after its maximum, it has declined to its climatological average. The atmosphere reacts fast to the variation of the ocean, therefore deviations from the mean are very small with a weaker circulation and a warmer atmosphere that contains more moisture. However, the sea ice lags behind the MOC, so that the poles are still covered with ice. Below the sea ice, the ocean is still fresher than usual, but the negative salinity anomalies have already declined. The warm waters close to the sea floor and at the poles have spread almost across the entire ocean. Colder temperatures can only be observed at the poles directly underneath the sea ice and in the upper tropical ocean.

In contrast to the oscillating climate states of this aquaplanet set-up, previous aquaplanet studies with coupled AOGCMs (e.g. Smith *et al.*, 2006; Marshall *et al.*, 2007; Enderton & Marshall, 2009; Ferreira *et al.*, 2010, 2011) found either cold or warm solutions or multiple steady states. The *warm* phase is similar to the one described by Ferreira *et al.* but not quite as warm as in Smith *et al.*. The cold solution of Marshall *et al.* and Enderton & Marshall (as well as Ferreira *et al.*, who found multiple climate states) is colder than the *cold* phase with a sea ice cover that reaches down to 55°N/S (compared to 65°N/S in the *cold* state). However, the features are very similar: the distribution of the potential temperature in atmosphere and ocean, as well as moisture and salinity patterns resemble the results of this study.

Held (2001) describes the concept of tropical mass fluxes being relatively equal in atmosphere and ocean. Directly from the definition of Ekman transport (mass transport in the boundary layer that produces a Coriolis force that balances the surface stress) follows that the oceanic Ekman transport is locally equal and opposite to the atmospheric Ekman transport. In the tropical atmosphere, the mass transport is well approximated by the Ekman transport. Usually, the zonally averaged ocean flow contains Ekman drift as well as a geostrophically balanced part. Since in the aquaplanet ocean there is no geostrophically balanced flow and the circulation is driven by surface wind stress, the results for the overturning circulations in atmosphere and ocean, where mass fluxes are nearly equal and opposite because they are coupled through the surface stress, offer a nice illustration of the type of coupling argued by Held for the present-day tropics. It should be noted, however, that the net mass fluxes in the atmosphere are much larger than the Eulerian mean circulations would suggest because the eddy terms dominate outside the tropics (see for example Czaja & Marshall, 2006).

The total energy transport of the coupled system is not only very similar to other aquaplanet simulations (e.g. Smith *et al.*, Marshall *et al.*), but also to observations (see for example Peixoto & Oort, 1992). After a concept by Bjerknes (1964) and Stone (1978) the sum of the oceanic and atmospheric meridional energy transports remains constant throughout changes imposed on the climate system. The controlling factors for the total meridional heat transport are identified by Stone: size, rotation rate, and axis tilt of the Earth, the solar constant, and the mean hemispheric albedo. He suggested that this concept should hold even under unusual conditions or scenarios (like the set-up of an aquaplanet). However, as the two different climate states revealed, the partition of the heat transport between atmosphere and ocean may change.

Marshall *et al.* (2007) and Czaja & Marshall (2006) note that the partition of heat transport between atmosphere and ocean in the aquaplanet simulation is remarkably

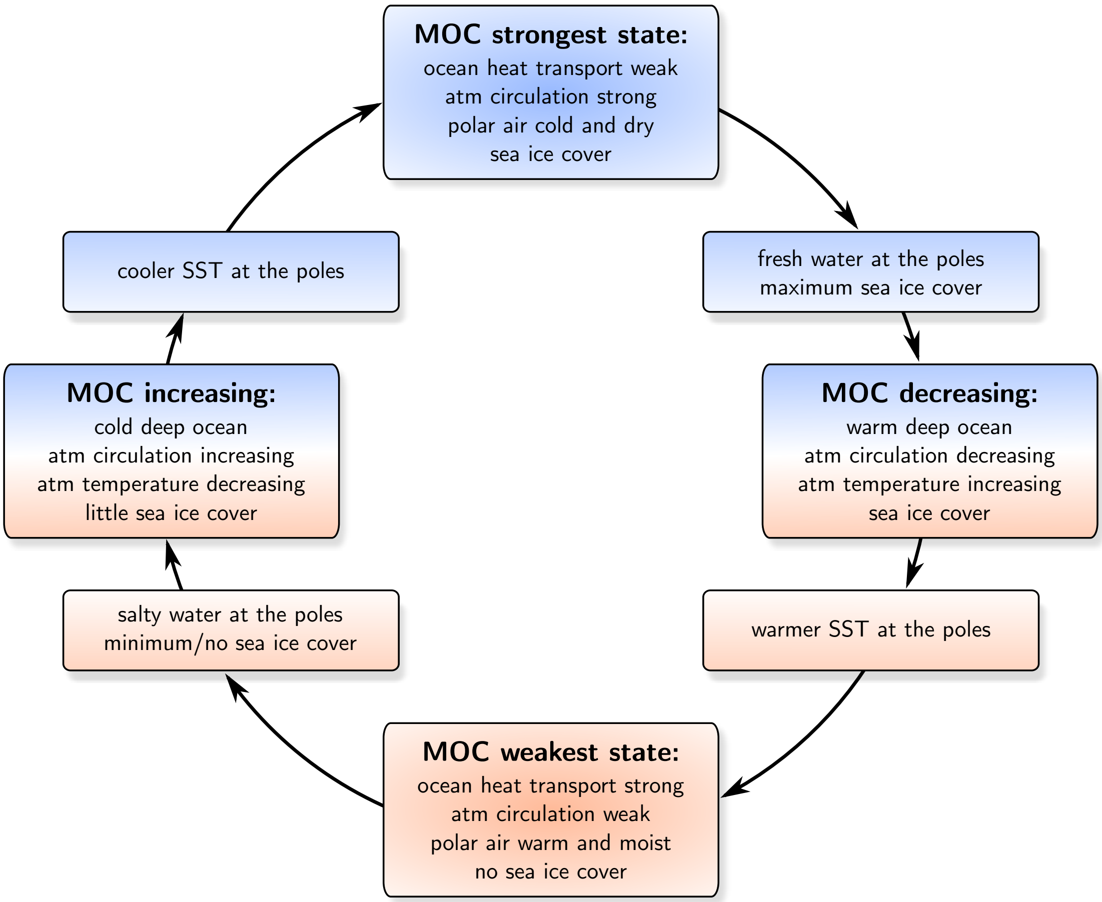

Figure 4.29: Schematic plot of the life cycle of the low-frequency oscillation

similar to that of the present climate: the atmosphere dominates in mid- to high latitudes and the ocean dominates in the tropics. The total heat transport in this study is somewhat smaller than the one from the Marshall *et al.* simulation. However, as in Marshall *et al.*, the oceanic heat transport dominates in the tropics and the atmospheric transport everywhere else, at least during *cold* climates.

It should be noted, however, that the OHT differs from the observed ocean heat transport as well as from the one in the aquaplanet of Ferreira *et al.* or Enderton & Marshall, which peaks at typically 2 PW around 20°N/S and is already very weak at 60°N/S. The maximum in this study is also approximately at 2 PW and located around 20°N/S, but there still is a very strong OHT of over 1 PW up to approximately 75°N/S. While the OHT in the aquaplanet shows the peak convergence poleward of 70°N/S, the maximum convergence in observations and in Ferreira *et al.* is located in the mid-latitudes. Consequently, in this aquaplanet the OHT carries much more heat into high latitudes, which affects the partition between atmosphere and ocean. In *warm* climates, the oceanic transport even exceeds the atmospheric energy transport at high latitudes. The location of the maximum OHT convergence is crucial for determining the (equatorward) sea ice extent. In a region of steep temperature gradients and isopycnal slopes, the model overestimates horizontal, diapycnal fluxes, and therefore permits a large heat transport into high latitudes. Much of the ocean heat transport is therefore diffusive, rather than advective.

Simplified topographical ocean set-ups have previously been used to analyze low-frequency oscillations or multiple climates states. Multiple steady states have been found by Marotzke & Willebrand (1991) in an idealized model of the ocean. Instead of a pure aquaplanet they insert two ocean barriers that have gaps in the southern ocean. Their steady states are characterized by deep-water formation in different basins. An ultra-low-frequency oscillation with a period of 13,000 years has been found by Haarsma *et al.* (2001). They applied a coupled AOGCM of intermediate complexity (with continents but a flat ocean bottom) and found quasi-periodical behavior with large rapid transitions between different quasi-stationary states and an MOC, which exhibits sudden (southern ocean) and gradual (Atlantic basin) changes between strong and weak states. Haarsma *et al.* found that the influence of sea ice on the heat and fresh water fluxes is the crucial.

Mikolajewicz & Maier-Reimer (1990) have integrated the LSG as an ocean-only model with mixed boundary conditions (present-day orography) and found that a spatially correlated white-noise freshwater flux generated a pronounced low-frequency signal with a period of approximately 320 years. They show that the variability is an advective phenomenon with feedback from the flux boundary conditions. Pierce *et al.* (1995) give a detailed description of this mechanism.

That the aquaplanet model can sustain low-frequency climate oscillations without external forcing is particularly relevant when interpreting paleoclimate records. Abrupt climate changes are documented for the last glacial period, the so-called Dansgaard–Oeschger (D/O) and Heinrich events (e.g. Heinrich, 1988; Dansgaard *et al.*, 1982, 1993). D/O events typically start with an abrupt warming over a few decades or less, which is followed by gradual cooling over several hundred or thousand years. In the aquaplanet the sea ice cover also changes abruptly (over about a centennial) from open waters to the maximum state (ice caps down to 65°). The time period for the transition back to an ice-free state is similar. Abrupt climate changes, like D/O and Heinrich events, have mostly been analyzed in the presence of freshwater forcing (for example Ganopolski & Rahmstorf, 2001) or Milankovitch solar forcings (e.g. Saltzman, 2002), however the aquaplanet results suggest that observed climate variability in the past could emerge naturally from interactions within the climate system, without a need for external forcing. As for example Wunsch (2004, 2010) has pointed out, there are major obstacles trying to link freshwater or solar forcings to the data recorded in ice-cores. The aquaplanet results could provide a possible way around these obstacles by demonstrating the possibility of large internal climate variability. This is consistent with the findings of Loving & Vallis (2005), who have shown that cooling alone, without any additional forms of external forcing or variability, can lead to a glacial climate that is less stable and characterized by intermittent, millennial-scale oscillations.

Sea ice seems to play a crucial role for the low-frequency oscillation found in aquaplanet, as other simulations (not presented here) revealed that an aquaplanet climate cannot sustain this oscillation without sea ice. Destabilizing heat loss to the atmosphere through the unfrozen sea surface is probably critical to (temporarily) maintaining the warm state of the system. Winton & Sarachik (1993) and Winton (1993) found self-sustaining low-frequency oscillations in their ocean model with strong steady salinity fluxes (salting at low latitudes and freshening at high latitudes). These "deep decoupling oscillations" arise when a steady overturning circulation encounters a contradiction: the poleward salt and heat transport needed to maintain convection in the polar ocean requires more overturning than is consistent with the reduced thermocline depth that results. Similar mechanisms could be responsible for the low-frequency oscillation found here, including the feedback between sea ice, polar salinity and thermocline, as well as the strength of the MOC.

Interactions and feedbacks between sea ice, salinity and the thermohaline circulation of the ocean have been analyzed by Yang & Neelin (1993, 1997). They found a self-sustaining interdecadal oscillation in 2D and 3D coupled ocean circulation–sea ice models. Sea ice significantly affects the salinity stratification, and hence the thermohaline circulation, through fresh water or brine release associated with melting–freezing processes. The periodic appearance and disappearance of a stable polar halocline is also an important aspect of the low-frequency oscillation in this study. However, the results of Yang & Neelin differ not only in the in the time scale (interdecadal instead of centennial). On an aquaplanet with a wind driven MOC the concept of the thermohaline circulation with a sinking region in the North Atlantic cannot be acurately adapted.

This is also true for the work of Broecker *et al.* (1990), who developed a "salt oscillator" concept to explain rapid climate shifts in the North Atlantic of the past: A working Atlantic thermohaline circulation causes the salinity (and hence the density) to decrease (through salt export and meltwater input). Consequently production of deep water slows and the conveyor stops (or decreases strongly), which increases the salt content until the thermocline circulation starts again. Even though there is no pronounced sinking region in the aquaplanet (like in the North Atlantic) and the temporal arrangement of the oscillation cycle differs, build-up and melting of sea ice at the poles and the following salinity changes might also influence the low-frequency oscillation of this study.

Since the sea ice cover is a key feature for the low-frequency oscillation, it is important to note that the model runs under perpetual equinoctial conditions. It is very possible that the absence of the seasonal cycle alters the behavior of the sea ice. The question is, whether the freezing period in the winter time is strong enough to compensate summer time melting, so that stable sea ice caps are sustained for several centennial during the *cold* climate states.

5 The Onset of the Antarctic Glaciation

> *"Truth is much too complicated to allow anything but approximations."*
> — John von Neumann

5.1 Introduction

In this part of the study[3], the aquaplanet concept of an idealized land–sea configuration is applied to model an externally forced climate change of the Earth's history, in contrast to the previous chapters, where different circulation regimes and an internally generated climate oscillation have been analyzed without reference to past, present, or future eras of the Earth.

One of the most outstanding climate changes of the history of the Earth is the onset of the Antarctic glaciation, which happened approximately 34 million years ago (near the Eocene–Oligocene transition). The Antarctic Ice Sheet (AIS) is a key feature of Earth's climate, but the cause of the glaciation onset is still under discussion. Different boundary conditions, such as the opening of ocean gateways, a change in atmospheric CO_2, or the orbital forcing, may have contributed to the cooling of the southern polar region and consequently to the glaciation of Antarctica.

Today Antarctica is the highest, driest, windiest and coldest continent on Earth (Turner *et al.*, 2009). Almost the entire continental area lies south of the southern

---

[3] Some of the results of this chapter are also presented in Dahms *et al.* (2012b)

polar circle and approximately 99.66 % of its area ($14\times10^6\,\mathrm{km}^2$) is covered with ice. The Antarctic Ice Sheet is a contiguous mass of glacial ice and the single largest solid object on Earth. It contains approximately $30\times10^6\,\mathrm{km}^3$ of ice, which equals 70 % of Earth's freshwater (Fox & Cooper, 1994). The very cold temperatures in Antarctica together with its isolation from warm, moist air masses, result in very low precipitation rates (approximately 5 cm/a water equivalent, King & Turner 1997). The Antarctic continent is therefore a desert for most parts, even though the low temperatures prevent large amounts of evaporation and sublimation.

The Antarctic climate system varies on a broad range of time scales. Although the Antarctic continent is isolated from mid- and low latitudes, its climate is closely coupled to the global climate system. Signals of low latitude climate variability can be found in the Antarctic continent and in the southern ocean (Turner, 2004) and there is also increasing evidence that signals can be transmitted from high to low latitudes (Turner *et al.*, 2009).

During the Cenozoic (the era when the continents moved into their current positions), Antarctica experienced tectonic, climatic and oceanographic events that led to a geographical isolation. As a consequence, colder conditions established. The deep ocean sedimentary record by Zachos *et al.* (2008) shows a long-term cooling of the climate over the past 50 million years.

The classical hypothesis to explain this Antarctic climate change is that climatic cooling and the development of the AIS were related to the opening of tectonic seaways. The Drake Passage between Antarctica and South America and the Tasman Gateway between Antarctica and Australia opened up around the Eocene–Oligocene transition. The opening of seaways permitted unrestricted circumpolar flow: the Antarctic Circumpolar Current (ACC) and consequently the Polar Frontal Zone (PFZ) developed, which progressively thermally isolated Antarctica (e.g. Kennett, 1977, 1978). The ACC is a powerful surface-to-bottom current that provides an effective barrier between Antarctica and warmer waters northward. It stretches over a length of approximately 20,000 km and is the only current to completely encircle the globe. The ACC is also the world's largest ocean current, transporting about $140\times10^6\,\mathrm{m}^3$ of water per second (140 Sv). It links the three main ocean basins (Atlantic, Pacific, and Indian Ocean) into one global system by transporting heat and salt (Turner *et al.*, 2009). Before the Drake Passage opened up, unrestricted circumpolar flow was not possible and the ocean currents had a stronger meridional component.

Furthermore, a change in atmospheric CO_2 might explain the onset of the Antarctic glaciation. Atmospheric CO_2 concentrations were much higher before the Eocene–Oligocene transition than today. Declining greenhouse gases could have caused the atmospheric temperatures to decrease, which would have permitted substantial ice formation on Antarctica. For example, DeConto & Pollard (2003) conclude that CO_2 forcing was the most crucial mechanism for the transition from a "greenhouse" to an "icehouse" climate.

Periodic changes in the parameters of the Earth's orbit around the sun affect the amount and distribution of incoming solar radiation and explain the periodic appearance of ice ages (Milankovitch, 1941). Milankovitch identifies three types of orbital variations, which could act as climate forcing mechanisms: obliquity of the Earth's axis, eccentricity of the Earth's orbit around the Sun, and precession of the equinoxes. The Eocene–Oligocene transition coincides with an orbital configuration comprising a phase of low eccentricity and low-amplitude change in obliquity, favoring cool austral summers, which hinder the melting of summer snow (Coxall *et al.*, 2005). Thus, the glaciation of the Antarctic continent could also have been caused by the configuration of Earth's orbital parameters, which favored ice sheet growth. Furthermore, the glaciation of Antarctica was probably accelerated by positive feedbacks triggered by a massive high-albedo ice cap.

A coupled model approach is essential to find an answer about the importance of the different influences on the Antarctic glaciation. The coupled model needs to include three-dimensional oceanic and atmospheric flow. Ocean heat fluxes force the atmosphere and, in turn, the distribution of atmospheric energy (heat flux), moisture (freshwater flux), and momentum (wind stress) are the prevalent driving mechanisms for the ocean.

Previous model studies exist, but a conclusive answer about the relative importance of the opening of ocean gateways, a change in atmospheric CO_2, and changing orbital parameters has not been given, since the results contradict each other. For example, Mikolajewicz & Maier-Reimer (1993) study the effect of Drake and Panama gateways on the ocean circulation and conclude that the temperature changes due to an opening of the Drake Passage are not large enough to have triggered the Antarctic glaciation. They suggest that some other mechanism (possibly CO_2) may be responsible for the AIS expansion. However, Mikolajewicz & Maier-Reimer have not applied a fully coupled model, but an ocean model with a strongly simplified description of the atmosphere. Toggweiler & Bjornsson (2000) use an idealized water planet model to examine the effect of the opening of the Drake Passage on Earth's climate and find that it cools the high latitudes of the southern hemisphere. They conclude that the effect of the Drake Passage opening is greater than previously supposed. Their model consists of a three-dimensional ocean general circulation model and a one-dimensional energy balance model of the overlying atmosphere. In contrast, DeConto & Pollard (2003) use a fully coupled atmosphere–ocean–ice sheet–sediment general circulation model to find that the opening of the Drake Passage has a smaller effect on the southern hemisphere climate, relative to changes in atmospheric CO_2. Cristini *et al.* (2012) conducted sensitivity experiments (opened and closed Drake Passage) with a coupled ocean–atmosphere–ice sheet model. They find that the AIS is more massive with a fully developed ACC and conclude that the opening of the Drake Passage contributed substantially to the Antarctic glaciation.

In this study the coupled atmosphere–ocean–sea ice model (Planet Simulator & LSG, introduced in chapter 2) is used for idealized numerical simulations concerning the onset of the Antarctic glaciation. To focus on the essentials, an expanded aquaplanet set-up is applied by including two topographical features in a planet covered by a single ocean: a circular continent at the south pole representing Antarctica and a meridional barrier in the ocean. The latter allows to mimic a closed or open Drake Passage. Simulations are carried out with different atmospheric CO_2 levels and orbital parameters to cover all three aspects of the hypothesis about the Antarctic glaciation onset. Note that the coupled model does not include a model for land ice and ice sheets may not form excluding the effect of mountainous terrain.

There are previous studies which apply the general concept of an aquaplanet with some topography included to analyze the ocean circulation in relevance to orographic barriers. A general circulation model, which comprises two identical idealized ocean basins that are connected by a circumpolar channel at the south pole (representing the Atlantic and Pacific Oceans), is used by Marotzke & Willebrand (1991) to investigate which fundamentally different equilibria of the global thermohaline circulation may exist. Toggweiler & Bjornsson (2000) apply an aquaplanet model with an opened and a closed meridional barrier similar to the one applied in this study. With the idealized set-up they realize deep and shallow ridges in the ocean in the area of the Drake Passage. However, the simulations of Toggweiler & Bjornsson (2000) do not include a continent at the south pole but two small polar islands, which are not treated as land-surface (i.e. which do not include snow cover or ice–albedo feedback). Smith *et al.* (2006) have been the first to apply a fully coupled atmosphere–ocean general circulation model to an aquaplanet. They analyze the large-scale ocean circulation in aquaplanets with meridional ocean barriers from pole-to-pole (including a gap either in the tropics or at the south pole). Enderton & Marshall (2009) use similar aquaplanet set-ups to explore to which degree the total meridional heat transport is sensitive to the details of its atmospheric and oceanic components and the differences that arise due to varying geometrical constraints on ocean circulation influencing the ocean's ability to transport heat poleward.

The idealized set-up of the experiments is described in section 5.2. Results for the mean climate state before and after the Antarctic climate transition are presented in section 5.3. The effects of declining atmospheric CO_2 (section 5.4), the opening of the Drake Passage (section 5.5), and of changing orbital parameters (section 5.6) are discussed separately, as well as the combined effect of all three forcing mechanisms (section 5.7). In section 5.8 the results are summarized and discussed.

5.2 Experimental Design

To simulate the onset of the Antarctic glaciation, different sensitivity simulations are conducted. The simulations are carried out with an idealized land–sea configuration, which expands the aquaplanet concept. In addition to the pure aquaplanet, two topographical features are included, which are displayed in figure 5.1:

1. A circular continent is placed at the south pole (poleward of 60°). The continent does not have any orographic features (a uniform height of 0 m above sea level) nor vegetation cover. However, snow may accumulate on the land surface.
2. A meridional barrier (in the ocean only) at 180°.

Three variations in the boundary conditions are chosen to explore the main hypotheses about the onset of the Antarctic glaciation:

Opening of the Drake Passage: The meridional barrier runs from the north pole down to the continent in the case of the closed *Drake Passage*

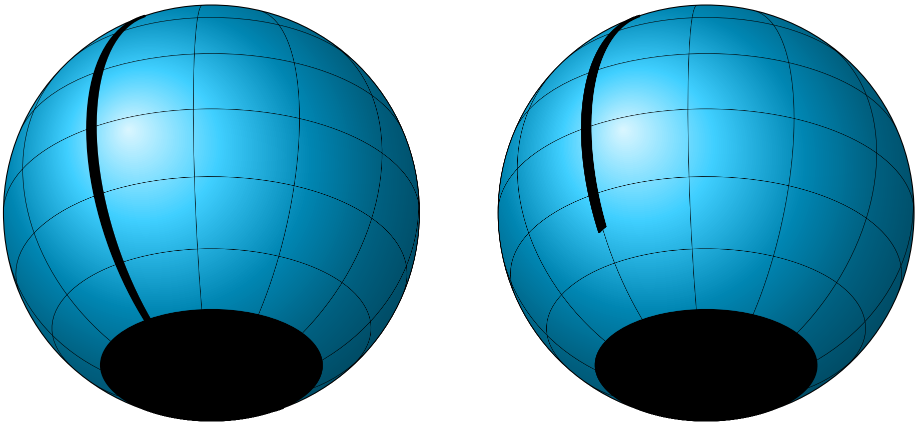
(a) closed *Drake Passage* **(b)** open *Drake Passage*

Figure 5.1: Set-up of expanded aquaplanets with idealized *Drake Passage* (tilted to highlight the southern hemisphere)

(figure 5.1a). For the opened *Drake Passage* (figure 5.1b), the barrier runs down to 30°S and thus leaves a gap in the southern ocean. Since the passage represents a very idealized case of a *Drake Passage*, it will be referred to in italic in the following.

Change in orbital parameters: As the orbital parameters were closer to equinoctial conditions during the Antarctic glaciation than before the Eocene–Oligocene transition and seasons were less pronounced, the change in the orbital parameters is represented by simulations with and without seasonality. Both represent extreme cases of the orbital parameters before and after the Eocene–Oligocene transition. The cases without seasons have completely equinoctial conditions. The cases with seasons have present-day orbital parameters.

Change in atmospheric CO_2: Before the Eocene–Oligocene transition, atmospheric CO_2 was very high and started to decrease during the transition. This change is represented by comparing simulations with the extreme cases of present-day CO_2 (360 ppm) and CO_2 values of 1,000 ppm.

An overview of the experiments is given in figure 5.2. The *control* experiment is the state of the climate system before the Eocene–Oligocene transition: high CO_2 levels, a closed *Drake Passage*, and orbital parameters that cause seasonality. After the Eocene–Oligocene transition, when Antarctica is covered with the Antarctic Ice Sheet (AIS), the climate state has shifted to the so-called *final* state: lower CO_2 levels, an open *Drake Passage*, and orbital parameters that suppress seasonality.

A comparison between the *final* and *control* case will be presented. Furthermore, sensitivity experiments are analyzed, where the different effects are studied separately:

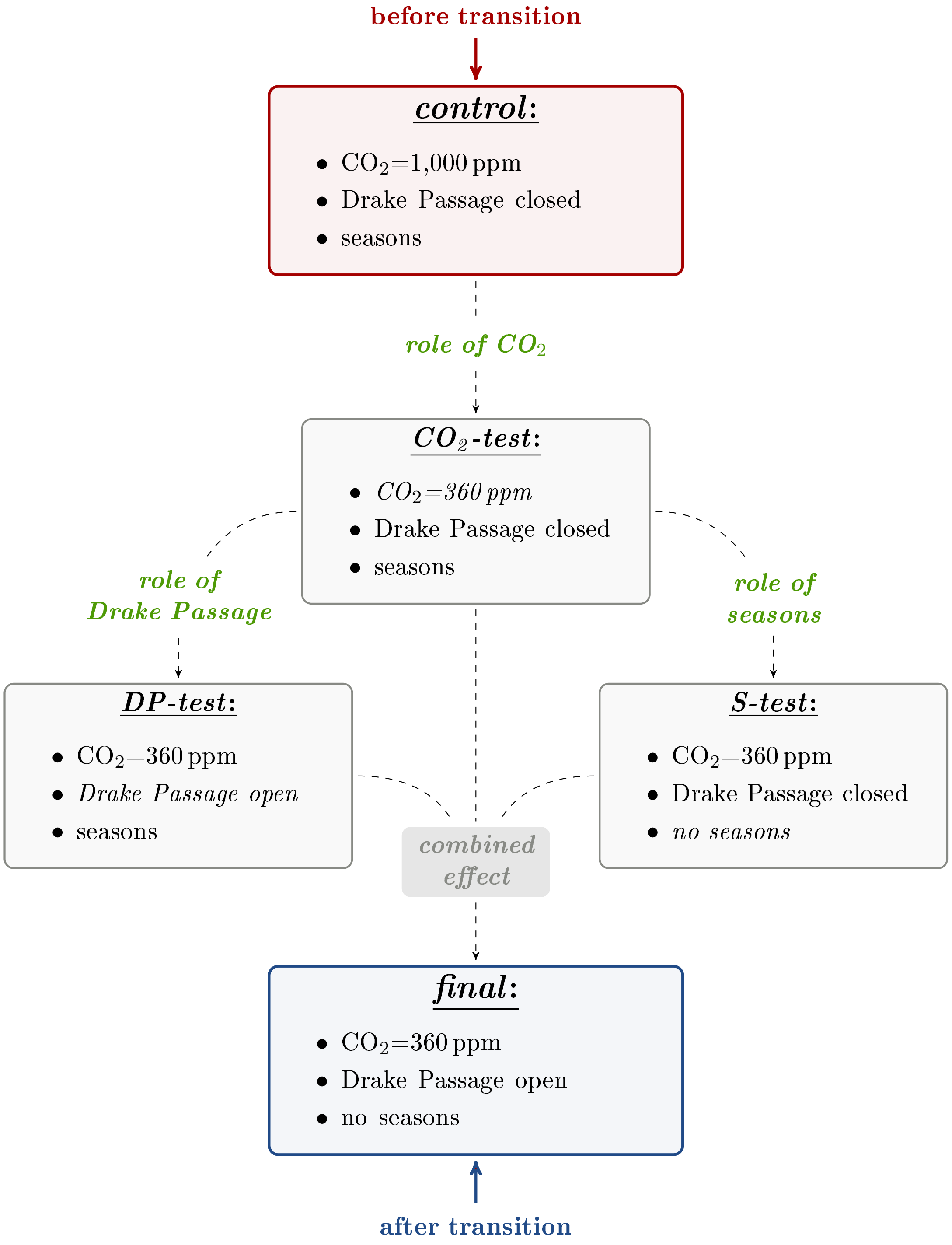

Figure 5.2: Overview of the sensitivity experiments on the onset of the Antarctic glaciation

1. change in atmospheric CO_2 concentrations only: *CO_2-test*
2. role of the *Drake Passage* only (with a lower CO_2 level): *DP-test*
3. role of the orbital parameters only (with a lower CO_2 level): *S-test*

The external forcings are kept constant throughout the entire integration period for all sensitivity simulations:

- The ocean has a flat bottom with a uniform depth of 5,500 m.
- The solar constant is fixed at 1,365 W/m^2.
- The integration starts from steady state.
- The simulations are run for 20,000 years since a very long spin-up time is needed for the ocean.
- All external forcings are kept constant throughout the entire integration period.
- Time averages are taken over the last 1,000 years of the integration period (i.e. the years 19,001 to 20,000) to ensure that the model has reached equilibrium and to obtain a robust average.

5.3 Mean Climate States Before and After the Transition

Two simulations are integrated out to equilibrium to represent the two states before and after the Antarctic climate transition. The *control* simulation represents the climate state before the onset of the Antarctic glaciation. The forcing is characterized by high CO_2 values, a closed *Drake Passage* that inhibits circumpolar flow around the southern polar continent, and orbital parameters that allow a yearly cycle with pronounced seasonality. During the transition to a colder climate, which leads to the glaciation of Antarctica, atmospheric CO_2 values decline dramatically, the *Drake Passage* opens up, and the orbital parameters change suppressing the seasonal cycle. The climate state after this transition is represented in the *final* simulation. Here, the mean climate states of *control* and *final* are introduced and compared.

5.3.1 Temperature and Water Cycle

Features of the temperature and water cycle of the two states before and after the transition (*control* and *final*) are discussed in the following. The surface air temperature (SAT) cools in the global mean by approximately 5 K from *control* to *final*. However, as seen in figure 5.3, the SAT does not equally decline at all latitudes. In the tropics and subtropics, both climate states show almost the same meridional temperature profile, but at mid- and higher latitudes, the temperatures in *final* are already significantly lower

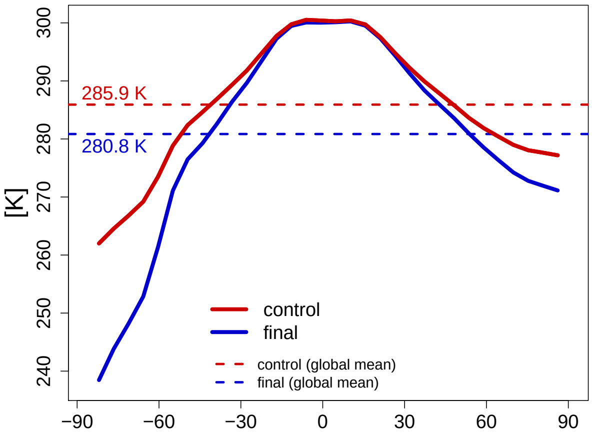

Figure 5.3: Zonal and global mean surface air temperature for *control* and *final*

than in *control*. In the northern hemisphere the differences amount up to 5 K. However, the greatest discrepancies in the meridional temperature profiles can be observed at the south pole over the continent, where a cooling of 10–20 K takes place.

Figure 5.4 shows the zonal mean atmospheric and oceanic temperature distributions as well as the specific moisture in the atmosphere and the salinity in the ocean for the climate states before (*control* simulation in figure 5.4a) and after the transition (*final* case in figure 5.4b).

In the tropics the zonal mean atmospheric temperature distribution at all heights hardly differs between the two climate states. However, poleward of approximately 30°N/S, the temperature patterns start to deviate significantly and, furthermore, are not symmetric about the equator anymore. The northern mid- and high latitudes of *control* are warmer than their counterparts in the southern hemisphere, where especially the temperatures close to the surface become very cold. The north/south temperature differences of *final* are even greater. The temperature deviations between *control* to *final* are also hemispherically asymmetric (in particular in the lower atmosphere). The *final* climate is much colder than the *control* climate at mid- and high latitudes, especially over the continent at the south pole where differences exceed 10 K up to the middle troposphere. Only in the upper subtropical atmosphere, the temperature increases in the *final* climate.

The specific moisture distribution closely follows the atmospheric temperature pattern. While the tropics show relatively similar moisture distributions in both the *control* and the *final* state, the relatively warm mid- and high latitudes of *control* exhibit rather high moisture contents and the cooler poles of *final* are dryer. Especially the atmosphere over the southern polar continent is very dry with specific moisture contents of less than 1 g/kg even close to the surface.

In the ocean the temperature decreases at all latitudes and at all depths between *control* and *final*. Contrasts are particularly high in the deep ocean and in the area of the closed/open *Drake Passage*, where the ocean of *control* is over 5 K warmer than the ocean of *final*. The salinity is higher in the southern hemisphere and in low latitudes

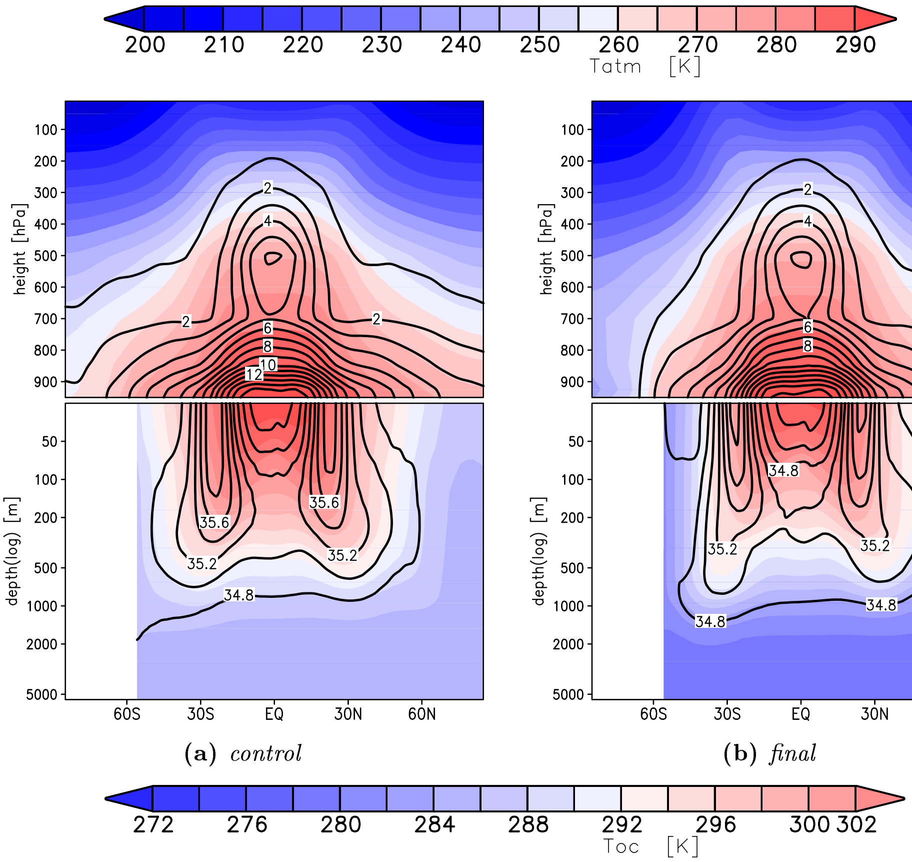

(a) *control* **(b)** *final*

Figure 5.4: Zonal mean temperature in atmosphere and ocean (shaded) as well as atmospheric specific moisture and oceanic salinity for *control* and *final* (contour lines in g/kg for the specific moisture and in psu for the salinity, note the logarithmic vertical axis for the ocean)

close to the sea surface of *control*, but differences are not as great as for the ocean temperature.

The total precipitation (large scale plus convective) is presented in figure 5.5. Furthermore, the zonal mean precipitation is shown in figure 5.6, where additionally the zonal mean evaporation and the surface fresh water flux (precipitation minus evaporation) are displayed. The general pattern of the total precipitation is very similar in *control* (figure 5.5a) and in *final* (figure 5.5b): The greatest amounts of precipitation occur over the warm water pools at the western boundary of the ocean basin. The equatorial precipitation zone is strong in both set-ups, as are the baroclinic zones of the mid-latitudes. Generally, the precipitation over the poles is low, but higher over the north pole than over the south pole.

Even though the overall precipitation patterns are the same, there are some differences between the atmospheric water cycles of *control* (figure 5.6a) and *final* (figure 5.6b): Both show a pronounced single equatorial precipitation peak, which is stronger in the

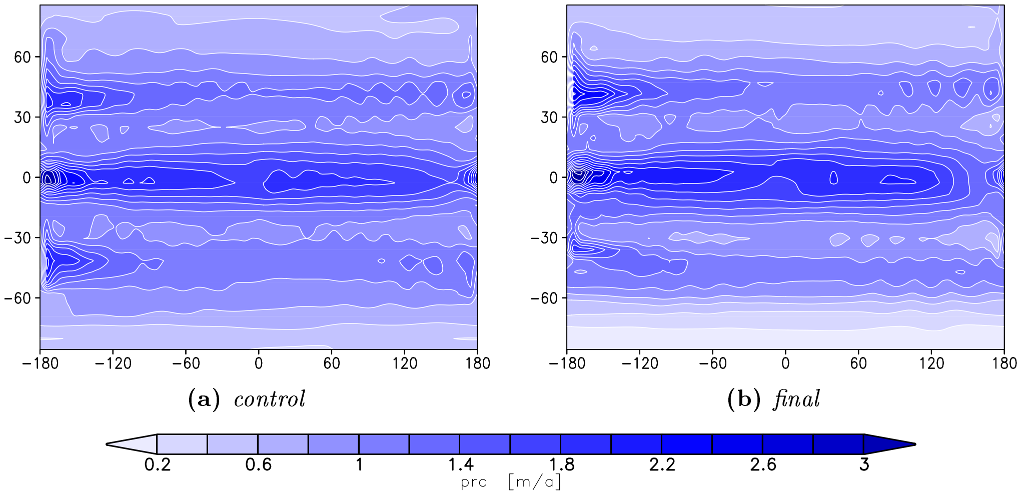

(a) *control* **(b)** *final*

Figure 5.5: Total precipitation (large scale plus convective) for *control* and *final*

final climate state. At low latitudes, evaporation is also slightly stronger in *final*, but at mid- and higher latitudes, the warm *control* climate shows highly increased precipitation rates. In the northern hemisphere, the precipitation peak of the mid-latitudes is comparable before and after the transition, however, the very cold southern polar ocean of *final* leads to a decreased mid-latitude precipitation. Over the cold southern polar continent of *final* hardly any precipitation nor evaporation occurs.

The surface fresh water flux shows slightly stronger extrema (positive in the tropics and negative in the subtropics) in *final*. Furthermore, a (positive, i.e. downward) peak in the surface fresh water flux in the southern mid-latitudes can be observed, which is absent in *control*. This can also be seen in the zonal mean vertically integrated meridional atmospheric moisture transport (figure 5.7). While both *control* (figure 5.7a) and *final* (figure 5.7b) show an equatorward tropical moisture transport that is solely achieved by the atmospheric mean circulation and an extra-tropical poleward transport that is mostly conducted by atmospheric large-scale eddies, the moisture transports differ in magnitude. The water vapor transports after the transition are much stronger than in the *control* climate state. Especially the extra-tropical moisture transport in the southern hemisphere (toward the southern polar continent) is very strong in *final*. However, it can be noted that the moisture transport at high southern latitudes (between 65°S and 75°S) before the transition is also relatively strong. The atmospheric moisture transport is computed in a similar manner as the atmospheric energy transport, which is explained in appendix E.

The atmospheric zonal mean potential and moist potential temperature before and after the transition is displayed in figure 5.8. In both cases, the tropical temperature gradient is very weak throughout the entire atmosphere. From the subtropics deep into the mid-latitudes a broad baroclinic zone exists and the poles have a weaker temperature gradient, especially at upper levels. The tropical air contains high amounts of moisture, which affects the moist potential temperature throughout all vertical levels of the troposphere. Great differences in the dry and moist potential temperature be-

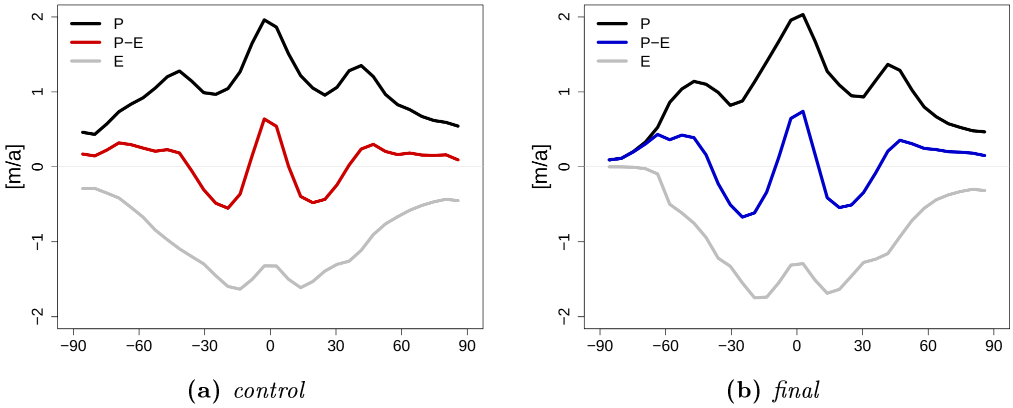

(a) *control* **(b)** *final*

Figure 5.6: Zonal mean precipitation (P), evaporation (E), and surface fresh water flux, i.e. precipitation minus evaporation ($P - E$) for *control* and *final*

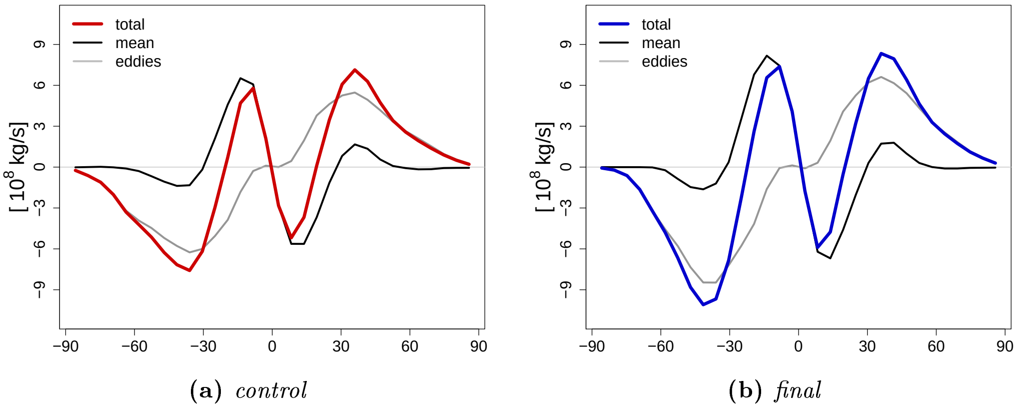

(a) *control* **(b)** *final*

Figure 5.7: Zonal mean vertically integrated meridional atmospheric moisture transport for *control* and *final*

tween the *control* climate before the transition (figure 5.8a) and the *final* climate after the transition (figure 5.8b) occur at the south pole: While the south pole of *control* is relatively warm and moist, the south pole in *final* is about 20 K colder. Furthermore, the air above the pole is very dry so that dry and moist temperature profiles are almost identical.

5.3.2 Circulation

The zonal mean zonal wind and the atmospheric stream function before and after the transition are displayed in figure 5.9. The atmospheric stream function shows a direct Hadley circulation in lower latitudes and an indirect Ferrel cell in the mid-latitudes. The strength and structure of the Hadley cells are strongly connected to the equator-to-pole temperature gradient, which can be explained, for example, by the model of Held

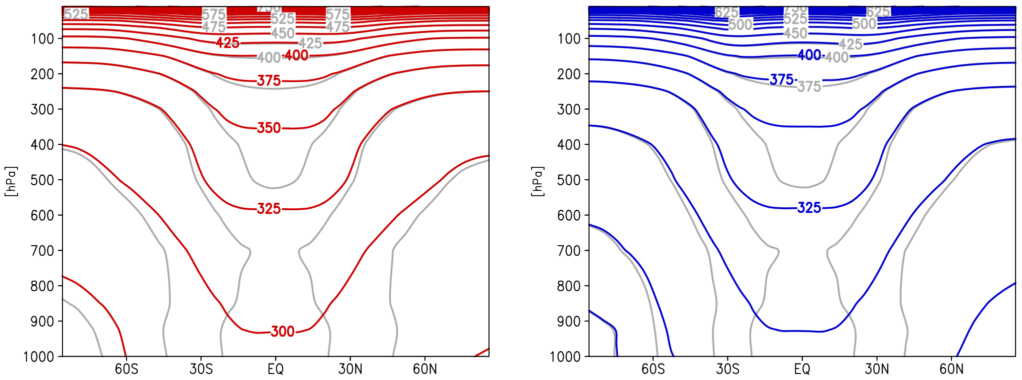

(a) *control* **(b)** *final*

Figure 5.8: Zonal mean atmospheric potential and moist potential temperature (dry potential temperature: colored lines; moist potential temperature: gray lines) for *control* and *final*

& Hou (1980). The Hadley cells have a maximum strength of $30 - 40 \times 10^9$ kg/s (the atmospheric stream function in 10^9 kg/s represents numerically about the same mass transport as an oceanic volume transport in Sverdrups; Czaja & Marshall 2006), which is comparable to present-day annual mean observations (see for example Peixoto & Oort, 1992). Since the Hadley cell is connected to the meridional temperature gradient, in each climate state the cell in the southern hemisphere is stronger than in the northern hemisphere. The southern Hadley circulation in the *final* climate is the strongest with a maximum of 40×10^9 kg/s, because of the great temperature difference between the very cold southern polar continent and the warm tropics. The Ferrel circulation has about half the strength of the Hadley cells (maxima of 10×10^9 kg/s in the *control* simulation, figure 5.9a, and 20×10^9 kg/s in the *final* climate after the transition, figure 5.9b).

In both cases the zonal wind is in thermal wind balance with the meridional temperature gradient: There are west-wind zones in the mid-latitudes and easterly winds in the tropics and at the poles. The tropical easterlies are the strongest in the *final* climate. Furthermore, after the transition the southern hemisphere shows the strongest equator-to-pole temperature gradient because of the very cold southern polar continent and, thus, the west winds of the mid-latitudes, including the subtropical jet streams at the upper poleward edge of the Hadley cells, are the strongest.

The meridional overturning circulation (MOC) in the ocean, which is also displayed in figure 5.9, is very much affected by the opening of the *Drake Passage*. A large cross-equatorial (positive) cell develops in the northern hemisphere (in each simulation), which reaches into the subtropics of the southern hemisphere. Only close to the surface there is a small negative cell in the northern hemispheric mid-latitudes. In the *control* climate, when the *Drake Passage* is closed, a (negative) cell develops in the southern hemisphere, which is the counterpart to the huge northern cell, even though it is much smaller and weaker (and of course bounded by the southern continent). In the case where the *Drake Passage* opens up (the *final* climate), this southern cell is confined to the very surface and a stronger and larger mid-latitude cell can be observed, which is connected to the

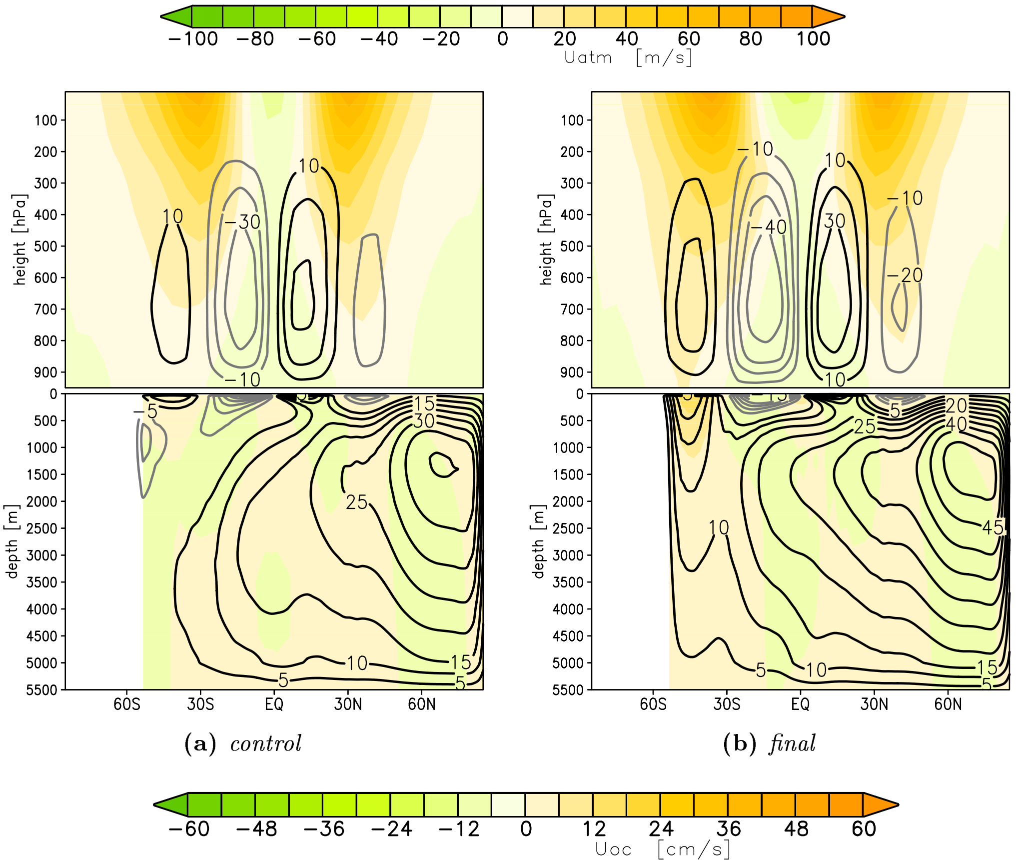

(a) *control* **(b)** *final*

Figure 5.9: Zonal mean zonal wind/ocean currents (shading) and atmospheric stream function/MOC (stream lines in 10^9 kg/s for the atmospheric stream function and in Sv for the MOC) for *control* and *final*

northern hemispheric tropical cell. Compared to other studies with an idealized *Drake Passage* (e.g. Marotzke & Willebrand, 1991; Toggweiler & Bjornsson, 2000; Smith *et al.*, 2006; Enderton & Marshall, 2009), the MOC in *control* and in *final* show similar patterns and magnitudes but slightly higher maxima.

Zonal mean zonal ocean currents are rather weak throughout all latitudes in the *control* climate (figure 5.9a) since the ocean barrier prevents circumglobal flow. However, when the *Drake Passage* opens in the *final* climate (figure 5.9b), a westerly current develops in the southern ocean, which is comparable to the Antarctic Circumpolar Current (ACC) of our present-day climate.

This strong ACC-like current in the southern ocean can also be observed in the surface currents (at a depth of 25 m), which are displayed in figure 5.10 together with the surface winds (at 925 hPa). Zonal surface winds (figure 5.10a) are stronger in the *final* climate at almost all latitudes. Only in the very deep tropics and at the north pole, the *control* climate surface winds are of similar strength. The zonal surface currents (figure 5.10b) are also stronger after the transition, however, the only region with a great difference

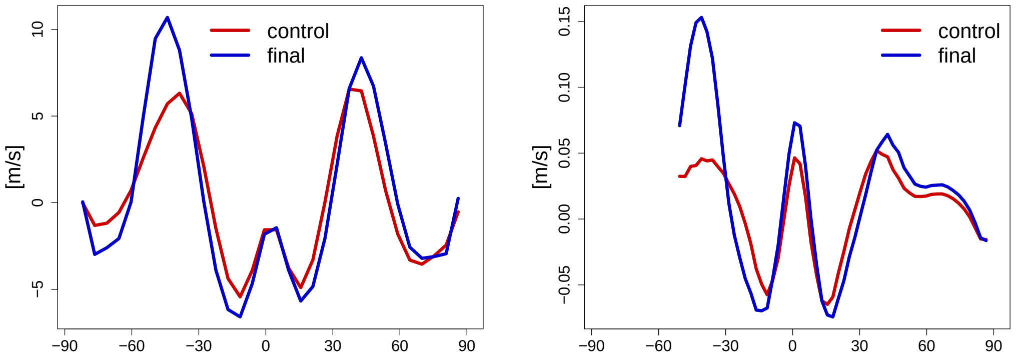

(a) zonal surface winds **(b)** zonal surface currents

Figure 5.10: Zonal mean zonal surface winds (at 925 hPa) and currents (at a depth of 25 m) for *control* and *final*

to the *control* climate (over 0.10 m/s stronger) is located in the area where the *Drake Passage* opens up.

Figure 5.11 shows the horizontal barotropic stream function and the deviation of the sea surface temperature (SST) from its zonal average. Northward of 30°S, both climates reveal approximately the same SST deviation patterns, even though in the *final* state SST contrasts are more pronounced. Warmer surface waters are located at the western boundary of the ocean basin, while the eastern boundary is much colder. The only exception is the northern polar ocean, which is warm close to both sides of the boundary and colder in the middle of the ocean basin. In the mid-latitudes the warm/cold contrast between west and east is particularly strong.

The barotropic stream function (i.e. the depth-integrated flow) is directly related to the pattern of surface wind stress. In the northern hemisphere, both *control* and *final* show a subtropical and a subpolar gyre with greater magnitudes in the *final* climate: up to 100 Sv compared to approximately 40 Sv in *control*. These values are similar to the ones found by Enderton & Marshall (2009), who observe maximum gyres between 80 Sv and 100 Sv in their *Drake Passage* simulation.

The subtropical gyre can also be found in the southern hemisphere of both *control* and *final*. The greatest deviations between *control* and *final* occur poleward of the southern mid-latitudes: In the *control* case (with a closed *Drake Passage*, figure 5.11a) the SST distribution is almost a mirror of the northern hemisphere (equatorward of the continent). In contrast to the *final* climate: when the *Drake Passage* is opened (figure 5.11b), hardly any zonal temperature deviations exist poleward of 30°S. This can be explained by the different circulation patterns: When the *Drake Passage* in the southern ocean opens up, a very strong circumpolar current develops, which is missing in the set-up with the closed barrier. This depth-integrated circumpolar flow is very strong (more than 500 Sv are transported), which is consistent with other idealized model studies comprising a flat ocean bottom (see for example Smith *et al.* 2006 or Enderton & Marshall 2009).

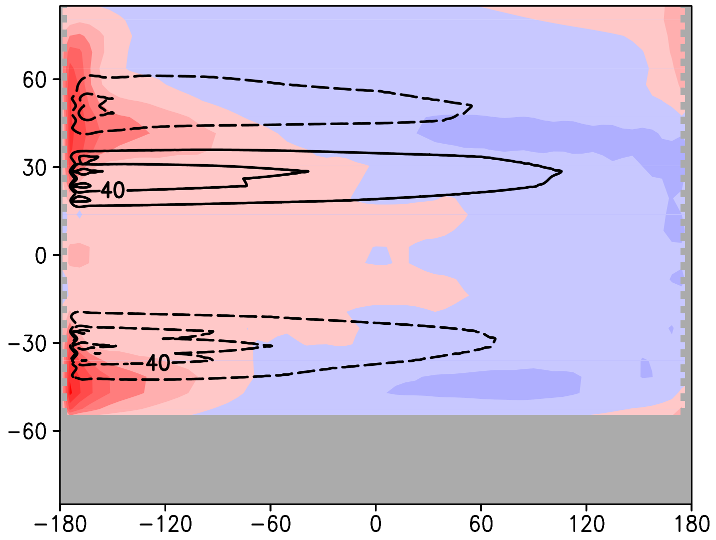

(a) *control*

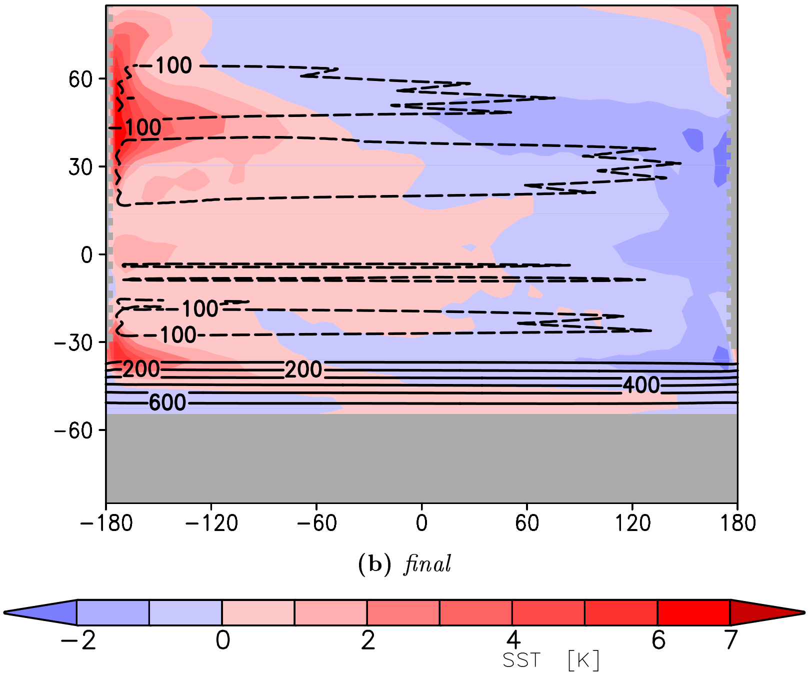

(b) *final*

Figure 5.11: Barotropic horizontal stream function (different contour intervals: 20 Sv in *control*; 50 Sv in *final* northward of 30°S and 100 Sv southward of 30°S) and deviations from zonal mean SST for *control* and *final*

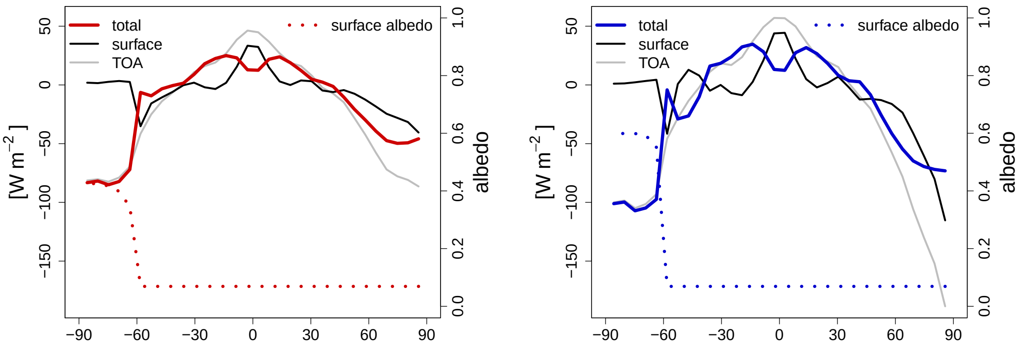

(a) *control* **(b)** *final*

Figure 5.12: Zonal mean atmospheric energy budget (total (TOA – surface), at the top of the atmosphere (TOA), and at the surface) and surface albedo for *control* and *final*

5.3.3 Energy

The energy budget for *control* and *final* is calculated in accordance with equations (3.1) to (3.3) from chapter 3. Figure 5.12 shows the zonal averages of the total energy budgets, as well as the balances at the top of the atmosphere (TOA) and at the surface. Zonal mean surface albedos are also displayed.

The total energy budget is distributed more uniformly in the warm climate of *control* (figure 5.12a). There is still a net energy surplus in the tropics and a deficit poleward of approximately 30°N/S, but the positive values in low latitudes are neither as high as the ones after the transition, nor are the deficits at high latitudes as strong as in the *final* climate (figure 5.12b). At the poles, the differences can partly be explained with deviations in the energy budget at the TOA, which shows a stronger deficit in the *final* climate. The surface energy budget also changes during the transition, which is mostly related to the sea surface temperature as well as sensible and latent heat flux. Furthermore, the surface albedo over the southern continent is not as high (about 40 %) as in the *final* state (approximately 60 %).

The zonal mean vertically integrated transport of energy is displayed in figure 5.13, as well as the partition of the transport between atmosphere and ocean. The computation of the energy transport is explained in appendix E. Bjerknes (1964) and Stone (1978) explain that the sum of the oceanic and atmospheric meridional energy transports remains mostly constant throughout changes imposed on the climate system. However, Stone found that the controlling factors on the strength and form of the transport are the size of the planet, the rotation rate, the axis tilt, the solar constant, and the mean hemispheric albedo. After Stone's concept it is not surprising that in the climates of *control* and *final* very different amounts of total energy are transported poleward. Some of the identified controlling factors change during the transition, namely the axis tilt of the Earth and the mean hemispheric albedo (when the onset of Antarctica's glaciation is triggered). In the *control* climate, the total heat transport peaks at almost 4 PW

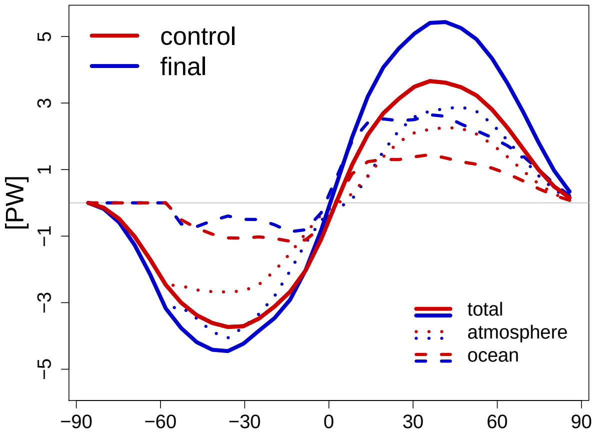

Figure 5.13: Zonal mean vertically integrated meridional energy transport (total, atmospheric and oceanic) for *control* and *final*

between 30° and 35° in each hemisphere, but with a slightly stronger transport in the south. After the transition, the total zonal mean meridional energy transport has increased dramatically. The maxima in the *final* climate exceed 5 PW and are located around 40°N/S, with higher values in the northern hemisphere.

In the northern hemisphere, the ocean heat transport (OHT) is very large and almost as high as the atmospheric energy transport. In contrast, in the southern hemisphere the atmospheric heat transport is significantly larger than the oceanic part. The *control* climate has a relatively constant OHT of about 1 PW in the lower and mid-latitudes in both hemispheres. The atmospheric transport is higher, in particular in the mid-latitudes and even more over the southern polar latitudes, where the continent inhibits OHT. In the northern tropics and subtropics, the OHT in the *final* climate reaches 2 PW and even exceeds the atmospheric transport at high latitudes. In the southern hemisphere, the OHT is significantly reduced compared to the northern hemisphere. In the area where the continent is located (poleward of 60°S), the atmosphere conducts the entire heat transport alone. Furthermore, especially in the case where the *Drake Passage* is opened and a strong circumpolar current develops, the OHT is very small and the majority of the poleward heat transport has to be achieved by the atmosphere. However, the atmosphere is only partly able to compensate the missing OHT and therefore the total heat transport is weaker in the southern hemisphere.

5.3.4 Conditions for the Glaciation of Antarctica

The coupled atmosphere–ocean model (PlaSim & LSG) only includes a thermodynamic sea ice model but there is no model for land ice. Thus, the build-up of the AIS cannot be simulated directly, but instead temperature and snow cover on the southern polar continent are studied.

For the Antarctic glaciation, the establishment of colder temperatures is a precondi-

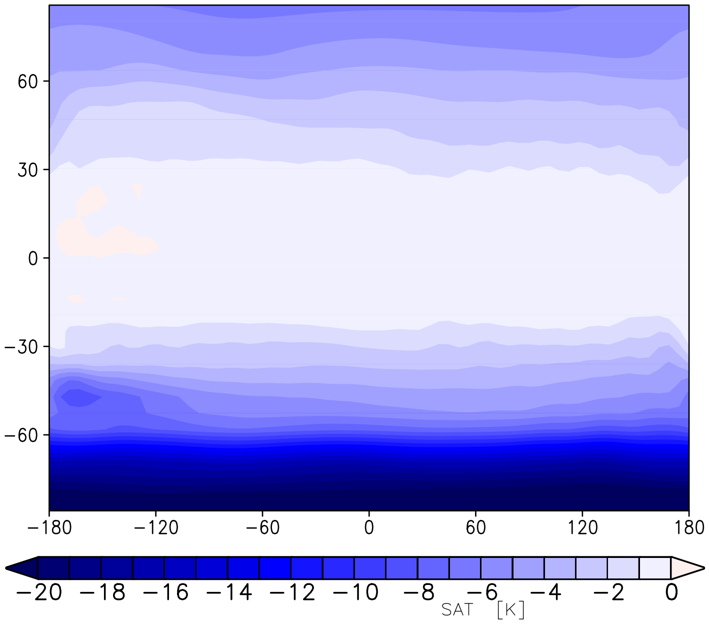

Figure 5.14: Surface air temperature differences between the *final* and *control* climate states

tion. Figure 5.14 shows the differences in surface air temperature (SAT) between the *control* and the *final* climate. During the transition the climate becomes colder at all latitudes, even though the cooling in the tropics is only very weak (in the range of 1–2 K and even a minimal warming occurs at the western boundary of the ocean basin). Mid- and especially high latitudes of the northern hemisphere experience a strong cooling of up to 6 K. However, the cooling in the southern hemisphere is even larger. Poleward of 30°S the SAT cools significantly, in particular at the western boundary of the ocean basin. The main cooling occurs over the continental area, where the temperature drops between 10 K and 20 K.

For ice sheets to build up, it has to be very cold all year long so that snow can accumulate. Figure 5.14 shows that there is indeed a very strong cooling from the *control* to the *final* climate state. The differences in snowfall are displayed in figure 5.15. Figure 5.15a displays the difference in snowfall between the *control* and *final* state and the snow depths individually before and after the transition.

A strong seasonal cycle can be observed for the snowfall: In the austral summer months, between December and February, there is significantly more snowfall in the *final* climate (almost 3 cm per month more). During the rest of the year, snowfall is reduced compared to the *control* climate, however, the reduction is 1 cm per month at most. Accumulated over the year, there is still an increase in snowfall of 0.8 cm/a after the transition.

Not surprisingly, the snow depth is much higher in the *final* than in the *control* climate. In contrast to *final* (where the snow cover has a constant depth of 5 m), there is a strong seasonal cycle in the *control* climate before the transition: Maximum snow depths can be observed in the late winter/early spring months (September and October) with approximately 14–15 cm (all values are liquid water equivalent depths) and during the austral summer months (between December and March) there is no snow cover in the southern continent. In the *final* climate, there is constant snow accumulation and the snow depth would grow continuously if it was not limited by the model to a height of 5 m (water equivalent).

Additionally, the snow depth change is shown in figure 5.15b. The snow depth change illustrates how important the melting period in the austral spring/early summer time is for the *control* climate. During most of the year, snow accumulates on the southern continent. However, just when the snow depth is highest, the temperatures start to increase and the snow depth decreases (with a maximum rate of over 12 cm per month in November). When the temperatures are highest, in December and January, there is already no snow cover left. For the *final* climate this parameter is zero all year long since snow accumulation over 5 m is balanced by artificial melting and fed into the ocean.

In summary, the experiments show that the onset of the glaciation of the continent can be triggered. The differences between *control* and *final* are pronounced and a transition from one climate state to the other indeed leads to much colder temperatures and higher snow covers, especially over the southern polar continent. However, the two simulations *control* and *final* differ in three parameters: the atmospheric CO_2 concentration, the closed/open *Drake Passage*, and the orbital parameters. To analyze the relative importance of each parameter and to explore which is the main forcing mechanism for the onset of the glaciation, three further sensitivity experiments are discussed.

5.4 The Influence of Atmospheric CO_2

At first, the role of the atmospheric CO_2 decrease during the transition is analyzed. A simulation with exactly the same set of parameters as *control*, but with lower CO_2 values (360 ppm, called *CO_2-test*) is compared to the *control* climate (1000 ppm) in figures 5.16 and 5.17.

Figure 5.16 shows the surface air temperature difference between the *CO_2-test* and *control* climate states. When atmospheric CO_2 is reduced, the air close to the surface becomes colder at all latitudes. The cooling is globally relatively constant with a temperature reduction of 2–3 K. Even though the reduction shows the largest values over the continent, the magnitude is not sufficient to explain the massive temperature decrease between the *control* and *final* climate (up to 20 K).

The difference in snowfall between the *control* and *CO_2-test* state and the snow depths for both climates are displayed in figure 5.17a. The snowfall differences are not very strong: In the austral summer months (November to March) there is more snowfall in the climate with reduced CO_2 values, however the differences do not exceed 1 cm per month. During the winter months (April to October) slightly increased snowfall can be observed in the *control* climate (between 0.1 cm and 0.5 cm per month more). The resulting snow depths in both climate states with higher and lower atmospheric CO_2 are almost identical. Only during the austral spring months (October and November) and to a lesser extent during fall (March to June) the snow depth is slightly increased in the

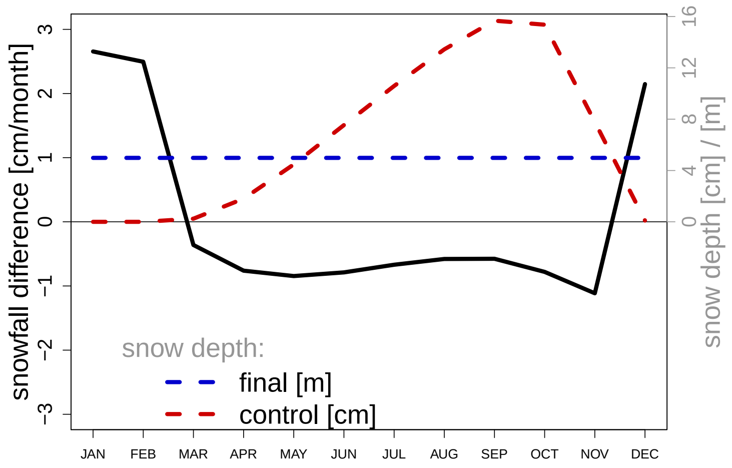

(a) snowfall and snow depth

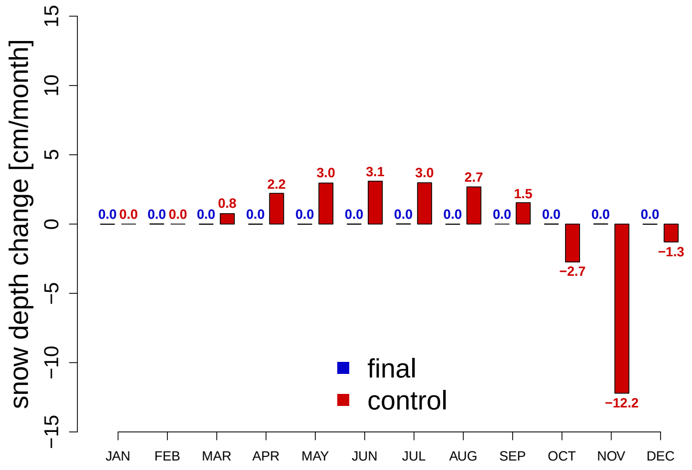

(b) snow depth change

Figure 5.15: Monthly mean snowfall differences, snow depth, and snow depth change for *control* and *final* averaged over the continental area (all values are in water equivalent units, note the different units: the snow depth for *control* in cm and for *final* in m)

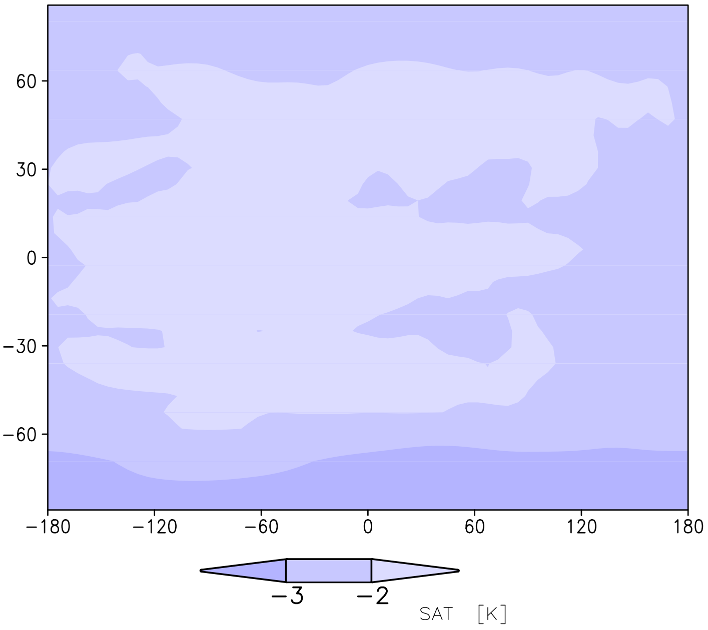

Figure 5.16: Surface air temperature differences between the *CO_2-test* and *control* climate states

CO_2-test climate. The snow depth change (figure 5.17b) of *CO_2-test* is very similar to the one with higher CO_2 values, i.e. snow accumulation between March and September, but strong melting periods in the austral summer months, so that the southern polar continent is completely snow-free from December to February.

When atmospheric CO_2 is reduced, the SAT cooling over the southern polar continent is only about 10 % of the overall temperature decrease from the *control* climate state to the *final* state after the transition. Furthermore, the snow cover still shows a strong seasonal cycle with a pronounced melting period in the austral spring and snow-free conditions in austral summer months. Therefore, it can be concluded that decreasing atmospheric CO_2 might not be the main forcing for the onset of the Antarctic glaciation.

5.5 The Influence of the Drake Passage

Since the cooling effect of atmospheric CO_2 decrease is relatively small compared to the overall cooling during the transition, other mechanisms must play a more crucial role. In the following step, the role of the opening of the *Drake Passage* is analyzed and the *CO_2-test* simulation is used as a reference climate state. The simulation *DP-test* is explored and compared to *CO_2-test*. Both have exactly the same set of parameters, but *DP-test* has an open *Drake Passage*, while *CO_2-test* has a closed barrier in the southern ocean.

The differences in the surface air temperature between *DP-test* and *CO_2-test* are displayed in figure 5.18. The SAT difference shows a distinct anti-symmetric pattern

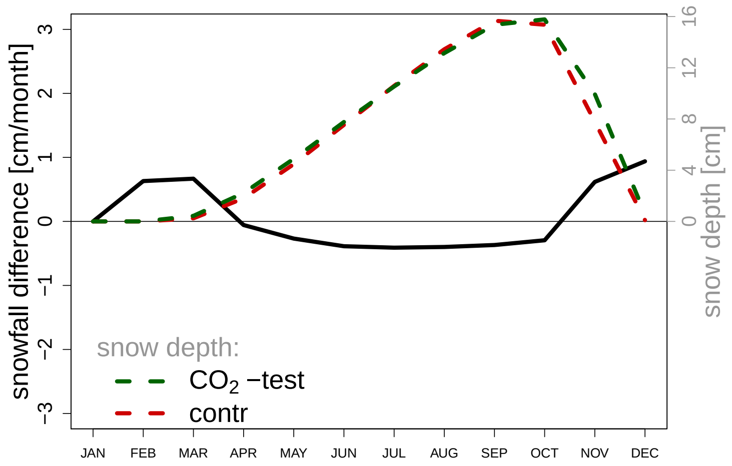

(a) snowfall and snow depth

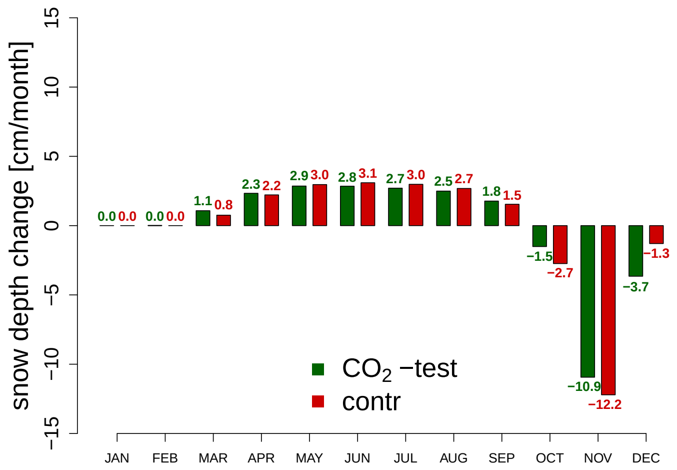

(b) snow depth change

Figure 5.17: Monthly mean snowfall differences, snow depth, and snow depth change for *CO$_2$-test* and *final* averaged over the continental area (all values are in water equivalent units)

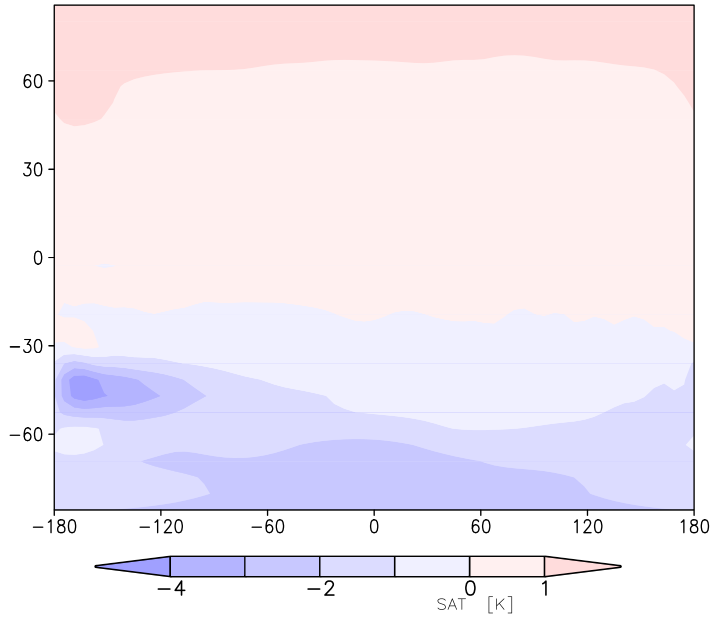

Figure 5.18: Surface air temperature differences between the *DP-test* and *CO$_2$-test* climate states

about the equator. The northern hemisphere experiences a warming when the *Drake Passage* opens up. The northern polar latitudes are warmed by over 1 K. However, poleward of 30°S (where the *Drake Passage* is located in this idealized set-up), the air close to the surface is cooled by 1–4 K. The areas with the strongest cooling can be found over the southern ocean east of the *Drake Passage* opening and at the center of the continent.

Characteristic features of the snow cover and differences between *DP-test* and *CO$_2$-test* are depicted in figure 5.19. Differences in snowfall (figure 5.19a) are minor but still depend on the seasonal cycle: Between December and March there is more snowfall in *DP-test* than in *CO$_2$-test*, however, during the other months (April to November) the snowfall is slightly increased (approximately 0.3–0.4 cm per month) when the *Drake Passage* is closed. Consequently, the snow depth is also very similar in both climate states, but slightly higher in the austral winter time when the *Drake Passage* remains closed. The snow depth change (figure 5.19b) of *DP-test* is in almost all months slightly reduced (in the absolute value) compared to the snow depth change of *CO$_2$-test*. However, the pronounced seasonal cycle, which includes a melting period in the austral summer months that causes the snow cover to completely disappear, also takes place when the *Drake Passage* opens up.

The cooling of the southern continent caused by the opening of the *Drake Passage* is also not strong enough to explain the large temperature drop during the transition from *control* to *final*. Even when added to the cooling accounted for by the CO$_2$ decrease, there is hardly more than a temperature reduction of 5–6 K. However, the differences between *control* and *final* exceed 20 K at the very high southern latitudes. The snow

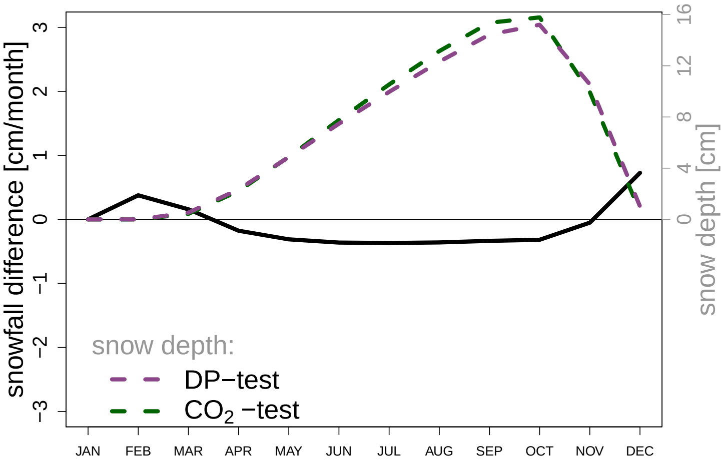

(a) snowfall and snow depth

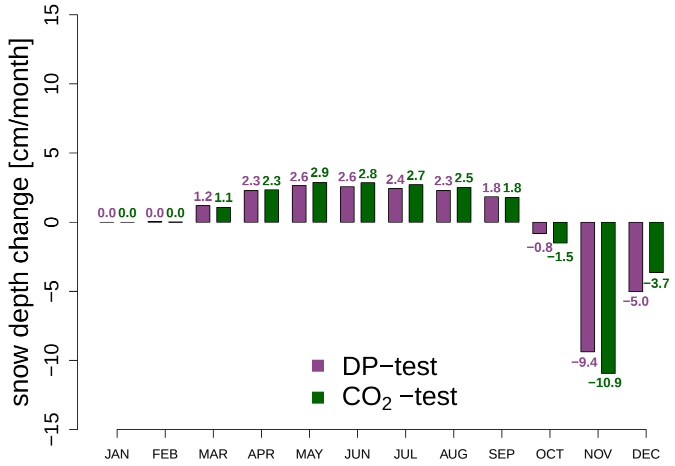

(b) snow depth change

Figure 5.19: Monthly mean snowfall differences, snow depth, and snow depth change for *DP-test* and *CO_2-test* averaged over the continental area (all values are in water equivalent units)

cover also reveals that changes are not large enough to trigger the build-up of a massive ice sheet when the *Drake Passage* opens up.

5.6 The Influence of the Orbital Parameters

Neither the decline of atmospheric CO_2 alone nor solely the opening of the *Drake Passage* is able to explain the reduction of the surface air temperature by almost 20 K during the transition from the *control* state to the *final* climate. Furthermore, constant snow accumulation without dramatic melting periods cannot be achieved by reducing atmospheric CO_2 or by opening the *Drake Passage*. In the following, the effect of the orbital parameters is analyzed. Again, the *CO_2-test* simulation is used as a reference climate state.

S-test has exactly the same set of parameters (and topographical set-up) as *CO_2-test*, except that the orbital parameters are changed to exclude the seasonal cycle. The SAT difference between *S-test* and *CO_2-test* is shown in figure 5.20. The seasonality causes temperature deviations which are almost symmetric about the equator: In the tropics and subtropics there is a warming (up to 2 K) and the extra-tropical air is cooled. Most prominently, it can be observed that temperatures at the poles, and especially at the south pole, are dramatically reduced. At the north pole, the high latitudes experience a strong cooling east of the ocean basin boundary (more than 10 K) and a moderate cooling (5–6 K) west of the boundary. The air above the southern continent is cooled almost uniformly and the temperature reduction exceeds 15 K poleward of the continental boundary.

The snow cover (figure 5.21) also reveals great changes in the simulations with and without seasonal cycle. In the austral summer months (December to February) the snowfall (figure 5.21a) is much greater in *S-test* (up to 3 cm per month). In the transitional months (March, April, May, and November) the set-up with a seasonal cycle experiences more snowfall (between 0.3 cm and 1.5 cm per month), while the deviations in snowfall are minor during the rest of the year (June to October). More importantly, the resulting snow depths have different orders of magnitudes (also displayed in figure 5.21a): While *CO_2-test* shows a strong seasonal cycle with maximum snow depths of 16 cm in October and no snow cover at all from December to February, there is constant snow accumulation in *S-test* and the snow depth would grow continuously if it was not limited by the model to a height of 5 m. Thus, the snow depth change (figure 5.21b) is zero all year long when the seasonal cycle is switched off, in contrast to *CO_2-test* which shows a strong melting period during the warm spring and summer months.

When analyzing all three parameters (atmospheric CO_2, opening of the *Drake Passage*, and seasonality) alone, it can be concluded that the main source for the strong cooling during the transition from the *control* to the *final* climate is the change in the orbital parameters. Furthermore, the seasons are responsible for the melting periods in the austral summer, so that the snow cover is substantially reduced, when orbital parameters allow a strong seasonal cycle.

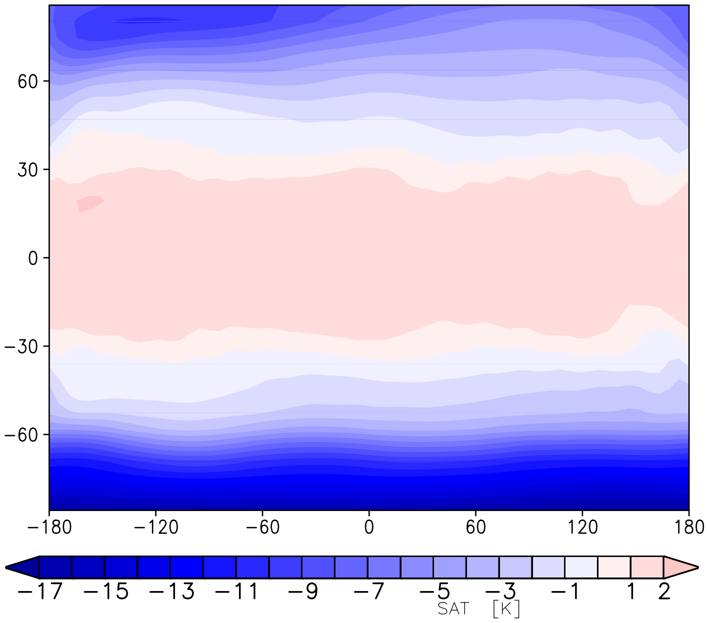

Figure 5.20: Surface air temperature differences between the *S-test* and *CO_2-test* climate states

5.7 Combined Effects

So far, the three different parameters have been analyzed separately. When adding the surface air temperature changes of the single effects, i.e. of:

1. decreasing CO_2,
2. opening of the *Drake Passage*, and
3. canceling seasonality

(adding the SAT differences shown in figures 5.16, 5.18, and 5.20) a picture very similar to the overall temperature change from *control* to *final* (figure 5.14) results.

SAT differences between the combined effect and the overall change from *control* to *final* are displayed in figure 5.22. At the north pole some non-linear effects occur, which might be connected to the sea ice cover that forms at high northern latitudes. Furthermore, there is a small area east of the *Drake Passage* opening where some (minor) SAT deviations occur, but everywhere else hardly any differences exist.

To explain the small temperature deviation at the southern polar continent, snowfall differences and differences in the snow depth change are displayed in figure 5.23. The differences between the combined effect of the three forcings (decreasing atmospheric CO_2, opening of the *Drake Passage*, and changing orbital parameters) and the overall transition from *control* to *final* are taken. Throughout the austral winter months, there are no significant discrepancies in the snowfall or in the snow depth change. The

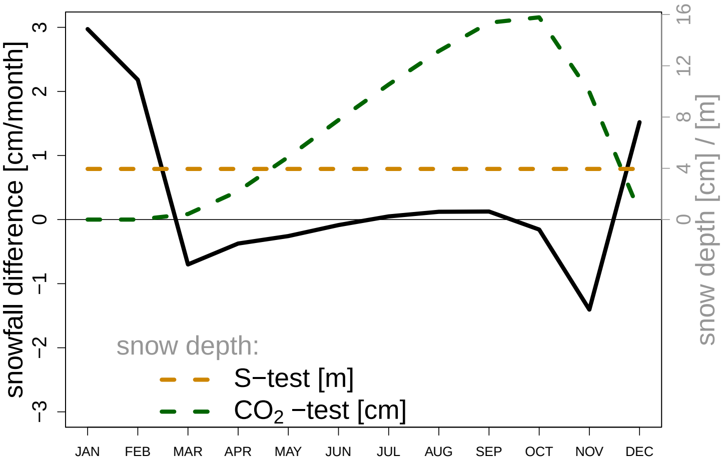

(a) snowfall and snow depth

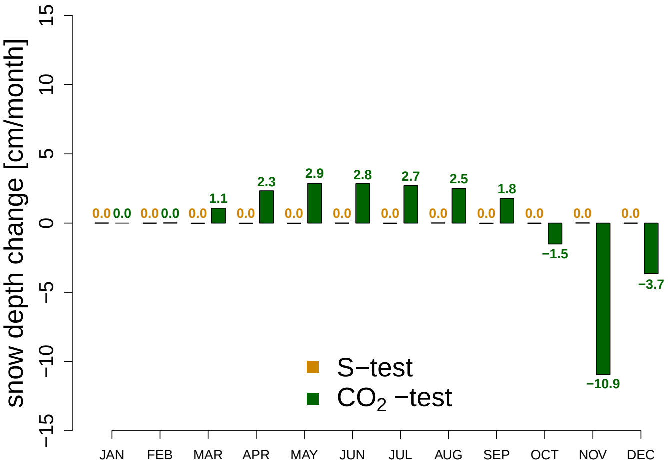

(b) snow depth change

Figure 5.21: Monthly mean snowfall differences, snow depth, and snow depth change for *S-test* and *CO_2-test* averaged over the continental area (all values are in water equivalent units, note the different units: the snow depth for *CO_2-test* in cm and for *S-test* in m)

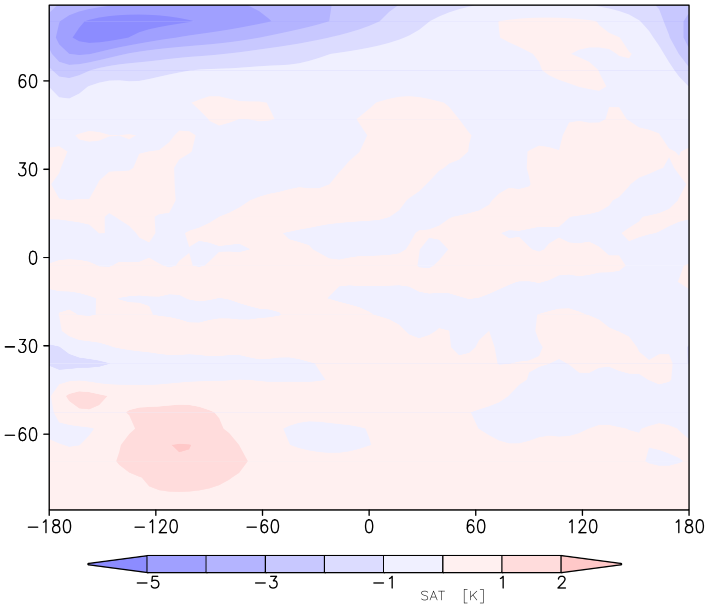

Figure 5.22: Surface air temperature differences: discrepancies between combined effect of atmospheric CO_2, opening of the *Drake Passage*, and the orbital parameters and the *final* simulation

snow depth change is also consistent (with both methods) during most of the warmer months and only shows some differences (still less than 2 cm per month) between October and December. However, in the snowfall greater deviations can be observed: between November and March there is clearly more snowfall (up to 1 cm per month) when the single effects are linearly superimposed in contrast to comparing the *final* climate directly to the *control* climate.

Still, the snow depths for both methods are constantly at 5 m (the model's limit) and surface air temperature differences are confined to a small region of the continent and amount to less than 2 K. Thus, the three different mechanisms cooling Antarctica can be linearly superimposed in the region of interest.

5.8 Summary and Discussion

During the Eocene–Oligocene transition the onset of the Antarctic glaciation was triggered. Here, coupled idealized simulations are presented to explore the roles of atmospheric CO_2 decrease, opening of sea gateways, and changing orbital parameters for this climate transition. An expanded aquaplanet, which includes a circular continent at the south pole and a meridional barrier in the ocean, is applied for the sensitivity experiments.

Comparing the respective simulations (*control* and *final*), it can be shown that the combined effects of decreasing CO_2, opening of the *Drake Passage*, and switching off the annual cycle can indeed trigger the onset of the Antarctic glaciation. This is doc-

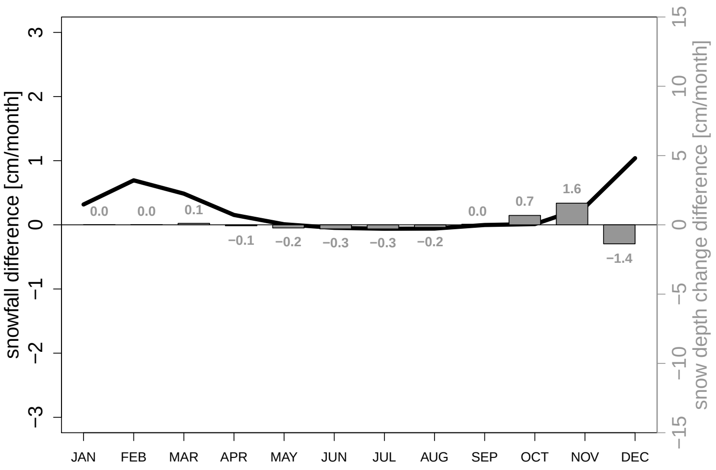

Figure 5.23: Differences in monthly mean snowfall and snow depth change averaged over the continental area: discrepancies between combined effect of atmospheric CO_2, opening of the *Drake Passage*, and the orbital parameters and the *final* simulation (all values are in water equivalent units)

umented, for example, by changes in temperature, snowfall (snow accumulation), and the meridional heat transport.

At the south pole the temperature decrease is by far the strongest, but the climate also slightly cools in the global mean. The surface air temperature over the continent decreases by almost 20 K between *control* and *final*. The simulated temperature reduction exceeds values from sedimentary records from the Eocene–Oligocene transition (see for example Zachos *et al.*, 2008). However, it is not expected that exact temperature changes are reproduced due to the degree of idealization.

A necessary prerequisite to build up the Antarctic Ice Sheet is annual snow accumulation. This is only the case in the *final* climate. In the *control* climate, there is a strong seasonal effect, which causes a melting period in the austral spring and summer months. Consequently, the snow depth alternates during the yearly cycle between a maximum of 15 cm in September and no snow cover between December and March.

The total poleward heat transport in the *final* climate exceeds the transport in the *control* simulation by far. Since the orbital parameters and the mean hemispheric albedo are altered during the transition, the concept of a constant total meridional energy transport (Stone, 1978) does not hold anymore. The ocean heat transport is very large in the northern hemisphere of the *final* climate. While peak values are located in the subtropics, a very strong OHT can still be observed at high latitudes. Furthermore, in the southern hemisphere of the *final* climate and in both hemispheres of the *control* climate, the OHT is relatively constant with values up to 1 PW. The OHT differs from present-day estimates (see for example Trenberth & Caron, 2001) as well as from the one seen in the simulation with an idealized *Drake Passage* by Enderton & Marshall (2009), which also peaks in the subtropics, but is already very weak poleward of the mid-latitudes.

To explore the relative importance of the individual forcings in setting the conditions for the Antarctic glaciation, three further sensitivity studies are analyzed. When only reducing atmospheric CO_2 concentrations and keeping all other parameters the same as in the *control* forcing (the *CO_2-test* simulation), the temperature decreases globally by approximately 2–3 K. The cooling is the strongest over the continent, which can mostly be attributed to the different heat capacities of ocean and land surfaces. The CO_2 effect explains only about 10 % of the overall cooling of the southern polar continent from *control* to *final* and can therefore not be considered the main forcing mechanism in the onset of the Antarctic glaciation. Furthermore, snow cover on the southern polar continent appears only seasonally because of summertime melting periods.

Most estimates of atmospheric CO_2 mixing ratios in the early Cenozoic range between 2× and 5× of the pre-industrial values and during the transition atmospheric CO_2 is believed to have dropped to nearly present-day values (Pagani *et al.*, 1999; Pearson & Palmer, 2000). The CO_2 level chosen here (1,000 ppm) is therefore a relatively high estimate of the mixing ratio before the transition to an Antarctic Ice Sheet. DeConto & Pollard (2003) analyze simulations with decreasing atmospheric CO_2 and find a threshold for the formation of an ice-cap between 3× and 2× CO_2 (pre-industrial). In contrast the results presented in this study, they identify declining atmospheric CO_2 as the main forcing for the Cenozoic climate change.

The sensitivity simulation *DP-test* explores the effect of the opening of the *Drake Passage* on the global climate and on the climate of the southern polar continent in particular. North of 30°S, the opening of the *Drake Passage* warms the climate and poleward the surface air temperature is reduced. The temperature decrease is the strongest in the southern ocean east of the *Drake Passage*, where circumpolar flow develops and the OHT is reduced. However, the temperature over the continent also declines by approximately 3–4 K. The cooling effect of the opening of the *Drake Passage* has approximately the same order of magnitude as the CO_2 reduction. Both alone are not sufficient to explain the massive temperature decrease from *control* to *final*, and even added together, the largest part of the cooling is still not accounted for. The opening of the *Drake Passage* is also not able to suppress the summer melting periods and to produce a stable snow cover all year long.

Cristini *et al.* (2012) present a sensitivity study aimed to understand if and how the opening of the Drake Passage served as a forcing for the Antarctic climate transition. In their simulations the SAT averaged over the Antarctic continent cools only by 0.4 K when the Drake Passage is opened, but they observe an additional growth of the AIS volume of about 20 % and conclude that the opening of the Drake Passage contributed substantially to the Antarctic glaciation. However, Cristini *et al.* do not modify atmospheric CO_2 concentrations or orbital parameters and, therefore, could not answer the question about the relative importance of these possible mechanisms.

When excluding the seasonal cycle by setting the orbital parameters to perpetual equinoctial conditions, there is no polar summer nor winter, i.e. at no time during the year the poles receive ample nor hardly any insolation. The incoming solar radiation at the poles is weak all year long, while the low latitudes receive more heating due to short wave radiation. In the simulation *S-test*, where the orbital parameters are set to perpetual equinoctial conditions (all other parameters remain the same), the global mean temperature cools by about 2 K, even though the tropics and subtropics experience an overall warming. This can be explained by the massive temperature decrease at high latitudes. Especially at the south pole over the continent, the air cools by over 15 K, which explains the largest part of the temperature reduction between *control* and *final*.

DeConto & Pollard (2003) also analyzed the role of orbital parameters and the opening of the *Drake Passage* for the onset of the Antarctic glaciation. While they conclude that the role of the *Drake Passage* is rather minor, they find that the orbital parameters do indeed affect the onset of the glaciation. Their threshold around 3× pre-industrial CO_2 can only establish a continental ice sheet if the orbital parameters favor cool austral summers. However, once the atmospheric CO_2 declines further, the AIS becomes almost insensitive to the orbital forcing.

In contrast to the studies by DeConto & Pollard and Cristini *et al.*, the set-up applied here does not include a model for land ice. The inclusion of a model for the AIS could have additional feedbacks, which are not included in these simulations. Today, the height of the Antarctic Ice Sheet exceeds 3,000 m over large areas (Lythe *et al.*, 2001). At this high elevation, there is a significant cooling effect caused by the uplift of air. This positive feedback (build-up of the AIS, higher elevation, uplift, additional cooling) is missing in our simulations since the idealized continent does not contain topographical features nor a model for land ice.

As the coupled model in the study presented here does not include an ice sheet model, only temperature and snow accumulation changes can be analyzed. However, these are the two most important parameters for the build-up of an ice sheet on the Antarctic continent. Since the temperature effect of the changing orbital parameters is about 5 times greater than the effect of declining CO_2 or the opening of the *Drake Passage* and snow accumulates constantly in the simulations without melting periods, the seasonal effect appears to be the main forcing for the onset of the Antarctic glaciation.

6 Conclusion

> *"Science never solves a problem without creating ten more."*
>
> — George Bernard Shaw

The purpose of this thesis is to analyze internally and externally forced climate variability under idealized conditions. A coupled atmosphere–ocean–sea ice general circulation model has been applied with various aquaplanet configurations to study different climate regimes. Aquaplanets can be very useful for understanding the climate in its most elemental form by reducing the complex Earth system to its basic governing processes.

The three questions asked in the introduction (chapter 1) cannot be conclusively answered in this study, however, the results contribute to a better understanding of the general problems addressed here:

1. *How do topographic boundaries define the circulation regime and the zonal mean climate state of atmosphere and ocean?*
2. *What kind of internally generated long-term variability mechanisms exist and what are their underlying physical processes?*
3. *Which processes are responsible for climate changes of the past, for example the onset of the Antarctic glaciation?*

6.1 Summary and Discussion

This thesis is divided into three parts (“Aquaplanets with Idealized Ocean Barriers” in chapter 3, “Low-frequency Climate Variability” in chapter 4, and “The Onset of the Antarctic Glaciation” in chapter 5). A detailed summary and discussion can be found at the end of each chapter and a brief recapitulation of the main results is given below.

The first part of the study mainly aims at analyzing how topographic boundaries in the ocean influence the circulation regime and, thus, the global climate. For that purpose the pure aquaplanet and expanded aquaplanets with idealized meridional ocean barriers are analyzed. The topographic features are located in the ocean only and do not protrude into the atmosphere.

The design of the meridional ocean barriers stepwise approximates scenarios occurring in reality. Besides the pure aquaplanet, a closed basin circulation is created in which afterward ocean gateways (like the isthmus of Panama and the Drake Passage) are inserted. A set-up with a second ocean basin resembles the arrangement of the Atlantic and Pacific Oceans of the present-day climate. The different aquaplanet configurations cover a wide spectrum of ocean circulation regimes and various climate states emerge:

- ***Aqua*** is a pure aquaplanet with an ocean of uniform depth and without any orographic barriers (which creates zonally and hemispherically symmetric boundary conditions). The ocean flow is predominantly zonal and the meridional overturning circulation (MOC) consists of two Ekman cells in each hemisphere with upwelling at the equator and Ekman pumping centered at 30°N/S. Because of the lack of zonal pressure gradients, mean meridional flow cannot be supported by geostrophy and Sverdrup balance is not possible. Even though there are no westerly boundary currents, the ocean heat transport (OHT) is relatively strong. Still, sea ice covers both poles and a pronounced meridional temperature gradient results. Since the strength of the Hadley circulation is related to the meridional temperature gradient (see for example Held & Hou, 1980), rather strong Hadley cells and a single intertropical convergence zone (ITCZ) develops.

- ***Ridge*** is an expanded aquaplanet with a meridional barrier in the ocean running from pole-to-pole and creating a closed ocean basin (with boundary conditions symmetric about the equator). The closed basin circulation allows zonal pressure gradients and, therefore, zonally integrated meridional flow is supported by geostrophy. A deep hemispherically symmetric MOC pattern results with sinking regions at both poles and upwelling at the equator. Instead of the predominantly zonal flow of *Aqua*, the horizontal ocean circulation consists of subtropical and subpolar gyres comparable to the ones found in the Atlantic or Pacific Ocean. These gyres contain westerly boundary currents and the OHT in lower and mid-latitudes is considerable. Both poles are covered with sea ice and a strong meridional temperature gradient leads to a zonal mean atmospheric circulation structure that is similar to *Aqua*.

- ***Panama*** is an expanded aquaplanet that contains a meridional ocean barrier like *Ridge*, but with a passage in the tropics (creating almost hemispherically symmetric boundary conditions). The MOC resembles the one of *Ridge*, but the lack of zonal pressure gradients in the tropics creates strong zonal flow at low latitudes. Pronounced equatorial upwelling leads to rather cool temperatures in low latitudes, but the OHT is very efficient and, thus, the poles are rather warm and (almost) ice-free. The meridional temperature gradient and, hence, the atmospheric circulation are reduced. Furthermore, hints for the formation of a double ITCZ regime can be found.

- ***Drake*** is an expanded aquaplanet with a meridional ocean barrier like *Ridge*, but leaving a passage in the southern ocean. An oceanic circulation pattern asymmetric about the equator develops with a strong circumpolar current in the southern ocean. The MOC consists of two shallow wind-driven cells and a clockwise interhemispheric circulation extending from deep sinking regions at the north pole southward to 60°S. The northward OHT is very strong while the southward OHT is highly decreased and in the southern ocean almost completely inhibited. Thus, the south pole is very cold with high sea ice cover, while the north pole is warm and ice-free. In the southern hemisphere the high equator-to-pole temperature gradient causes a very strong Hadley cell, while the atmospheric circulation in the northern hemisphere is reduced. A single ITCZ can be observed.

- ***DDrake*** is an expanded aquaplanet that contains two meridional barriers with passages in the southern ocean and, thus, two basins of different dimensions. On the global scale, the zonal mean circulation and the climate state are almost identical to the *Drake* set-up (with only one ocean barrier). However, the MOC in the small basin (*SB*) is characterized by two deep-reaching cells which are confined to higher latitudes and in the large basin (*LB*) there is a large cell stretching from the north pole to approximately 30°S. Furthermore, *SB* is warmer and saltier with an increased northward OHT.

In summary, the ocean circulation changes most drastically when going from *Aqua* to *Ridge*, i.e. when the ocean barrier allows Sverdrup balance and gyral flow. However, the global mean climate states of both set-ups closely resemble each other, including ocean heat transports that are of similar strength and structure and almost the same meridional temperature gradients develop with sea ice covered poles. Furthermore, it can be concluded that ocean gateways seem to play a crucial role for the global climate of the Earth. Not only the ocean circulation regime changes when the barrier contains a passage, but also the OHT is dramatically altered and, hence, the meridional temperature distributions and the sea ice cover is greatly affected by an ocean gateway.

The ocean circulation regimes and zonal mean climate states of *Aqua*, *Ridge*, *Panama*, *Drake*, and *DDrake* stepwise approximate the present-day climate of the Earth. However, before applying the expanded aquaplanet in a set-up that is closer to reality, the variability of the pure aquaplanet (*Aqua*) is analyzed in more detail.

This part of the study aims at studying internally generated long-term variability mechanisms in the climate system and their underlying physical processes. A very dominant low-frequency oscillation between colder and warmer climate states can be observed. While this aquaplanet climate oscillation cannot be transferred directly to our past or present-day climate, a thorough and detailed analysis of this purely internally generated climate variability may contribute to a better understanding of the variability of the climate system on very long time scales.

The coupled system oscillates with a period of approximately 700 years and all compartments of the aquaplanet are affected, i.e. atmosphere, ocean, and sea ice. In both hemispheres the low-frequency oscillation is in phase.

The long-term mean state of the aquaplanet has been introduced in the discussion of the zonal mean climate of *Aqua*, however, a stationary state is not achieved. Thus, averages over extreme periods are taken and *cold* and *warm* states are analyzed and compared. Furthermore, two different time series analysis techniques are applied to obtain a detailed picture of the low-frequency oscillation. At first, empirical orthogonal function (EOF) analyses are applied to individual atmospheric and oceanic fields. While EOF analysis is a suitable method to reveal dominant modes of variability, it has to be interpreted with caution because it is a mathematical construct that finds orthogonal patterns which maximize explained variance, but does not necessarily find dynamically significant components. Thus, a second method is used to complement the EOF analysis: a composite life cycle of the low-frequency oscillation is computed to find relations and feedbacks between atmospheric and oceanic fields. It turns out that the results of the EOF analysis as well as the *cold* and *warm* mean states are in accordance with the composite life cycle.

The meridional overturning circulation of the ocean is chosen as a representative variable. Main characteristics of the life cycle are presented when PC 1 of the MOC is at its minimum, at its zero-crossing and increasing, at its maximum, and at its zero-crossing and decreasing:

- **Minimum:** The minimum MOC state is characterized by warmer temperatures and ice-free poles. The atmospheric and oceanic circulation are both weaker and subtropical jets are closer to the equator. The air above the poles contains more moisture and the polar ocean has a higher salinity concentration. The OHT is stronger and warm temperature anomalies can be observed in the upper and middle ocean. Colder temperatures are located at the sea floor and at the poles.

- **Increasing:** The transition from a weak to a strong MOC phase features a climate state which is close to the climatological average and only small deviations from the mean occur. The sea surface temperature (SST) is colder at the poles, but there is still no sea ice. The salinity in the polar ocean is higher than usual and the OHT is greater than in the mean. Surface ocean currents are stronger at high latitudes and weaker in the tropics. The cold temperature anomalies in the ocean have spread from the sea floor upward so that the entire ocean shows a negative temperature anomaly, except for an area in the upper equatorial ocean which is warmer than usual.

- **Maximum:** During the maximum state of the MOC, the deviations from the climatological average are reversed compared to the minimum state: The poles are cold and covered with sea ice. Both atmospheric and oceanic circulation are stronger and the subtropical jets are displaced poleward. The air above the poles is very dry and the polar oceans show fresh water anomalies. The upper and middle ocean is colder, while the deep ocean and the polar oceans are warmer. If sea ice covers the poles, the OHT is almost zero below the ice cover, however, the atmospheric transport becomes stronger with the increased meridional temperature gradient.

- **Decreasing:** Approximately 300 years after its maximum, the MOC has declined to its climatological average. During this phase deviations from the mean are very small with a weaker circulation and a warmer atmosphere that contains more moisture. However, sea ice still covers the poles and below the sea ice the ocean is fresher than usual. Warmer waters have spread almost across the entire ocean. Only at the poles, directly underneath the sea ice, as well as in an area at the upper tropical ocean there are still colder temperatures.

The last part of this work aims at identifying processes that may be responsible for climate changes of the past, in particular for the onset of the Antarctic glaciation during the Eocene–Oligocene transition (approximately 34 mio. years ago).

There are three main hypotheses to explain the onset of the Antarctic glaciation: The classical concept is based on the opening of ocean gateways, i.e. the Drake Passage between Antarctica and South America and the Tasman Passage between Antarctica and Australia. The opening caused the formation of the Antarctic Circumpolar Current (ACC), which dramatically decreased poleward ocean heat transport and, as a result, thermally isolated Antarctica. Declining greenhouse gases could also have triggered the build-up of the Antarctic Ice Sheet (AIS). Atmospheric CO_2 concentrations were very high and started to decrease during the transition, which caused temperatures to decline. Another possible forcing for the onset of the Antarctic glaciation is a change in orbital parameters, which favor cool austral summers, hinder the melting of summer snow and, thus, create an ideal environment for the formation of the AIS.

Sensitivity simulations are conducted to test these three hypotheses and their roles for the onset of the Antarctic glaciation. The simulations are carried out under idealized conditions to focus on the essentials: The opening of the *Drake Passage* is modeled with an expanded aquaplanet, which includes a circular continent at the south pole and a meridional ocean barrier with and without a passage in the southern ocean. Furthermore, atmospheric CO_2 and orbital parameters are varied.

When comparing the simulations that represent the state before and after the transition, i.e. the *control* and *final* simulation, it can be shown that the onset of the Antarctic glaciation indeed might have been triggered by these three forcings. The coupled model does not include a model for land ice, but conditions for an AIS are created: Surface air temperatures (SAT) are drastically reduced over the continental area and snow accumulates all year long.

Between the *control* and *final* set-up, all three forcing mechanisms differ: atmospheric CO_2 is reduced, the *Drake Passage* is opened, and the seasonal cycle is switched off. To determine which of these forcings has the greatest impact on the global climate and on the climate transition of the southern polar continent, several sensitivity experiments are analyzed separately:

- **Declining atmospheric CO_2:** The CO_2 decrease has a great cooling effect on the global scale. The climate with higher CO_2 values (*control*) is characterized by warm temperatures, shallow meridional temperature gradients, and a weak circulation in the atmosphere. When comparing this to a climate state with the same parameters but lower CO_2 values (*CO_2-test*), the temperatures are globally reduced, but the reduction over the continent (2–3 K) is not strong enough to explain the huge temperature reduction from *control* to *final* (up to 20 K). Most notably, there is still a pronounced melting period which causes completely snow-free summer months on the southern polar continent.

- **Opening of the *Drake Passage*:** The oceanic circulation is most strongly affected by the opening of the *Drake Passage*. When the southern ocean gateway opens up, a very strong circumpolar current develops. As a consequence, the southward OHT is almost completely inhibited in the area of the *Drake Passage* and the southern ocean becomes thermally isolated and very cold. Thus, the temperatures above the southern continent indeed decline when the *Drake Passage* is opened (while the latitudes northward of the passage are warmed). However, when only the *Drake Passage* is opened and all other forcings remain the same (*DP-test*), the temperatures over the continent only reduce by approximately 2–3 K, which explains only about 10 % of the overall cooling from *control* to *final*. Furthermore, the melting period causing the snow-free summer months is still present.

- **Changing orbital parameters:** Under perpetual equinoctial conditions the low latitudes receive more insolation and experience an overall warming, while the poles become much colder when seasons are excluded. Under present-day seasonality, the poles receive ample insolation during polar summers and hardly/no insolation during polar winters. Thus, the high latitudes are more strongly affected by the change in orbital parameters than low and mid-latitudes. When the seasonal cycle is suppressed (and all other parameters remain the same, *S-test*), the temperatures over the southern polar continent decline by up to 15 K. Hence, changing orbital parameters explain the greatest part of the massive temperature reduction from the *control* to the *final* climate state. Because of the missing seasonality there is no summertime melting period and snow accumulates all year long.

In summary, all three forcings cool the climate of the southern polar continent and may have contributed to the build-up of the AIS. However, even though declining atmospheric CO_2 and the opening of the *Drake Passage* reduce the temperatures over the southern continent, the cooling caused by the changing orbital parameters is significantly stronger. Furthermore, the summertime melting period which prevents the constant accumulation of snow is only suppressed when orbital parameters are altered. While all three processes play a role in the Antarctic climate transition, it can be concluded that the changing orbital parameters have the greatest effect. When the seasonal cycle is suppressed, temperatures on the southern polar continent cool dramatically and snow accumulates persistently.

When comparing the results of this study to previous work on aquaplanets with coupled atmosphere–ocean models (for example Smith *et al.*, 2006; Marshall *et al.*, 2007; Enderton & Marshall, 2009; Ferreira *et al.*, 2010, 2011), they agree relatively well. There are some deviations that are mostly related to sea ice and the corresponding meridional temperature gradient. Furthermore, the OHT is rather large in this study compared to others. However, the circulation regimes are very similar when barriers are introduced into the aquaplanet ocean.

The low-frequency oscillation, which is found in the pure aquaplanet, has not been documented before in connection with aquaplanet experiments. In contrast to oscillating climate phases, either cold or warm solutions or multiple stable states have been found in previous aquaplanet studies conducted with coupled models (Smith *et al.*; Marshall *et al.*; Ferreira *et al.*), which resemble the *cold* and *warm* states defined in this study.

There are many previous modeling studies, which deal with the onset of the Antarctic glaciation, however, these usually focus on the opening of the Drake Passage only (e.g. Mikolajewicz & Maier-Reimer, 1993; Toggweiler & Bjornsson, 2000; Sijp & England, 2004; Cristini *et al.*, 2012). While most agree that temperatures in the southern high latitudes indeed declined when the Drake Passage opened up, the question, whether the cooling was strong enough to have triggered the onset of the glaciation of Antarctica, remains to be answered.

Sensitivity experiments including all three forcings (atmospheric CO_2, the opening of the Drake Passage, and changing orbital parameters) are also conducted by, for example, DeConto & Pollard (2003). In contrast to the present study, they found declining greenhouse gases to be the greatest forcing for the Antarctic climate change. However, a direct comparison between the results proves to be difficult, since DeConto & Pollard apply realistic topographic boundary conditions and reduce atmospheric CO_2 in multiple (smaller) steps. Furthermore, they only reduce the seasonal cycle, instead of completely excluding seasonality.

An idealized land–sea configuration can be very useful for reducing the climate system to its most elemental features and, thus, help to identify the main characteristics of the governing processes. Hence, such a set-up is applied to study the onset of the Antarctic glaciation. However, while the idealized model contains the same basic processes as more complex systems, one has to be careful when interpreting the results and relating them to reality.

The total meridional heat transport can be subdivided into the transport conducted by the atmosphere and the ocean heat transport (OHT). The various circulation regimes which are presented in this study offer a good test case to verify the hypothesis about the constancy of the total meridional energy transport (Bjerknes, 1964; Stone, 1978). As explained in chapter 1, the sum of the oceanic and atmospheric meridional energy transports should not change as long as the size of the Earth, the rotation rate, the axis tilt, the solar constant, and the mean hemispheric albedo remain constant. These external factors have been identified by Stone (1978), who suggests that this concept should hold even under extreme conditions and for scenarios like the idealized land–sea configurations applied in this study.

In fact, all aquaplanets with and without idealized topographic features show almost exactly the same total poleward heat transport. The small differences that do occur are related to the mean hemispheric albedo, which is the only parameter that varies because of changes in the sea ice cover. However, the sensitivity experiments studying the onset of the Antarctic glaciation are an exception. Between the *control* and *final* climate states great differences in the total poleward heat transports can be observed, which are caused by the changing orbital parameters: The axis tilt of the Earth deviates strongly between simulations with and without a seasonal cycle. Furthermore, the mean hemispheric albedo increases significantly after the climate transition (even in this study without a model for land ice, since the snow cover increases substantially on the southern polar continent).

The structure of the total energy transport of the pure aquaplanet is not only very similar to other aquaplanet simulations (e.g. Smith *et al.*, Marshall *et al.*), but also to observations (see for example Peixoto & Oort, 1992). When comparing the total energy transports of the aquaplanets with ocean barriers to the results of Enderton & Marshall, the general structure is also the same but the absolute values differ, just as for the pure aquaplanet. This is not surprising, since the model set-ups of Smith *et al.*, Marshall *et al.*, and Enderton & Marshall include a seasonal cycle and the axis tilt is changed.

Czaja & Marshall (2006) and Marshall *et al.* (2007) note that the partition of heat transport between atmosphere and ocean in the aquaplanet simulation is remarkably similar to that of the present-day climate: the atmosphere dominates in mid- to high latitudes and the ocean dominates in the tropics. However, while the total energy transports are mostly consistent with other studies (and, thus, with the theory of Bjerknes 1964 and Stone 1978), the partition into atmospheric and oceanic transports may deviate.

The ocean heat transport typically peaks at 2 PW around 20°N/S, which can be observed in this study and in previous aquaplanet simulations. However, important features of the OHT differ from the observed OHT as well as from previous studies by Ferreira *et al.* or Enderton & Marshall. In this study, there still is a very strong OHT of over 1 PW up to approximately 75°N/S, while the OHT in the aquaplanet of Ferreira *et al.* is already very weak at 60°N/S. Furthermore, the region of peak OHT convergence is located poleward of 70°N/S, while the maximum convergence in observations and in the aquaplanet of Ferreira *et al.* is located in the mid-latitudes. Consequently, the OHT carries much more heat into high latitudes, where the oceanic transport even exceeds the atmospheric energy transport during *warm* climates.

In a region of steep temperature gradients and isopycnal slopes, the model overestimates horizontal, diapycnal fluxes, and therefore permits a large heat transport into high latitudes. Much of the ocean heat transport is therefore diffusive, rather than advective. Even though the ocean model is very diffusive, it has been successfully employed in numerous studies (see for example Mikolajewicz & Maier-Reimer, 1990; Prange *et al.*, 2002; Lohmann, 2003).

When comparing results, it has to be kept in mind that not only very different general circulation models but also other model set-ups are applied. Most notably, Smith *et al.*, Marshall *et al.*, Enderton & Marshall, and Ferreira *et al.* all set orbital parameters to present-day values, in contrast to this study, where perpetual equinoctial conditions are used in most of the simulations. This might seriously influence the results, since in the absence of polar winter or summer, the poles never receive ample nor hardly any insolation. Instead, the incoming solar radiation at high latitudes is weak all year long, while the low latitudes receive more heating due to short wave radiation. In particular differences in the sea ice cover could be caused by deviations in the set-up of the orbital parameters.

Aquaplanets are applied for studying the fundamental processes of the climate system and in particular the main characteristics of the zonal mean climate of the Earth are hardly affected by the presence of land masses. However, it is emphasized that aquaplanets (with or without idealized topographical barriers in the ocean) are only a crude approximation of the Earth and are not meant to produce very "realistic" climate simulations. This has to be kept in mind when interpreting the results of this study.

6.2 Outlook

In the first part of this thesis, the pure aquaplanet and four different cases with idealized meridional ocean barriers are studied. There are, of course, many more possible set-ups that create interesting scenarios and which might bring the system stepwise closer to reality. In the analysis of Antarctica's glaciation an idealized continent is introduced into the system. This concept could be expanded by exchanging the meridional barrier for a continent, possibly with an idealized form: Comparing a rectangular continent to a triangular one, additionally allows to study how the orientation of the boundary influences the ocean circulation.

A logical next step would be to repeat the five simulations from the first part of the study with the inclusion of a seasonal cycle. The adjustment of the orbital parameters would improve the comparability of the results when discussing them in the context of previous work (Smith *et al.*, 2006; Marshall *et al.*, 2007; Enderton & Marshall, 2009; Ferreira *et al.*, 2010, 2011). Furthermore, the results might be better comparable to observations.

For the pure aquaplanet, a further simulation including a seasonal cycle is of special interest when analyzing the low-frequency climate oscillation. Sea ice is a key feature for the oscillation and it is very possible that the absence of the seasonal cycle alters the behavior of sea ice. The question is, whether the freezing period in the winter time is strong enough to compensate summer time melting, so that stable sea ice caps are sustained for several centuries during the *cold* climate states. Whether the low-frequency oscillation still takes place when seasonal variations are included and how the period is affected, has to be determined by further simulations.

Furthermore, when interpreting this oscillation, one has to keep in mind that with the seasonal cycle of the solar forcing a source of potential destabilizing variability is missing.

The total ocean volume in the aquaplanet is substantially larger than the one found on Earth, since the aquaplanet ocean has a uniform depth of 5,500 m, while the ocean of the Earth has an average depth of 3,682.2 m (after Charette & Smith, 2010) and includes continents. This affects the heat capacity and might influence the time scales for warming and cooling and therefore the period of the oscillation. Further sensitivity studies with different ocean depths are called for to determine the extent of this effect.

The missing model for land ice in the set-up presents a caveat on the results for the study on the Antarctic glaciation. While surface air temperature and snow are helpful representative variables for the onset and growth of a massive ice sheet, some feedbacks are missing. The inclusion of a model for the AIS would, for example, consider elevation effects: the build-up of an ice sheet creates high glaciers and the air above Antarctica is lifted up and experiences an additional cooling. Further simulations with a fully coupled model including a model for the AIS are needed to challenge or confirm the results of this study.

Furthermore, the simulated temperature reduction exceeds values from sedimentary records from the Eocene–Oligocene transition (see for example Zachos *et al.*, 2008). It is not expected that exact temperature changes are reproduced due to the degree of idealization, but further sensitivity studies could complement this set of experiments.

A more detailed analysis of the role of the topographical set-up could be conducted by a stepwise transition to a more realistic continental distribution, which could include a passage in the tropics (representing the isthmus of Panama), a second oceanic barrier with a passage in the southern ocean (representing the Tasman Passage), topographical features on the ocean floor, and more (idealized) continents.

The role of CO_2 could be further analyzed following the line of DeConto & Pollard (2003) by reducing the atmospheric CO_2 level in multiple (smaller) steps. Transient CO_2 changes could also affect the results (see for example Bordi *et al.*, 2012).

Since in this work, seasonal effects have been identified as the main controlling mechanism for the Antarctic climate transition, further sensitivity studies with smaller changes in the orbital parameters would be a natural next step.

Appendix

Appendix A: List of Symbols

Symbol	Description	Value
a	radius of the earth	6.37×10^{6} m
c_o	specific heat of ocean water	4,187 J/kg K
c_p	atmospheric specific heat at constant pressure	1,004 J/kg K
c_v	atmospheric specific heat at constant volume	717 J/kg K
D	horizontal divergence	
d	dry static energy	
e	moist static energy	
E	kinetic energy per unit mass	
E_{srf}	energy budget at the surface	
E_{TOA}	energy budget at the TOA	
E_{total}	total atmospheric energy budget	
f	Coriolis parameter	$\sim10^{-4}\,\mathrm{s}^{-1}$
g	gravitational acceleration	$9.81\,\mathrm{m/s}^2$
H	mean depth of the ocean	5,500 m (*Aqua*)
J	diabatic heating per unit mass	
l	latent energy	
L	latent heat of vaporisation or condensation	2.5×10^{6} J/kg K
$LH^{\uparrow}_{srf}$	upward latent heat flux at the surface	
$LW^{\uparrow}_{srf}$	upward longwave radiation at the surface	
$LW^{\uparrow}_{TOA}$	upward longwave radiation at the TOA	
p	pressure (vertical coordinate in p-system)	
p_s	surface pressure	
q	specific humidity	
$SH^{\uparrow}_{srf}$	upward sensible heat flux at the surface	
S	salinity	
$SW^{\downarrow}_{srf}$	downward shortwave radiation at the surface	
$SW^{\downarrow}_{TOA}$	downward shortwave radiation at the TOA	
T	temperature	

Continued on next page

List of Symbols – continued from previous page

Symbol	**Description**	**Value**
T_0	temperature on a reference level	
t	time	
u	zonal velocity (atmosphere or ocean)	
v	meridional velocity (atmosphere or ocean)	
w	vertical velocity (atmosphere or ocean, in z-system)	
x	horizontal coordinate in latitudinal direction	
z	height (vertical coordinate in z-system)	
ζ	sea surface elevation	
θ	potential temperature	
κ	adiabatic exponent/coefficient	
λ	longitude	$-180° \leq \lambda \leq 180°$
μ	latitudinal coordinate	$\mu = \sin\varphi$
ξ	vorticity	
ρ	density of air	
ρ_0	density on a reference level	
ρ_w	density of sea water	$\sim 1{,}030\,\mathrm{kg/m^3}$
σ	vertical coordinate (in σ-system)	$\sigma = {}^{p}/_{p_s}$
$\dot{\sigma}$	vertical velocity (in σ-system)	$\dot{\sigma} = {}^{d\sigma}/_{dt}$
τ	wind stress	
ϕ	geopotential	
φ	latitude	$-90° \leq \varphi \leq 90°$
ω	vertical velocity (in p-system)	$\omega = {}^{dp}/_{dt}$

Appendix B: List of Abbreviations

Abbreviation	**Denotation**
ACC	Antarctic Circumpolar Current
AGCM	Atmospheric General Circulation Model
AIS	Antarctic Ice Sheet
AMO	Atlantic Multidecadal Oscillation
AOGCM	Atmosphere–Ocean General Circulation Model
EBM	Energy Balance Model
ENSO	El Niño–Southern Oscillation
EOF	Empirical Orthogonal Function
ESM	Earth System Model
D/O	Dansgaard–Oeschger events
GCM	General Circulation Model
GUI	Graphical User Interface
ITCZ	InterTropical Convergence Zone
LSG	Large Scale Geostrophic
MIC	Model of Intermediate Complexity
MOC	Meridional of Overturning Circulation
N	North
OGCM	Ocean General Circulation Model
OHT	Ocean Heat Transport
PC	Principal Component
PCA	Principal Component Analysis
PFZ	Polar Frontal Zone
PlaSim	Planet Simulator
PUMA	Portable University Model of the Atmosphere
QBO	Quasi-Biennal Oscillation
S	South

Continued on next page

List of Abbreviations – continued from previous page

Abbreviation	**Denotation**
SAT	Surface Air Temperature
SST	Sea Surface Temperature
THC	ThermoHaline Circulation
TOA	Top Of Atmosphere

Appendix C: List of Figures

2 The Coupled Model **11**

3 Aquaplanets with Idealized Ocean Barriers **23**

Appendix D: Statistical Methods

A short overview of the statistical methods applied in this work is given here. While zonal averaging and vertically integrating is used throughout the three parts of the study (chapters 3 to 5), the moving average, the EOF analysis, and lead–lag correlations are applied in chapter 4 only. The variales used here are explained in appendix A.

1 Averaging

Since different climate regimes and climate transitions on long time scales are of interest, time averages of the atmospheric and oceanic fields taken. Furthermore, the zonal mean state of the climate is analyzed. Vertical integrals are mostly applied when dealing with atmospheric and oceanic transports (see appendix E).

1.1 Zonal Mean and Time Average

The seasonal cycle is removed from the model set-ups for most of the experiments. Even though, random intra- (and inter-) annual variability is still expected. A time average of a scalar quantity A is denoted $\overline{A}$ and defined after James (1995) in equation (D.1).

The boundary conditions of the aquaplanet are zonally uniform and, therefore, zonal variations are random and stationary eddies are negligibly small. However, there are still zonal variations and, moreover, the boundary conditions of expanded aquaplanets which include topographical constraints on the ocean circulation are not zonally symmetric. The zonal mean of atmospheric or oceanic fields is often of interest. The zonal average of a scalar quantity A is denoted $[A]$ and defined after James (1995) in equation (D.2).

$$\overline{A} = \frac{1}{\tau} \int_{0}^{\tau} A \; dt \tag{D.1}$$

$$[A] = \frac{1}{2\pi} \int_0^{2\pi} A \, d\lambda \tag{D.2}$$

The transient parts (A') of a quantity A are deviations from the time mean and the zonal asymmetries (A^*) are deviations from the zonal mean, as displayed in equations (D.3) and (D.4).

$$A' = A - \overline{A} \tag{D.3}$$

$$A^* = A - [A] \tag{D.4}$$

1.2 Vertical Average

The vertical integral of a quantity A is denoted $\{A\}$. It has to be differentiated between taking a vertical integral in the atmosphere or in the ocean, because of the different physical properties of air and sea water.

Vertical Averaging in the Atmosphere

The mass weighted integral of a quantity A is calculated as the vertical integral over the mass of the atmosphere from the bottom (at $z = 0$, $p = p_s$, or $\sigma = 1$) to the top (at $z = \infty$, $p = 0$, or $\sigma = 0$). Using the hydrostatic relation (equation D.5), the integration in the z-coordinate system can be converted into the p- or the σ-system, as shown in equation (D.6).

$$\rho dz = -\frac{dp}{g} \qquad = -\frac{p_s}{g} d\sigma \tag{D.5}$$

$$\{A\} = \int_0^{\infty} \rho A \, dz = -\frac{1}{g} \int_{p_s}^{0} A \, dp = -\frac{p_s}{g} \int_1^0 A \, d\sigma = \frac{p_s}{g} \int_0^1 A \, d\sigma \tag{D.6}$$

Vertical Averaging in the Ocean

The near-incompressibility of sea water can be taken advantage of when taking a vertical average in the ocean, as displayed in equation (D.7).

$$\{A\} = \frac{1}{H} \int_{-H}^{0} A \, dz \tag{D.7}$$

2 Moving Average

A moving average (or running mean) is applied to filter high-frequency noise from a time series. The running mean at a time t takes an equal number of time steps before and after t into consideration. In this study a 101-year running mean is calculated following equation (D.8).

$$\overline{x}\left(t\right)=\frac{x\left(t-50\right)+\cdots+x\left(t-1\right)+x\left(t\right)+x\left(t+1\right)+\cdots+x\left(t+50\right)}{101} \tag{D.8}$$

3 EOFs – Empirical Orthogonal Functions

EOFs are a multivariate analysis technique to derive the dominant patterns of variability from a statistical field. Furthermore, an EOF analysis may significantly reduce the amount of data while still representing a high fraction of variance from the original data set. If there are substantial correlations among the variables in the original set, the data compression is most effective.

Principal Component Analysis (PCA) was introduced by Pearson (1901) and by Hotelling (1935). In meteorology, where PCA is called empirical orthogonal function (EOF) analysis, the method was first adopted by Lorenz (1956). A short introduction into the concept of EOF analysis is given here (mostly following von Storch & Zwiers, 1999), however, more detailed explanations can be found, for example, in von Storch & Zwiers (1999), in Schönwiese (2006), or in Wilks (2006).

EOFs of an m-dimensional random vector $\overrightarrow{\boldsymbol{X}}$ (with a mean of $\overrightarrow{\mu}=0$) are calculated as followed: The first “pattern” $\overrightarrow{e}^1$ (EOF 1) with the vector norm $\left\|\overrightarrow{e}^1\right\|=1$ has to be found, so that ϵ_1 in equation (D.9) is minimized. It can be shown that ϵ_1 is minimized when $\overrightarrow{e}^1$ is an eigenvector of $\boldsymbol{\Sigma}$, the covariance matrix of $\overrightarrow{\boldsymbol{X}}$ with its largest eigenvalue λ_1.

$$\epsilon_1=\varepsilon\left(\left\|\overrightarrow{\boldsymbol{X}}-\left\langle\overrightarrow{\boldsymbol{X}},\overrightarrow{e}^1\right\rangle\overrightarrow{e}^1\right\|^2\right)=\mathrm{Var}\left(\overrightarrow{\boldsymbol{X}}\right)-\mathrm{Var}\left(\left\langle\overrightarrow{\boldsymbol{X}},\overrightarrow{e}^1\right\rangle\right) \tag{D.9}$$

The next EOF, $\overrightarrow{e}^2$, which minimizes equation (D.10), is the eigenvector of $\boldsymbol{\Sigma}$ that belongs to the second largest eigenvalue λ_2. Since eigenvectors of a Hermitian matrix are orthogonal to one another, the first and second pattern (EOF 1 and EOF 2) are also orthogonal to each other.

$$\epsilon_2=\varepsilon\left(\left\|\left(\overrightarrow{\boldsymbol{X}}-\left\langle\overrightarrow{\boldsymbol{X}},\overrightarrow{e}^1\right\rangle\overrightarrow{e}^1\right)-\left\langle\overrightarrow{\boldsymbol{X}},\overrightarrow{e}^2\right\rangle\overrightarrow{e}^2\right\|^2\right) \tag{D.10}$$

This concept can be expanded to higher order EOFs. The total variance of the original m-dimensional vector $\overrightarrow{\boldsymbol{X}}$ is broken in to m components. The contribution of the k^{th} component to the total variance is the value of the k^{th} eigenvalue λ_k. The fraction of the total variance that is represented by the k^{th} pattern (EOF k) is the according eigenvalue devided by the sum of all eigenvalues: ${}^{\lambda_k}/\sum\limits_j\lambda_j$.

The first few EOFs often represent the vast majority of the variance of $\overrightarrow{\boldsymbol{X}}$ and, thus, not only the amount of data can be diminished but also the description of the field $\overrightarrow{\boldsymbol{X}}$ can be reduced to its most dominant variability patterns. However, while the first EOF can often be associated with a known physical process, the second EOF must be orthogonal to the first. Since climate processes are not necessarily orthogonal to one another, higher order EOFs may not be as easily related to a dynamical structure.

4 Lead–Lag Correlations

Time series of two variables a and b may be correlated with each other. The inclusion of a time lag τ is applied to find the point the correlation between the two variables is highest (it does not necessarily have to be at zero-lag). After Schönwiese (2006), the cross-correlation function r_C for two time series containing n time steps at a lag τ is calculated as described in equation (D.11):

$$r_C\left(\tau\right) = \frac{\sum\limits_{i=1}^{n-\tau} a_i \; b_{i+\tau}}{\sqrt{\sum\limits_{i=1}^{n-\tau} a_i^2 \sum\limits_{i=1+\tau}^{n} b_i^2}} \tag{D.11}$$

with

$\tau = 0, 1, \ldots, M < n$

$-1 \leq r_C \leq +1$

Appendix E: Meridional Transport of Energy

Energy needs to be transported from the low latitudes, a region of net energy surplus, to the high latitudes, which are characterized by a net energy deficit. Atmosphere and ocean conduct the energy transport to maintain equilibrium in the climate system.

1 Atmospheric Energy Transport

The meridional transport of energy in the atmosphere is decomposed into transport of dry static and latent energy. Furthermore, it can be subdivided into transport conducted by the mean circulation, the transient eddies, and the stationary eddies.

As explained, for example, by Peixoto & Oort (1992), energy is stored in the atmosphere in form of internal energy, potential energy, latent heat, and kinetic energy (see equation E.1). Global annual mean observations (Peixoto & Oort, 1992, p. 320) give the fractional parts of the different types of energy. Internal energy (70.4 %), potential energy (27.1 %), and latent energy (2.5 %) are the most important parts. Kinetic energy (0.05 %) can be neglected in this calculation.

$$\underbrace{energy}_{\text{total energy}} = \underbrace{c_v T}_{\text{internal energy}} + \underbrace{gz}_{\text{potential energy}} + \underbrace{Lq}_{\text{latent energy}} + \underbrace{\frac{1}{2}\left(u^2+v^2\right)}_{\text{kinetic energy}} \tag{E.1}$$

To calculate the zonal mean, time averaged, and vertically integrated meridional transport of energy in the atmosphere, the moist static energy e (equation E.2) needs to be multiplied by the meridional velocity v. The integral over all vertical σ-levels and the zonal and time average have to be taken (equation E.3). The decomposition of the moist static energy of the atmosphere, e, into dry static energy, d, and latent energy, l, is displayed in equations (E.2) to (E.4).

$$\underbrace{e}_{\text{moist static energy}} = \underbrace{c_p T + gz}_{\text{dry static energy}} + \underbrace{Lq}_{\text{latent energy}} \tag{E.2}$$

$$\overline{\left[\frac{p_s}{g}\int_0^1 v\cdot e\ d\sigma\right]} = \overline{\left[\frac{p_s}{g}\int_0^1 v\cdot\left(c_pT+gz+Lq\right)\ d\sigma\right]} \tag{E.3}$$

$$\begin{aligned}\overline{\left[\frac{p_s}{g}\int_0^1 v\cdot e\ d\sigma\right]} &= \overline{\left[\frac{p_s}{g}\int_0^1 v\cdot\left(d+l\right)\ d\sigma\right]}\\ &= \overline{\left[\frac{p_s}{g}\int_0^1 \left(v\cdot d\right)\ d\sigma\right]} + \overline{\left[\frac{p_s}{g}\int_0^1 \left(v\cdot l\right)\ d\sigma\right]}\end{aligned} \tag{E.4}$$

Atmospheric energy is transported by the mean circulation, transient eddies, and stationary eddies. The decomposition is explained in the following. Averaging and the deviations from time and zonal averages follow the methods explained in appendix D.

First, the moist static energy, e, is multiplied by the surface pressure, p_s, which yields a density of energy, E (equation E.5). v and E are split into time mean and transient parts (equation E.6) and the multiplication $(v\cdot E)$ is carried out (equation E.7). Since the time average of the atmospheric transport is of interest, the mixed terms, $\overline{v}E'$ and $v'\overline{E}$, can be neglected. The time averaged meridional wind $(\overline{v})$ and atmospheric energy $(\overline{E})$ from equation (E.7) are further decomposed into zonal mean and stationary eddy parts (equation E.8), which leads to the relation in equation (E.9).

$$E = p_s\cdot e \tag{E.5}$$

$$\begin{aligned} v &= \overline{v}+v'\\ E &= \overline{E}+E'\end{aligned} \tag{E.6}$$

$$vE = \overline{v}\overline{E}+\overline{v}E'+v'\overline{E}+v'E' \tag{E.7}$$

$$\begin{aligned}\overline{v} &= [\overline{v}]+\overline{v}^*\\ \overline{E} &= \left[\overline{E}\right]+\overline{E}^*\end{aligned} \tag{E.8}$$

$$vE = [\overline{v}]\left[\overline{E}\right]+\overline{v}^*\overline{E}^*+v'E' \tag{E.9}$$

In the following (equation E.10), the vertical integral of all three terms of equation (E.9) is computed, then zonally averaged, and a time mean is taken. Afterwards, the results are multiplied by the factor $2\pi a\cos\varphi$ to convert the energy transport into units of 10^{15} W. $2\pi a\cos\varphi$ describes the length of a latitude circle, where a is the radius of the earth and φ the latitude.

$$\begin{aligned}
\overline{\left[\frac{p_s}{g}\int\limits_0^1 ve\ d\sigma\right]} &= \overline{\left[\frac{1}{g}\int\limits_0^1 vE\ d\sigma\right]} \\
&= \overline{\left[\frac{1}{g}\int\limits_0^1 [\overline{v}]\ [\overline{E}]\ \ d\sigma\right]} + \overline{\left[\frac{1}{g}\int\limits_0^1 \overline{v}^*\overline{E}^*\ d\sigma\right]} + \overline{\left[\frac{1}{g}\int\limits_0^1 v'E'\ d\sigma\right]} \\
&= \overline{\left[\frac{1}{g}\int\limits_0^1 [\overline{v}]\cdot\left([\overline{c_pT\cdot p_s}] + [\overline{Lq\cdot p_s}] + [\overline{gz\cdot p_s}]\right)\ d\sigma\right]} \\
&\quad + \overline{\left[\frac{1}{g}\int\limits_0^1 \overline{v}^*\cdot\left(c_p\overline{(T\cdot p_s)}^* + L\overline{(q\cdot p_s)}^* + g\overline{(z\cdot p_s)}^*\right)\ d\sigma\right]} \\
&\quad + \overline{\left[\frac{1}{g}\int\limits_0^1 v'\cdot\left(c_p(T\cdot p_s)' + L(q\cdot p_s)' + g(z\cdot p_s)'\right)\ d\sigma\right]}
\end{aligned} \tag{E.10}$$

The atmospheric moisture transport is calculated in accordance with equations (E.5) to (E.10), substituting energy for moisture.

2 Ocean Heat Transport

Peixoto & Oort (1992) define the northward transport of energy across a latitudinal wall in the ocean as in equation (E.11):

$$T_{oc} = \iint\limits_{\text{wall}} \rho_w\left(c_oT + gz + \frac{c^2}{2} + \frac{p}{\rho_w}\right) v\ dx\ dz \tag{E.11}$$

However, as in the atmosphere, the kinetic energy can be neglected. Additionally, the flux of potential energy and the pressure work term nearly cancel each other because sea water is almost incompressible. Thus, the total energy transport in the ocean reduces to the heat transport only (see equation E.12).

$$T_{oc} = \iint\limits_{\text{wall}} \rho_w c_o T v\ dx\ dz \tag{E.12}$$

In this work the ocean heat transport is computed via the surface fluxes (net short- and longwave radiation as well as sensible and latent heat fluxes at the surface for all ocean points).

Appendix F: LSG Ocean Model

As an addition to the short model description in chapter 2, the Hamburg Large Scale Geostrophic ocean model is further described here. The basic information can be found in the model description by Maier-Reimer & Mikolajewicz (1992), however, some updates (which are mostly related to the coupling to the Planet Simulator) have not been documented.

1 Model Grid and Resolution

The LSG ocean model is run on a semi-staggered grid type "E" (Arakawa & Lamb, 1977). The horizontal E-type grid is displayed in figure F.1. On the vector points (red), the components of the horizontal velocity (u and v) are defined as well as the wind stress (τ). The blue points denote the scalar variables: potential temperature (θ), salinity (S), heat and fresh water fluxes, sea surface elevation (ζ), pressure (p), and vertical velocity (w). To avoid singularity near the equator (because of the vanishing Coriolis term), the grid is arranged so that the equator is halfway between the two nearest latitude lines, which are located at approximately 1.25°N/S.

The depth at the scalar-points is defined as the maximum depth of the four surrounding vector-points. Consequently, each ocean vector-point is surrounded by four ocean scalar-points. The vertical velocity is computed in-between two scalar-points. The vertical grid is displayed in a zonal cross-section in figure F.2.

2 System and Program Description

The LSG model is subdivided into individual subroutines. A flow diagram (figure F.3) shows how coupling routine (*cpl.f90*) calls the subroutines *LSGINI*, *LSGSTEP*, and *LSGSTOP*, which in turn call further subroutines of the model. The diagrams in figures F.4 and F.5 show the initialization of the model, *START*, and the computation of the time steps, *STEP*. The flow diagrams sketch the order of the subroutine calls, while the list below explains the purpose of each subroutine in alphabetical order.

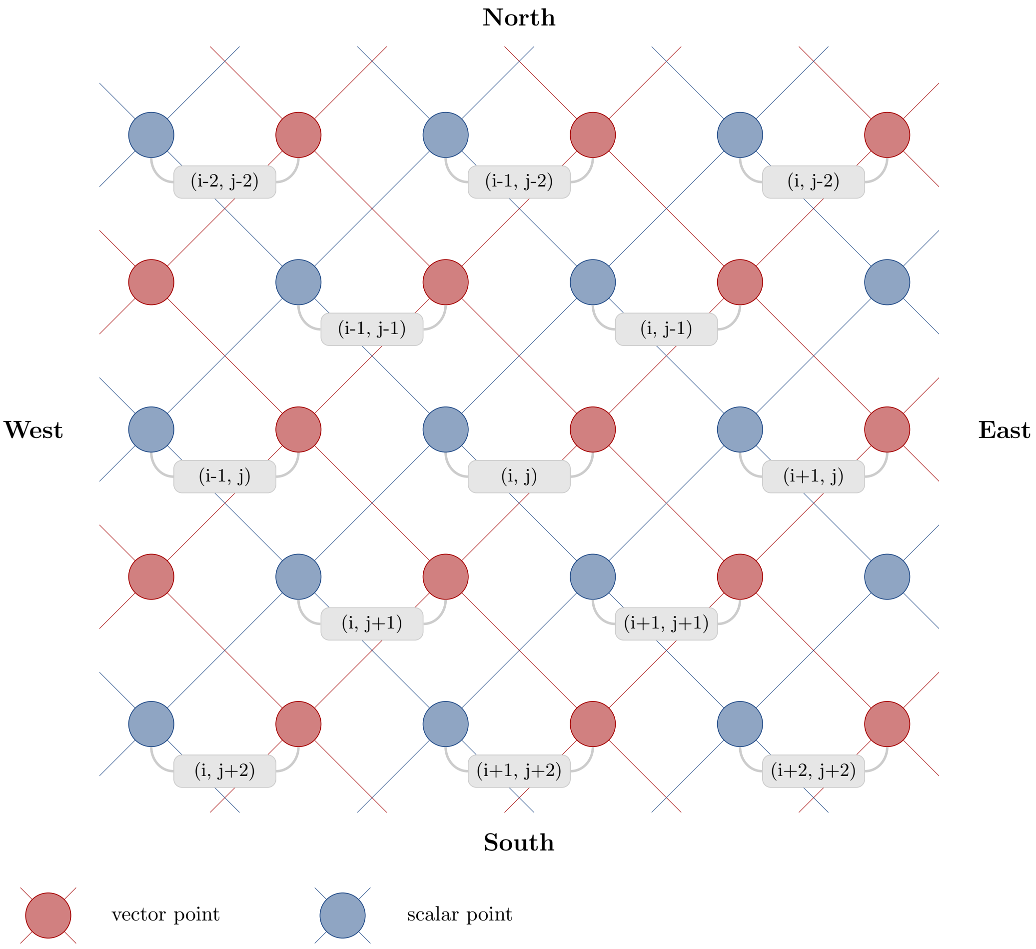

Figure F.1: Horizontal E-type grid applied in the LSG ocean model (after Maier-Reimer & Mikolajewicz, 1992)

2.1 Subroutines

- **subroutine actdate(kdate, ktime):** gives back the actual date (YYMMDD) and time (HHMMSS)
- **subroutine adv_quick:** solves the advection–diffusion equation for temperature and salinity using a numerical scheme based on the scheme by Leonard (1979) (the actual formulation is due to Farrow & Stevens 1995)
- **subroutine cont2:** computes the vertical velocities from the divergence of the horizontal velocities using the equation of continuity
- **subroutine dens:** computes the actual density-field and the potential density differences from the potential temperature and salinity (UNESCO, 1981) and adjusts

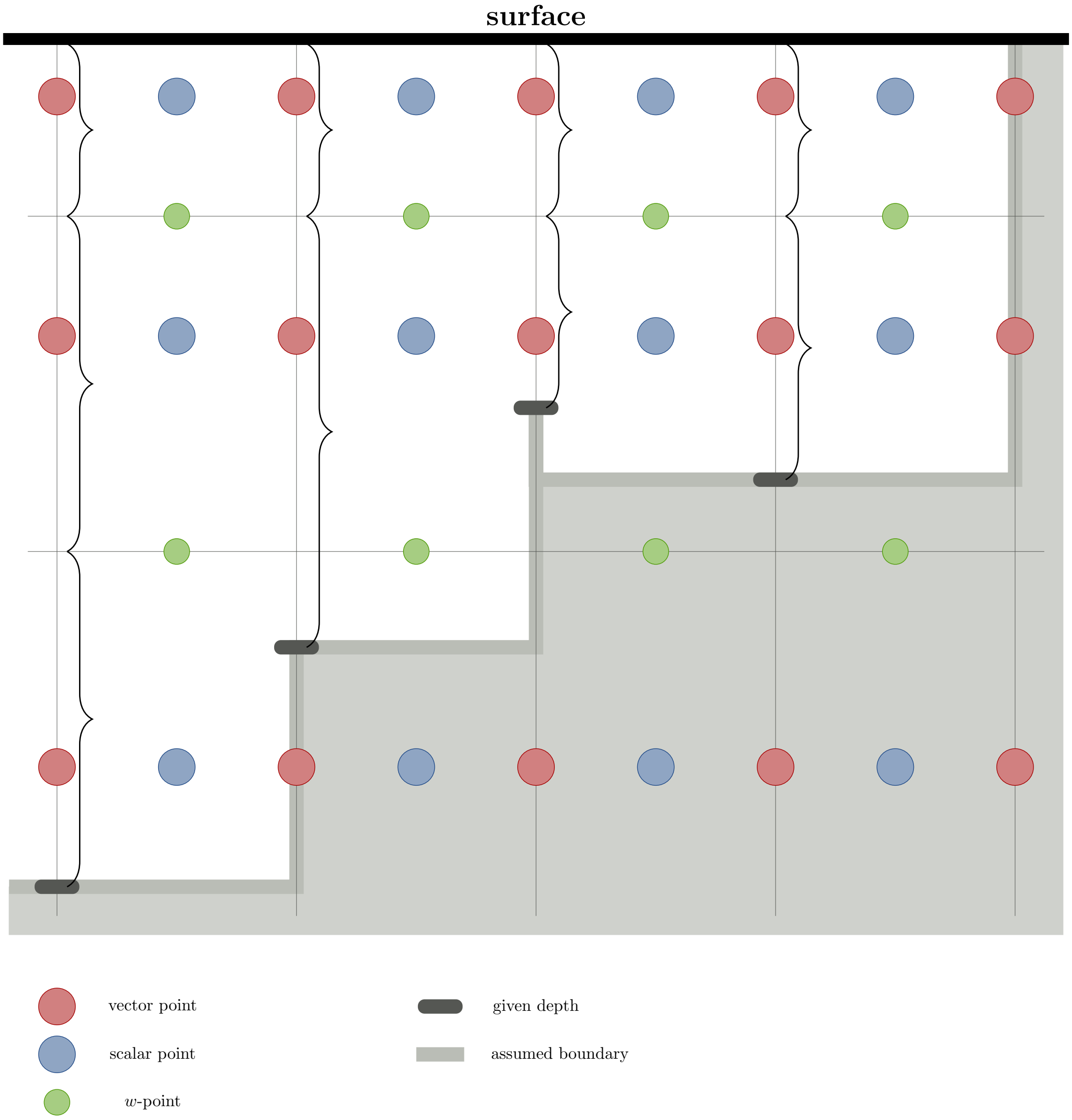

Figure F.2: Vertical grid applied in the LSG ocean model (after Maier-Reimer & Mikolajewicz, 1992)

the stratification due to convective adjustment

- **subroutine densin:** computes the actual density-field and the potential density differences from the potential temperature and salinity (same as *dens*, but without convective adjustment)
- **subroutine diva2:** controls the computation of pressure and velocities and computes total velocities from barotropic and baroclinic components
- **subroutine geost2:** computes baroclinic velocities by decomposition of the field

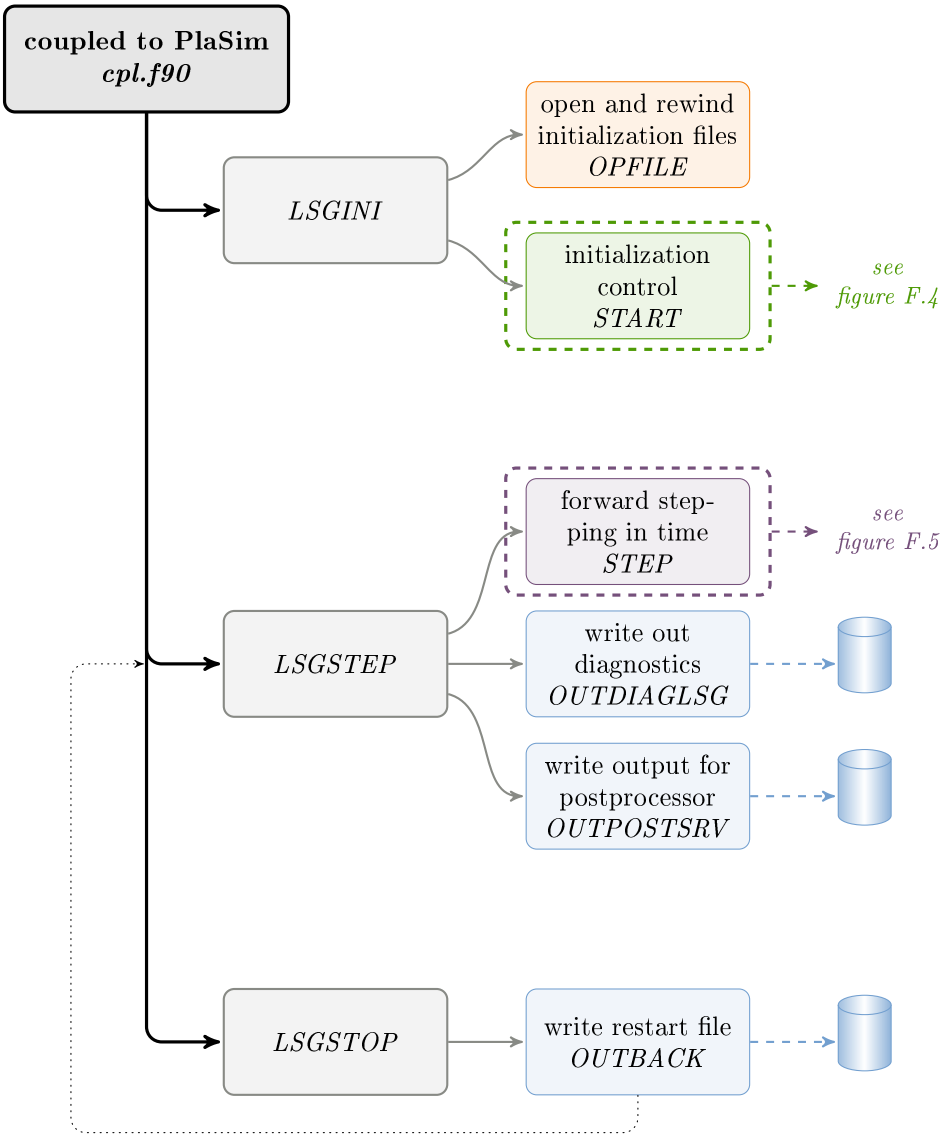

Figure F.3: Flow diagram of LSG main chain (when coupled to the Planet Simulator)

of motion into different baroclinic modes (the system is solved by iteration)

- **subroutine inicoz:** initializes the thermodynamic constants of the ocean
- **subroutine inigr:** initializes several variables only dependent on the grid and the Coriolis parameter
- **subroutine inipar:** reads important control parameters from an input file (e.g. time step, names of files, layer depths etc.)

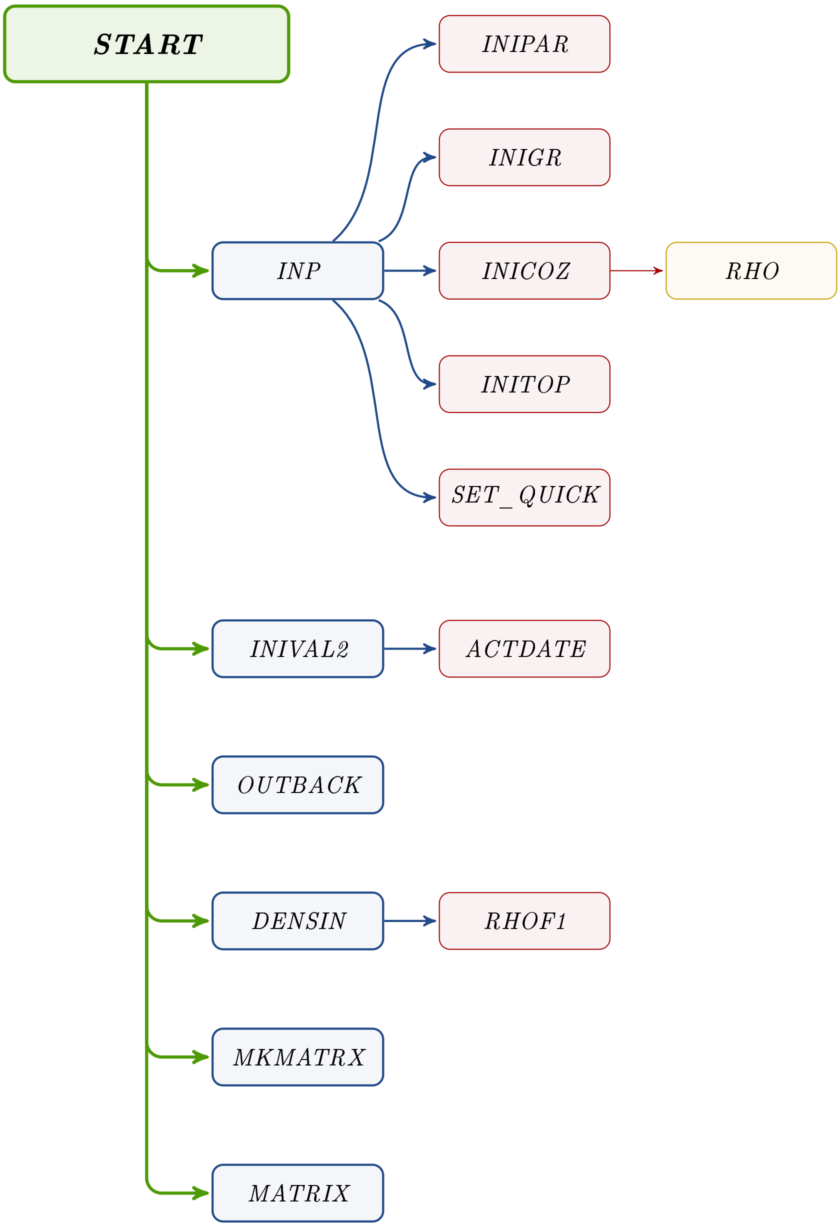

Figure F.4: Flow diagram of LSG initialization *START*

- **subroutine initop:** reads the topography from a file and computes several topography-dependent variables
- **subroutine inival2(noread,yfile):** reads a restart file produced by the subroutine *outback* containing variables as potential temperature, salinity, barotropic velocities, baroclinic modes, ice distribution, and surface elevation, gives initial values to variables
- **subroutine inp:** controls initialization of variables which are not dependent on

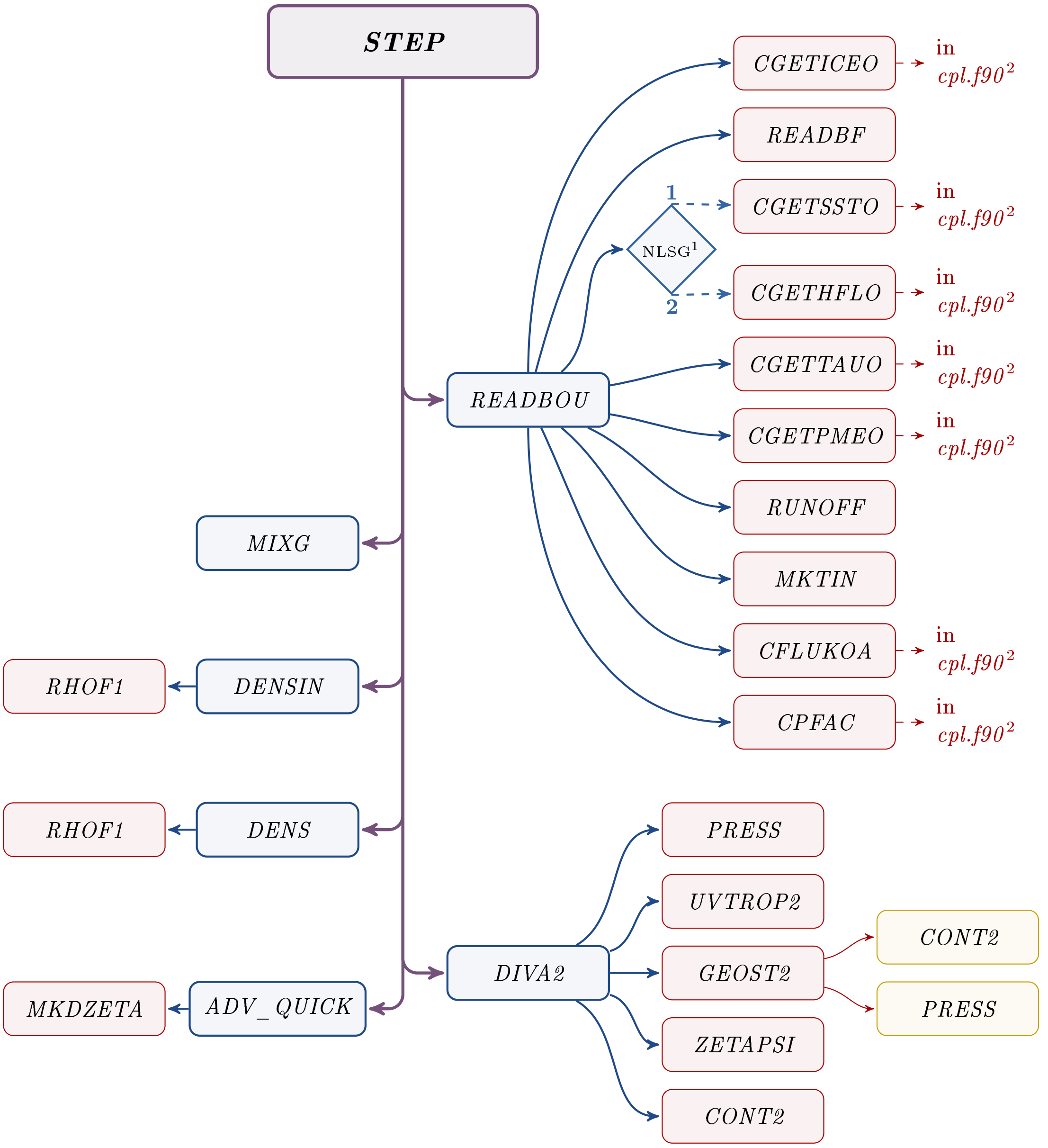

Figure F.5: Flow diagram of LSG time step *STEP* (1: NLSG in namelist *oceanmod*; 2: coupling to atmosphere)

the distribution of potential temperature and salinity

- **subroutine lsgini:** initializes the model
- **subroutine lsgstep:** controles main loop of LSG when coupled to the Planet Simulator
- **subroutine lsgstop:** controles end of LSG when coupled to the Planet Simulator

- **subroutine matrix:** computes the matrix for the barotropic velocities, performs the triangularization of the matrix by Gauss elimination
- **subroutine mixg:** connects the ocean surface to atmospheric temperature tendencies and freshwater fluxes
- **subroutine mkmatrx:** computes the dimension of the matrix and sets/allocates parameters/arrays accordingly
- **subroutine mkdzeta(pu, pv, pw, pzeta, pdt, pdzdt):** computes new height of surface layer (ζ)
- **subroutine mktin(ptinb, piinb):** computes a boundary temperature from input data
- **subroutine opfile:** opens and rewinds files during the initialization phase
- **subroutine outback(ktape, ktswit, kswit, yfile):** writes a restart file
- **subroutine outdiaglsg:** writes some diagnostic parameters (for example maximum of the barotropic stream function, average potential temperature, average salinity, average kinetic energy, sum of upward and downward transports, ice-diagnostics, extremes of temperature and salinity in surface layer) for a quick look on a file (e.g. for a first check)
- **subroutine outpostsrv:** writes output data on “file.srv” (in srv-format)
- **subroutine press:** computes the normalized pressure from the actual density
- **subroutine readbf(kpar, ktape, kmonth, pfield):** reads values for fields of boundary values from file, controls whether the file contains the correct parameter, determines the positioning of the tape according to the requested date itself
- **subroutine readbou:** computes boundary values using PlaSim and file-input
- **function rho(s, t, p):** computes the density as a function of potential temperature, salinity, and pressure, according to UNESCO (1981)
- **subroutine rhof1(tp, s, p, rh, kdim):** computes density according to the UNESCO (1981) formula
- **subroutine runoff(pwinb, ptinb):** simple runoff model
- **subroutine set_quick:** initializes the common block containing the number of advection—diffusion sub-cycles, the horizontal diffusion coefficient, the vertical diffusion coefficient and the coefficients for the 3^rd^ order advective scheme
- **subroutine start:** controls initialization of the model
- **subroutine step:** controls execution of one time step of the model

- **subroutine uvtrop2:** computes barotropic velocities and stream function
- **subroutine zetapsi:** computes the surface elevation and its time derivative from the depth-integrated equation of continuity

Appendix G: Aquaplanet Set-up in the Coupled Model

1 Planet Simulator

The atmospheric model, the Planet Simulator, is very flexible. Thus, the aquaplanet configuration is easily applied in the model. A surface file containing the land–sea mask (code=172) has to be computed. In the case of the pure aquaplanet, all points are set to 0 (ocean only). When the southern polar continent is introduced into the system, the points south of 60°S are set to 1 (land surface). Furthermore, since all simulations are implemented with the sea surface temperature (SST) profile "*Control*" from Neale & Hoskins (2001a) (see equation G.1), an additional surface file has to be created containing the initial SST (code=169). If no file for the orography is provided, all heights are set to 0 m.

$$SST_{Control}\left(\varphi\right) = \begin{cases} 27.0\,\mathrm{K}\cdot\left(1-\sin^2\left(\frac{3\varphi}{2}\right)\right)+273.15\,\mathrm{K}, & -\frac{\pi}{3}<\varphi<\frac{\pi}{3} \\ 273.15\,\mathrm{K}, & \text{otherwise} \end{cases} \tag{G.1}$$

Furthermore, for most of the experiments conducted in this study, the orbital parameters are changed to perpetual equinoctial conditions. This is set in the *puma_namelist* "`PLANET`" as shown in listing G.1.

```
&PLANET
NFIXORB = 1
ECCEN = 0
MVELP = 0
OBLIQ = 0
&END
```

Listing G.1: *puma_namelist*: PLANET

Furthermore, the annual cycle of the atmospheric ozone concentration has to be switched off, which is realized in line 37 of the "`RADPAR`" namelist of the *puma_namelist* (see listing G.2). In the same namelist (“`RADPAR`”, listing G.2), the atmospheric CO_2 concentration (line 34) and the solar constant (line 36) are set.

```
32  &RADPAR
33  NDCYCLE =     0
34  CO2     =   360.0000
35  DAWN    =     0.0000
36  GSOLO   =  1365.0000
37  ACO3    =  0
38  &END
```

Listing G.2: *puma_namelist*: RADPAR

2 LSG Ocean Model

The restart files for the ocean model (*kleiauf*, *kleiin1*, and *kleiswi*), which have been created for the aquaplanet configuration, can be applied for all experiments. However, topography files need to be constructed for each experiment individually. The topography file for the ocean, *topogr*, contains the ocean depths (5,500 m) and the land–sea mask: if the depth of an ocean point is set to 0.0 m it is counted as land surface. Meridional ocean barriers and the southern polar continent are inserted in the aquaplanet ocean via the topography file.

To be able to run the LSG ocean model in an aquaplanet mode (or more specifically, with a changed land–sea mask), the parameter `NAQUA` of the namelist *input* has to be set to 1 in (as shown in line 2 of listing G.3). The namelist *input* also shows the 22 vertical levels ranging from from 25 m to 5,500 m (lines 18–39 of listing G.3) that are applied in the ocean model. The last level (6,500 m, listed in line 40 of listing G.3) is not used in the simulation.

```
1   &param
2    naqua=1,
3    ndiagfl=1,
4    bblthick=300.,
5    nsmix=3,
6    nsve= 2,
7    nsflu=2,
8    ntcont=1,
9    ntout=1,
10   ntaver=600,
11   ntback=1,
12   ntsurf=3,
13   iyear=1000000,
14   idate=-1230,
15   nscoup=1,
16   grad1=5.,
17   phinor=93.75,
18   du(001)=  25.,
19   du(002)=  75.,
```

```
  du(003)= 125.,
  du(004)= 175.,
  du(005)= 225.,
  du(006)= 275.,
  du(007)= 350.,
  du(008)= 450.,
  du(009)= 550.,
  du(010)= 650.,
  du(011)= 750.,
  du(012)= 850.,
  du(013)= 950.,
  du(014)=1100.,
  du(015)=1300.,
  du(016)=1500.,
  du(017)=1800.,
  du(018)=2250.,
  du(019)=2750.,
  du(020)=3500.,
  du(021)=4500.,
  du(022)=5500.,
  du(023)=6500.,
```

Listing G.3: *input* (LSG namelist)

Bibliography

Arakawa, A., & Lamb, V. R. 1977. Computational design of the basic dynamical processes of the UCLA General Circulation Model. *Pages 173–265 of:* Chang, J. (ed), *General circulation models of the atmosphere.* Methods in Computational Physics, vol. 17. Academic Press.

Bjerknes, J. 1964. Atlantic air-sea interactions. *Pages 1–82 of:* Landsberg, H. E., & van Mieghem, J. (eds), *Advances in Geophysics*, vol. 10. Academic Press.

Bjornsson, H., & Toggweiler, J. 2001. The climatic influence of Drake Passage. *Pages 243–259 of: The Oceans and Rapid Climate Change: Past, Present and Future.* Geophysical Monographs, vol. 126. American Geophysical Union.

Boer, G. J., McFarlane, N. A., Laprise, R., Henderson, J. D., & Blanchet, J.-P. 1984. The Canadian Climate Centre Spectral Atmospheric General Circulation Model. *Atmosphere-Ocean*, **22**(4), 397–429.

Bordi, I., Fraedrich, K., Sutera, A., & Zhu, X. 2012. Transient response to well-mixed greenhouse gas changes. *Theoretical and Applied Climatology*, **109**(1–2), 245–252.

Broecker, W. S., Peteet, D. M., & Rind, D. 1985. Does the ocean-atmosphere system have more than one stable mode of operation? *Nature*, **315**(6014), 21–26.

Broecker, W. S., Bond, G., Klas, M., Bonani, G., & Wolfli, W. 1990. A salt oscillator in the glacial Atlantic? 1. The concept. *Paleoceanography*, **5**(4), 469–477.

Bryan, F. 1986. High-latitude salinity effects and interhemispheric thermohaline circulations. *Nature*, **323**(6086), 301–304.

Bryan, K., Manabe, S., & Pacanowski, R. C. 1975. A global ocean-atmosphere climate model. Part II: The oceanic circulation. *Journal of Physical Oceanography*, **5**(1), 30–46.

Budyko, M. I. 1969. The effect of solar radiation variations on the climate of the Earth. *Tellus*, **21**(5), 611–619.

Chao, W. C., & Chen, B. 2004. Single and double ITCZ in an aqua-planet model with constant sea surface temperature and solar angle. *Climate Dynamics*, **22**(4), 447–459.

CHARETTE, M. A., & SMITH, W. H. 2010. The volume of Earth's ocean. *Oceanography*, **23**(2), 112–114.

CLAUSSEN, M., MYSAK, L., WEAVER, A., CRUCIFIX, M., FICHEFET, T., LOUTRE, M.-F., WEBER, S., ALCAMO, J., ALEXEEV, V., BERGER, A., CALOV, R., GANOPOLSKI, A., GOOSSE, H., LOHMANN, G., LUNKEIT, F., MOKHOV, I., PETOUKHOV, V., STONE, P., & WANG, Z. 2002. Earth system models of intermediate complexity: Closing the gap in the spectrum of climate system models. *Climate Dynamics*, **18**(7), 579–586.

CLAUSSEN, M. 1998. On multiple solutions of the atmosphere–vegetation system in present-day climate. *Global Change Biology*, **4**(5), 549–559.

CLEMENT, A., & SEAGER, R. 1999. Climate and the tropical ocean. *Journal of Climate*, **12**(12), 3383–3401.

COX, M. D. 1989. An idealized model of the world ocean. Part I: The global-scale water masses. *Journal of Physical Oceanography*, **19**(11), 1730–1752.

COXALL, H., WILSON, P., PÄLIKE, H., LEAR, C., & BACKMAN, J. 2005. Letter to Nature. Rapid stepwise onset of Antarctic glaciation and deeper calcite compensation in the Pacific Ocean. *Nature*, **433**(7021), 53–57.

CRISTINI, L., GROSFELD, K., BUTZIN, M., & LOHMANN, G. 2012. Influence of the opening of the Drake Passage on the Cenozoic Antarctic Ice Sheet: A modeling approach. *Palaeogeography, Palaeoclimatology, Palaeoecology*, **339-341**(1), 66 – 73.

CRUCIFIX, M., LOUTRE, M.-F., TULKENS, P., FICHEFET, T., & BERGER, A. 2002. Climate evolution during the Holocene: A study with an Earth system model of intermediate complexity. *Climate Dynamics*, **19**(1), 43–60.

CZAJA, A., & MARSHALL, J. 2006. The partitioning of poleward heat transport between the atmosphere and ocean. *Journal of the Atmospheric Sciences*, **63**(5), 1498–1511.

DAHMS, E. 2009. *Single and Double ITCZ and the Zonal Mean Tropical Circulation: Experiments With the Planet Simulator*. Diplomarbeit, University of Hamburg, Germany.

DAHMS, E., BORTH, H., LUNKEIT, F., & FRAEDRICH, K. 2011. ITCZ splitting and the influence of large-scale eddy fields on the tropical mean state. *Journal of the Meteorological Society of Japan*, **89**(5), 399–411.

DAHMS, E., LUNKEIT, F., & FRAEDRICH, K. 2012a. Low-frequency climate variability of an aquaplanet. *Manuscript submitted for publication.*

DAHMS, E., LUNKEIT, F., & FRAEDRICH, K. 2012b. The role of atmospheric greenhouse gases, orbital parameters, and ocean gateways: an idealized model study. *Manuscript submitted for publication.*

Dansgaard, W., Clausen, H. B., Gundestrup, N., Hammer, C. U., Johnsen, S. F., Kristinsdottir, P. M., & Reeh, N. 1982. A new Greenland deep ice core. *Science*, **218**(4579), 1273–1277.

Dansgaard, W., Johnsen, S. J., Clausen, H. B., Dahl-Jensen, D., Gundestrup, N. S., Hammer, C. U., Hvidberg, C. S., Steffensen, J. P., Sveinbjörnsdottir, A. E., Jouzel, J., & Bond, G. 1993. Evidence for general instability of past climate from a 250-kyr ice-core record. *Nature*, **364**(6434), 218–220.

DeConto, R. M., & Pollard, D. 2003. Rapid Cenozoic glaciation of Antarctica induced by declining atmospheric CO_2. *Nature*, **421**(6920), 245–249.

Eliasen, E., Machenhauer, B., & Rasmussen, E. 1970. *On a numerical method for integration of the hydrodynamical equations with a spectral representation of the horizontal fields.* Report No 2, Institute for Theoretical Meteorology, Copenhagen University, Denmark.

Enderton, D., & Marshall, J. 2009. Explorations of atmosphere-ocean-ice climates on an aquaplanet and their meridional energy transports. *Journal of Atmospheric Sciences*, **66**(6), 1593–1611.

Farrow, D. E., & Stevens, D. P. 1995. A new tracer advection scheme for Bryan and Cox type ocean general circulation models. *Journal of Physical Oceanography*, **25**(7), 1731–1741.

Ferreira, D., Marshall, J., & Campin, J.-M. 2010. Localization of deep water formation: Role of atmospheric moisture transport and geometrical constraints on ocean circulation. *Journal of Climate*, **23**(6), 1456–1476.

Ferreira, D., Marshall, J., & Rose, B. 2011. Climate determinism revisited: Multiple equilibria in a complex climate model. *Journal of Climate*, **24**(4), 992–1012.

Fox, A. J., & Cooper, A. P. R. 1994. Measured properties of the Antarctic ice sheet derived from the SCAR Antarctic digital database. *Polar Record*, **30**(174), 201–206.

Fraedrich, K., Jansen, H., Kirk, E., Luksch, U., & Lunkeit, F. 2005a. The Planet Simulator: Towards a user friendly model. *Meteorologische Zeitschrift*, **14**(3), 299–304.

Fraedrich, K., Kirk, E., Luksch, U., & Lunkeit, F. 2005b. The portable university model of the atmosphere (PUMA): Storm track dynamics and low-frequency variability. *Meteorologische Zeitschrift*, **14**(6), 735–745.

Fraedrich, K. 2012. A suite of user-friendly global climate models: Hysteresis experiments. *The European Physical Journal Plus*, **127**(53), 1–9.

Ganopolski, A., & Rahmstorf, S. 2001. Rapid changes of glacial climate simulated in a coupled climate model. *Nature*, **409**(6817), 153–158.

Haarsma, R. J., Opsteegh, J. D., Selten, F. M., & Wang, X. 2001. Rapid transitions and ultra-low frequency behaviour in a 40 kyr integration with a coupled climate model of intermediate complexity. *Climate Dynamics*, **17**(7), 559–570.

Haltiner, G. J., & Williams, R. T. 1980. *Numerical Prediction and Dynamic Meteorology.* Wiley.

Hasselmann, K. 1982. An ocean model for climate variability studies. *Progress In Oceanography*, **11**(2), 69–92.

Heinrich, H. 1988. Origin and consequences of cyclic ice rafting in the Northeast Atlantic Ocean during the past 130,000 years. *Quaternary Research*, **29**(2), 142–152.

Held, I. M. 2005. The gap between simulation and understanding in climate modeling. *Bulletin of the American Meteorological Society*, **86**(11), 1609–1614.

Held, I. M., & Hou, A. Y. 1980. Nonlinear axially symmetric circulations in a nearly inviscid atmosphere. *Journal of the Atmospheric Sciences*, **37**(3), 515–533.

Held, I. M. 2001. The partitioning of the poleward energy transport between the tropical ocean and atmosphere. *Journal of the Atmospheric Sciences*, **58**(8), 943–948.

Hess, P. G., Battisti, D. S., & Rasch, P. J. 1993. Maintenance of the intertropical convergence zones and the large-scale tropical circulation on a water-covered Earth. *Journal of the Atmospheric Sciences*, **50**(5), 691–713.

Hoskins, B. J., & Simmons, A. J. 1975. A multi-layer spectral model and the semi-implicit method. *Quarterly Journal of the Royal Meteorological Society*, **101**(429), 637–655.

Hotelling, H. 1935. The most predictable criterion. *Journal of Educational Psychology*, **26**(2), 139–142.

Hotinski, R. M., & Toggweiler, J. R. 2003. Impact of a Tethyan circumglobal passage on ocean heat transport and "equable" climates. *Paleoceanography*, **18**(1), 7(1–15).

Houghton, J. T., Ding, Y., Griggs, D. J., Noguer, M., van der Linden, P. J., & Xiaosu, D. 2001. *Climate Change 2001: The Scientific Basis.* Cambridge University Press.

Hubert, L. F., Krueger, A. F., & Winston, J. S. 1969. The double intertropical convergence zone — fact or fiction? *Journal of the Atmospheric Sciences*, **26**(4), 771–773.

James, I. A. 1995. *Introduction to Circulating Atmospheres.* Cambridge Atmospheric and Space Science Series. Cambridge University Press.

Jouzel, J., Vaikmae, R., Petit, J. R., Martin, M., Duclos, Y., Stievenard, M., Lorius, C., Toots, M., Mélières, M. A., Burckle, L. H., Barkov, N. I., & Kotlyakov, V. M. 1995. The two-step shape and timing of the last deglaciation in Antarctica. *Climate Dynamics*, **11**(3), 151–161.

Jungclaus, J. H., Haak, H., Latif, M., & Mikolajewicz, U. 2005. Arctic-North Atlantic interactions and multidecadal variability of the meridional overturning circulation. *Journal of Climate*, **18**(19), 4013–4031.

Katayama, A. 1972. *A Simplified Scheme for Computing Radiative Transfer in the Troposphere*. Tech. rept. 6. Department of Meteorology, University of California, Los Angeles, CA.

Kennett, J. P. 1977. Cenozoic evolution of Antarctic glaciation, the circum-Antarctic ocean, and their impact on global paleoceanography. *Journal of Geophysical Research*, **82**(27), 3843–3860.

Kennett, J. 1978. The development of planktonic biogeography in the Southern Ocean during the Cenozoic. *Marine Micropaleontology*, **3**(4), 301 – 345.

King, J., & Turner, J. 1997. *Antarctic meteorology and climatology*. Cambridge Atmospheric and Space Science Series. Cambridge University Press.

Kleidon, A. 2006. The climate sensitivity to human appropriation of vegetation productivity and its thermodynamic characterization. *Global and Planetary Change*, **54**(1–2), 109–127.

Knorr, G., & Lohmann, G. 2007. Rapid transitions in the Atlantic thermohaline circulation triggered by global warming and meltwater during the last deglaciation. *Geochemistry, Geophysics, Geosystems*, **8**(12), 12006.

Kuo, H. L. 1965. On formation and intensification of tropical cyclones through latent heat release by cumulus convection. *Journal of the Atmospheric Sciences*, **22**(1), 40–63.

Kuo, H. L. 1974. Further studies of the parameterization of the influence of cumulus convection on large-scale flow. *Journal of the Atmospheric Sciences*, **31**(5), 1232–1240.

Lacis, A. A., & Hansen, J. E. 1974. A parameterization for the absorption of solar radiation in the Earth's atmosphere. *Journal of the Atmospheric Sciences*, **31**(1), 118–133.

Laursen, L., & Eliasen, E. 1989. On the effects of the damping mechanisms in an atmospheric general circulation model. *Tellus A*, **41**(5), 385–400.

Leonard, B. P. 1979. A stable and accurate convective modelling procedure based on quadratic upstream interpolation. *Computer Methods in Applied Mechanics and Engineering*, **19**(1), 59 – 98.

LEVITUS, S. 1982. Climatological atlas of the world ocean. *NOAA Professional Paper*, **13**, 163pp. U.S. Government Printing Office, Washington, D.C.

LOHMANN, G. 2003. Atmospheric and oceanic freshwater transport during weak Atlantic overturning circulation. *Tellus A*, **55**(5), 438–449.

LORENZ, E. N. 1956. *Empirical orthogonal functions and statistical weather prediction.* Statistical Forecast Project Report 1 49pp. Department of Meteorology, MIT.

LORENZ, E. N. 1968. Climate determinism. *Meteorological Monographs*, **8**(30), 1–3.

LORENZ, E. N. 1970. Climatic change as a mathematical problem. *Journal of Applied Meteorology*, **9**(3), 325–329.

LOUIS, J.-F. 1979. A parametric model of vertical eddy fluxes in the atmosphere. *Boundary-Layer Meteorology*, **17**(2), 187–202.

LOUIS, J. F., TIEDTKE, M., & GELEYN, J. F. 1982. *A Short History of the Operational PBL - Parameterization at ECMWF.* Proceedings, ECMWF workshop on planetary boundary layer parameterization, Reading, 25.-27. November 1981.

LOUTRE, M., & BERGER, A. 2000. Future climatic changes: Are we entering an exceptionally long interglacial? *Climatic Change*, **46**(1–2), 61–90.

LOVING, J. L., & VALLIS, G. K. 2005. Mechanisms for climate variability during glacial and interglacial periods. *Paleoceanography*, **20**(4), PA4024(1–19).

LUCARINI, V., FRAEDRICH, K., & LUNKEIT, F. 2010. Thermodynamic analysis of snowball earth hysteresis experiment: Efficiency, entropy production, and irreversibility. *Quarterly Journal of the Royal Meteorological Society*, **136**(646), 2–11.

LUNKEIT, F., BORTH, H., BÖTTINGER, M., FRAEDRICH, K., JANSEN, H., KIRK, E., KLEIDON, A., LUKSCH, U., PAIEWONSKY, P., SCHUBERT, S., SIELMANN, F., & WAN, H. 2011 (June). *Planet Simulator Reference Manual Version 16.* Meteorological Institute, University of Hamburg.

LYTHE, M. B., VAUGHAN, D. G., & BEDMAP CONSORTIUM. 2001. BEDMAP: A new ice thickness and subglacial topographic model of Antarctica. *Journal of Geophysical Research*, **106**(B6), 11335–11352.

MAIER-REIMER, E., & MIKOLAJEWICZ, U. 1992 (February). *The Hamburg Large Scale Geostrophic Ocean General Circulation Model Cycle 1.* Report 2. Max-Planck-Institut für Meteorologie. Edited by: Modellberatungsgruppe.

MAIER-REIMER, E., MIKOLEJEWICZ, U., & HASSELMANN, K. 1993. Mean circulation of the Hamburg LSG OGCM and its sensitivity to the thermohaline surface forcing. *Journal of Physical Oceanography*, **23**(4), 731–757.

MANABE, S., & MÖLLER, F. 1961. On the radiative equilibrium and heat balance of the atmosphere. *Monthly Weather Review*, **89**(12), 503–532.

Manabe, S., Bryan, K., & Spelman, M. J. 1975. A global ocean-atmosphere climate model. Part I: The atmospheric circulation. *Journal of Physical Oceanography*, **5**(1), 3–29.

Marotzke, J., & Willebrand, J. 1991. Multiple equilibria of the global thermohaline circulation. *Journal of Physical Oceanography*, **21**(9), 1372–1385.

Marshall, J., Ferreira, D., Campin, J.-M., & Enderton, D. 2007. Mean climate and variability of the atmosphere and ocean on an aquaplanet. *Journal of the Atmospheric Sciences*, **64**(12), 4270–4286.

McManus, J. F., Francois, R., Gherardi, J.-M., Keigwin, L. D., & Brown-Leger, S. 2004. Collapse and rapid resumption of Atlantic meridional circulation linked to deglacial climate changes. *Nature*, **428**(6985), 834–837.

Mikolajewicz, U., & Maier-Reimer, E. 1990. Internal secular variability in an ocean general circulation model. *Climate Dynamics*, **4**(3), 145–156.

Mikolajewicz, U., & Maier-Reimer, E. 1993. Effect of Drake and Panamian Gateways on the circulation of an ocean model. *Paleoceanography*, **8**(4), 409–426.

Milankovitch, M. M. 1941. *Canon of Insolation and the Ice Age Problem.* Königlich Serbische Akademie, Belgrade. English translation by the Israel Program for Scientific Translations, United States Department of Commerce and the National Science Foundation, Washington D.C.

Monin, A. S., & Obukhov, A. M. 1954. Basic laws of turbulent mixing in the surface layer of the atmosphere. *Tr. Inst. Teor. Geofiz. Akad. Nauk. S.S.S.R.*, **24**(151), 163–187. In Russian.

Neale, R. B., & Hoskins, B. J. 2001a. A standard test for AGCMs including their physical parametrizations. I: The proposal. *Atmospheric Science Letters*, **1**(2), 101–107.

Neale, R. B., & Hoskins, B. 2001b. A standard test for AGCMs including their physical parametrizations. II: Results for the Met Office Model. *Atmospheric Science Letters*, **1**(2), 108–114.

Neelin, J. D., Battisti, D. S., Hirst, A. C., Jin, F.-F., Wakata, Y., Yamagata, T., & Zebiak, S. E. 1998. ENSO theory. *Journal of Geophysical Research*, **103**(C7), 14261–14290.

Obukhov, A. M. 1946. Turbulence in an atmosphere with a non-uniform temperature. *Tr. Inst. Teor. Geofiz. Akad. Nauk. S.S.S.R.*, **1**, 95–115. In Russian.

Obukhov, A. M. 1971. Turbulence in an atmosphere with a non-uniform temperature. *Boundary-Layer Meteorology*, **2**(1), 7–29. English translation of the 1946 Russian original paper.

Orszag, S. A. 1970. Transform method for the calculation of vector-coupled sums: Application to the spectral form of the vorticity equation. *Journal of the Atmospheric Sciences*, **27**(6), 890–895.

Pagani, M., Arthur, M. A., & Freeman, K. H. 1999. Miocene evolution of atmospheric carbon dioxide. *Paleoceanography*, **14**(3), 273–292.

Pearson, K. 1901. LIII. On lines and planes of closest fit to systems of points in space. *Philosophical Magazine Series 6*, **2**(11), 559–572.

Pearson, P. N., & Palmer, M. R. 2000. Atmospheric carbon dioxide concentrations over the past 60 million years. *Nature*, **406**(6797), 695–699.

Peixoto, J. P., & Oort, A. H. 1992. *Physics of Climate.* American Institute of Physics.

Pierce, D. W., Barnett, T. P., & Mikolajewicz, U. 1995. Competing roles of heat and freshwater flux in forcing thermohaline oscillations. *Journal of Physical Oceanography*, **25**(9), 2046–2064.

Pike, A. C. 1971. Intertropical convergence zone studied with an interacting atmosphere and ocean model. *Monthly Weather Review*, **99**(6), 469–477.

Prange, M., Romanova, V., & Lohmann, G. 2002. The glacial thermohaline circulation: Stable or unstable? *Geophysical Research Letters*, **29**(21), 24(1–4).

Prange, M., Lohmann, G., & Paul, A. 2003. Influence of vertical mixing on the thermohaline hysteresis: Analyses of an OGCM. *Journal of Physical Oceanography*, **33**(8), 1707–1721.

Rahmstorf, S., Crucifix, M., Ganopolski, A., Goosse, H., Kamenkovich, I., Knutti, R., Lohmann, G., Marsh, R., Mysak, L. A., Wang, Z., & Weaver, A. J. 2005. Thermohaline circulation hysteresis: A model intercomparison. *Geophysical Research Letters*, **32**(23), L23605.

Rahmstorf, S. 1995. Bifurcations of the Atlantic thermohaline circulation in response to changes in the hydrological cycle. *Nature*, **378**(6553), 145–149.

Rodgers, C. D. 1967. The use of emissivity in atmospheric radiation calculations. *Quarterly Journal of the Royal Meteorological Society*, **93**(395), 43–54.

Roeckner, E., Arpe, K., Bengtsson, L., Brinkop, S., Dümenil, L., Esch, M., Kirk, E., Lunkeit, F., Ponater, M., Rockel, B., Sausen, R., Schlese, U., Schubert, S., & Windelband, M. 1992 (October). *Simulation of the Present-Day Climate with the ECHAM Model: Impact of Model Physics and Resolution.* Report 93. Max-Planck-Institut für Meteorologie.

Saltzman, B. 2002. *Dynamical Paleoclimatology. Generalized Theory of Global Climate Change.* Academic Press.

Sasamori, T. 1968. The radiative cooling calculation for application to general circulation experiments. *Journal of Applied Meteorology*, **7**(5), 721–729.

Schönwiese, C.-D. 2006. *Praktische Statistik für Meteorologen und Geowissenschaftler*. Gebrüder Borntraeder.

Sellers, W. D. 1969. A global climatic model based on the energy balance of the earth-atmosphere system. *Journal of Applied Meteorology*, **8**(3), 392–400.

Semtner, A. J. J. 1976. A model for the thermodynamic growth of sea ice in numerical investigations of climate. *Journal of Physical Oceanography*, **3**(3), 379–389.

Sijp, W. P., & England, M. H. 2004. Effect of the Drake Passage throughflow on global climate. *Journal of Physical Oceanography*, **34**(5), 1254–1266.

Simmons, A. J., & Burridge, D. M. 1981. An energy and angular-momentum conserving vertical finite-difference scheme and hybrid vertical coordinates. *Monthly Weather Review*, **109**(4), 758.

Slingo, A., & Slingo, J. M. 1991. Response of the National Center for Atmospheric Research Community Climate Model to improvements in the representation of clouds. *Journal of Geophysical Research*, **96**(D8), 341–357.

Smith, R. S., Dubois, C., & Marotzke, J. 2006. Global climate and ocean circulation on an aquaplanet ocean-atmosphere general circulation model. *Journal of Climate*, **19**(18), 4719–4737.

Stephens, G. L. 1978. Radiation profiles in extended water clouds. II: Parameterization schemes. *Journal of the Atmospheric Sciences*, **35**(11), 2123–2132.

Stephens, G. L. 1984. The parameterization of radiation for numerical weather prediction and climate models. *Monthly Weather Review*, **112**(4), 826–867.

Stephens, G. L., Ackerman, S., & Smith, E. A. 1984. A shortwave parameterization revised to improve cloud absorption. *Journal of the Atmospheric Sciences*, **41**(4), 687–690.

Stommel, H. 1961. Thermohaline convection with two stable regimes of flow. *Tellus*, **13**(2), 224–230.

Stone, P. H. 1978. Constraints on dynamical transports of energy on a spherical planet. *Dynamics of Atmospheres and Oceans*, **2**(2), 123 – 139.

Swingedouw, D., Fichefet, T., Huybrechts, P., Goosse, H., Driesschaert, E., & Loutre, M.-F. 2008. Antarctic ice-sheet melting provides negative feedbacks on future climate warming. *Geophysical Research Letters*, **35**(17), L17705(1–4).

Tiedtke, M. 1983 (28 November - 1 December). The sensitivity of the time-mean large-scale flow to cumulus convection in the ECMWF model. *Pages 297–316 of: Large-Scale Models*. European Centre for Medium-Range Weather Forecasts, Reading, England.

Toggweiler, J. R., & Bjornsson, H. 2000. Drake Passage and palaeoclimate. *Journal of Quarternary Science*, **15**(4), 319–328.

Trenberth, K. E., & Caron, J. M. 2001. Estimates of meridional atmosphere and ocean heat transports. *Journal of Climate*, **14**(16), 3433–3443.

Tuenter, E., Weber, S., Hilgen, F., Lourens, L., & Ganopolski, A. 2005. Simulation of climate phase lags in response to precession and obliquity forcing and the role of vegetation. *Climate Dynamics*, **24**(2–3), 279–295.

Turner, J., Bindschadler, R., Convey, P., di Prisco, G., Fahrbach, E., Gutt, J., Hodgson, D., Mayewski, P., C., & Summerhayes. 2009. *Antarctic Climate Change and the Environment.* A contribution to the International Polar Year 2007-2008. Cambridge University Press.

Turner, J. 2004. The El Niño–southern oscillation and Antarctica. *International Journal of Climatology*, **24**(1), 1–31.

UNESCO. 1981. *Tenth report of the joint panel on oceanographic tables and standards.* Technical papers in marine sciences 36. UNESCO.

von der Heydt, A., & Dijkstra, H. A. 2006. Effect of ocean gateways on the global ocean circulation in the late Oligocene and early Miocene. *Paleoceanography*, **21**(1), 1011.

von Storch, H., & Zwiers, F. W. 1999. *Statistical Analysis in Climate Research.* Cambridge University Press.

Wang, R., Fraedrich, K., & Pawson, S. 1995. Phase-space characteristics of the tropical stratospheric quasi-biennial oscillation. *Journal of Atmospheric Sciences*, **52**(24), 4482–4500.

Warren, B. A. 1999. Approximating the energy transport across oceanic sections. *Journal of Geophysical Research*, **104**(C4), 7915–7920.

Weber, S., Crowley, T., & der Schrier, G. 2004. Solar irradiance forcing of centennial climate variability during the Holocene. *Climate Dynamics*, **22**(5), 539–553.

Weber, S. L. 2010. The utility of Earth system Models of Intermediate Complexity (EMICs). *Wiley Interdisciplinary Reviews: Climate Change*, **1**(2), 243–252.

Wenzel, M., & Schröter, J. 2007. The global ocean mass budget in 1993–2003 estimated from sea level change. *Journal of Physical Oceanography*, **37**(2), 203–213.

Wilks, D. S. 2006. *Statistical Methods in the Atmospheric Sciences.* 2 edn. International Geophysics Series, vol. 91. Academic Press.

Winton, M. 1993. Deep decoupling oscillations of the oceanic thermohaline circulation. *Pages 417–432 of:* Peltier, W. R. (ed), *Ice in the Climate System.* NATO ASI Series. Springer-Verlag.

WINTON, M. 2003. On the climatic impact of ocean circulation. *Journal of Climate*, **16**(17), 2875–2889.

WINTON, M., & SARACHIK, E. S. 1993. Thermohaline oscillations induced by strong steady salinity forcing of ocean general circulation models. *Journal of Physical Oceanography*, **23**(7), 1389–1410.

WUNSCH, C. 2004. Quantitative estimate of the Milankovitch-forced contribution to observed Quaternary climate change. *Quaternary Science Reviews*, **23**(9-10), 1001–1012.

WUNSCH, C. 2010. Towards understanding the Paleocean. *Quaternary Science Reviews*, **29**(17-18), 1960 – 1967.

YANG, J., & NEELIN, J. D. 1993. Sea-ice interaction with the thermohaline circulation. *Geophysical Research Letters*, **20**(2), 217–220.

YANG, J., & NEELIN, J. D. 1997. Decadal variability in coupled sea-ice-thermohaline circulation systems. *Journal of Climate*, **10**(12), 3059–3076.

ZACHOS, J. C., DICKENS, G. R., & ZEEBE, R. E. 2008. An early Cenozoic perspective on greenhouse warming and carbon-cycle dynamics. *Nature*, **451**(7176), 279–283.

ZHU, X., FRAEDRICH, K., & BLENDER, R. 2006. Variability regimes of simulated Atlantic MOC. *Geophysical Research Letters*, **33**, L21603(1–4).

Acknowledgments

> *"I get by with a little help*
> *from my friends"*
> — The Beatles

At this point I would like to take the opportunity to thank all the people who have supported me during the past three years.

I thank Klaus Fraedrich for taking me as a PhD student and for giving me the opportunity to work on this interesting topic. I am grateful to him for the independence he has allowed me in my research and the interest he has shown in my work. I would also like to thank my advisor Frank Lunkeit for the great support. I am especially thankful for the open door, for answering all my questions (and for still believing that there are no stupid questions), for helping me to get the model running in the first place, and for many productive and interesting discussions.

Furthermore, I want to thank the entire group *Theoretical Meteorology* (past and present members) for great times. I am sincerely grateful to everyone, who patiently endured me taking up so much disk space... A big thanks is directed to Frank Sielmann and Edilbert Kirk for the great IT support and for saving me (and my computer) numerous times. Thanks to Kerstin for sharing many cups of coffee and for making me laugh even during the most stressful times.

I would also like to mention Peter Herrmann, who helped me at the very beginning of my work and who introduced me to the LSG ocean model.

I am very grateful for the financial support from the *Max Planck Institute for Meteorology*. This PhD project was also supported by a (non-material) scholarship from the *German National Academic Foundation* (*Studienstiftung des deutschen Volkes*).

Last but not least, I would like to thank my family and friends for being there for me and for believing in me. I don't know what I would do without your companionship and your humor, supporting me and encouraging me all the way. I especially want to mention Jenny and Denise: thank you so much, my tireless proofreaders! Angela, Paula, and Kai, thanks for being there, as always. Christian, thank you for everything.

ISSN 1614-1199